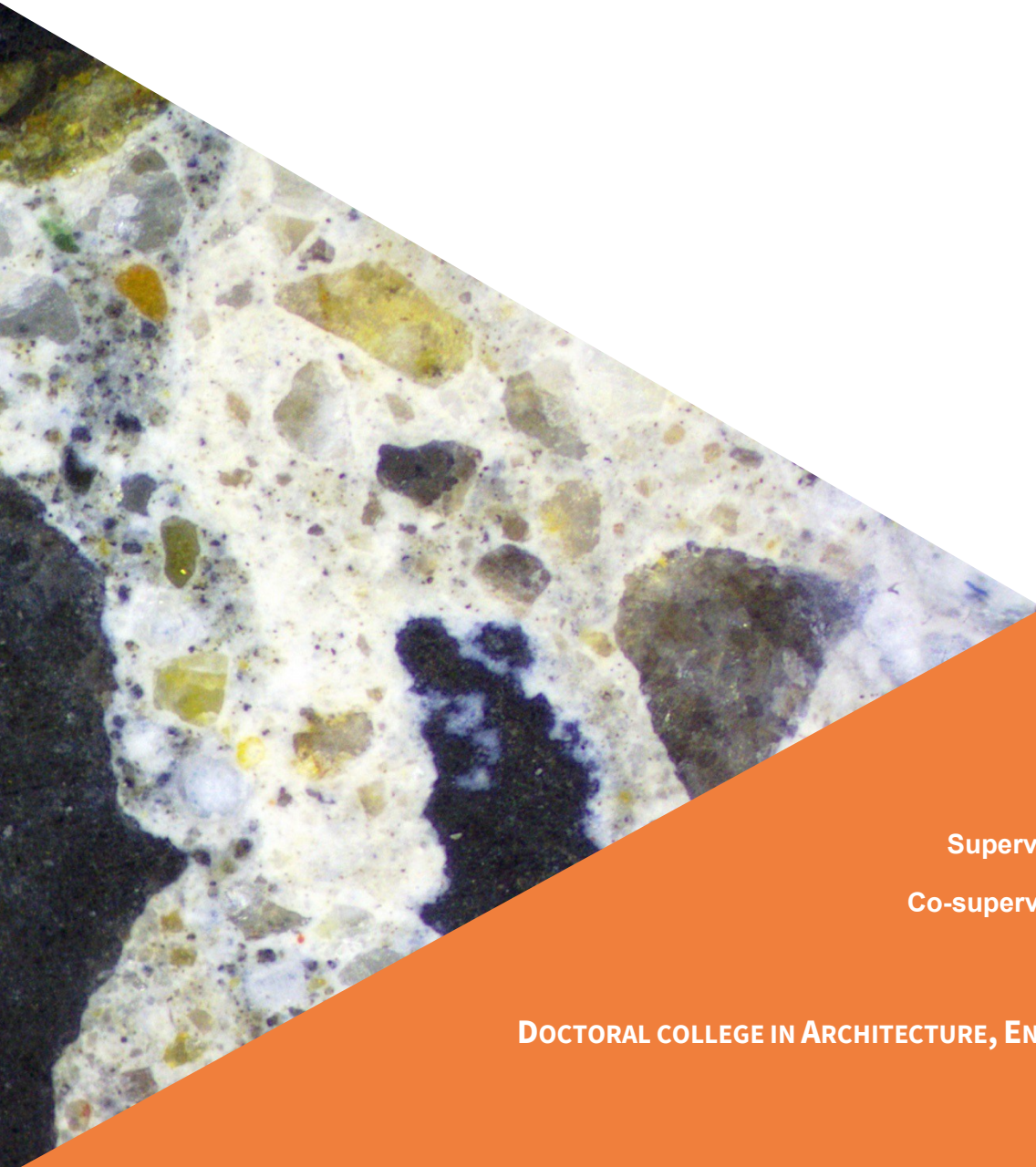# FE^2 Multiscale Modelling of Chloride Ions Transport in Recycled Aggregates Concrete

Thesis submitted in partial fulfillment of the requirements
for the degree of Doctor of Philosophy (Phd)
in Engineering Science

by

Arthur FANARA

Supervisor: Pr. Frédéric COLLIN

Co-supervisor: Pr. Luc COURARD

DOCTORAL COLLEGE IN ARCHITECTURE, ENGINEERING AND GEOLOGY

MAY 2024

Jury:

Prof. Angélique LÉONARD (President)	Université de Liège
Prof. Frédéric COLLIN (Supervisor)	Université de Liège
Prof. Luc COURARD (Co-supervisor)	Université de Liège
Prof. Alain SELLIER	INSA-Toulouse (France)
Prof. Thierry MASSART	Université Libre de Bruxelles
Prof. Sébastien REMOND	Université d'Orléans (France)
Dr. Julien HUBERT	Université de Liège

SCIENTIA

OPTIMVM

REMERCIEMENTS

Maintenant que ces quatre années de recherche se terminent, il est temps pour moi de me sentir nostalgique au travers de ces remerciements. Faire une thèse, c'est avant tout rencontrer de nombreuses personnes, échanger et passer de bons moments avec elles, et visiter des endroits magnifiques lors de conférences.

Tout d'abord, je me dois de remercier ceux sans qui tout cela n'aurait pas été possible : **Frédéric** et **Luc**, mes deux promoteurs. Je me rappelle encore avoir été appelé par Luc à venir discuter dans son bureau, un bon matin de Master 1. Discussion qui a directement tourné à une proposition de TFE et, par la suite, de thèse. Je me suis dit : "Et pourquoi pas ? C'est maintenant ou jamais après tout.". Me voilà donc embarqué dans cette aventure de 5 ans, sans trop savoir où cela allait m'amener, mais impatient de le découvrir. Rétrospectivement, je me dis que j'ai eu beaucoup de chance de vous avoir tous les deux comme promoteurs. Je pense que l'ingrédient principal qui fait le succès d'une thèse, c'est avant tout la bonne entente entre un doctorant et son ou ses promoteur(s). Je ne pouvais donc mieux tomber. Quel bonheur d'avoir pu participer à la vie de vos deux équipes en même temps. Certes, cela faisait deux fois plus de réunions, mais surtout deux fois plus de rencontres et de moments inoubliables. Luc, merci d'avoir cru en moi, depuis ta proposition d'élève-moniteur à aujourd'hui. Les team buildings que l'on a vécus m'ont permis de voir quel homme formidable il y a derrière ce professeur sérieux que j'avais pu connaître en cours. Frédéric, merci pour nos fameuses pauses café, qui étaient tout autant un moyen de parler de tout et de rien, comme de réaliser des réunions informelles. Tu es certainement la source de mon addiction au café, mais ça en valait la peine. Ta bonne humeur à toute épreuve et ton sérieux tout au long de l'accompagnement de mon travail m'ont permis d'arriver où j'en suis aujourd'hui.

Outre les promoteurs, ce sont les équipes toutes entières qui m'ont fait vivre de merveilleux moments au cours de ces quatre années. Merci donc à mes collègues proches, anciens comme nouveaux. Tout d'abord, merci à **Julien** pour ton accompagnement lors de mon travail de fin d'étude, ainsi que lors de ma thèse. Nos nombreuses discussions au détour d'une expérience ou d'un couloir m'ont fait perdre toute notion du temps. Merci également de m'avoir permis de jouer l'incruste au Canada, c'était vraiment chouette. J'espère que tu te plais bien aux States, mais n'oublie pas d'en revenir !
Merci ensuite à **Gilles** pour ton accueil dans ton bureau. Il faut dire que depuis ce jour ensoleillé d'Août ou j'ai emménagé, on ne s'est plus vraiment quitté. Tu étais ma motivation, toi qui travaillais tout le temps alors que moi je restais sur mon téléphone. Nos discussions permettaient de faire de petites pauses au cours de la journée, et les lundis n'étaient plus forcément maussades.
Merci à **Sophie D.** pour nos (trop) nombreuses pauses café, nos toutes aussi nombreuses discussions, notamment dans le cadre de ton EVJF et de ton mariage, ainsi que pour nos balades à Aussois.

Arthur.

ABSTRACT

Reinforced concrete structures are subjected to various degradation processes throughout their service life. Chloride-induced corrosion is one of the most common; it usually occurs by the roads where de-icing salts are used, as well as in coastal regions. This corrosion leads to a continuous increase in maintenance costs for bridges and other infrastructure.

The use of Recycled Concrete Aggregates (RCA) instead of Natural Aggregates (NA) in concrete can worsen durability concerns due to the adherent mortar paste that reduces the mechanical and durability properties of concrete. Nevertheless, Recycled Aggregates Concrete (RAC) is a sustainable approach for reducing waste and preserving natural resources. Therefore, understanding chloride ingress in recycled aggregate concrete is crucial for its development and use.

An extensive experimental campaign was conducted on concretes produced with 100% natural aggregate or recycled concrete aggregate, as well as equivalent mortar and cement pastes, in order to evaluate their intrinsic properties in terms of water transport and chloride ion ingress. It enabled a better understanding of the effect of replacing NA with RCA in concrete. The findings revealed that recycled aggregate concrete is more porous and permeable, and promotes the diffusion of chloride ions in comparison to Natural Aggregates Concrete (NAC).

The Finite Element Square (FE²) method was subsequently used to develop a multiscale chemo-hydraulic model, which was implemented in Lagamine software (from the University of Liège). The model was verified numerically, analytically, and then calibrated experimentally. The model's constitutive equations are based on intrinsic properties obtained from experimental results. The model demonstrated its accuracy in replicating experiments and providing additional insight into chloride ingress in both saturated and unsaturated concrete.

The implementation of Water Retention Curves (WRC) and their hysteresis takes into account unsaturated conditions, following an empirical model by Van Genuchten (1980). The water retention curves are calibrated experimentally and then used to assess the degree of water saturation in concrete, which is a crucial factor for the ingress of chloride ions.

The results suggest that the durability of recycled aggregate concrete may be comparable to that of natural aggregate concrete under specific mixture quality and environmental conditions. A modelling application was carried out to evaluate this, replicating actual conditions on a maritime lock wall.

Résumé

Les structures en béton armé sont soumises à divers processus de dégradation tout au long de leur durée de vie. L'un de ces processus est la corrosion induite par les chlorures, qui se produit en raison de la pénétration d'ions chlorure dans le béton, dans les zones proches des routes où des sels de déverglaçage sont utilisés, ainsi que dans les régions côtières. Cette corrosion entraîne une augmentation constante des coûts d'entretien des ponts et autres infrastructures. L'utilisation de granulats de béton recyclés au lieu de granulats naturels dans le béton peut aggraver les problèmes de durabilité en raison de la pâte de mortier adhérente qui réduit les propriétés mécaniques et de durabilité du béton. Néanmoins, le béton de granulats recyclés est une approche durable qui permet de réduire la quantité de déchets placés en enfouissement technique et de préserver les ressources naturelles. Il est donc essentiel de comprendre la pénétration du chlorure dans le béton de granulats recyclés pour pouvoir le développer et l'utiliser.

Une vaste campagne expérimentale a été menée sur des bétons composés à 100% d'agrégats naturels ou d'agrégats de béton recyclé, ainsi que sur des mortiers et pâtes de ciment, afin d'évaluer leurs propriétés intrinsèques en termes de transport d'eau et de pénétration des ions chlorure. Cela a permis de mieux comprendre l'effet du remplacement des granulats naturels par des granulats de béton recyclé dans le béton. Les résultats ont révélé que le béton de granulats recyclés est plus poreux et perméable, et qu'il favorise la diffusion des ions chlorure par rapport au béton de granulats naturels.

La méthode des éléments finis au carrés a ensuite été utilisée pour développer un modèle chimio-hydraulique à double échelle, qui a été implémenté dans le logiciel Lagamine (de l'Université de Liège). Le modèle a été vérifié numériquement et analytiquement, puis calibré expérimentalement. Les équations constitutives du modèle sont basées sur les propriétés intrinsèques obtenues à partir des résultats expérimentaux. Le modèle a démontré sa précision en reproduisant les expériences et en permettant une meilleure compréhension de la pénétration d'ions chlorure dans le béton saturé et non saturé.

La mise en œuvre des courbes de rétention d'eau et de leur hystérésis prend en compte les conditions non saturées, suivant un modèle empirique de Van Genuchten (1980). Les courbes de rétention d'eau sont calibrées expérimentalement et ensuite utilisées pour évaluer le degré de saturation en eau du béton, qui est un facteur crucial pour la pénétration des ions chlorure.

Les résultats suggèrent que la durabilité du béton de granulats recyclés peut être comparable à celle du béton de granulats naturels dans des conditions spécifiques de qualité du mélange et d'environnement. Une application de modélisation a été réalisée pour évaluer cela, reproduisant les conditions réelles d'un mur d'écluse maritime.

PREFACE

The research conducted for this thesis has resulted in numerous presentations at international conferences, as well as several articles in conference proceedings and scientific journals. Below, you will find all available published work, along with their direct link to Orbi.

A new paper should soon be proposed at Cement and Concrete Research, on the subject of the hysteresis of the water retention curve, as well as two papers in proceedings (with a SCOPUS reference): one for the ECCOMAS 2024 and the other for the FIB ICCS 2024.

Update: 28-05-2024

Article in Scientific Journals

1. Fanara, A., Courard, L., & Collin, F. (2024). Numerical FE^2 Study of Chloride Ingress in Unsaturated Recycled Aggregates Concrete. Available at SSRN: `https://doi.org/10.2139/ssrn.4756062`. ORBI: `https://hdl.handle.net/2268/317438`. *Currently under review at Cement and Concrete Research*.

2. Fanara, A., Courard, L., Collin, F., & Hubert, J. (24 February 2022). Transfer Properties in Recycled Aggregates Concrete: Experimental and Numerical Approaches. Construction and Building Materials, 326, 126778. DOI: `https://doi.org/10.1016/j.conbuildmat.2022.126778` ORBI: `https://hdl.handle.net/2268/288432`
Scopus citations: 4 (4 without autocitations) CiteScore 2022: 12.4 – SNIP 2022: 2.214 – SJR 2022: 1.888

Article in Proceedings

1. Fanara, A., Hubert, J., Michel, F., Collin, F., & Courard, L. (05 July 2023). Étude expérimentale et numérique de l'influence des granulats recyclés sur les cycles humidification séchage dans un béton. Journées Scientifiques du Réseau (RF)²B, Montréal, Canada. `https://hdl.handle.net/2268/305019`

2. Fanara, A., Courard, L., & Collin, F. (2023). Numerical and Experimental Study of Chloride Ion Transport in Recycled Aggregates Concrete. In Special Issue - NoMaD 2022 (Vol. 40 No.2). Academic Journal of Civil Engineering. ORBI: `https://hdl.handle.net/2268/299774`

3. Courard, L., Grigoletto, S., Muy, Y., Michel, F., Fanara, A., & Hubert, J. (2023). NEW DEVELOPMENTS IN THE RECYCLING OF CONSTRUCTION AND DEMOLITION WASTES FOR THE CONCRETE INDUSTRY. In J. Sustercic, Multi-component fine-grained concretes and mortars. Ljubljana, Slovenia: CIP Katalozni zapis o publikaciji

- Narodna in univerzitetna knjiznica Ljubljana. ORBI: `https://hdl.handle.net/2268/308562`

4. Fanara, A., Courard, L., & Collin, F. (25 November 2022). Development of a FE² Multiscale Model of Chloride Ions Transport in Recycled Aggregates Concrete. ECCOMAS CONGRESS 2022. DOI: `https://doi.org/10.23967/eccomas.2022.088` ORBI: `https://hdl.handle.net/2268/297041`

5. Fanara, A., Courard, L., & Collin, F. (2022). FE² multiscale modelling of chloride ions transport in recycled aggregates concrete. In Günther Meschke, Bernhard Pichler, Jan G. Rots (Eds.), Computational Modelling of Concrete and Concrete Structures (1st, pp. 66-75). CRC Press. DOI: `https://doi.org/10.1201/9781003316404-8` ORBI: `https://hdl.handle.net/2268/291345`

Presentations at International Conferences

1. Fanara, A. (05 July 2023). Étude expérimentale et numérique de l'influence des granulats recyclés sur les cycles humidification séchage dans un béton. Journées Scientifiques du Réseau (RF)²B, Montréal, Canada. ORBI: `https://hdl.handle.net/2268/305009`

2. Fanara, A., Courard, L., & Collin, F. (16 November 2022). Numerical and Experimental Study of Chloride Ion Transport in Recycled Aggregates Concrete. Nouveaux Matériaux et Durabilité 2022 (NoMaD), Montpellier, France. ORBI: `https://hdl.handle.net/2268/296935`

3. Fanara, A., Courard, L., & Collin, F. (06 July 2022). Development of a FE² multiscale model for chloride ingress inside unsaturated concrete. LAGASHOP 2022, Villard-de-Lans, France. ORBI: `https://hdl.handle.net/2268/293200`

4. Fanara, A., Courard, L., & Collin, F. (06 June 2022). Development of a FE² Multiscale Model of Chloride Ions Transport in Recycled Aggregates Concrete. ECCOMAS CONGRESS 2022, Lillestrom, Oslo, Norway. ORBI: `https://hdl.handle.net/2268/291996`

5. Fanara, A., Courard, L., & Collin, F. (23 May 2022). FE² Multiscale Modelling of Chloride Ions Transport in Recycled Aggregates Concrete. EURO-C 2022, Vienne, Austria. ORBI: `https://hdl.handle.net/2268/291210`

Others

1. Fanara, A. (2022). Poster Journée UEE 2022: FE² Multiscale Modeling of Chloride Ions Ingress in Recycled Aggregates Concrete. ORBI: `https://hdl.handle.net/2268/296931`

2. Fanara, A. (2021). 347th CERES Conference - FE² Multiscale Modelling of Chloride Ions Transport in Recycled Aggregates Concrete. 347ième Conférence CERES, Liège, Belgium. ORBI: `https://hdl.handle.net/2268/265310`

Contents

LIST OF FIGURES

XIV

Glossary

Acronyms

BET	Brunauer-Emmet-Teller (model)
CDW	Construction and Demolition Wastes
CRP	Constant Rate Period
CTP	Centre Terre et Pierre
DEM	Discrete Element Method
DOF	Degree Of Freedom
E-CP	Equivalent Cement Paste
E-M	Equivalent Mortar
EU/EU-27	European Union
FEM	Finite Element Method
FE^2	Finite Element Square (method)
IDE	Integrated Development Environment
ITZ	Interfacial Transition Zone
NA	Natural Aggregates
NAC	Natural Aggregates Concrete
PSD	Particle Size Distribution
RAC	Recycled Aggregates Concrete
RCA	Recycled Concrete Aggregates
RH	Relative Humidity
RVE	Representative Volume Element
SeRaMCo	Secondary Raw Materials for Concrete Precast Products
SF	Surface Fraction
UEPG	Union Européenne des Producteurs de Granulats

W/C	Water-to-cement ratio	
WA	Water Absorption	
WAI	Water Absorption by Immersion	
WP	Work Package	
WRC	Water Retention Curve	

Constants

χ_w	Water compressibility	5×10^{-10} Pa at 20°C
ϵ_0	Permittivity of a vacuum	8.854×10^{-12} C/(V.m)
F	Faraday's constant	9.64846×10^{-4} C/mol
g	Gravitational acceleration	9.81 m/s^2
M	Molar mass of water	18.016 g/mol
p_{atm}	Atmospheric pressure	101325 Pa
R	Universal constant of ideal gases	8.3143 J.mol/K
U_c	Activation energy of chloride diffusion	35 kJ/mol

Concrete: a Porous Material

α_{vG}	Air-entry pressure (van Genuchten model)	[Pa]
η	Volume fraction (Theory of mixture)	-
ρ_i	Density of the phase i	[kg/m^3]
σ_{ij}	Surface tension between the phases i and j	[N/m]
θ	Contact angle	[°]
e	Void ratio	-
h	Degree of hydration	-
h_c	Capillary pressure head	[m]
m	Mass	[kg]
m_{vG}	Model parameter associated to the curvature of the water retention curve	-
n	Porosity	[% mass]
n_{vG}	Model parameter associated to the rate of desaturation of the porous system	-
p_c	Capillary pressure	[Pa]
p_g	Gas pressure	[Pa]
p_l	Liquid pressure	[Pa]

r_c	Capillary radius	[m]
RH	Relative Humidity	-
s	Matrix suction	[Pa]
S_{res}	Residual degree of saturation of the porous medium	-
S_r	Degree of saturation of the porous medium	-
S_{sat}	Maximum degree of saturation of the porous medium	-
T	Temperature	[K]
V	Total volume of the porous medium	[m^3]
V_g	Volume of the gas phase	[m^3]
V_l	Volume of the liquid phase	[m^3]
V_s	Volume of the solid phase	[m^3]
V_v	Pore volume	[m^3]
V_{cp}	Volume of the capillary pores	-
w/c	Water-to-cement ratio	-

Degradation Processes

α	First binding coefficient for the Langmuir isotherm	-
β	Second binding coefficient for the Langmuir isotherm	-
ϵ_r	Relative permittivity of water	[C/(V.m)]
Φ	Electrochemical potential	[V]
ϕ	Open porosity of concrete	-
ρ_c	Density of saturated concrete	[kg/m^3]
ρ_s	Density of solid state concrete	[kg/m^3]
C_b	Concentration of bound chlorides	-
C_f	Concentration of free chlorides	-
C_s	Surface concentration of chloride ions	-
C_t	Concentration of total chlorides	-
D	Diffusion coefficient of chloride ions	[m^2/s]
D_{app}	Apparent diffusion coefficient of chloride ions	[m^2/s]
D_{ref}	Effective diffusion coefficient of chloride ions	[m^2/s]
F	Flow of chloride ions	[kg/(m^2.s)]

K_b	Binding capacity of concrete towards chloride ions	-
n_b	Model parameter governing the binding intensity	-
q	Convection flux of chloride ions	[m/s]
w_e	Water content of the porous system	-
z	Charge number of the ionic species	-

Experimental Analysis

μ_w	Dynamic viscosity of water	$[\mathrm{kg/(m.s)}]$
ρ_d	Dry density	$[\mathrm{kg/m^3}]$
ρ_h	Humid bulk density	$[\mathrm{kg/m^3}]$
ρ_w	Water density	$[\mathrm{kg/m^3}]$
ρ_a	Apparent density	$[\mathrm{kg/m^3}]$
ρ_{rd}	Real density	$[\mathrm{kg/m^3}]$
A	Cross-sectional area of the member	$[\mathrm{m^2}]$
b	Hysteresis fitting parameter [Zhou et al., 2012]	[-]
e	Width of the sample	[m]
H	Height of the member	[m]
h	Hydraulic head	[m]
I	Intensity of the electric current	[A]
i	Hydraulic gradient	-
J	Ionic flow of chloride ions	$[\mathrm{kg/(m^2.s)}]$
$K(10°\mathrm{C})$	Water-saturated conductivity corrected at $10°\mathrm{C}$	[m/s]
k_{int}	Intrinsic permeability of the porous medium	$[\mathrm{m^2}]$
K_{sat}	Water-saturated conductivity of the porous medium	[m/s]
m_{dry}	Dry mass	[g]
m_{hum}	Humid mass (in the air)	[g]
m_{sat}	Saturated mass (under water)	[g]
n	Porosity	[% mass]
n_w	Water accessible porosity	[% volume]
Q	Electric charge passing through the sample	[C]
Q_w	Discharge of water	$[\mathrm{m^3/s}]$

$X_{0.4\%t.m.}$	Depth at which the chloride content reaches 0.4% of the binder mass	[m]
WA	Water Absorption	[% mass]
WA$_{NA}$	Water absorption of the natural aggregates	[% mass]
WA$_{RCA}$	Water absorption of the recycled aggregates	[% mass]

Multiscale Multiphase Modelling

$\alpha_{b.l.m.}$	Mass transfer coefficient of the Boundary Layer Model	[m/s]
α_{vG}	Air-entry pressure (van Genuchten model)	[Pa]
$\bar{g}$	Gradient of the scalar field	-
$\bar{J}$	Volume average of the flux inside the subscale	-
$\bar{q}$	Vapour flux between the ambient air and the exchange surface	[kg/m^2.s]
$\bar{x}$	Center of the subscale	[m]
Γ	Boundaries of the subscale	-
μ_g	Dynamic viscosity of gas	[kg/(m.s)]
μ_w	Dynamic viscosity of water	[kg/(m.s)]
Ω	Domain of the subscale	-
ϕ	Scalar field	-
ϕ_f	Fluctuation part of the scalar field	-
ϕ_M	Macroscale part of the scalar field	-
ϕ_s	Subscale part of the scalar field	-
ρ_g	Gas density	[kg/m^3]
ρ_w	Water density	[kg/m^3]
ρ_{g0}	Initial gas density	[kg/m^3]
$\rho_{v,air}$	Vapour density of the ambient air	[kg/m^3]
$\rho_{v,surf}$	Vapour density at the surface of the sample	[kg/m^3]
ρ_{w0}	Initial water density	[kg/m^3]
b	Fitting parameter for the hysteresis model [Zhou et al., 2012]	-
C	Chloride ions mean concentration	-
C_0	Chloride ions concentration at the limit state condition	-
C_M	Concentration in chloride ions at the macroscale	-
C_m	Concentration in chloride ions at the mesoscale	-

D	Chloride ions diffusion coefficient	$[\mathrm{m^2/s}]$
ds	Increment of suction	Pa
g_i	Gravitational acceleration along the i direction	$[\mathrm{m/s^2}]$
J	Flux	-
$K_{i,j}$	Term i of the stiffness matrix obtained by perturbation j	$[\mathrm{kg/m^3}]$
k_{int}	Intrinsic water permeability of the porous matrix	$[\mathrm{m^2}]$
$k_{rel,g}$	Relative gas permeability of the porous matrix	$[\mathrm{m^2}]$
$k_{rel,w}$	Relative water permeability of the porous matrix	$[\mathrm{m^2}]$
L_c^M	Characteristic length of the macroscopic field	$[\mathrm{m}]$
l_c^s	Characteristic length of the subscale field	$[\mathrm{m}]$
m_{vG}	Van Genuchten model parameter	-
N_L	Interpolation function of node L	
n_{vG}	Van Genuchten model parameter	-
$P_{g,average}$	Average gas pressure inside the RVE	$[\mathrm{Pa}]$
P_{g0}	Initial gas pressure inside the RVE	$[\mathrm{Pa}]$
$P_{w,average}$	Average water pressure inside the RVE	$[\mathrm{Pa}]$
P_{w0}	Initial water pressure inside the RVE	$[\mathrm{Pa}]$
s	Suction	$[\mathrm{Pa}]$
S_c	Chloride ions storage term	-
S_g	Gas storage term	$[\mathrm{kg/m^3}]$
S_w	Water storage term	$[\mathrm{kg/m^3}]$
$S_{r,w}$	Water saturation degree of the porous matrix	$[\mathrm{m^2}]$
S_{res}	Residual degree of saturation of the porous medium	-
S_{sat}	Maximum degree of saturation of the porous medium	-
u	Fluid flow	$[\mathrm{m/s}]$
$v_{i,\text{homogenised}}^c$	Homogenised chloride ions flow rate along the i direction	$[\mathrm{m/s}]$
$v_{i,\text{homogenised}}^g$	Homogenised gas flow rate along the i direction	$[\mathrm{m/s}]$
$v_{i,\text{homogenised}}^w$	Homogenised water flow rate along the i direction	$[\mathrm{m/s}]$
v_i^c	Chloride ions flow rate per unit area	$[\mathrm{m/s}]$
v_i^g	Gas flow rate per unit area	$[\mathrm{m/s}]$

v_i^w	Water flow rate per unit area	[m/s]

Numerical Results

u	Fluid flow	[m/s]
μ_w	Dynamic viscosity of water	[kg/(m.s)]
b	Fitting parameter for the hysteresis model [Zhou et al., 2012]	-
C_0	Limit state chloride concentration	-
C_s	Chloride concentration at the surface	-
D	Diffusion coefficient	[m^2/s]
ds	Increment of suction	Pa
k_{int}	Intrinsic water permeability of the porous matrix	[m^2]
P_w	Water pressure	[Pa]
t	Time	[s]
x	Depth inside the sample	[m]

Application to a Real Life Scenario

α_{vG}	Air-entry pressure (van Genuchten model)	[Pa]
ρ_d	Dry density	[kg/m^3]
b	Fitting parameter for the hysteresis model [Zhou et al., 2012]	-
C_s	Chloride concentration at the surface	-
n	Porosity	[% volume]
n_{vG}	Van Genuchten model parameter	-
P_w	Water pressure	[Pa]
RH	Relative Humidity	-
T	Temperature	[K]

1

GLOBAL CONTEXT

Contents

1.1 Introduction

The construction industry is one of the most important industries worldwide. Concrete is the most widely used material in this industry, with an estimated production of 1.2 billion tons in 2019, according to the European Cement Association for the European Union (EU-27) [CEMBUREAU, 2021, Pacheco et al., 2023]. Concrete is composed of water, cement, sand, and aggregates, with the latter accounting for 75% of the concrete volume. The construction aggregates sector is the world's largest non-energy extractive industry, surpassing fossil fuels [Gebremariam et al., 2020]. According to the European Aggregates Association's (UEPG) Annual Review 2020-2021, Natural Aggregates (NA) extraction in the EU-27 reached 2.55 billion tons in 2019, with 45% of that volume used exclusively for concrete [UEPG, 2021, Pacheco et al., 2023].

The construction industry is one of the most energy-consuming industries globally, particularly in the production of concrete and cement-based materials. Additionally, the Construction and Demolition sector generates a significant amount of waste (CDW), a stream that is expected to increase over time as the existing building environment ages. EUROSTAT reports that CDW accounts for 36% of the waste stream generated in the EU-27, with a total of 800 million tons in 2021, including excavated soils [EUROSTAT, 2023, Hubert et al., 2023, Pacheco et al., 2023]. In 2016, CDW generation, excluding excavated soils, was 374 million tons [European Environment Agency, 2020]. As shown in Figure 1.1, CDW generation continues to increase over time in the EU-27 and Belgium.

The generated CDW is heterogeneous and contains various materials, including concrete, brick, glass, wood, and gypsum. Concrete is estimated to make up between 32% and 75% of the total CDW volume [Meyer, 2008, Zhao et al., 2020].
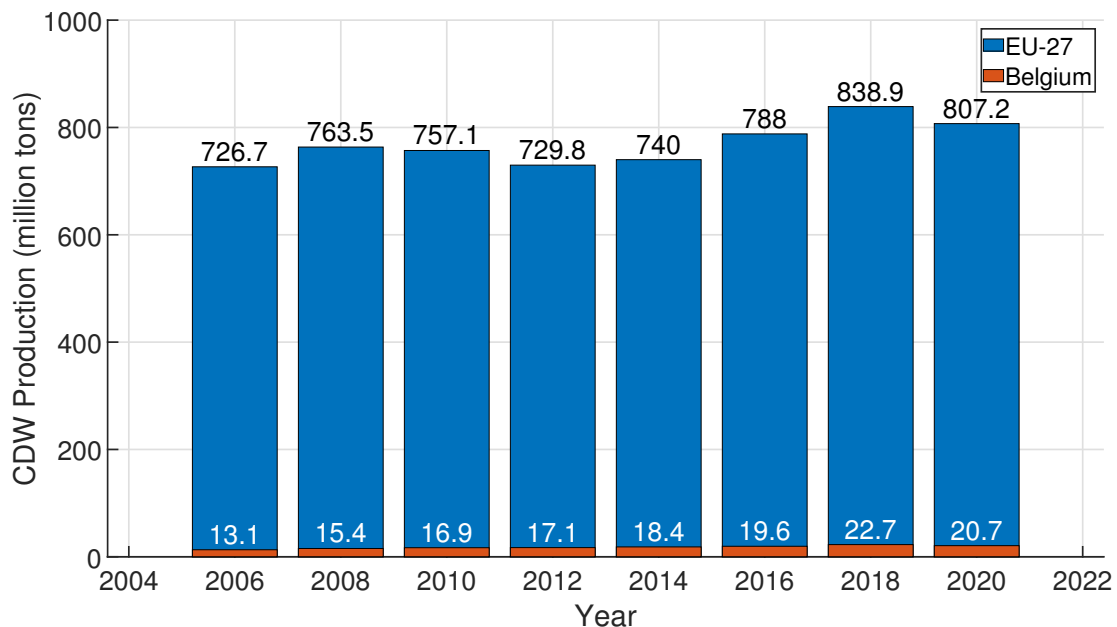
Figure 1.1: Generation of Construction and Demolition Waste in Europe (EU-27) and in Belgium (from [EUROSTAT, 2023]).

The EU Waste Framework Directive (2008/98/EC) states in Article 11(2)(b) that members of the EU must take appropriate actions to ensure that 70% of non-hazardous CDW are

prepared for re-use, recycling and other material recovery (including backfilling operations) using waste as a substitute for other materials, by 2020 [EU, 2008]. The European Commission has recently taken initiatives for the construction sector, including the European Green Deal, the New European Bauhaus, the Circular Economy Action Plan, and the EU Renovation Wave [Pacheco et al., 2023].

In the EU-27, around 80% of non-hazardous CDW is recycled, while the remaining is either backfilled (7%), landfilled (7%) or burned for energy recovery (6%). In many states, backfilling is reported as recycling in order to meet legal requirements, thus reducing the true recycling rate [Pacheco et al., 2023].

The European Aggregates Association's 2019-2020 annual review revealed that recycled and reused aggregates accounted for 10.6% (327 million tons) of total aggregate production in the EU in 2019. In Belgium, this figure rises to 21%, which is noteworthy but still insufficient [UEPG, 2020].

The construction industry is exploring the use of CDW as a substitute for natural materials and is developing processes to incorporate recycled products into building materials. Recycled Concrete Aggregates (RCA) are being studied as a replacement for Natural Aggregates (NA) in new concrete materials. RCA is made up of fine and coarse particles that contain NA and residual adherent mortar. An example of RCA is shown in Figures 1.2 and 1.3. Therefore, RCA can serve as a secondary raw material that can replace primary materials, aligning with the strategic goals of the European Union [Hubert et al., 2023, Pacheco et al., 2023]. The scientific community has studied RCA for years, arguing that it is a technically suitable material for use in structural concrete. However, the adherent mortar paste of the RCA induces differences in the behaviour of Recycled Aggregates Concrete (RAC) compared to Natural Aggregates Concrete (NAC).
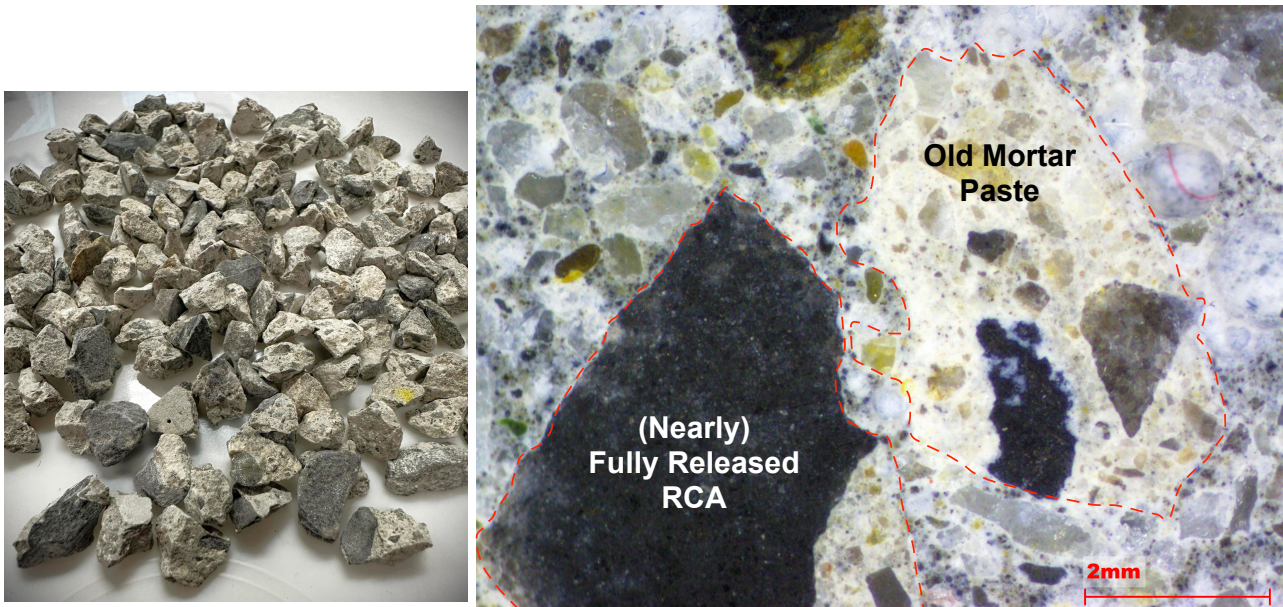
Figure 1.2: Recycled Concrete Aggregates (used in this work).

Figure 1.3: Recycled Aggregate Concrete (RAC) with two types of Recycled Concrete Aggregates (RCA): on the left, a (nearly) fully released RCA, with a small amount of adherent cement paste. On the right, a RCA made of a conglomerate of small NA embedded into a mortar matrix.

Currently, RCA is primarily used in low-grade applications such as backfill or road construction. Only a negligible amount of RCA is used in concrete applications, but promoting its use in concrete could have several benefits. Firstly, it would reduce the amount of CDW disposed of, which has a local impact on the construction sector. Secondly, it would reduce the amount of NA extracted. Finally, the overall carbon footprint of RAC is lower than that of NAC [Braga et al., 2017, Zhao et al., 2020, Sabău et al., 2021], mainly due to transportation [Fraj & Idir, 2017].

The scientific community has extensively studied RCA over the last few decades, characterising its mechanical and durability properties through multiple means. While the mechanical performance of RAC meets the needs of the construction sector [Fathifazl et al., 2011, Lovato et al., 2012, Biglarijoo et al., 2017, Zhao et al., 2018], its material behaviour, particularly in terms of durability properties, is not yet fully understood [Levy & Helene, 2004, Chen & Mahadevan, 2008, Debieb et al., 2010, Arredondo-Rea et al., 2012]. Substituting NA with RCA increases the heterogeneity of the concrete, making its material behaviour more difficult to understand. While it is possible to produce RAC with excellent durability properties, this comes at the expense of increased cement consumption, which offsets the smaller carbon footprint associated with the use of RCA.

The limited substitution rate of NA by RCA in concrete may be due to a poor understanding of the material behaviour of RAC with respect to durability. Reinforced concrete buildings are typically designed to have a service life of at least a century, and using RAC without being sure that this promise will be met is a gamble. The upkeep and restoration of reinforced concrete structures incur substantial costs, which are continuously rising as the built infrastructures age and environmental conditions worsen [Courard & Bissonnette, 2016]. Chloride-induced corrosion is the primary cause of degradation of reinforced concrete structures in areas near roads where de-icing salts are commonly used, as well as in coastal zones [Tian et al., 2019]. Chloride ions from de-icing salts or seawater can penetrate the concrete's porous system and reach the steel reinforcement. If recycled aggregates are used, chloride ions can also be sourced from previous contamination of the parent concrete [Debieb et al., 2010, Diotti et al., 2020]. When the concentration at those reinforcements exceeds a certain threshold, corrosion of the steel begins. This leads to pitting and loss of section, eventually reducing the mechanical performance of the reinforcement and ultimately resulting in structural failure [Tian et al., 2019, Li & Song, 2022].

The use of RAC in certain conditions may have a negative impact on the service life of the structure. This is due to the increased porosity and water absorption that is often associated with the use of RCA. Harmful ions diffuse through the porous system of concrete with the help of water: the greater the porosity and water absorption, the faster they can reach greater depths. Therefore, it is essential to gain a better understanding of the material behaviour of Recycled Aggregates Concrete concerning durability properties, such as chloride ion diffusion. The following section presents the specificities of RCA, followed by an apprehension of concrete durability, with a focus on chloride-induced corrosion.

1.2 Recycled Concrete Aggregates

Aggregates account for approximately 75% of the total concrete volume. They can be Natural Aggregates (NA), industrial aggregates, or recycled aggregates, specifically Re-

cycled Concrete Aggregates (RCA) for the most part. The properties of these aggregates have a significant impact on concrete performance, and it is necessary for these aggregates to comply with various chemical, geometrical, and physical properties [Pedro et al., 2014b, Pacheco et al., 2023]. Standards have already accounted for the difference between natural aggregates and recycled concrete aggregates, with recommendations for the use of RCA in concrete, or more specifically for RAC directly [CEN, 2008, CEN, 2013, Pacheco et al., 2023]. The literature often discusses a maximum substitution rate of NA by RCA, with around 30% considered optimal [Gonzalez & Etxeberria, 2014]. This is higher than what is currently available from CDW if all concrete is produced with partial substitution of NA by RCA [Pacheco et al., 2023]. In Belgium, the standard NBN B15-001:2022 indicates the maximum substitution rate in reinforced concrete to be up to 30% for concrete class lower or equal to C30/37. For non-reinforced concrete, the maximum substitution rate increases to 50% [Pacheco et al., 2023]. There are also requirements depending on the environmental class of the concrete. For example, if the concrete may be in contact with de-icing salts, the maximum substitution rate is reduced from 30% to 0%.

The production of RCA requires the crushing, screening and possibly washing of the concrete CDW. Various fragmentation techniques are available to convert demolished concrete elements into usable RCA, including impact crushers, jaw crushers, and cone crushers. Each type of crusher has its advantages and drawbacks, particularly in terms of aggregate size and morphology, production of fines, and energy consumption. The production method of RCA is the first factor that may affect the quality of the aggregates.
Another important factor to consider is the management of CDW at a local level, as well as the option to carry out selective demolition [Pacheco et al., 2023]. There are two types of CDW management plants: fixed plants and mobile plants. Fixed plants group together CDW from multiple sites, which can provide a greater number of equipment for the production of RCA. However, this method has less control over the quality of incoming wastes. On the other hand, mobile plants often comprise only one crusher and sieve, but they have better quality control of the wastes recycled. Selective demolition may also be performed to ensure the greater quality of the RCA produced.

One significant disadvantage of crushing concrete elements to produce recycled aggregates is the creation of microcracks. This, in turn, makes the recycled aggregate concrete more susceptible to capillary absorption [Nagataki et al., 2004]. Recycled aggregates are made up of natural aggregates (65-70% by volume) embedded in a hardened, porous, and cracked mortar matrix (30-35% by volume), resulting in higher water absorption than natural aggregates [Hussain et al., 2000, García-González et al., 2014, Hu et al., 2018, Bao et al., 2020].
New fragmentation techniques have been developed to minimise intra-granular breaks, with the aim of producing mono-mineral particles that have a particle size distribution similar to that of natural aggregates. These techniques include grinding, microwave treatment, heating treatment, electro-dynamic fragmentation, and high-performance sonic pulses [Salomao, 2019]. The potential of these new techniques is to further release natural aggregates from the hardened adherent mortar, resulting in better quality RCA. However, at present, they are not commercially viable. Additionally, their energy consumption may be too high, which would offset the ecological benefits of RCA.

There are three types of adherent mortars in recycled aggregates, mainly depending on the size of the RCA obtained [Akbarnezhad et al., 2013]:

- Coarser RCA often consist of a layer of cementitious mortar that adheres to the surface of a coarse natural aggregate;

- Adherent mortar can also be found in a conglomerate RCA that consists of multiple smaller NA and cementitious mortar that binds them together;

- Smaller RCA that are primarily composed of mortar residues with little or no NA.

The amount of residual mortar in RCA is influenced by several parameters, including the initial paste content and its properties, as well as the mechanical properties of the Interfacial Transition Zone (ITZ) at the interface between the initial natural aggregates and the mortar paste [Rangel et al., 2020]. As previously mentioned, the amount of adherent cement paste is also influenced by the crushing process and particle size of the RCA, which are considered external parameters [Akbarnezhad et al., 2013, Belin et al., 2014, Pedro et al., 2014b, Hubert et al., 2023].

According to the literature, the cement content in coarse RCA decreases as the diameter of the RCA increases [Etxeberria et al., 2007, de Juan & Gutiérrez, 2009, Akbarnezhad et al., 2013, Florea & Brouwers, 2013, Pedro et al., 2014b, Zhao et al., 2017, Guo et al., 2018, Hubert et al., 2023]. de Juan et al. (2019) discovered that the 4/8mm fraction had a cement content ranging from 33% to 55% (by mass), while the larger 8/16mm fractions had a mortar content ranging from 23% to 44% [de Juan & Gutiérrez, 2009]. Etxeberria et al. (2007) found that the cement content varied from 20% to 40% (by mass) for 10/25mm and 4/10mm RCA, respectively [Etxeberria et al., 2007]. Zhao et al. (2017) reported that the cement content for 14/20mm and 0/2mm RCA ranged from 10% to 17%, respectively [Zhao et al., 2017]. For this reason, fine recycled concrete aggregates are less suitable for use in concrete [Pacheco et al., 2023].
These results must be referred to with precaution as a large scatter can be observed due to the overlapping influence of the parameters mentioned above, as well as due to the diversity of methods available to characterise this mortar content [de Juan & Gutiérrez, 2009, Hubert et al., 2023, Zhao et al., 2022].
A weaker parent concrete may result in RCA with a smaller amount of adherent mortar, as it sheds more easily during the crushing process, increasing the liberation degree of the NA. However, it is not known with certitude if the properties of the parent concrete have a greater influence on the quantity of adherent mortar or if it is the crushing process that prevails [Akbarnezhad et al., 2013].

The properties of RCA are those of a heterogeneous multiphasic material. The overall quality of the RCA worsens with an increase in adherent mortar content, which has weaker properties than natural aggregates. It is widely known in the scientific community that RCA have a lower density, higher porosity and water absorption capacity, and higher Los Angeles abrasion coefficient than natural aggregates [Rao et al., 2007, Debieb et al., 2010, Xiao et al., 2012, Akbarnezhad et al., 2013, Pedro et al., 2014a, Xuan et al., 2017, Hu et al., 2018, Ghorbani et al., 2019, Thomas et al., 2013, Sun et al., 2020, Rangel et al., 2020, Russo & Lollini, 2022].
The properties of Recycled Aggregates Concrete made from RCA are usually negatively affected by the substitution ratio of NA with RCA [José M.V Gómez-Soberón, 2002, Guo et al., 2018].

Another concern is the difference of specific area. The greater specific surface area of RCA, combined with the higher water absorption of the mortar content, reduces the workability of

fresh concrete. To address this issue, the water-to-cement ratio is often increased, which can lead to an increase in the porosity and permeability of concrete [Guo et al., 2018, Tian et al., 2019].

However, one positive aspect of using RCA is that they are often stored outside and therefore prone to carbonation. The carbonation reaction increases the density of the microstructure by filling the porous system, which improves the resistance of the aggregate, and consequently the concrete, to mass transport, including water and ions [Xuan et al., 2017, Bao et al., 2020].

Verification of chemical compatibility between the new cement paste and the residual paste of the RCA is necessary to ensure that the properties of the concrete are not affected [Belin et al., 2014]. Recycled concrete may contain aggressive ions such as sulphates and chlorides from sources like de-icing salts, sewage, or sea water, which can negatively impact the properties of the RAC in both its fresh and hardened state, leading to decreased durability [Debieb et al., 2010]. Another possible cause of degradation when using RCA is the Alkali-Silica Reaction (ASR), which is based on the reactivity of the NA within these recycled aggregates [Barreto Santos et al., 2020, Grigoletto & Courard, 2022].

For chloride ions, studies have shown that they are not bound to the RCA structure and can be considered free chlorides. Washing the aggregates before use, allowing the pollutants to leach out of the porous structure and reducing their concentration to a level comparable to that found in NA, could be a viable industrial solution [Debieb et al., 2010, Martin-Morales et al., 2011, Colman et al., 2023, Abedin Khan et al., 2024].

In terms of the durability of Recycled Aggregates Concrete, two properties are of major interest, depending on the quality of the RCA: water absorption and chloride diffusion coefficient:

- Water absorption is correlated with morphological and mechanical properties of aggregates [Deodonne, 2015]. RCA exhibit a higher water absorption range of 3-12% compared to NA which range from 0.5-2% [Rao et al., 2007, Belin et al., 2014, Pedro et al., 2014a], depending on the calibre of the aggregates [Hubert et al., 2023].

- Chloride ions primarily diffuse through the mortar and ITZ phases via connected partially-saturated pores. It is often assumed that natural aggregates are impervious, resulting in a diffusion coefficient of concrete with RCA greater than that of concrete made from NA [Hu et al., 2018]. Scientific studies show that replacing NA with RCA results in a decrease in chloride penetration resistance ranging from 10% to 32% [Pedro et al., 2014a]. This is attributed to the greater porosity and average pore diameter of concrete made from RCA, that induces a greater diffusion coefficient with larger scatter [Xiao et al., 2012].

If the recycled concrete aggregates are decomposed into their several phases, the following comparisons can be made [Xiao et al., 2012, Hu et al., 2018]:

- The adherent mortar from the RCA exhibits a diffusion coefficient up to 5 times greater than that of the new mortar phase;

- The ITZ displays a diffusion coefficient up to 16 times greater than the mortar.

1.3 Durability and Degradation Processes

The durability of concrete refers to its ability to withstand external aggressive agents over an extended period without compromising its intended performance. Investigating the durability of concrete made from natural or recycled concrete aggregates is crucial to the development and application of this material.

Degradation processes that decrease the durability of concrete, with the exception of mechanical damage, all involve the flow of aggressive ions and fluids through the porous system of concrete. Durability of concrete greatly depends on its ability to withstand the penetration of aggressive ions as well as the temperature, humidity, wind and rain that are the source of natural degradation in severe environments [Rangel et al., 2020].

Most of the reinforced concrete structures are designed with a service life of a century. Steel rebars are embedded in concrete with a cover of a few centimetres, which protects the reinforcement from environmental threats. When located near roads or coastal areas, one of the primary reasons for the deterioration of modern reinforced concrete structures is the corrosion of reinforcement caused by chloride ingress [Morga & Marano, 2015]. This type of deterioration necessitates maintenance and incurs significant costs. Predicting the long-term corrosion of steel embedded in concrete is crucial to alleviate or reduce financial implications [Mangat & Molloy, 1994].

Chloride ions typically originate from de-icing salts or salts in seawater/wind. In the past, $CaCl_2$ was used as a concrete accelerator, which made it an internal source of chloride ions [Courard, 2019, Jones et al., 2020].

Chloride-induced corrosion occurs when the necessary ionic species for the pitting corrosion process, namely chloride Cl^-, oxygen O^{2-}, and water H_2O, percolate through the concrete cover and make it to the reinforcement. These species eventually concentrate and reach a critical content known as the concentration threshold. Once this threshold is attained, the steel undergoes depassivation, leading to the onset of pitting corrosion [Neville, 1995, Angst, 2011].

Good quality concrete must be able to prevent or partially prevent the corrosion of steel rebars. This is achieved through low porosity and permeability, which reduces the ingress of corrosive agents such as chlorides, water, and oxygen. Moreover, such concrete usually displays a high electrical resistivity, reducing the corrosion rate as corrosion requires an electrical current to flow between an anodic and a cathodic site [Chen & Mahadevan, 2008].

1.4 Goal of this Thesis

Considering the worse properties of RCA compared to NA, the substitution of natural aggregates by recycled concrete aggregates inside concrete has its share of disadvantages. Specifically, it facilitates transfer mechanisms between the material and its environment, leading to decreased resistance to chloride ingress. This weakening of properties can affect the durability of concrete made from RCA, potentially reducing its longevity.

Therefore, this thesis aims to address the following scientific question: "**How does the incorporation of Recycled Concrete Aggregates affect the durability of concrete in terms of chloride attacks?**"

Figure 1.4: Pictures of a Natural Aggregates Concrete (NAC, left) and Recycled Aggregates Concrete (RAC, right) produced for this research.

To answer this question, it is essential to understand the effect of substituting natural aggregates with recycled concrete aggregates on the transfer properties of concrete. Two approaches are used to achieve this:

1. Experimental approach: concretes made from either 100% natural aggregates or 100% recycled concrete aggregates were produced in the laboratory, after a thorough characterisation of the RCA. They are presented in Figure 1.4. Additionally, a cement paste and a mortar were produced to gain a better understanding of how the aggregates affect transfer properties. Several experiments were conducted in the laboratory to obtain intrinsic properties for water and chloride ion transfer.

2. Numerical approach: a multi-scale multi-physics model was developed using the Finite Element Square (FE²) method. It aims at producing results for the diffusion and advection of chloride ions in a scenario with real environmental conditions where concrete would be prone to chloride-induced corrosion. The model accounts for both saturated and unsaturated conditions and has been validated experimentally, analytically and numerically.

To achieve the set goals, planning is necessary. This thesis is divided into three major parts that will take place sequentially:

- Part 1 - Saturated Conditions: the beginning of the modelling work focuses on multiscale modelling of water flows only. Subsequently, a model of advection/diffusion of chloride ions is incorporated into this multiscale model. In parallel, the experimental campaign is conducted and is used to validate the model developed;

- Part 2 - Multiphase Flow: the second part focuses on unsaturated conditions, and therefore, the previously developed model is adapted to account for multiphase flows. The experimental campaign is performed to validate the multiphase model of water flow and chloride diffusion;

- Part 3 - Concrete Structure Modelling: the final part of this research involves modelling a concrete structure. A sensitivity analysis is conducted to identify the parameters that have the greatest impact on chloride ingress. The durability of the concrete structure is then evaluated to determine whether RCA can be used in concrete or if it significantly reduces durability.

1.5   Outline of this Thesis

This manuscript comprises four main parts: the **Literature Review**, which begins with this introduction, the **Experimental Programme**, and the **Multiscale Modelling of Chloride Ingress**. Finally, a general **Conclusion** is presented, based on the experimental and numerical results of this work.

Literature Review   After the *Global Context* which provides context for the research from both durability and sustainability perspectives, a first chapter, *Concrete: a Porous Material*, covers the topic of concrete comprehensively, from its composition to the transfer properties of its porous structure. The last chapter looks at the *Degradation Processes* that can occur in a reinforced concrete structure, with a focus on chloride-induced corrosion. The key elements of this corrosion are introduced, followed by a literature review of the current state of modelling.

Experimental Programme   The second part of this manuscript presents the experimental campaign conducted for this work. Firstly, the *Experimental Approach* is introduced, providing an overview of the material compositions developed and prepared in the laboratory. The recycled concrete aggregates are highlighted, investigating their source and properties to better understand their possible effect on durability. Finally, each experiment performed is described in detail, and the expected outputs are presented. Subsequently, the chapter *Experimental Results* provides the intrinsic properties of our developed materials obtained through the previously explained water and chloride transfer experiments.

Multiscale Modelling of Chloride Ingress   The third part of this work presents the numerical work carried out for this research. The chapter on *Multiscale Multiphasic Modelling* introduces the Finite Element Square (FE²) method, followed by the constitutive equations implemented in the model, and concludes with the algorithm used to model the mesostructure of concrete. The *Numerical Results* are then presented. The model is initially validated under saturated conditions through analytical, numerical, and experimental means. Subsequently, it is numerically validated under unsaturated conditions. A sensitivity analysis on the mesoscale is then presented, investigating the influence of the size of the mesoscale, as well as the diffusion properties and adherent cement content of the recycled concrete aggregates. Finally, this study examines the influence of the parameters for the hysteresis of the water retention curve.
The eighth chapter concludes with an analysis of an engineering structure, serving as a final *Application to a Real Life Scenario*. A maritime lock wall is modelled numerically to investigate the ingress of chloride ions in concrete made of natural aggregates and recycled concrete aggregates.

Conclusion   This research ends with a conclusion on both the experimental results and the numerical results. Perspectives for this work are also presented.

PART

1

LITERATURE REVIEW

2

CONCRETE: A POROUS MATERIAL

Contents

2.1 Introduction

Concrete is considered to be a multiphasic and multiscale material. Its different components are of different size, and their influence on the properties can be seen at different scales. Throughout this chapter, one will embrace the complexity of that artificial geomaterial. It begins with an overview of its composition, from the chemistry of cement and the chemical reactions involved in its hardening, to the attributes of its aggregates. The porous structure of concrete will then be examined, with a focus on the migration of the fluid and gaseous phases within the intricate pore system.

Finally, since this work focuses on the modelling of complex transport phenomena and ion ingress, the theory of porous media will attract our attention. The theory of mixtures will be introduced first, followed by the concepts of capillarity and suction.

2.1.1 Composition of Concrete

The complex properties of concrete are closely linked to its components and the intricate reactions in between them. It is therefore advisable to go back to basics in order to better understand the porous structure of concrete and the various transport phenomena that can take place within it. This section focuses on the composition of concrete and serves as an introduction to the porous system of concrete.

Concrete is a construction material produced with water, cement (which gives rise to a cement paste), sand (that produces a mortar with the cement paste), and aggregates to enhance its strength. A typical composition should yield a density of approximately 2400 kg/m^3 and is classically composed of [Courard, 2018]:

- 1300 kg/m^3 of aggregates for a volume fraction of 0.5;

- 650 kg/m^3 of sand for a volume fraction of 0.25;

- 325 kg/m^3 of cement for a volume fraction of 0.1;

- 170 kg/m^3 of water for a volume fraction of 0.15.

A major concern in the mix design is the water-to-cement ratio (W/C): the higher it is and the higher the porosity of the cement paste and, consequently, of the concrete.

Concrete is therefore a multiphasic material whose internal structure is highly heterogeneous, consisting of coarse (natural) aggregates embedded in a mortar matrix itself consisting of fine (natural) aggregates, hydrated and unhydrated cement and finally the pore system [Winslow et al., 1994, Kumar & Bhattacharjee, 2003]. Substituting natural aggregates with recycled concrete aggregates increases this complexity and heterogeneity by introducing a new phase: the old mortar paste and its own pore system, which is not necessarily identical to the new one.

In addition, the pore system of the mortar matrix is also different from the one found in plain mortar, even if the proportions of the relevant constituents are identical. This is due to the Interfacial Transition Zone (ITZ), that is the transition zone between the aggregates and the cement paste [Kumar & Bhattacharjee, 2003]. Furthermore, these two porous systems are again different from the pore system of plain cement paste. In fact, Mercury Intrusion Porosimetry (MIP) has shown that the paste in concrete contains larger pores with a higher degree of interconnection than plain cement paste [Winslow et al., 1994].

2.1.2 Constituents of Concrete

2.1.2.1 Cement

Cement acts as an hydraulic binder, meaning it maintains cohesion between non-reactive elements. It comprises a fine powder with hydraulic properties, i.e. it solidifies in water (whether submerged or in the air) to produce an insoluble material [Courard, 2017]. Hydraulicity denotes the capacity of a substance to set and harden in the presence of water, resulting in the formation of stable compounds.

The main constituents of the Portland cement (Table 2.1), the basis of most cements, are the tricalcium and dicalcium silicates (C_3S and C_2S), as well as the aluminates and ferroaluminates of calcium (C_3A and C_4AF respectively) [Bertolini et al., 2004, Courard, 2017]. Abbreviations are used in concrete and cement chemistry: S (SiO_2), A (Al_2O_3), F (Fe_2O_3), H (H_2O), $\bar{S}$ (SO_3) and C (CaO).

Name	Chemical formula	Abbreviation	Percentage by mass
Before clinkerisation process			
Calcium oxide (Quicklime)	CaO	C	65%
Silicon dioxide (Silicate)	SiO_2	S	20%
Alumina	Al_2O_3	A	10%
Iron trioxide	Fe_2O_3	F	5%
After clinkerisation process			
Tricalcium silicate	$3CaO.SiO_2$	C_3S	60%
Dicalcium silicate	$2CaO.SiO_2$	C_2S	20%
Tricalcium aluminate	$3CaO.Al_2O_3$	C_3A	10%
Tetracalcium ferroaluminate	$4CaO.Al_2O_3.Fe_2O_3$	C_4AF	8%
Gypsum	$CaSO_4.H_2O$	$C\bar{S}$	2%

Table 2.1: Main constituents of the Portland cement [Bertolini et al., 2004, Courard, 2017].

As mentioned above, the constituents of Portland cement react with water to form hydrated products with very low solubility.
The first components to react are the aluminates, which are responsible for the solidification of the cement paste: the hydration of C_3A and C_4AF, in presence of gypsum, produces hydrated sulfoaluminates of calcium ($C_6A\bar{S}_3H_{32}$ and $C_4A\bar{S}H_{18}$) [Nilenius, 2014].
The development of strength that follows solidification, which is called hardening of the cement paste, is governed by the hydration of silicates C_2S and C_3S, which gives rise to Calcium Silicate Hydrates that form a rigid gel indicated as $C - S - H$ [Powers, 1958, Bertolini et al., 2004]:

$$C_3S + 6H \rightarrow C_3S_2H_3 + 3Ca(OH)_2$$
$$2C_2S + 4H \rightarrow C_3S_2H_3 + Ca(OH)_2$$

(2.1)
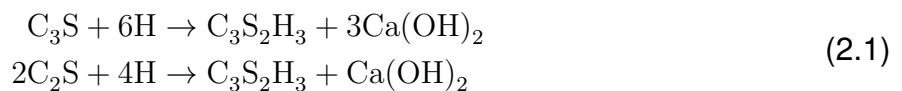
$C - S - H$ is a gel made up of extremely small particles with a high surface area, which gives the cement paste considerable strength, but also consists of spaces between these particles, called gel pores, which are induced by chemical shrinkage. $C - S - H$ represents about 50-60% of the volume of the fully hydrated cement paste. A model describing its structure is shown in the Figure 2.1.

Hydration of the calcium silicates may also produce hexagonal crystals of calcium hydroxide $Ca(OH)_2$, called Portlandite, which account for 20 to 25% of the volume of the solids. They do not contribute to the strength of the cement paste [Bertolini et al., 2004] but they are the main regulator of the pH of concrete, being highly alkaline.

Within this field, cement (and therefore concrete) is a material whose composition varies in space and time and whose physical and mechanical properties depend on several factors [Nilenius, 2014].
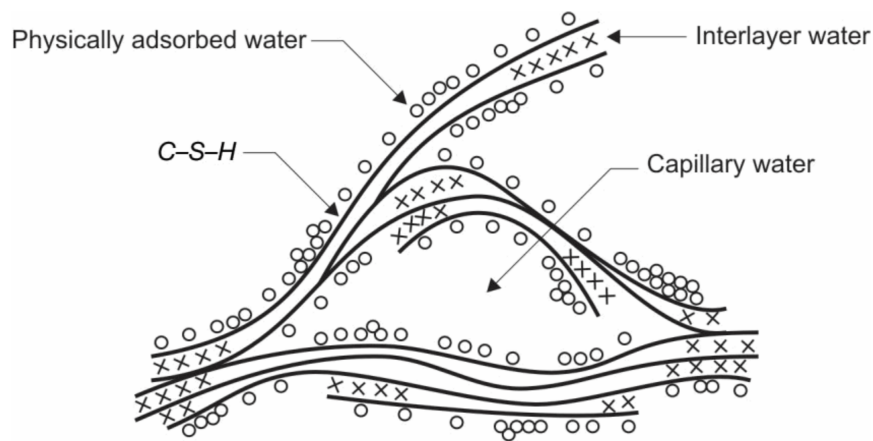
Figure 2.1: Feldman–Sereda model for C–S–H [Bertolini et al., 2004].

Besides Portland clinker, cement may also contain blast furnace slag, fly ash, calcined shale and other by-products. There are several types of cement on the market. In Europe, we use four main types of cement based on their composition:

- CEM I: "pure" Portland cement;

- CEM II: Portland cement with either blast furnace slag (S), fly ashes (V), limestone (L) or a mix of those (M);

- CEM III: blast furnace cement (S);

- CEM V: compound cement.

It is generally accepted that in composite or blended cements, the hydration or pozzolanic reaction of blast-furnace slag and pozzolanic materials (pozzolana, fly ash, ...) results in a microstructure that is denser than that of pure Portland cement. This has been attributed to the slower reaction rate, which produces fewer capillary pores but more fine pores: the resulting pore structure is then more impervious [Angst, 2011].

2.1.2.2 Water

Water is a necessary component of concrete, required for the hydration of the cement particles. The quality of the water must not be underestimated, as waste water or sea water contains suspended solids and dissolved salts that can interact with the cement grain and slow the hydration reaction or decrease the strength of the concrete. Within this field, water used in concrete mixing must be of good quality (according to the standard NBN EN 1008) and is often tap water.

2.1.2.3 Natural and Recycled Aggregates

An aggregate is a building material that is inert to its environment. Several types of aggregates may be used in concrete, as according to the standard NBN EN 12620:2013 [Courard, 2018]:

- The most commonly used type of aggregate is natural aggregate of mineral origin and that has only undergone a mechanical treatment such as crushing, screening, and so on;

- If the aggregate is the result of an industrial process, it is considered as an artificial or industrial aggregate. For example, an aggregate of mineral origin that has undergone a heat treatment (e.g. industrial residues) is called an industrial aggregate;

- Finally, recycled aggregates come from the treatment and transformation of inorganic (and harmless) materials that have already been used in construction (CDW).

Aggregates are also classified according to their size (D is the largest diameter of the grain), from filler to gravel [Courard, 2018]:

- Filler : $D \leq 0.063$mm ;

- Sand : $D < 4$mm ;

- Large aggregate : $D \geq 4$mm ;

- Gravel : $D \geq 6.3$mm ;

Finally, aggregates are classified as rolled or crushed depending on their origin (from a watercourse or quarry respectively). This aspect is quite important as crushed aggregates have an angular shape which increases their resistance to movement, resulting in poorer workability. Nowadays, almost all aggregates are crushed aggregates, with the exception of some sands that still originate from the Rhine river or the sea.

The most important characteristic when working with aggregates is their granulometric curve as the composition of the concrete largely depends on this characteristic. The granulometric curve represents the size distribution of the aggregates and must be continuous in order to promote a concrete of better quality, with optimised compactness. The granulometric curve is said to be continuous when each grain size between a lower and an upper limit (from the smallest sand grain to the largest aggregate) is equally represented.
The EN 480-1:2014 standard gives an example of the maximum and minimum Particle Size

Distribution (PSD) to be used for aggregates in a reference concrete (for experimental purposes), as shown in Figure 2.2. This standard is not the only one but gives a reference to be used (Table 2.2).

Sieve opening	0.125	0.25	0.5	1	2	4	8	16	31.5
% of Passers-by (min.)	1	4	10	20	25	35	45	75	100
% of Passers-by (max.)	8	12	25	35	40	50	70	98	100

Table 2.2: Particle Size Distribution (also called granulometric curve) of aggregates for a reference concrete according to the EN 480-1:2014 standard.
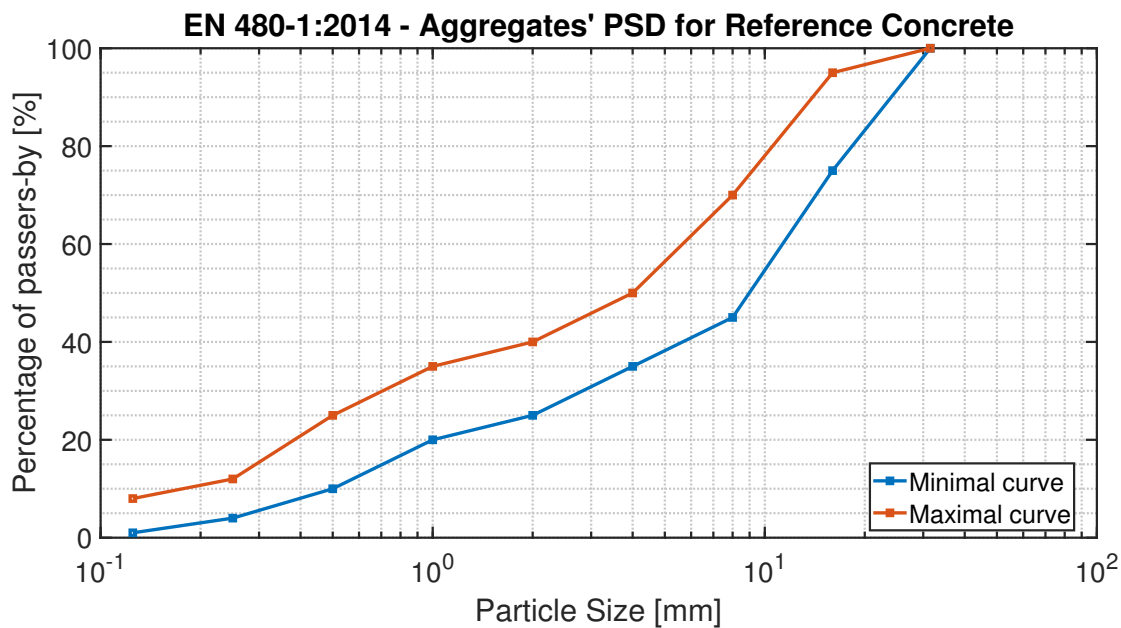
Figure 2.2: Particle Size Density (also called granulometric curve) of aggregates for a reference concrete according to the EN 480-1:2014 standard.

2.2 Porous Structure of Concrete

As it was already mentioned, hardened concrete is a multiphase material: the aggregates, hydrates and non-hydrated parts of the cement form the solid phase. The liquid phase consists of the interstitial solution, while the gaseous phase is a mixture of air and water vapour [Ollivier & Torrenti, 2008, Sun et al., 2011]. These liquid and gaseous phases coexist within the pore structure of concrete.

In fact, cement grains react with water throughout the hydration reaction. The quantity of water chemically fixed by the cement represents almost 25% of the cement mass used in the composition, depending on several parameters such as the type of cement and the degree of hydration of the constituent grains. This water then undergoes a morphological transformation that reduces its volume by 25%, resulting in small pores scattered throughout the solid phase, called "gel pores" [Courard, 2018]. These gel pores, together with several other types of pores, make up the porous structure of the concrete.

2.2.1 Types of Pores in Concrete

Concrete is a material with a complex porous structure that can be divided into two main families: open porosity, which is connected to the surface, and closed porosity, which isn't. Obviously, only open porosity can be filled with liquid and gas coming from the environment [Sun et al., 2011, Courard, 2018].
In addition, the degree of interconnection of the porosity strongly depends on the composition of the concrete as well as on the water-to-cement ratio. In fact, studies have shown that a continuous pathway formed at an aggregate volume fraction of 50% (or even less), which is almost always the case for classical concrete. This is in part due to the interfacial transition zones that interconnect to create the open porosity [Xi & Bažant, 1999].
A schematic description of concrete is given in the Figure 2.3.
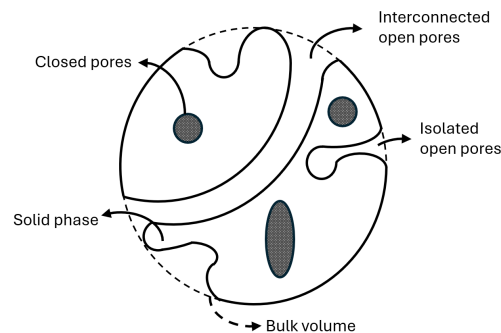
Figure 2.3: Schematic description of concrete: a porous material
(modified from [Ollivier & Torrenti, 2008]).

The different types of pores mentioned here above are, from the smallest to the coarsest one [Sun et al., 2011, Apers & de Schutter, 2018, Zhou et al., 2019]:

- "Gel" pores due to the hydration reaction of the cement grains, the volume of the product being smaller than the volume of the reagents;

- Capillary pores due to excess water not required for the hydration reaction;

- Pores due to internal (endogenous) shrinkage, of a size relatively similar to the capillary pores. These are important for the freeze-thaw resistance of concrete;

- Aggregate pores, which have less influence on the transport mechanisms because they are often discontinuous;

- Internal microcracks due to shrinkage, creep, freezing, etc., often located in the interfacial transition zone. As these are tortuous and rarely interconnected, they do not play an important role in the transport mechanisms;

- Volume due to entrained air (admixture);

- Entrapped air void;

- External cracks due to a restrained shrinkage, overloading ... .

A schematic representation of these different types of pores is shown in the Figure 2.4.
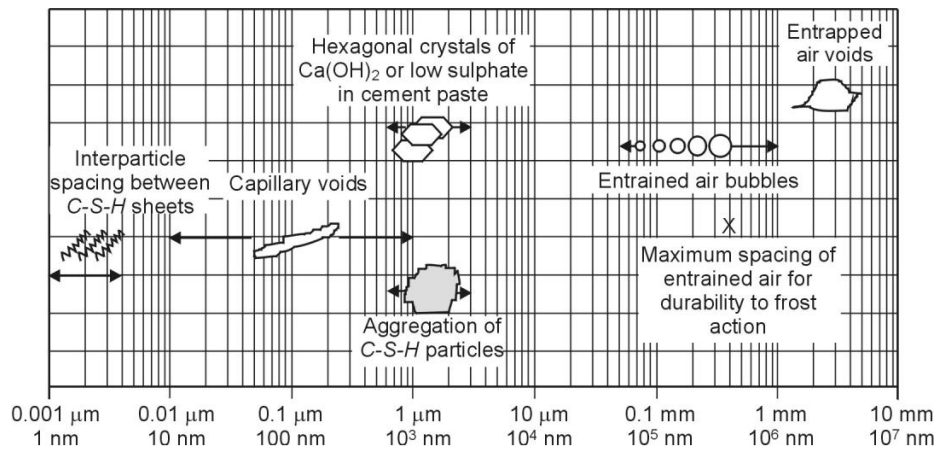
Figure 2.4: Distribution of pores according to size [Bertolini et al., 2004].

Porosity has a major influence on the durability of concrete. However, not all pores are equal in terms of this influence: capillary pores are the most important. Capillary pores are created from excess water (which is less bound to the cement grains) that evaporates during curing. They are larger than the pores resulting from the hydration process: that's why they play a greater role in the degradation of concrete.

Open porosity consists of accessible pores that can be filled with water depending on the environmental conditions. Furthermore, water is already present in the hydrated cement paste, under several forms, classified from the easiest to the most difficult to remove [Bertolini et al., 2004, Zingg, 2013]:

- Capillary water: the water contained in the capillary pores accounts for most of the water in concrete. According to the Jurin law, as these pores are the largest, the water they contain requires the least energy to remove;

- Adsorbed water: once the capillary water has been removed from the concrete, some water remains adsorbed on the internal surface in the form of a very thin layer of adsorbed water. This thin layer of water can be removed when the external humidity drops below 30% and requires more energy as the contact forces are greater the closer you are to the surface of the solid;

- Interlayer water: the $C - S - H$ layers also hold water between them, which can only be removed when the relative humidity drops below 11%;

- Chemically bound water: there is also water that is chemically bound to cement grains and other constituents of the concrete, which requires extreme temperatures to be removed.
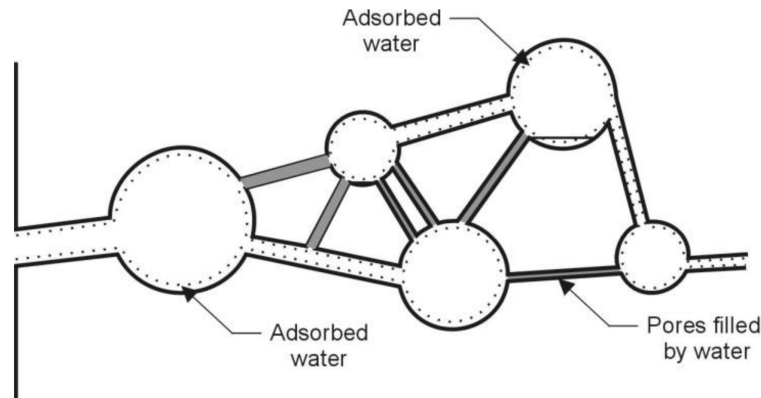
Figure 2.5: Representation of water present in capillary pores in concrete in equilibrium with a non-saturated atmosphere [Bertolini et al., 2004].

Under equilibrium conditions and in the absence of direct wetting, the water content of a concrete exposed to the atmosphere is a function of the relative humidity (RH) of the atmospheric air. An increase in relative humidity therefore fills the capillary pores until equilibrium is reached: water is first adsorbed on the surface of the pores and then condensates and fills these pores, from the smallest to the largest [Bertolini et al., 2004]. This concept is easily understood thanks to the Figure 2.5. Indeed, one can see that the capillary pores (represented as spherical cavities) are connected by smaller capillary cylinders. Under equilibrium conditions, only the pores whose diameter is below a certain value are filled with the liquid phase, while the others are filled with a mixture of liquid and gas, the liquid being adsorbed on the walls of the pores [Bertolini et al., 2004].

2.2.2 Transport Phenomena

Liquid and gaseous phases migrate through the accessible porosity of concrete by means of various transport mechanisms. These mechanisms can be divided into three main types: permeability, diffusion and capillary adsorption, which will be explained hereafter. Permeation and capillary absorption involve mechanical forces (gravity, pressure potential, etc.), while diffusion requires chemical forces (osmosis, concentration gradient, etc.) [Courard, 2018].

The first concept to grasp our attention is permeability. Indeed, permeability is the ability of a fluid to penetrate and migrate through a porous system. The main necessary condition to allow the flow of a fluid is therefore the presence of voids and pores, connected into open porosity [Apers & de Schutter, 2018].
The second transport mechanism involving mechanical forces is capillary adsorption: when a pore is in contact with a water surface, adsorption causes the formation of a meniscus that rises up the walls of the pore [Apers & de Schutter, 2018]. According to Jurin's law [Bear & Verruijt, 1987], the suction force resulting from this meniscus formation is inversely proportional to the pore diameter, while the rate at which the water rises is proportional to the square of this diameter.
Diffusion of a fluid, on the other hand, is due to a difference in relative humidity between two points in the medium or between the concrete and its environment. This difference in relative humidity (and temperature) creates a pressure gradient that forces water vapour into

the pores until the properties of the gas phase inside and outside the solid are in equilibrium in terms of temperature and relative humidity. Once inside the pores, the water vapour is transformed into liquid water by condensation and adsorption on the capillary surfaces [Apers & de Schutter, 2018].

While liquid and gas phases move inside the porous system, ions can also diffuse and migrate within the liquid phase itself. Chloride ions can be transported through the porosity in several ways, depending on the saturation state of the concrete. Under saturated conditions, and at constant pressure, ions can move by diffusion (caused by a concentration gradient) and migration (caused by an electrical potential gradient), with diffusion being predominant over migration. If the applied pressure changes, fluid fluxes can also occur, while remaining saturated, inducing further movements of ions. However, once the concrete is in unsaturated conditions, convection due to wetting and drying cycles is mainly responsible for ions transportation within the liquid phase [Nagesh & Bhattacharjee, 1998, Ababneh et al., 2003, Baroghel-Bouny et al., 2011, Di Pillo & Todisco, 2020].

Transport phenomena are complex and can be influenced by numerous properties of the pore structure, such as [Courard, 2018]:

- Connectivity of the porosity: the larger the porosity, the greater the connectivity, which increases the permeability by opening the pores. In addition, if the water-to-cement ratio is higher than 0.7, connectivity cannot be avoided.

- Pore constrictivity: constrictivity is a parameter that qualitatively reflects the cross-sectional variation that pores offer to flow [Ollivier & Torrenti, 2008]. Low constrictivity means that there may be fewer pores, but at equal porosity, those pores will be of higher volume. As in hydraulic theory, there will be less pressure drop in a large capillary than in several fine capillaries. Therefore, low constriction (large capillaries) leads to higher permeability.

- Porosity: the greater the porosity, the greater the permeability. However, only the open porosity allows transport phenomena. In addition, the pores must have a diameter at least equal to the size of the water molecule, i.e. about $0.3\,\mathrm{nm}$ [Apers & de Schutter, 2018].

- Tortuosity: the more tortuous the capillaries are, the longer they will be for the same separation distance between the start and the end. This results in higher pressure drops. Therefore, low tortuosity results in high permeability. In addition, the faster the water evaporates as the concrete sets, the straighter the capillaries will be.

2.2.3 Parameters Influencing the Porosity

The porous structure of concrete is constantly evolving due to the hydration of the cement particles and the various effects that the environment can have on it. In addition, several parameters influence the porosity of concrete. The first parameter that comes to mind is the water-to-cement ratio. In fact, excess water that is not required for the hydration process will evaporate during the curing of the concrete and create capillary pores: the higher the W/C ratio, the more capillary pores are created and the higher the porosity, as shown in the Figure 2.6. Furthermore, the connectivity of the porosity is also directly proportional to the water-to-cement ratio [Courard, 2018, Apers & de Schutter, 2018].
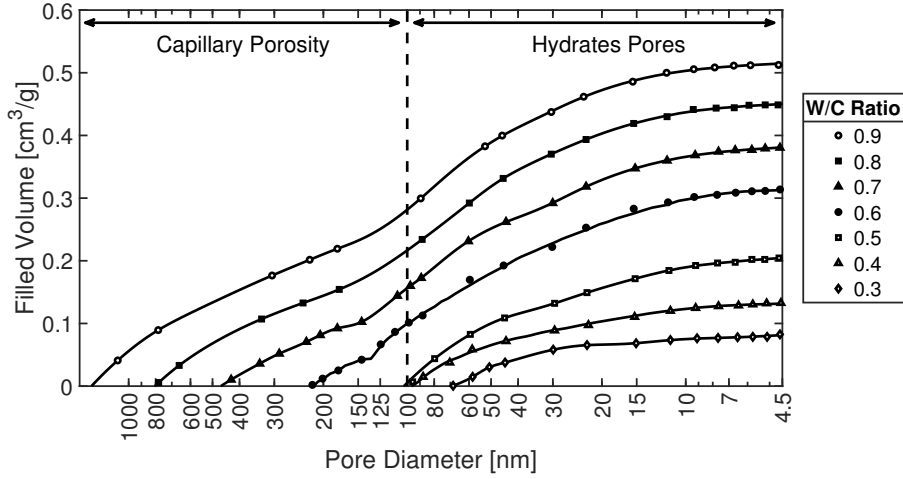
Figure 2.6: Influence of the W/C ratio on the porosimetric evolution of 28 day-old Portland cement pastes (modified from [Ollivier & Torrenti, 2008, Courard & Michel, 2014]).

Another important parameter to limit permeability is the hydration conditions during curing. In fact, a sufficient curing time with high relative humidity limits evaporation and therefore the formation of capillaries (Figure 2.7) [Sun et al., 2011, Courard, 2018]. Indeed, it is as important to ensure adequate curing as it is to specify a low water-to-cement ratio [Dhir et al., 1989]. Moreover, the longer the curing time, the smaller the porosity: as the cement cures, it absorbs water and creates gel pores which are smaller in diameter than capillary pores [Apers & de Schutter, 2018], inducing a continuous closure of the porosity with $C - S - H$ [Bertolini et al., 2004].

The volume of the capillary pores (V_{cp}) in the cement paste can be related to the two parameters aforementionned: the amount of water used, through the water-to-cement ratio (w/c), and the degree of hydration (h), in particular according to the following formula [Bertolini et al., 2004]:

$$V_{cp} = \left(\frac{w}{c} - 0.36\, h \right)$$

(2.2)
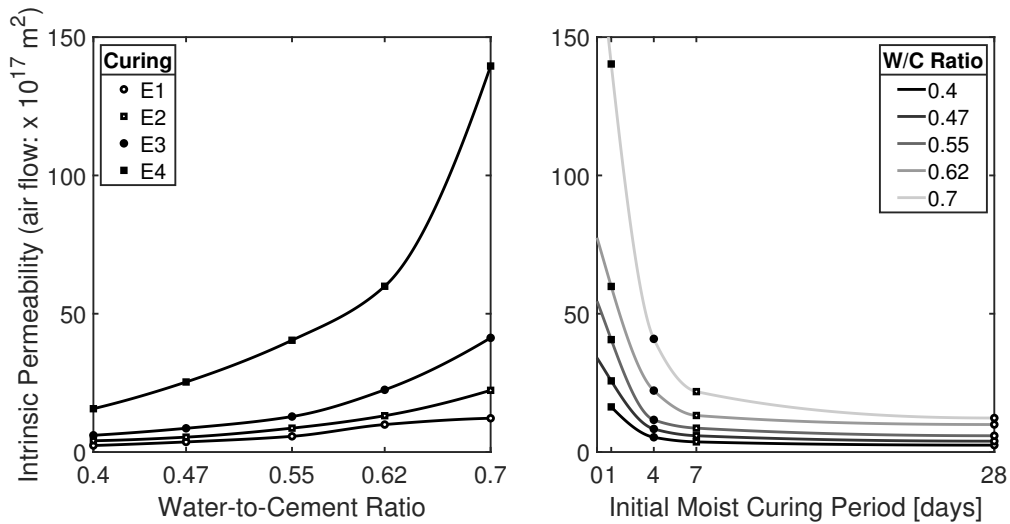
Figure 2.7: Effect of initial moist curing period and water/cement ratio on intrinsic permeability of concrete (modified from [Dhir et al., 1989, Courard & Michel, 2014]).

26

The water-to-cement ratio and curing time mentionned above are the main factors influencing the porous structure of concrete. Nonetheless, the presence of aggregates and the creation of the resulting Interfacial Transition Zone (ITZ) also play an important role in the porous system.

With regard to aggregates, research has shown that the larger the aggregate, the greater the permeability (Figure 2.8). Indeed, the cement paste creates an interface (ITZ) around the aggregates due to the restriction of the hydration reaction near the contact area between the cement and the aggregate [Courard, 2018]. The width of this zone, which is highly permeable, can be estimated to be in the range of 10 to $100\mu m$ which is the same order of magnitude as the size of a grain of cement [Bentur & Odler, 1996]. The larger the aggregate and the larger the ITZ, the greater is the chance of interconnection between the ITZs of two adjacent aggregates.
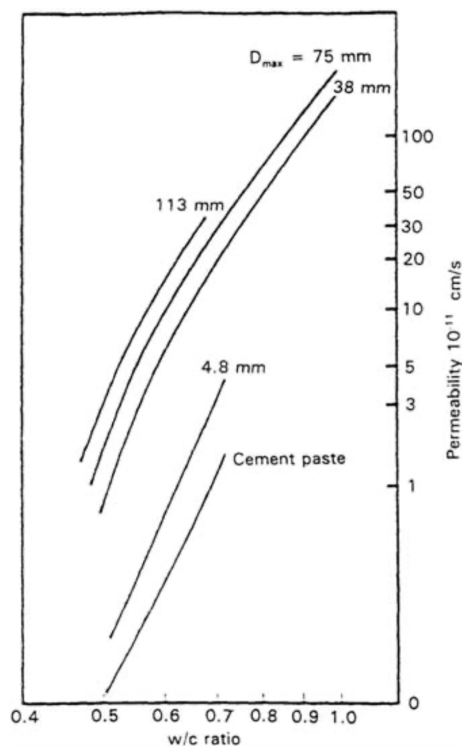
Figure 2.8: Influence of water/cement ratio and maximum aggregate size on concrete permeability [Ollivier & Massat, 1996, Courard & Michel, 2014]
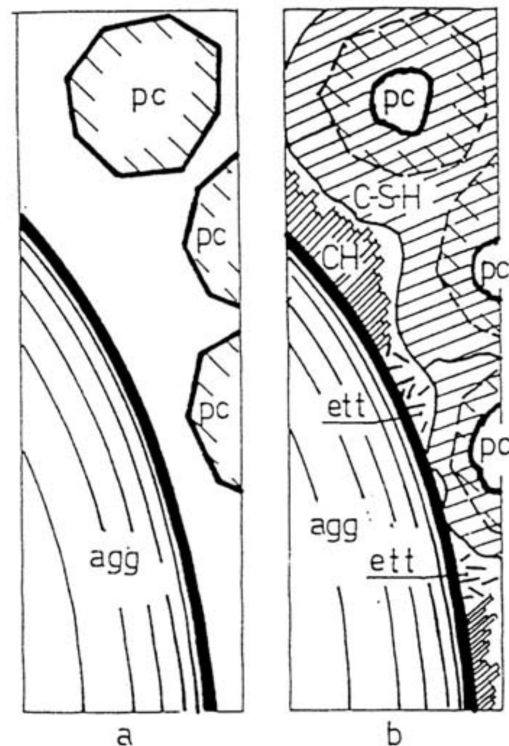
Figure 2.9: Schematic description of the mode and nature of formation of the ITZ around aggregates in a cementitious mix, before (a) and after (b) hydration of the cement particles. Before, the fresh concrete exhibits a water-filled space due to bleeding, while after the ITZ is partially filled with CH and $C - S - H$ [Bentur & Odler, 1996].

The formation of the ITZ is mainly due to the formation of water-filled spaces around the aggregates of the fresh mix, i.e. the water distribution around the aggregates is non-uniform, where the water-to-cement ratio peaks locally. The non-uniform distribution can be caused by bleeding, in addition to a wall effect that prevents the effective filling of the space adjacent to the aggregate with cement grains larger than $10\mu m$ in diameter. This results in a zone around the aggregates that is less filled with products of the hydration reaction, generating what one can call a "hydrate malformation" (Figure 2.9). This malformation, at the porosity

level in the ITZ, results in a greater tendency to develop larger crystals such as CH and ettringite as the pores are larger, compared to the bulk paste [Mehta & Monteiro, 1988, Bentur & Odler, 1996, Hussain et al., 2000]. The resulting porosity is then two to three times that of the bulk paste [Ollivier et al., 1995].

If we now apply this theory to the recycled concrete aggregates, the influence of the ITZ is even more significant as the transition zone of the original concrete is found in the cement matrix surrounding the recycled aggregates. Therefore, when these replacement aggregates are introduced into the cement paste to make a new concrete mix, a new type of ITZ is created around the mortar gangue. It has been shown that the difference in weakness between the ITZ in the reference concrete versus the one with RCA increases as the difference in porosity between the NA and RCA increases [Hussain et al., 2000]. However, other authors have found that the ITZ in Recycled Aggregates Concrete is much more compact and therefore less porous than for Natural Aggregates Concrete [Thomas et al., 2013].

2.3   Theory of the Porous Media

As one should have understood by now, concrete is a porous medium, i.e. it contains pores. What is called the "solid phase" is the matrix or skeletal part of the material, composed of the aggregates, sand and cement particles. The volume in between the solid grains forms the pores.
A porous medium is often characterised by its porosity n, defined as the ratio of the pore volume (V_v) to the total volume of the medium (V) [Verruijt & Van Baars, 2007]. Another characteristic of the porous media is the void ratio (e), defined as the ratio of the pore volume to the solid volume (V_s):

$$n = \frac{V_v}{V} \quad \text{and} \quad e = \frac{V_v}{V_s} \tag{2.3}$$

A porous medium can be defined as "saturated" or "unsaturated" (Figure 2.10). In a saturated porous medium, the pores are filled by only one fluid, whereas in an unsaturated porous medium, the porosity is filled by two fluids. These fluids form different phases: a liquid phase (wetting fluid) and a gas phase (non-wetting fluid) [Hubert, 2018].
In concrete, the gas phase traditionally consists of dry air and water vapour, while the liquid phase consists of water and dissolved air [Collin & de Ville de Goyet, 2019].

(a)   (b)

■ Solid grains

■ Water

□ Air
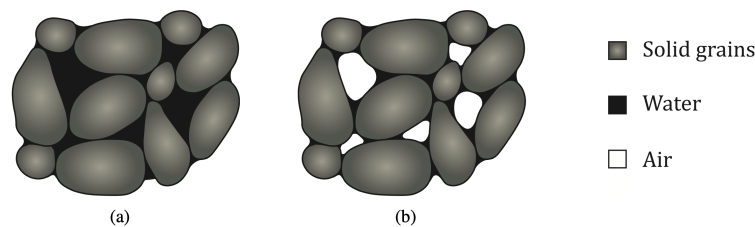
Figure 2.10: Saturated (a) and unsaturated (b) porous medium [Hubert, 2018].

Another important property of a porous medium is its degree of saturation (S_r), which is defined as the fraction of the porosity occupied by each fluid phase, in particular for unsaturated media:

$$S_{r,l} = \frac{V_l}{V_v} \quad \text{and} \quad S_{r,g} = \frac{V_g}{V_v} \tag{2.4}$$

where V_l and V_g are the volumes of the liquid and gas phases respectively, and V_v is the pore volume.

One approach to describe this complex system in a simplified manner is to construct an idealised homogeneous continuum [Dieudonné, 2016]. Among the many theories, one draws our attention: the theory of mixtures. In the theory of mixtures, the porous medium is studied on a macroscopic scale and is considered as a mixture of various incompressible phases that make up every point of the idealised system, so that each point (in space) is simultaneously occupied by a finite number of particles, one for each constituent of the mixture [Concha, 2014].

However, the balance equations are expressed for each constituent separately [Bowen, 1980]. Within this framework, the mixture is defined as a superposition of continuous media, each following its own motion, subject to the constraints imposed by the interactions between the constituents [Concha, 2014]. All phases are assumed to occupy the same region of space simultaneously as the superposition of different interpenetrating continua (Figure 2.11), which allows the use of continuum mechanics methods [Hubert, 2018]. Therefore, each phase obeys the laws of conservation of momentum and mass, taking into account for the exchange of mass and momentum between the components [Concha, 2014].
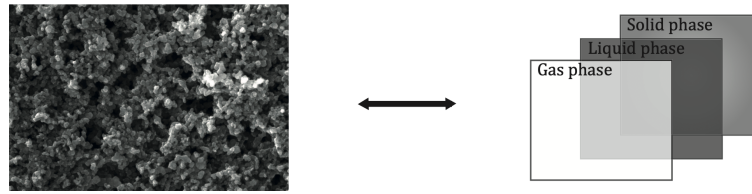
Figure 2.11: Definition of equivalent continua [Hubert, 2018].

In order to apply continuum mechanics methods, the definition of volume fractions must be established to create homogenised continua [Hubert, 2018]:

$$\eta_i = \frac{V_i}{V} \quad \text{where} \quad \sum_i \eta_i = 1 \tag{2.5}$$

where V_i is the volume of the phase i.

The following volume fractions can be defined:

$$\eta_s = 1 - n \tag{2.6}$$
$$\eta_l = S_{r,l}\, n \tag{2.7}$$
$$\eta_g = S_{r,g}\, n = (1 - S_{r,l})\, n \tag{2.8}$$

where s, l and g correspond respectively to the solid, liquid and gas phase.

The density (ρ_i) of a given phase i is defined as:

$$\rho_i = \frac{m_i}{V_i} \tag{2.9}$$

with m_i the mass of said phase.

It was decided to use the mixture theories approach as it allows the description of the deformation of the porous medium as well as fluid flows, heat transfer and coupled phenomena [Bowen, 1980, Dieudonné, 2016, Hubert, 2018].

2.3.1 Capillarity

Surface tensions are forces that result from the difference in intermolecular forces between different particles. For example, two immiscible fluids in contact will develop such forces between the particles at the interface and those in the fluid (Figure 2.12) [Hubert, 2018]. These forces result from a lack of equilibrium: the particles within the fluid are in equilibrium, while those at the interface are not. It induces surface tensions (σ_{GL}) to restore the force equilibrium, where G is the gas phase and L is the liquid phase.
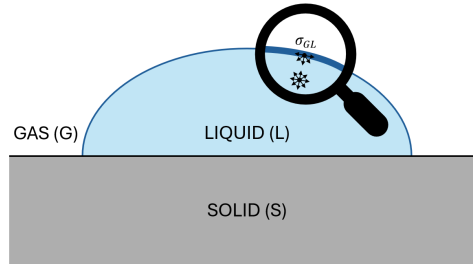
Figure 2.12: Molecular forces on a particle of water (modified from [Collin, 2003, Hubert, 2018]).

If we now add a perfectly plane solid phase S in contact with the two fluids L and G (Figure 2.13), there are surface tensions σ_{SL}, σ_{GL} and σ_{SG} at the interfaces. This equilibrium is formulated using the Young-Dupré formula [Dupré & Dupré, 1869]:

$$\sigma_{SG} = \sigma_{SL} + \sigma_{GL} \, \cos\theta \tag{2.10}$$

where the product $\sigma_{GL} \, \cos\theta$ is defined as the adhesion tension and expresses which of the two fluids is more likely to wet the solid, i.e. adhere to it and have a tendency to spread over it [Bear & Verruijt, 1987].

The parameter θ is defined as the contact angle, i.e. the angle between the interface of the two fluids and the surface of the solid. It depends on the fluid-solid surface affinity and is the most widely used technique to characterise the hydrophobicity and overall surface properties of solids [Courard et al., 2011]. The higher the contact angle, the more hydrophobic the solid surface. The condition to ensure contact is:

$$\cos\theta = \frac{\sigma_{SG} - \sigma_{SL}}{\sigma_{GL}} < 1 \longrightarrow \theta < \frac{\pi}{2} \tag{2.11}$$
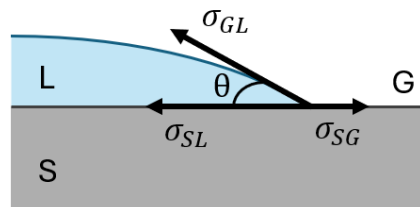
Figure 2.13: Surface tension (modified from [Collin, 2003, Hubert, 2018]).

There is contact if the contact angle is less than 90°: the fluid is therefore called a wetting fluid. Conversely, if $\theta > 90°$, the fluid is said to be a non-wetting fluid.

The capillary effect shown in the experiment in the Figure 2.14 is caused by the surface tensions. In this experiment, a capillary tube of radius r_c is immersed in a few centimetres of water, and the water level in the tube rises to a certain height, noted as h_c and called the capillary pressure head. Jurin's law is able to predict this level by expressing the vertical equilibrium [Bear & Verruijt, 1987, Collin & de Ville de Goyet, 2019]:

$$h_c = \frac{p_c}{\rho_l \ g} \quad \text{with} \quad p_c = p_g - p_l = \frac{2 \ \sigma_{GL} \ \cos\theta}{r_c} \tag{2.12}$$

where p_c, p_g and p_l are the capillary, gas and liquid pressures respectively, and ρ_l and g are the liquid density and the gravitational acceleration, respectively.
Jurin's law therefore states that the smaller the radius of the capillary, the higher the level of the water as the capillary effect increases.
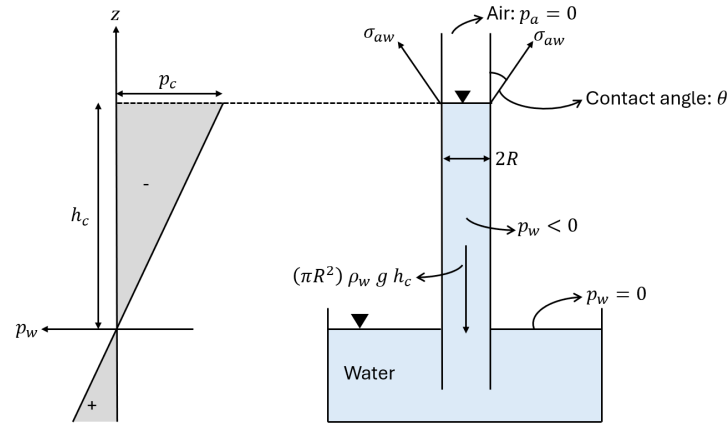
Figure 2.14: Experimental configuration (adapted from [Bear & Verruijt, 1987]).

This concept can be applied to an unsaturated porous medium with two fluids, where the pores act as capillaries [Delage, 1987]. The capillary pressure is related to the relative quantity of each fluid in the pore volume, i.e. the degree of saturation of the liquid phase [Hubert, 2018].

2.3.2 Concept of Suction

Suction is the development of capillary menisci within the porous structure, causing a negative value of water pressure [Delage, 1987]. The capillary pressure is a function of the radius of the capillaries [Bear & Verruijt, 1987, Xi et al., 1994], so as the porous material dries, smaller and smaller capillaries are affected.

In fact, the value of atmospheric pressure is conventionally assumed to be zero. Therefore, the Equation 2.12 expresses that the capillary pressure is negative and the suction increases as the capillary radius decreases.
In other words, since pores have various dimensions, they will not empty at the same suction. Therefore, the larger pores (large channels of entry) will empty at low suctions while those with narrow channels of entry will empty at higher suctions as they support interfaces of greater curvature [Bear & Verruijt, 1987].
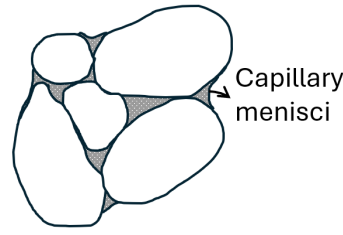
Figure 2.15: Suction phenomenon in granular structure, showing capillary menisci (modified from [Delage, 1987]).

The total suction was defined by the Jurin law in the Equation 2.12:

$$s = p_c = p_g - p_l \tag{2.13}$$

where, as a reminder, p_g and p_l are the gas and liquid pressures respectively. The total suction is related to the amount of water stored in a porous medium by the water retention curves [Pham et al., 2005, Nuth & Laloui, 2008, Beckett & Augarde, 2013, Pap et al., 2018a]. The quantity of water can be expressed in terms of water content or degree of saturation, but the latter is preferred as it already appears in the mass balance equation.
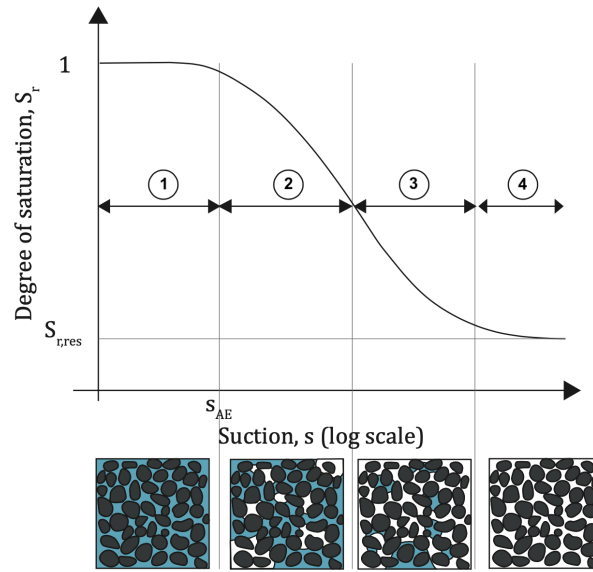
Figure 2.16: Typical water retention curve (from [Nuth & Laloui, 2008, Hubert, 2018]).

The shape of the water retention curve depends significantly on the grain size distribution [Pap et al., 2018b]. A generic water retention curve is shown in the Figure 2.16, where four domains are depicted [Hubert, 2018]:

1. If the suction is smaller than the air-entry pressure (noted s_{AE} in Figure 2.16), then the medium is almost, if not completely, saturated, as no air can enter the pores and therefore no water is pushed out. This section is almost horizontal and is called the boundary effect zone because of the exchange that takes place between the surface of the sample and the environment [Nuth & Laloui, 2008, Fredlund et al., 2011, Pap et al., 2018a, Pap et al., 2018b];

32

2. Once this air-entry pressure is reached, the curve enters a funicular state where the liquid phase is continuous and the gas phase consists of isolated bubbles. The water content is therefore largely reduced as the air content increases. This region is the first half of what some authors call the transition zone, from funicular to pendular state [Nuth & Laloui, 2008, Fredlund et al., 2011, Pap et al., 2018a, Pap et al., 2018b];

3. After the funicular state, neither the gas nor the liquid phase is continuous: this is the pendular state, where the liquid phase forms bonds between the granular skeleton;

4. Finally, the last region observed consists of a residual state [Pap et al., 2018a], where the saturation is said to be equal to the residual saturation degree, noted $S_{r,res}$, corresponding to the quantity of water that can never be extracted from the medium without extreme heating.

Some porous media exhibit a water retention curve whose shape does not fit the unimodal characteristic shown in Figure 2.16, but rather a bimodal or multimodal shape, as it may be the case for concrete (Figure 2.17). This is due to the porosity of the medium, which does not have only one series of pores, but also larger pores (macropores) and smaller pores (capillary pores) [Pap et al., 2018b].

For such a porous medium, one would see a plateau in the middle of the water retention curve due to the change from one pore size to another. As the water is quickly removed from the open macropores of the concrete at low suction due to the gravitational flow, the water retention curve of the concrete may show a curve change at very low suction corresponding to the end of the emptying of the macropores and the beginning of the drying of the capillary pores.
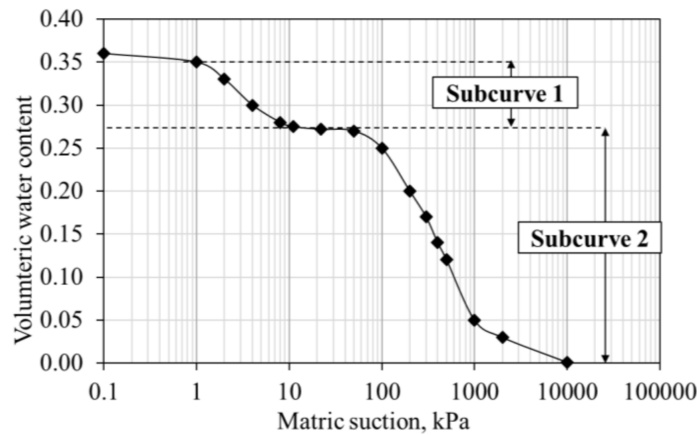
Figure 2.17: Bimodal characteristic of concrete [Pap et al., 2018b].

Whether the surface is undergoing rewetting or drainage, the water retention curve can follow different paths. This phenomenon is called hysteresis and is primarily due to two phenomena [Bear & Verruijt, 1987, Simunek et al., 1999, Pham et al., 2005, Nuth & Laloui, 2008, Abbasi et al., 2012, Likos et al., 2014, Pap et al., 2018a, Capparelli & Spolverino, 2020]:

1. The first one is called the ink-bottle effect and is due to water re-entering narrow channels, requiring a local increase in suction;

2. The second effect is called the raindrop effect, which is simply an expression of the difference in the value of the contact angle between an advancing and receding meniscus.

Finally, entrapped air is another factor causing hysteresis as liquid is required to push the air out of the porous material before rewetting. That air entrapment accounts for approximately 10% of the volume of a soil, which is non negligible [Pham et al., 2005].

This phenomenon is shown in the Figure 2.18 for a coarse material. The retention curve is expressed in terms of capillary pressure head h_c rather than suction s, but the behaviour is identical. It can also be seen that the relationship between the two variables of the retention curve, i.e. the capillary pressure head and the saturation, depends on the wetting and drying history of the sample [Bear & Verruijt, 1987, Likos et al., 2014].
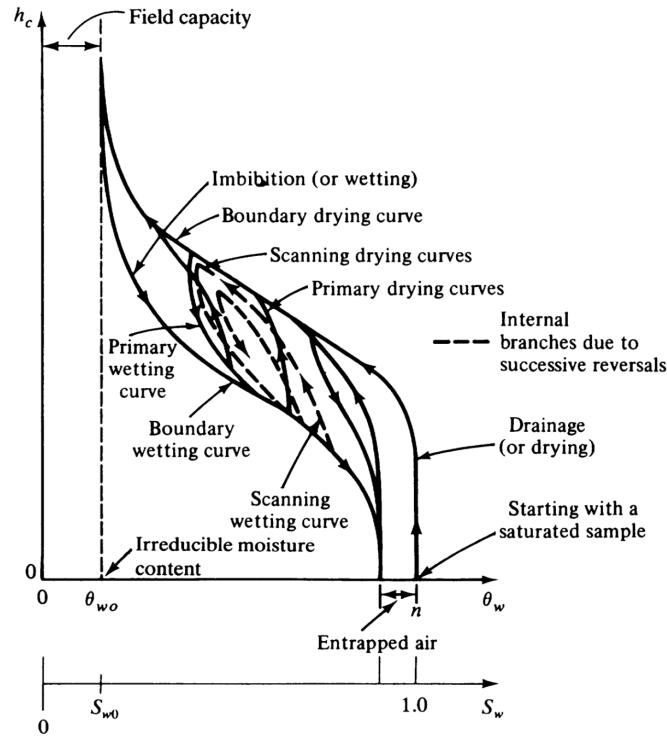
Figure 2.18: Hysteresis in the retention curve for a coarse material [Bear & Verruijt, 1987].

The water retention curve of a granular material can be determined by fitting an empirical formulation to several experimental points using the following analytical formulation, called the Kelvin law:

$$s = -\frac{\rho_w \, R \, T}{M} \, \ln(RH) \tag{2.14}$$

with s the matrix suction [Pa], ρ_w the water density [kg/m³], R the constant of ideal gases (equal to 8.3143 [J/K.mol]), M the molar mass of water (equal to 18.016 [g/mol]) and, finally, T and RH are the temperature [K] and Relative Humidity [%], respectively. The most famous empirical formulation is that proposed by Van Genuchten [Van Genuchten, 1980, Gerard et al., 2010, Likos et al., 2014, Capparelli & Spolverino, 2020]:

$$S_{r,w} = S_{res} + (S_{sat} - S_{res}) \left(1 + \left(\frac{s}{\alpha_{vG}} \right)^{n_{vG}} \right)^{-m_{vG}} \quad \text{with} \quad m_{vG} = 1 - \frac{1}{n_{vG}} \tag{2.15}$$

where n_{vG} is an adimensional model parameter related to the rate of desaturation of the porous system through the pore size distribution, and m_{vG} is another adimensional model parameter related to the symmetry or the curvature (slope) of the water retention curve. The last model parameter, denoted α_{vG}, is related to the air-entry pressure and is also proportional to the pore radius [Kohgo, 2008, Likos et al., 2014]. Finally, one can see the maximum

saturation S_{sat} and the residual saturation S_{res}, as well as the suction s.

This empirical relationship is initially asymptotic in nature and is therefore only used to represent the water retention curve between the air-entry value and the residual value of the porous material [Fredlund et al., 2011]. Here the terms S_{res} and S_{sat} come into play to allow the modelling of the entire curve.

2.3.3 Sorption Isotherms

For a given temperature, it is possible to relate the equilibrium water content of the porous medium to the moisture content of its surroundings with curves called sorption isotherms. These sorption isotherms are analogous to the water retention curves explained earlier, the only difference being that the x-axis represents the relative humidity instead of the suction, these two concepts being similar and linked by the Kelvin law (Equation 2.14). Nevertheless, sorption isotherms are presented in this thesis as they provide another way of characterising sorptivity.

Sorptivity is a material property that describes the tendency of a porous hygroscopic medium to absorb water and transfer it to the surrounding medium by capillarity [Hall, 1989, Kowalski, 2003], i.e. the many interactions that take place at the microscopic level between the solid skeleton and the water molecules. They therefore make it possible to describe the hygroscopic behaviour of the solid [Léonard, 2002].

The sorption isotherm expresses the coverage of the solid surface by one or more layers of gas molecules, in our case water vapour. These isotherms can be seen as a picture of the affinity that exists between a solid surface (the adsorbent) and the vapour (the adsorbate) [Xi et al., 1994, Beckett & Augarde, 2013, Desaar, 2015].

Adsorption or desorption isotherms can be determined by subjecting the sample to increasing (water uptake) or decreasing (water loss) humidity.

Depending on the nature of the material, the adsorption isotherms of gases on the surface of a solid can take different forms among five types well described in the literature [Brunauer et al., 1940]. These isotherms represent the adsorbed volume as a function of the partial pressure, as shown in the Figure 2.19.
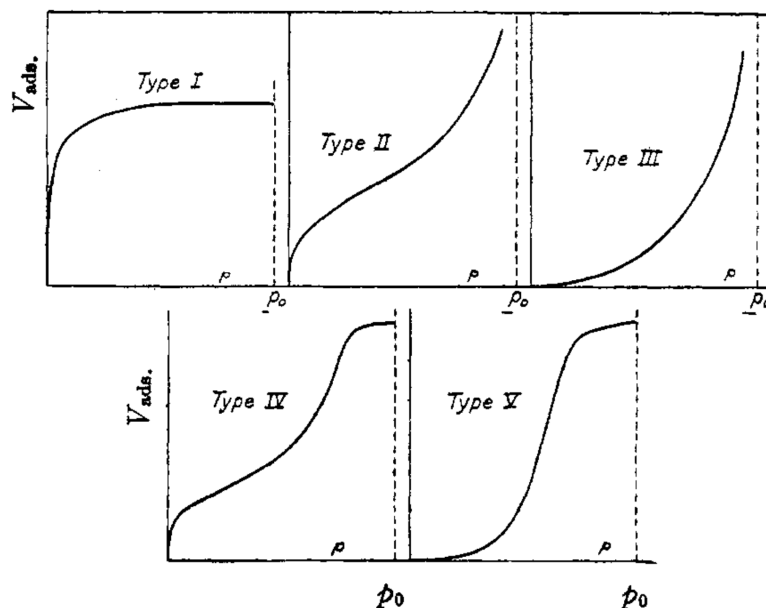
Figure 2.19: The five types of Van der Waals adsorption isotherms [Brunauer et al., 1940].

Type I corresponds to a single-layer adsorption, also known as the Langmuir isotherm. Types II and III are found for macroporous solids, while types IV and V correspond to mesoporous and microporous solids, respectively, and often include hysteresis related to capillary condensation [Léonard, 2002, Inglezakis et al., 2018]. Type II is also obtained for non-porous material and represents unrestricted multi-layer adsorption [Inglezakis et al., 2018]. All types, except for type I, correspond to multi-layer adsorption [Baroghel-Bouny, 1994]. However, it is often difficult to assign a material to a specific isotherm as it may belong to several classes of sorption isotherms at the same time [Léonard, 2002].

The different types of isotherms therefore correspond to different porosities. In fact, a microporous material contains pores smaller than 2 nm in diameter, while the pores of a macroporous material are larger than 50 nm in diameter and the ones of a mesoporous material are between the two others, i.e. between 2 and 50 nm [Rouquerol et al., 1994].
In concrete, mesopores (2.5 to 50nm) and micropores (less than 2.5nm) represent the majority of the pores, while macropores (from 50nm to 10000nm) constitute only a small portion [Xi et al., 1994].

Type II, IV and V are all S-shaped isotherms with one or more inflection points. The middle section of the isotherms, which is almost linear, is often referred to as the stage where mono-layer coverage is completed, and multilayer adsorption begins. These S-shaped isotherms originate from two opposing mechanisms: cooperative adsorption due to solute-solute attractive forces at the surface, and inhibition of solute sorption by a competing reaction within the solution [Limousin et al., 2007, Inglezakis et al., 2018].

When the adsorbed species is in equilibrium with the gas phase, its surface concentration on a solid depends on the nature of the gas and the solid, as well as on the gas pressure (or the partial pressure of water vapour in the case of humid air) and the temperature [Ollivier & Torrenti, 2008]. In this study, the adsorbed species is water and the gas phase is water vapour.

For water isotherms, the x-axis often represents the relative humidity while the y-axis represents the equilibrium water content. Furthermore, the isotherms often encountered with water are classified as type II (Figure 2.20) [Léonard, 2002].
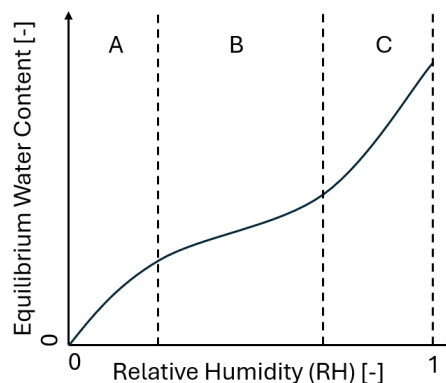
Figure 2.20: Isotherm of type II also called S-shape isotherm (adapted from [Léonard, 2002]).

The type II sorption isotherm can be divided into three parts for better understanding [Léonard, 2002]. At the beginning of the curve, i.e. for low relative humidity (section A), a first layer of water is bound to the solid skeleton. As Langmuir theory shows, the binding energy is very strong and the water molecules are therefore not very mobile.

For intermediate relative humidities or pressures (section B), the slope of the curve begins to increase. Indeed, a second layer of water molecules is formed and the adsorption is therefore characterised as multilayer, originating from adsorbate-adsorbate interactions [Giles & Smith, 1974]. However, the binding energy is lower than for the first layer, as demonstrated by the BET (Brunauer-Emmet-Teller) model [Brunauer et al., 1938].

At pressures close to saturation (section C), the slope of the curve increases even more, and the last water molecules attach themselves to the irregularities of the material surface: this phenomenon is called capillary condensation [Ollivier & Torrenti, 2008], and the binding energy is once again lower than for the previous layers.

In summary, at a given temperature, the number of layers of water vapour molecules adsorbed on the surface of the sample is an increasing function of the partial pressure of water and therefore of the relative humidity. The binding energy of these different layers of water decreases with increasing distance from the solid, thus limiting the amount of water fixed [Ollivier & Torrenti, 2008].

The BET equation, while still the most widely used of all sorption equations, has no finite solid phase concentration limit and therefore no saturation, even when the liquid phase reaches its saturation [Inglezakis et al., 2018].

Hygroscopicity expresses the ability of a material to adsorb (or desorb) and retain water, either by surface molecular adsorption or by capillary condensation, depending on the relative humidity of the ambient air [Desaar, 2015]. Hence the use of (de)sorption isotherms to characterise the hygroscopicity of the material.

Maximum hygroscopicity is reached when the solid is in equilibrium with the surrounding saturated air: this water content defines the hygroscopic threshold, below which the moist material is in the so-called hygroscopic region [Léonard, 2002].

As for the water retention curve, sorption isotherms show a phenomenon called hysteresis: adsorption and desorption isotherms have different profiles depending on whether they were determined by increasing or decreasing moisture content, which is incompatible with the notion of equilibrium. In fact, both curves have the same values only at their RH extremum, i.e. for 0% and 100% [Kowalski, 2003].

3

DEGRADATION PROCESSES

Contents

3.1 Introduction

This chapter provides a review of degradation processes, with a specific emphasis on chloride-induced corrosion. Firstly, a general overview of degradation processes is given, outlining different forms of degradation that may occur on concrete structures. The focus then shifts to chloride-induced corrosion, describing the corrosion process and the reactions that occur during chloride attack. Some technical concepts are explained, including the binding of chloride ions, the maximum phenomenon, and the threshold concentration required to initiate the corrosion process.

Following the presentation of these theoretical concepts, the modelling of chloride ingress and the existing developments are also explained. An overview of the evolution of the models over time is provided from the literature, followed by several models for each mechanism. The complexity of these models increases to consider the various physical and chemical processes involved.

Lastly, a summary of the effect of recycled concrete aggregates on chloride induced corrosion is presented.

3.2 Degradation Processes

Concrete structures are constructed with a focus on long-term durability: typically, they are designed to have a service life of over 100 years. Throughout this period, concrete undergoes several degradation processes, which can be classified into five main categories [Bertolini et al., 2004]:

1. Physical: freeze-thaw cycles, fires, ...;

2. Mechanical: abrasion, erosion, impact, ...;

3. Chemical: attack by chemicals (acids, sulphates, ...), alkali aggregates reactions, ...;

4. Biological: biogenic attack by bacteria, ...;

5. Structural: overloading, settlement, ...

Additionally, the reinforcements embodied in the concrete are prone to corrosion, which is often closely tied to concrete degradation. Indeed, the corrosion of the reinforcement leads to the creation of rust, resulting in an expansion of the reactants which may induce cracking of the concrete and, possibly, spalling.
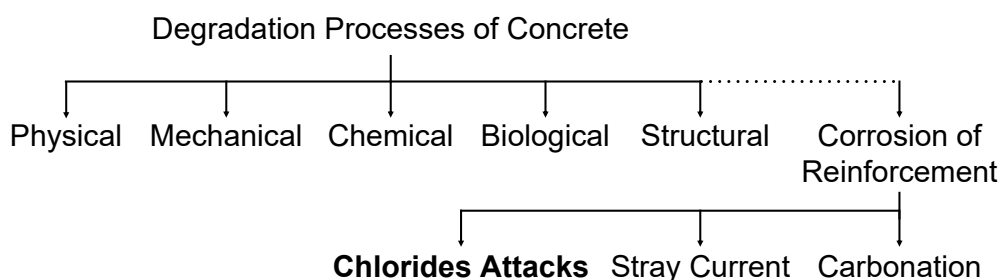
Figure 3.1: Degradation processes applied to concrete.

41

All degradation processes (depicted in the Figure 3.1), which can affect the concrete either directly or indirectly, may be interconnected and can influence each other, thereby potentially exacerbating the degradation [Patel et al., 2017]. For instance, mechanical deterioration, such as cracking, can increase the flow of water and thus encourage additional forms of deterioration. In any case, water is required for all the processes of degradation.

3.3 Chloride-Induced Corrosion

3.3.1 Introduction to the Process

Concrete, as detailed in Chapter 2, is a material made up of sand, aggregates, and cement grains that react with water to produce a composite mixture of ill-crystallised $C-S-H$ gel and other crystalline phases like portlandite $Ca(OH)_2$ [Samson et al., 2000, Samson & Marchand, 2007]. This hydration of cement creates a highly alkaline pore solution, with a pH between 13 and 13.8. Its alkalinity is derived from the cement hydration products and is mainly due to $Ca(OH)_2$ and alkali metal ions Na^+ and K^+ [Liu et al., 2015]. The highly charged ionic pore solution comprises numerous ions including hydroxyl OH^-, sulphate SO_4^{2-}, sodium Na^+, potassium K^+, and calcium Ca^{2+} among others [Tang, 1996, Samson et al., 2000, Samson & Marchand, 2007, Bertolini et al., 2004]. Its high pH level passivates the steel reinforcement, meaning it shields them from corrosion. Consequently, iron oxide (Fe_2O_3) and oxyhydroxide compounds form a thin, protective oxide film known as the passive film, which is thermodynamically stable [Neville, 1995, Martin-Perez et al., 2001, Bertolini et al., 2004, Angst, 2011].
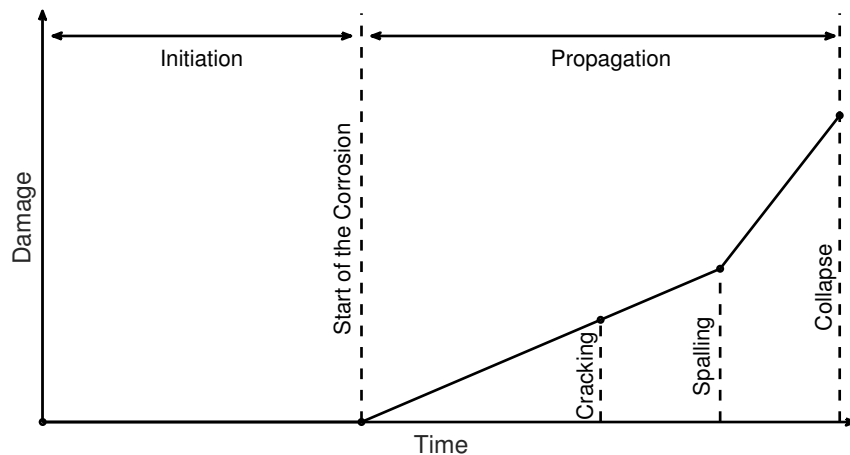
Figure 3.2: Timeline of degradations occuring due to chloride ions ingress (modified from [Gjørv, 2011]).

To initiate corrosion in reinforced concrete, a drop in the pH of the pore solution is necessary. This process is known as depassivation of the reinforcement and can be caused by two degradation processes: carbonation and chloride ingress [Mangat & Molloy, 1994]. As this study focuses on chloride attacks, we assume that depassivation is exclusively due to chloride penetration through the concrete cover.

Chloride ions migrate through the porous concrete structure. The time taken for the chlorides to reach the embedded reinforcement may vary depending on the thickness and quality of the concrete cover. When the concentration of chlorides reaches a certain threshold at

the surface of the reinforcement, there may be local destruction of the passive layer due to a significant drop in pH. The threshold is mainly dependent on the amount of oxygen that reaches the surface of the steel, which is strongly related to the saturation degree [Martin-Perez et al., 2001, Bertolini et al., 2004]. The depassivation and resulting corrosion are classified as local phenomena due to various processes that will be elaborated on after. The corrosion induced by chloride is commonly referred to as "pitting corrosion", providing a distinction from the more evenly distributed corrosion caused by carbonation on the entire reinforcement.

The corrosion of reinforcement can have significant impacts on both the serviceability and safety of a structure, as the pitting of steel reduces its structural resistance. This is especially true in cases of chloride-induced corrosion which can lead to a reduction in the rebars' cross-sectional area and a loss of bond at the steel-concrete interface. As a result of the increase of volume in the surrounding of the pitting corrosion, induced by rust formation, spalling and cracking can occur locally within the concrete [Martin-Perez et al., 2001, Chen & Mahadevan, 2008, Balafas & Burgoyne, 2010, Nilenius, 2014].
Visual damage is observable before structural damage, enabling a proactive approach to minimize and control the degradation process. Figure 3.2 illustrates the timeline of chloride ingress degradation [Balafas & Burgoyne, 2010, Gjørv, 2011].

3.3.1.1 Source of Chloride Ions

Chloride-induced corrosion is caused by the ingress of chloride ions, which can originate from either the environment or constituents within the concrete [Page et al., 1981, Neville, 1995, Poulsen, 1995, Debieb et al., 2010, Courard, 2019]:

- environmental sources include sea water, sea wind and de-icing salts ($NaCl$);

- constituents may include marine aggregates that were poorly washed, contaminated recycled aggregates, sea water used in the concrete, and accelerators ($CaCl_2$, now prohibited).

Chloride ions that originate from the constituents of concrete, are now restricted by European and national standards. The maximum permissible concentration of Cl^- within fresh concrete is 0.2-0.4% by mass of cement for reinforced concrete and 0.1-0.2% for prestressed concrete, according to the NBN EN 206:2013 [Bertolini et al., 2004]. In this work, the only source of chloride ions considered is external.

3.3.1.2 Driving Forces for the Chloride Ingress

In saturated conditions, such as immersion in seawater, ions are transported through the porous system by two primary driving forces. These are diffusion, resulting from a concentration gradient of chloride ions, and migration, arising from an internal imbalance in several ionic species that creates an electric potential gradient. Of the two forces, diffusion is the predominant one. In unsaturated conditions, such as in coastal areas or on roads treated with de-icing salts, wetting-drying cycles cause water movement that transports chloride ions. Consequently, a third driving force arises: convection [Poulsen, 1995, Nagesh & Bhattacharjee, 1998, Martin-Perez et al., 2001, Ababneh et al., 2003, Baroghel-Bouny et al., 2011, Liu et al., 2015, Wu et al., 2017, Xiong et al., 2020, Jin et al., 2022].

The interplay of these driving forces means that the primary force can vary depending on the depth and saturation of the concrete being studied.

3.3.1.3   Parameters Influencing the Chloride Ingress

In cement-based materials like concrete, the chloride penetration is primarily influenced by the porous structure's connectivity, and cracking. Specifically, the transport properties of concrete are subjected to the porosity, pore size and pore size distribution of the material [Xi et al., 1994, Li et al., 2015, Zhou et al., 2019, Zhang et al., 2022]. The material microstructure, including the Interfacial Transition Zone (ITZ) between aggregates and cement paste, also plays a role in the diffusion of ions [Sun et al., 2011, Jin et al., 2022], even though it was proven to be less meaningful than the impact of the aggregates themselves [Li & Song, 2022]. Furthermore, it is worth noting that the saturation degree significantly affects the mechanisms of chloride ion transport, as the primary driving force involved vary depending on the water content of the pore network [Wu et al., 2017, Li & Song, 2022].

In addition, mix properties, such as the type of cement used, water-to-cement ratio, curing conditions, and initial chloride concentration, also play a vital role in determining chloride ingress. Moreover, plastic and drying shrinkage induce cracking that may promote chloride ingress. The stated parameters do indeed have an impact on the properties of the porous system and the chemical composition of the concrete. It must be noted that external factors, including temperature and ion concentration, have a direct influence on diffusion mechanisms [Xi & Bažant, 1999, Morga & Marano, 2015, Alsheet & Razaqpur, 2018, Jin et al., 2022].

It is also important to consider the role that time plays in determining chloride diffusion inside the porous system. Even after 28 days of curing, the hydration reaction progresses, and subsequently generates hydration products, thus closing the pore system and diminishing the diffusivity of ions [Xi et al., 1994, Nokken et al., 2006].

3.3.2   Corrosion Reactions due to Chloride Attacks

Once corrosion begins, the concrete and steel reinforcements witness the formation of a galvanic cell system: parts of the reinforcements that are no longer protected by the passive film become anodes to their surroundings, while the passivated sections behave like cathodes, where oxygen reduction reactions take place. Pitting corrosion occurs in the anodic regions, where the initial corroded sections of the reinforcement act as sacrificial anodes, and the remaining portions of the reinforcement are cathodically protected. Therefore, the corrosion is limited to these areas [Neville, 1995, Gjørv, 2011].
The transfer of negatively charged ions from the cathode to the anode occurs in the pore water. The characteristics of the porous system, the degree of water saturation, and the ionic concentration of the pore solution are key factors in corrosion propagation [Neville, 1995, Balafas & Burgoyne, 2010].

The electrochemical reactions in this system can be summarised by Figure 3.3, which illustrates the four main steps of the process [Neville, 1995, Bertolini et al., 2004, Angst, 2011]:

1. Anodic reaction involving iron dissolution;

2. Electrical current flowing through the reinforcement;

3. Cathodic reaction involving oxygen reduction;

4. Ionic current flowing through the electrolyte solution in the pore.
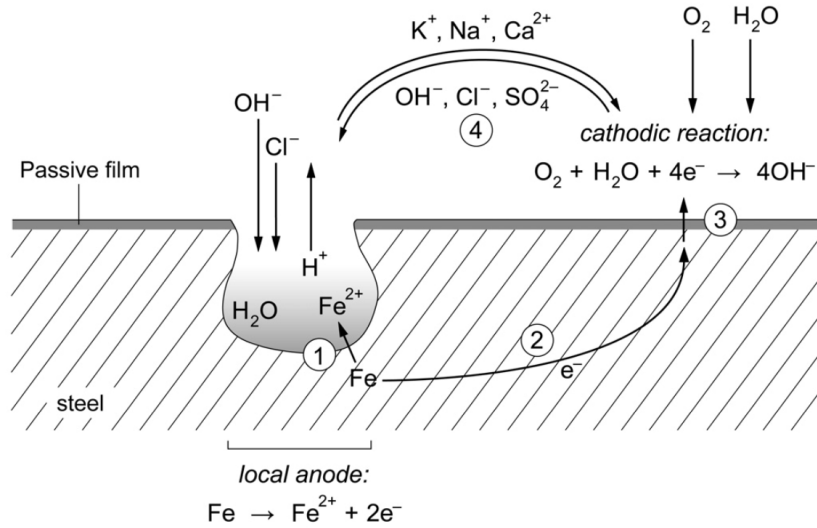
Figure 3.3: Schematic representation of the chloride-induced corrosion [Angst, 2011].

The half-cell reactions lead to the reinforcement's pitting caused by corrosion. The anodic reaction of iron dissolution and the cathodic reaction of oxygen reduction are as follows [Neville, 1995, Isgor & Razaqpur, 2006]:

$$2 \, \mathrm{Fe} \longrightarrow 2 \, \mathrm{Fe}^{2+} + 4 \, \mathrm{e}^-$$

$$\mathrm{O_2} + 2 \, \mathrm{H_2O} + 4 \, \mathrm{e}^- \longrightarrow 4 \, \mathrm{OH}^-$$

$$2 \, \mathrm{Fe} + \mathrm{O_2} + 2 \, \mathrm{H_2O} \longrightarrow 2 \, \mathrm{Fe}^{2+} + 4\mathrm{OH}^- \longrightarrow 2 \, \mathrm{Fe(OH)_2} \tag{3.1}$$
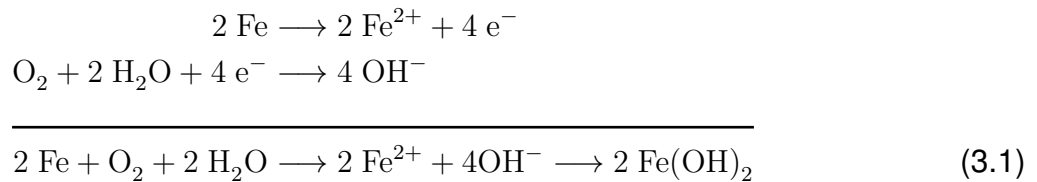
Water and dissolved oxygen are necessary for steel corrosion to occur. As a result, the corrosion of steel is more pronounced under unsaturated conditions than in dry or saturated conditions [Liu & Weyers, 1998, Balafas & Burgoyne, 2010, Angst, 2011].

However, these reactions do not lead to rust formation. Instead, the iron ions keep reacting within the pore solution to produce the so-called red rust $\mathrm{Fe_2O_3}$ [Neville, 1995, Isgor & Razaqpur, 2006]:

$$4 \, \mathrm{Fe(OH)_2} + 2 \, \mathrm{H_2O} + \mathrm{O_2} \longrightarrow 4 \, \mathrm{Fe(OH)_3} \tag{3.2}$$

$$2 \, \mathrm{Fe(OH)_3} \longrightarrow 2 \, \mathrm{H_2O} + \mathrm{Fe_2O_3} \cdot \mathrm{H_2O} \tag{3.3}$$
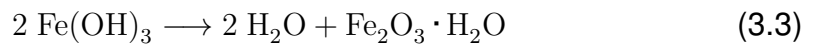
Corrosion products therefore consist of multiple oxides and oxyhydroxides (e.g. magnetite, geothite, ...), which occupy a greater volume than the reagents. This results in the reinforcement expanding, leading to localised concrete cracking [Balafas & Burgoyne, 2010, Liu et al., 2020].

When chloride ions are sourced from de-icing salts, the ionic flow within the electrolyte solution initiates chemical reactions between the iron in the rebars and the salts [Neville, 1995, Courard, 2019]:

$$2\,NaCl \longrightarrow 2\,Na^+ + 2\,Cl^- \tag{3.4}$$

$$Fe^{2+} + 2\,Cl^- \longrightarrow FeCl_2 \tag{3.5}$$

Moreover, the second reaction is autocatalytic: the rust produced dissolves in water to liberate the chloride ions:

$$FeCl_2 + 2\,OH^- \longrightarrow Fe(OH)_2 + 2\,Cl^- \tag{3.6}$$
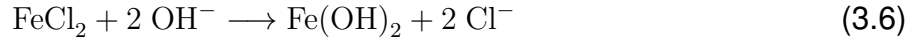
which accelerates the corrosion process.

The ionic current formed during the corrosion process attracts chloride ions owing to their negative charge, resulting in an increase in chloride content and concurrent decrease in the alkalinity of the pore solution present near the corroded steel bars. Conversely, this same current strengthens the passive film by elevating the alkalinity of the cathodic area through the reduction in chloride content as chloride ions migrate from this area to the anodic one [Bertolini et al., 2004].

The formation of oxidised products is determined by both the pH of the pore solution and the electrode potential. The Pourbaix diagram illustrated in Figure 3.4 displays this phenomenon in relation to iron ions. Within the grey zone, the iron remains stable and does not create oxides nor dissolve: this is known as the immunity zone [Nilsson et al., 1996, Angst, 2011]. The rebar is passivated in the green zone, whereas in the red zone, the risk of corrosion increases [Nilsson et al., 1996, Ployaert, 2008].
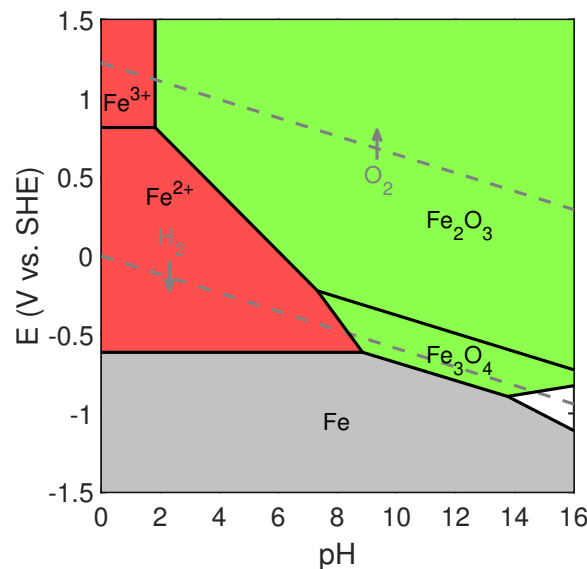
Figure 3.4: Pourbaix diagram of Fe in water (ion concentration of 10^{-6} mol/l and 25°C) (modified from [Nilsson et al., 1996, Ployaert, 2008, Angst, 2011]).

3.3.3 Binding of Chlorides

Chloride ions can bind to the porous system, through physical binding or ionic exchange. The chloride ions present within the material can be classified into two types [Tang & Nilsson,

1993, Saetta et al., 1993, Poulsen, 1995, Nilsson et al., 1996, Xi & Bažant, 1999, Isgor, 2001, Nokken et al., 2006, Khan et al., 2017, Sun et al., 2022]:

1. the free chlorides which are soluble in water and located inside the pore solution;

2. the bound chlorides that can adhere physically to the pore walls, which are located on the surface of the $C-S-H$ gel, or chemically react with the hydration products present in the cement paste (such as calcium aluminate hydrates).

Free chlorides are commonly known as water-soluble chlorides, while the total quantity of chlorides is referred to as acid-soluble chlorides. The difference between the free and total chlorides provides the bound chlorides [Poulsen, 1995, Shi et al., 2012].

Only the free chlorides are responsible for the corrosion of steel reinforcements. As a result, the governing equations must be written in terms of the free chloride rather than the total chloride content [Poulsen, 1995, Xi & Bažant, 1999, Liu et al., 2020].
However, it is imperative to consider the bound chloride ions during the diffusion process of chlorides as they decrease the chloride concentration in the pore solution, subsequently reducing the rate of free chloride transport [Saetta et al., 1993, Xi & Bažant, 1999, Isgor, 2001, Martin-Perez et al., 2001, Ababneh et al., 2003, Glasser et al., 2008, Shi et al., 2012, Spiesz et al., 2012, Li et al., 2015, Khan et al., 2017]. As the chloride concentration in the pore solution declines, bound chlorides can dissolve, contributing to the equilibrium between bound and free chlorides [Neville, 1995, Li et al., 2015].

Bound chlorides have been found to diffuse twice as quickly as free chlorides [Lu et al., 2002, Shi et al., 2012]. If included in the model, the total diffusivity of chloride ions (which is the addition of free and bound chlorides) becomes three times that of free chlorides only [Lu et al., 2002]. However, because bound chlorides are not responsible for the corrosion of reinforcement and because they reduce the chloride concentration in the pore solution, the corrosion initiation time could be increased by up to 200% [Zuquan et al., 2018].

Chloride binding is typically characterised through adsorption isotherms in the literature [Glasser et al., 2008]. At low chloride ion concentrations, adsorption is considered to be monolayer adsorption and can be described by the Langmuir isotherm. Conversely, at higher concentrations (above $0.5 \mathrm{mol/l}$), multilayer adsorption takes place and is more accurately described by the Freundlich isotherm [Yuan et al., 2009]. This method does not make a distinction between chemical or physical binding.

The key factors influencing the process of chloride binding are the cement type and composition, pH levels, amount of $C-S-H$, and the surrounding environmental conditions including relative humidity and temperature. It is worth noting that the overall concentration of chloride ions also has an impact on the chloride binding capacity [Glasser et al., 2008, Angst, 2011, Zuquan et al., 2018].
The bounding chloride ions react chemically with C_3A, C_4AF and their hydration products, resulting in the formation of Friedel's salt and calcium oxychlorides (CaOxy). These compounds possess a less porous structure which in turn reduces the rate of chloride ion transport [Saetta et al., 1993, Neville, 1995, Xi & Bažant, 1999, Samson et al., 2000, Han, 2007, Glasser et al., 2008, Yuan et al., 2009, Khan et al., 2017, Zuquan et al., 2018, Liu et al.,

2020, Jones et al., 2020]:

$$Ca(OH)_2 + 2\,NaCl \longrightarrow CaCl_2 + 2\,Na + 2\,OH^- \tag{3.7}$$

$$C_3A + CaCl_2 + 10\,H_2O \longrightarrow C_3A \cdot CaCl_2 \cdot 10\,H_2O \text{ (Friedel's salt)} \tag{3.8}$$

$$3Ca(OH)_2 + CaCl_2 + 12H_2O \longrightarrow 3Ca(OH)_2 \cdot CaCl_2 \cdot 12H_2O \text{ (CaOxy)} \tag{3.9}$$
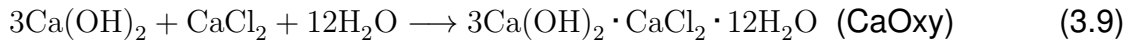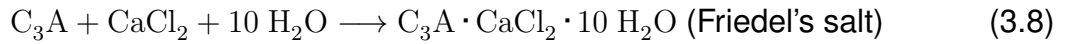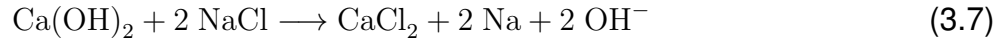
Among the different components of cement, C_3A has the most significant effect [Neville, 1995]. C_3S and C_2S are, on the other hand, the primary components responsible for physical bonding [Yuan et al., 2009]. Furthermore, calcium oxychlorides may form from solutions containing $MgCl_2$ and $NaCl$ [Jones et al., 2020]. It is now widely accepted that the main mechanism of chloride binding is through ionic exchange, where components of the cement paste will release an OH^- ion in exchange for a Cl^- ion [Glasser et al., 2008]:

$$[X - OH] + Cl^- \leftrightarrow [X - Cl] + OH^- \tag{3.10}$$

where X is an ion exchange site. The same may be observed for SO_4^{2-} and $2Cl^-$. Chemical binding contributes significantly more than physical binding, the difference between both increasing as the chloride concentration increases [Glasser et al., 2008].

3.3.4 Threshold Value for Initiation of Corrosion

Corrosion in alkaline concrete begins once the concentration of chloride ions on the reinforcement surface has surpassed a critical threshold, known as the chloride threshold value or critical chloride content [Glasser et al., 2008, Angst et al., 2009].
Following a duration of time, identified as corrosion initiation, chlorides reach the reinforcement. The initiation time depends on the exposure conditions (i.e. chloride content at the surface), cover thickness and concrete properties (i.e. permeability and chloride binding capacity) [Angst, 2011]. It comprises two periods: the time for chlorides to reach the reinforcement and the time for the chloride threshold to be reached.

In this thesis, the threshold is defined as the level of chloride required to initiate the corrosion of the reinforcement by depassivating the steel. However, the critical chloride content may refer to the amount associated with an acceptable deterioration of the reinforcement, as reported by some authors [Angst et al., 2009].
This critical threshold value can be expressed in various units. The most common is the total chloride content by mass of the cement [Glasser et al., 2008, Angst et al., 2009].

This threshold is influenced by various factors from both the steel reinforcement and concrete, with some of them being interdependent. Nevertheless, only two of these factors are significant enough to warrant an explanation [Angst et al., 2009]:

1. State of the steel-concrete interface: the interfacial zone, which is similar to the ITZ with aggregates, forms a firm barrier comprising hydration products. The above-mentioned components act as a pH buffer for the pore solution and impede charge transfer reactions by creating a physical barrier. Furthermore, the interface area has been found to contain elevated levels of $Ca(OH)_2$. This necessitates a higher amount of chloride ions to be diffused in order to depassivate the steel. Unfortunately, assessment of the condition of the steel-concrete interface remains challenging.

2. The pH of the pore solution, which initially rises to about 12.5 due to the presence of Portlandite, reduces corrosion of steel reinforcement. However, this pH can decline due to the diffusion of chloride ions and carbonation.

The degree of saturation of the concrete during its lifetime is also a critical factor which promotes corrosion initiation, particularly in relative humidity of 90-95% or when exposed to wetting-and-drying cycles. Additionally, the ratio of free and bound chloride ions is reliant on the water content of the porous system [Angst et al., 2009].
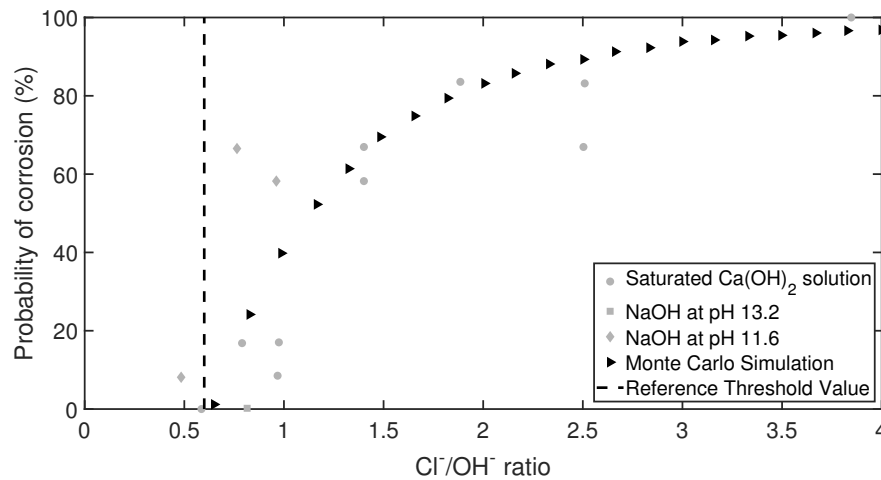
Figure 3.5: Probabilities of steel corrosion induced by chloride ingress, determined experimentally and predicted by a Monte Carlo simulation (modified from [Broomfield, 2007]).
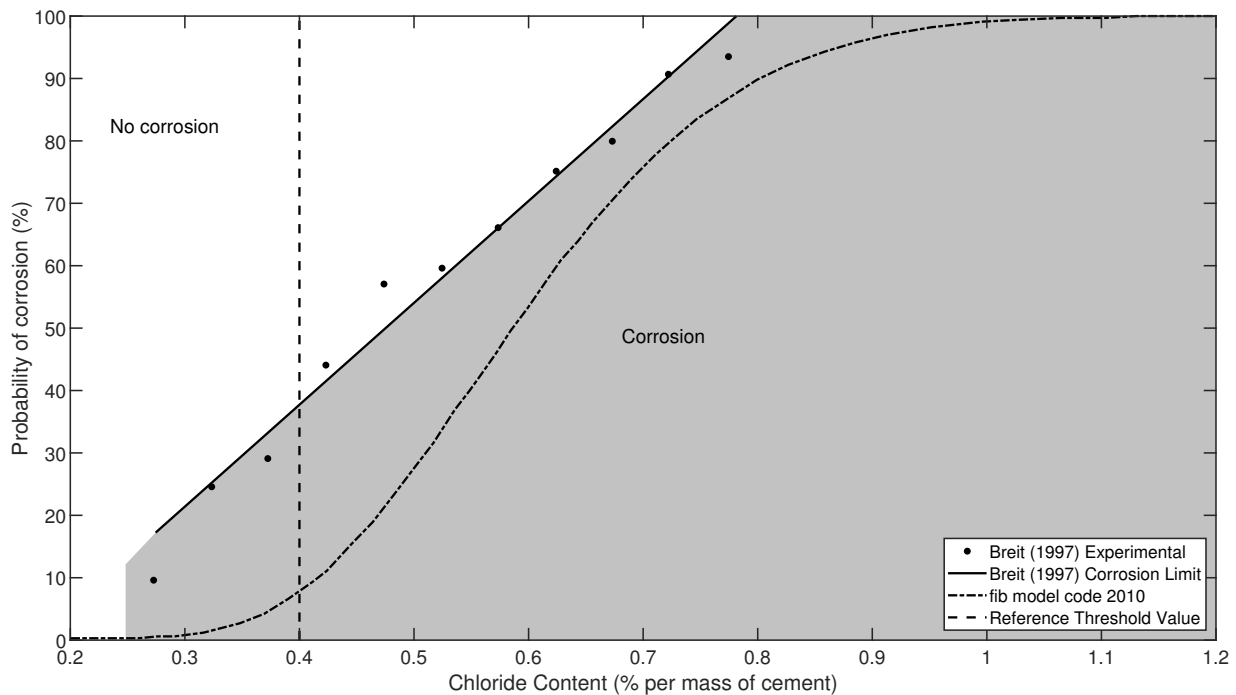
Figure 3.6: Probabilities of steel corrosion induced by chloride ingress, determined experimentally according to Breit (1997) as well as according to the fib model code 2010 (modified from [Raupach & Büttner, 2014]).

Over time, experimental programmes have assessed the risk of corrosion based on the chloride ion concentration in the pore solution, as depicted in Figure 3.5 and Figure 3.6 [Broomfield, 2007, Raupach & Büttner, 2014].

In this study, C_{crit} is set at 0.4% by mass of cement, which complies with the code's maximum allowed initial chloride content for reinforced concrete [Neville, 1995, Gjørv, 2011]. It has been suggested in previous experimental research that critical chloride content levels may reach up to 3.1% [Angst, 2011]. Figure 3.6 illustrates the experimental findings of Breit (1997) and the results of the fib model code (2010). Corrosion occurs on the right side of each line (either the Breit or fib one), while on the left side no corrosion occurs.

In other studies, it has been recommended that the value of C_{crit} in terms of the Cl^-/OH^- ratio should be considered as 0.6 [Saetta et al., 1993, Broomfield, 2007, Angst et al., 2009].

3.3.5 Maximum Phenomenon

Under saturated conditions, chloride ions diffuse from the surface of the concrete to the porous system, due to a concentration gradient. The surface is where the maximum value of chloride content is detected. In unsaturated concrete, however, drying-and-wetting cycles generate flows from inside the concrete to the surface, creating a maximum phenomenon. Chloride content rises to its maximum and then declines with distance from the exposed surface [Neville, 1995, Andrade et al., 2015, Chang et al., 2017, Petcherdchoo, 2018]. The convection (zone) depth marks the point at which maximum concentration is achieved and typically lies between 5 to 15mm from the surface of non-damaged concrete [Neville, 1995, Liu et al., 2020].

Another possible explanation for this phenomenon lies in the surface layer of the concrete surface, which is known to behave differently than the bulk of the material [Petcherdchoo, 2018]. The diffusion coefficient of this surface layer is often affected by factors such as carbonation, which causes the pores in the surface layer to close. Furthermore, the surface layer is frequently in contact with the formwork, causing an increased concentration of cement at the surface and consequently leading to greater porosity [Xi & Bažant, 1999].
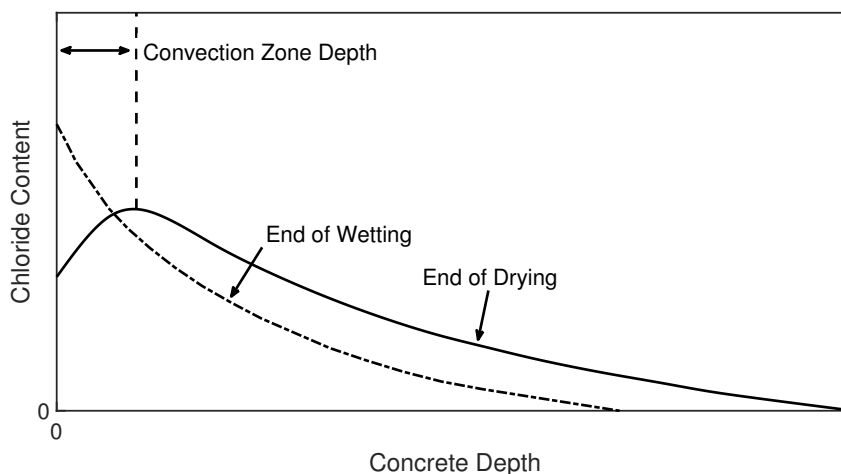
Figure 3.7: Maximum phenomenon due to drying and wetting cycles in unsaturated concrete (modified from [Petcherdchoo, 2018]).

The phenomenon of maximum concentration can be included in the governing equations by expressing the diffusion coefficient as a function of depth. Additionally, the solution of Fick's

second law can be adjusted to shift the maximum concentration from the surface to its actual depth [Xi & Bažant, 1999].

3.3.6 Conclusion

In this section, several theoretical phenomena related to chloride-induced corrosion have been put forward. These include: the binding of chloride ions, the maximum phenomenon and the threshold value for the initiation of corrosion. These phenomena are of relative importance when considering corrosion of the reinforcement. In the following chapter, the modelling of chloride ingress will be introduced. It is therefore important to consider these phenomena when undertaking the modelling.

3.4 Modelling of Chloride Ingress

3.4.1 State of the Art

Research into chloride ingress in concrete has been ongoing since the 1960s. The research employs experimental, analytical and numerical methods. The modelling of ionic transport within concrete's porous structure began a decade later. Initially, the models considered only the transport of a single ionic species within a single-phase medium. Subsequently, multiple ionic species were introduced within a monophasic medium. Other studies focused on single species in a multiphasic medium. Finally, advanced models examine the transportation of various species within multiphasic media [Liu et al., 2015].
The benefit of the multiphasic media is its ability to numerically investigate the effect of each constituent of the microstructure, including the aggregates and their ITZ, among other parameters.

As far back as 1955, researchers investigated the impact of de-icing salts on concrete. The study by Grieb et al. (1962) characterised the resistance of the concrete surface to scaling by de-icing agents. They investigated the potential effects of admixtures, curing techniques, as well as de-icing agents on concrete [Grieb et al., 1962]. In 1965, Snyder evaluated various coatings and analysed their effectiveness in preventing the deterioration of concrete caused by de-icing agents, with a focus on scaling [Snyder, 1965]. Although these studies do not exclusively focus on the ingress of chloride ions, they demonstrate an awareness of the damage caused by chlorides as early as 1955.

One of the earliest studies on chloride ingress in concrete was conducted by Collepardi et al. (1972). They employed the Fick's second law of diffusion solution under non-steady state conditions for a single ionic species in a semi-infinite solid (along one axis) to determine the diffusion coefficient of diverse cement pastes and concretes. At 25$°C$, the diffusion coefficient of chloride ions in cement pastes was approximately 10^{-12} m^2/s, as they discovered [Collepardi et al., 1972].
In 1993, Tang and Nilsson conducted a study on the binding of chlorides to cement pastes and mortars, and found that the Freundlich isotherm accurately represents the relationship between free and bound chlorides at high concentrations, while the Langmuir isotherm is better suited for lower concentrations [Tang & Nilsson, 1993].
Saetta et al. (1993) concurrently developed a finite element model for the diffusion of chloride in fully and partially saturated concrete, which integrates the pure ion diffusion with the

influence of moisture flux [Saetta et al., 1993].

In 1994, Mangat and Molloy derived a differential equation by applying Fick's second law. This equation takes into account the dependence of the diffusion coefficient over time, which they verified through experiments [Mangat & Molloy, 1994].

In 1996, Nilsson et al. produced a report on chloride penetration in concrete. The report contained predictive models and presented the most up-to-date research in the field. The focus was on explaining the appropriate way to use Fick's second law, with consideration given to the dependence of the diffusion coefficient on various parameters such as time, and accounting for the binding of chloride to the porous system [Nilsson et al., 1996].

In 1997, Delagrave et al. directed their attention towards the interfacial transition zone (ITZ) and its influence on the chloride diffusivity of mortars, ultimately concluding that the presence of the ITZ promotes the transportation of chloride ions [Delagrave et al., 1997].

A number of modelling studies were released in 1998, including the work of Liu and Weyers, Nagesh and Bhattacharjee, and Garboczi and Bentz which drew our interest. The dynamic corrosion process in bridge decks contaminated with chloride ions was modelled by Liu and Weyers (1998) [Liu & Weyers, 1998]. On the other hand, Nagesh and Bhattacharjee (1998) modelled chloride ingress in both saturated and unsaturated concrete, taking into account both diffusion and convection, which was uncommon at that time [Nagesh & Bhattacharjee, 1998]. Additionally, Garboczi and Bentz (1998) went even further by achieving a multiscale modelling of chloride diffusivity in concrete. The researchers were able to model an aggregate and its interfacial transition zone at a millimetre-scale to examine their impact on the overall diffusivity of concrete. They also modelled the cement paste and its microstructure at a micrometre-scale [Garboczi & Bentz, 1998].

Meanwhile, Xi and Bazant (1999) developed a multiphasic model for chloride ingress into saturated concrete, taking into account chloride binding as well as the effect of temperature, time, aggregates and ion concentration, among others [Xi & Bažant, 1999]. Ababneh et al. (2003) furthered the research by applying the conventional diffusion theory to unsaturated concrete. The model is represented by an equation dependent on both ion and moisture diffusivities. Composite theory at the mesoscopic level is used to investigate the effect of aggregates, while binding isotherms are used to account for chloride binding [Ababneh et al., 2003].

Bertolini et al. wrote a book in 2004 which covers in detail the corrosion of steel in concrete by both chloride attack and carbonation [Bertolini et al., 2004]. It provides an accurate summary of the current state of the art and consolidates the available knowledge at the time.

In the diffusion model, cracking as a result of rust expansion has been introduced by Chen and Mahadevan (2008) and Guzmán et al. (2011), among others [Chen & Mahadevan, 2008, Guzmán et al., 2011]. Additionally, Fu et al. (2010) conducted a study on the diffusion of chloride ions through sound and cracked concrete, with the diffusivity of the ions being increased by the presence of cracks [Fu et al., 2010].

In 2011, Baroghel-Bouny et al. developed a multi-species model using the Nernst-Planck equation to study coupled moisture-ion transport in cementitious materials. The model takes into consideration electro-diffusion of ions and advection of the liquid phase [Baroghel-Bouny et al., 2011].

Xiao et al. (2012) and Ying et al. (2013) investigated the impact of recycled concrete aggregates on chloride ingress by developing a model to describe the effect of these aggregates on

chloride diffusion. They modelled concrete as a composite material with five phases (three continuous phases and two interphases) at the mesoscale [Xiao et al., 2012, Ying et al., 2013a].

In 2015, Nilenius et al. developed a FE^2 model operating at both macroscale and mesoscale to simulate the occurrence of transient and coupled moisture-chloride ion diffusion in concrete. The mesoscale comprises cement paste, aggregates, and their ITZ [Nilenius et al., 2014].

Previous research has extensively investigated the issue of chloride infiltration in concrete under both saturated and unsaturated conditions, utilising both natural and recycled aggregates. Considering the constant increase in computational power, an increasing number of authors are incorporating multiphasic composite materials into their multiscale models, leading to a rise in parameters that influence the problem simultaneously.

Throughout the following sections, readers will gain an understanding of the different models that have been developed over time, along with their respective benefits, drawbacks, and limitations.

3.4.2 Consideration of Binding in the Model

The total chloride content previously discussed can be separated into two components: the bound and free chlorides. The correlation between these two types is non-linear and is often explained using chloride binding isotherms, also known as adsorption isotherms. The Langmuir, Freundlich, and BET isotherms are the most commonly employed [Yuan et al., 2009, Spiesz et al., 2012, Alsheet & Razaqpur, 2018].

The selection of an isotherm model is dependent on the concentration of free chlorides present in the pore solution. The Langmuir isotherm represents bonding adequately for low levels of free chloride ions (less than 0.05 $\mathrm{mol/dm}^3$), while the Freundlich isotherm is accurate for concentrations from 0.01 to 3 $\mathrm{mol/dm}^3$ [Tang & Nilsson, 1993, Yuan et al., 2009, Spiesz et al., 2012].

Moreover, when considering multilayer adsorption, the Freundlich isotherm provides a more accurate representation of the nonlinear relationship between free and bound chlorides.

The equation for describing the Freundlich isotherm is as follows [Yuan et al., 2009, Baroghel-Bouny et al., 2011, Spiesz et al., 2012, Alsheet & Razaqpur, 2018]:

$$C_b = K_b \, C_f^{n_b} \tag{3.11}$$

where C_b represents the concentration of bound-chlorides, C_f represents the concentration of free chlorides in the pore solution, K_b represents the binding capacity of concrete towards chloride ions, which is dependent on the $\mathrm{C-S-H}$ content, and n_b is a parameter that governs the binding intensity. It is logical that the value of K_b is lower in concrete as compared to mortar due to the lesser amount of cement. Additionally, with time, K_b decreases due to continuous hydration process [Spiesz et al., 2012]. The values of the two empirical coefficients K_b and n_b can be determined through linear log-log regression analysis of the chloride binding isotherms.

The relationship between free and bound chlorides can also be expressed by the Langmuir isotherm, through the following equation [Samson et al., 2000, Yuan et al., 2009, Ukrainczyk

& Koenders, 2016, Alsheet & Razaqpur, 2018]:

$$C_b = \frac{\alpha\, C_f}{1 + \beta\, C_f} \tag{3.12}$$

where α and β are coefficients dependent on cement properties, which are obtained by fitting experimental data.

Figure 3.8 displays the Langmuir and Freundlich isotherms. It is worth mentioning that the system depends on thermodynamic equilibrium, with the equations assuming direct equilibrium through direct binding reactions.
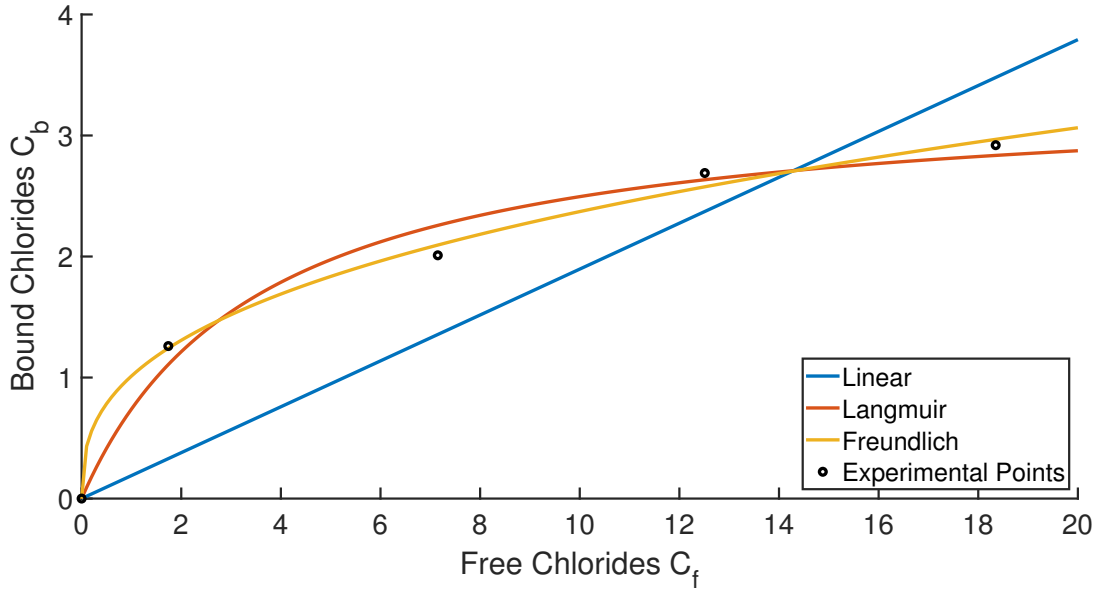
Figure 3.8: Binding isotherms used in the literature, with experimental points from [Martin-Perez et al., 2001, Yuan et al., 2009].

Once the relationships between free and bound chlorides have been established, it is possible to investigate the relationship between total chlorides and free chlorides. Total chlorides content is obtained through acid reaction and selective titration, and under saturated conditions, it is classified into free and bound chloride according to [Spiesz et al., 2012]:

$$C_t = \frac{\phi\, C_f + (1 - \phi)\rho_s\, C_b}{\rho_c} \tag{3.13}$$

where ϕ represents the open porosity of concrete and ρ_s and ρ_c represent respectively the density of solid-state concrete and the density of saturated concrete.

The ratio of $\partial C_b / \partial C_f$ indicates the binding capacity, which can be determined via binding isotherms as previously explained. The following equation relating free, bound, and total chloride contents can be used to calculate the concrete's binding capacity [Nilsson et al., 1996, Xi & Bažant, 1999, Chen & Mahadevan, 2008]:

$$\frac{\partial C_f}{\partial C_t} = \frac{1}{1 + \dfrac{\partial C_b}{\partial C_f}} \tag{3.14}$$

3.4.3 Modelling the Diffusion

3.4.3.1 Steady-State One Dimensional Diffusion

Diffusion acts as the primary transport mechanism for free chloride ions in saturated concrete. The ions diffuse due to a concentration gradient in the pore solution, which is expressed by Fick's first law [Nilsson et al., 1996]:

$$F = -D \, \frac{\partial C_t}{\partial x} \qquad (3.15)$$

This law states that the flow of ions, represented by F [kg/(m^2.s)], is directly proportional to the diffusion coefficient, represented by D [m^2/s]. This equation is based on steady-state diffusion, with the gradient of chloride ions determined by the concentration difference between the inside and outside of the concrete, specifically the concentration of free chlorides [Nilsson et al., 1996].

However, it must be noted that this diffusion process is oversimplified when compared to reality. In fact, chloride ions do not behave as simple particles, but are influenced by other ions and the walls of the pores [Nilsson et al., 1996]. If chloride ions migrate within concrete, their movement must be balanced by positive ions, such as Na^+ if they result from de-icing salts, and ions produced by the decomposition of $Ca(OH)_2$.
These ion movements can alter the composition of the pore solution, which may affect the substances' solubility and binding to the pore walls. The variation of chloride diffusion is neglected at this stage, and should be considered objectively. Chloride diffusion is viewed as the diffusion of an inert substance within a material with a certain binding capacity. Therefore, the diffusion of chloride ions in concrete is defined as [Nilsson et al., 1996]:

$$F = -D_{ref} \, \frac{\partial C_t}{\partial x} \qquad (3.16)$$

where C_t represents the concentration of chlorides in the solution, while D_{ref} is the effective diffusion coefficient of concrete, assumed constant and determined experimentally.
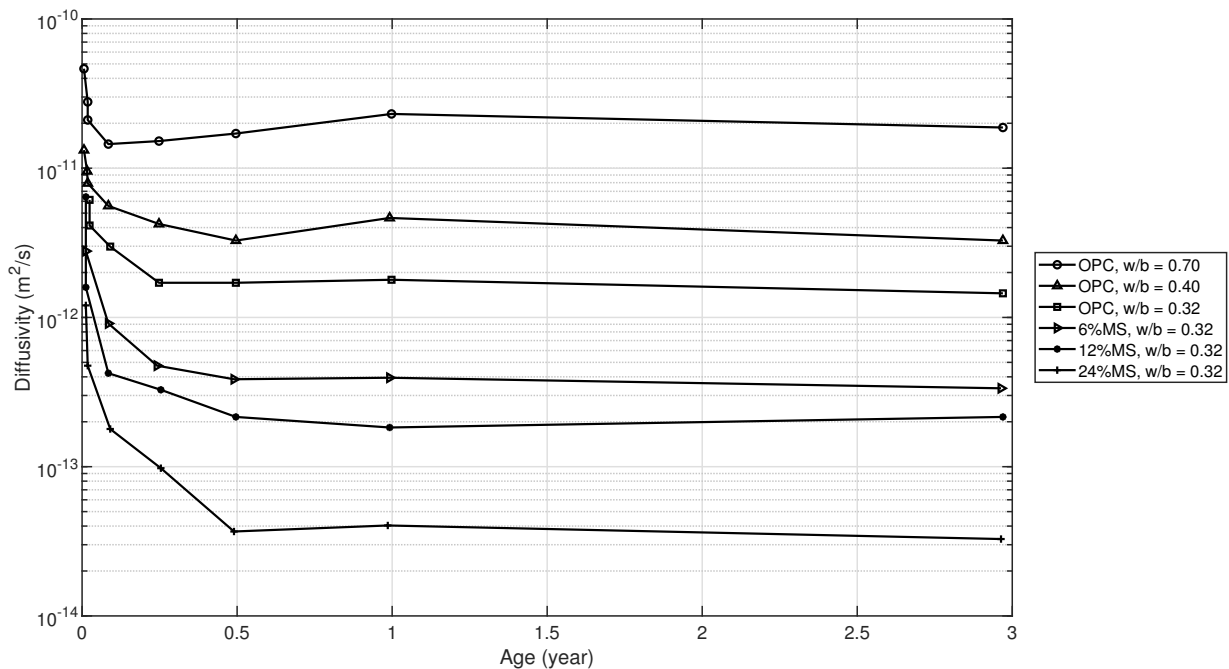
Figure 3.9: Evolution of the coefficient of diffusion with time (modified from [Tang, 1996]).

The diffusivity of a porous system is influenced by several properties, such as tortuosity and constrictivity, as well as the water-to-cement ratio and degree of hydration [Xi et al., 1994, Nilsson et al., 1996, Abyaneh et al., 2013].

The quantity and type of aggregates have a dual impact on diffusivity: the tortuosity decreases it, while the ITZ effect increases it, resulting in opposing effects. Indeed, with an increase in aggregates, the diffusivity may increase or decrease depending on the prevailing effect. However, the diffusivity largely reduces due to the change in length of the chloride ions pathway. Additionally, the aggregates are denser than the cement paste, thus making it possible to ignore the movement of ions through them [Delagrave et al., 1997, Abyaneh et al., 2013, Choi et al., 2017, Tian et al., 2019].

As the degree of hydration is dependent on time, the diffusion coefficient can be expressed as a function of time. During the reaction between cement and water through the process of hydration, the diffusion coefficient decreases, as demonstrated in Figure 3.9 [Tang, 1996, Nilsson et al., 1996]. Neglecting the effect of time on the coefficient diffusion leads to an overestimation of the chloride content [Li & Song, 2022].

The diffusion coefficient will not reflect the parameters related to the composition of the concrete and its porous system. Nevertheless, the diffusion coefficient can be directly influenced by time (α_t) and environmental conditions such as temperature (α_T) and relative humidity (α_{RH}) [Isgor, 2001, Martin-Perez et al., 2001, Guzmán et al., 2011, Wu et al., 2017, Alsheet & Razaqpur, 2018]:

$$D(t, T, RH) = D_{ref} \underbrace{\left(\frac{t_{ref}}{t}\right)^m}_{\alpha_t} \underbrace{\exp\left[\frac{U_c}{R}\left(\frac{1}{T_{ref}} - \frac{1}{T}\right)\right]}_{\alpha_T} \underbrace{\left[1 + \frac{(1-RH)^4}{(1-RH_c)^4}\right]^{-1}}_{\alpha_{RH}} \quad \forall t < t_{ref} \quad (3.17)$$

where U_c represents the activation energy needed for chloride diffusion (equal to 35 kJ/mol), R is the ideal gas constant (8.314 J/mol/K), T_{ref} denotes the reference temperature (equal to 293 K), T indicates the temperature [K], RH represents relative humidity [-] and RH_c indicates the humidity at which the diffusion coefficient is halfway between its extremum values (generally considered to be 75-80% in literature, as expressed in Figure 3.10 [Balafas & Burgoyne, 2010]).
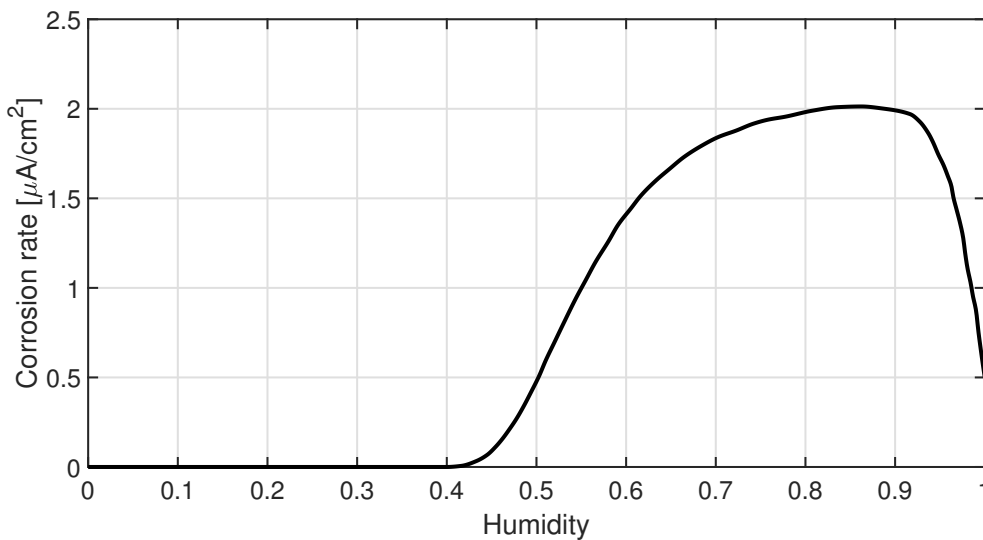
Figure 3.10: Influence of relative humidity on the corrosion rate for a 1 year old concrete element with a chloride concentration of 1.8kg/m³ under 23°C [Balafas & Burgoyne, 2010].

The coefficient m is determined by the particular concrete composition, which includes factors such as the type of cement and water-to-cement ratio. As a result, the following equation can be used to determine its value [Isgor, 2001, Angst, 2011]:

$$m = 2.5\frac{w}{c} - 0.6 \tag{3.18}$$

The time of reference t_{ref} is when there is no longer a variation in the diffusion coefficient over time, which is usually around six months (Figure 3.9). After complete hydration of the cement, the diffusion coefficient remains constant, hence $\alpha_t = 1 \; \forall t > t_{ref}$ [Mangat & Molloy, 1994, Nilsson et al., 1996, Angst et al., 2009].

In the early stages of corrosion, the diffusion coefficient varies depending on time but for distinct reasons. The corrosion rate decreases over time as rust formation closes the porosity, hence decreasing the diffusion coefficient of iron ions exiting the steel surface and chloride ions reaching it. Furthermore, as the ratio of anode area to cathode area decreases, it also slows down the corrosion rate [Liu & Weyers, 1998].

Additionally, the diffusion coefficient is influenced by the concentration of chloride ions in the pore solution and the saturation degree of the porous system. Therefore, the diffusion coefficient is reliant on the concentration of ions present in the solution. By adjusting Equation 3.17, we can determine the impact of these factors [Nilsson et al., 1996, Chatterji, 1999, Xi & Bažant, 1999]:

$$D(t, T, RH, C) = D_{ref} \left(\frac{t_{ref}}{t}\right)^m \exp\left[\frac{U_c}{R}\left(\frac{1}{T_{ref}} - \frac{1}{T}\right)\right] \left[1 + \frac{(1 - RH)^4}{(1 - RH_c)^4}\right]^{-1} (1 - k_C \, C^n) \tag{3.19}$$

where k_C represents a parameter that incorporates the matrix's pore characteristics, while n is a constant that depends on the ions and their concentration.

If we maintain a steady-state, we must integrate Equation 3.19 accross the concentration range examined. For monovalent ions, such as chloride (Cl^-), the following equation can be used [Chatterji, 1999]:

$$D_m(t, T, RH, C_f) = \frac{1}{C_f} \int_0^{C_f} D(t, T, RH, C) \, \mathrm{d}C = D(t, T, RH) \left(1 - \frac{2}{3} \, k_c \, \sqrt{C_f}\right) \tag{3.20}$$

where $D_m(t, T, RH, C_f)$ represents the measured diffusivity at concentration C_f. It should be noted that for chloride ions, the coefficient n equals 0.5 for concentrations up to 0.7 $\mathrm{mol/l}$.

3.4.3.2 Unsteady-State One Dimensional Diffusion

Stationary conditions are rarely met for the diffusion of ions in porous materials such as concrete. Thus, Fick's first law is unsuitable, and the second law is more appropriate to describe chloride flux during unsteady-state conditions. In the case of a one-dimensional problem, the equation can be written as follows [Mangat & Molloy, 1994, Nilsson et al., 1996, Bertolini et al., 2004, Angst, 2011]:

$$-\frac{\partial F}{\partial x} = \frac{\partial C_t}{\partial t} = \frac{\partial}{\partial x}\left(D \, \frac{\partial C_t}{\partial x}\right) \tag{3.21}$$

where C_t represents the concentration of the diffusing ion and D represents the diffusion coefficient that can take the form of Equation 3.19, for instance.

Literature rarely presents the diffusion coefficient in terms of depth from the concrete surface. Hence, it can be relocated outside of the derivative, transforming Fick's second law:

$$-\frac{\partial F}{\partial x} = \frac{\partial C_t}{\partial t} = D_{app}\frac{\partial^2 C_t}{\partial x^2} \tag{3.22}$$

Assuming a constant diffusion coefficient, regardless of position and often time, simplifies the equation for transport mechanisms in concrete. Though this model overlooks certain aspects of ions transport, it has demonstrated sufficient accuracy even for unsaturated scenarios [da Costa et al., 2013].

Equation 3.22 can be integrated over time under two assumptions [Nilsson et al., 1996, Bertolini et al., 2004]:

- The concentration of chloride ions diffusing at the surface of the concrete remains constant over time and equals C_s:

$$C_t = C_s \text{ for } x = 0 \; \forall t \tag{3.23}$$

  We assume that the concentration of chloride ions in the fresh concrete is zero:

$$C_t = 0 \text{ for } t = 0 \; \forall x > 0 \tag{3.24}$$

- The diffusion coefficient D_{app} remains constant over time and throughout the thickness of the concrete, indicating that the concrete is homogeneous.

Under these assumptions, a solution was derived for the unidirectional diffusion of chloride ions in a semi-infinite medium [Collepardi et al., 1972, Mangat & Molloy, 1994, Nilsson et al., 1996, Bertolini et al., 2004]:

$$C_t(x,t) = C_s\left[1 - \mathrm{erf}\left(\frac{x}{2\sqrt{D_{app}\,t}}\right)\right] \tag{3.25}$$

where erf is the error function:

$$\mathrm{erf}(z) = \frac{2}{\pi}\int_0^z e^{-t^2}\mathrm{d}t \tag{3.26}$$

An illustration of the solution of the Equation 3.25 is given in Figure 3.11. This equation uses an apparent diffusion coefficient D_{app} and remains one of the most frequently used equations for explaining and modeling the diffusion of chloride ions in concrete [Nilsson et al., 1996]. The level of surface concentration C_s is reliant on various environmental factors, as well as on the porosity at the surface of the concrete and its capacity for binding chloride [da Costa et al., 2013].

The Equation 3.25 does not consider any initial impurities present. If there is any initial chloride content in concrete, the equation needs to be modified accordingly [da Costa et al., 2013]:

$$C_t(x,t) = C_0 + (C_s - C_0)\left[1 - \mathrm{erf}\left(\frac{x}{2\sqrt{D_{app}\,t}}\right)\right] \tag{3.27}$$

where C_0 represents the initial concentration of chlorides. This value can typically be considered negligible and can be taken as either the maximum concentration of chlorides prescribed by the standards or the minimum chloride content obtained from experiments.
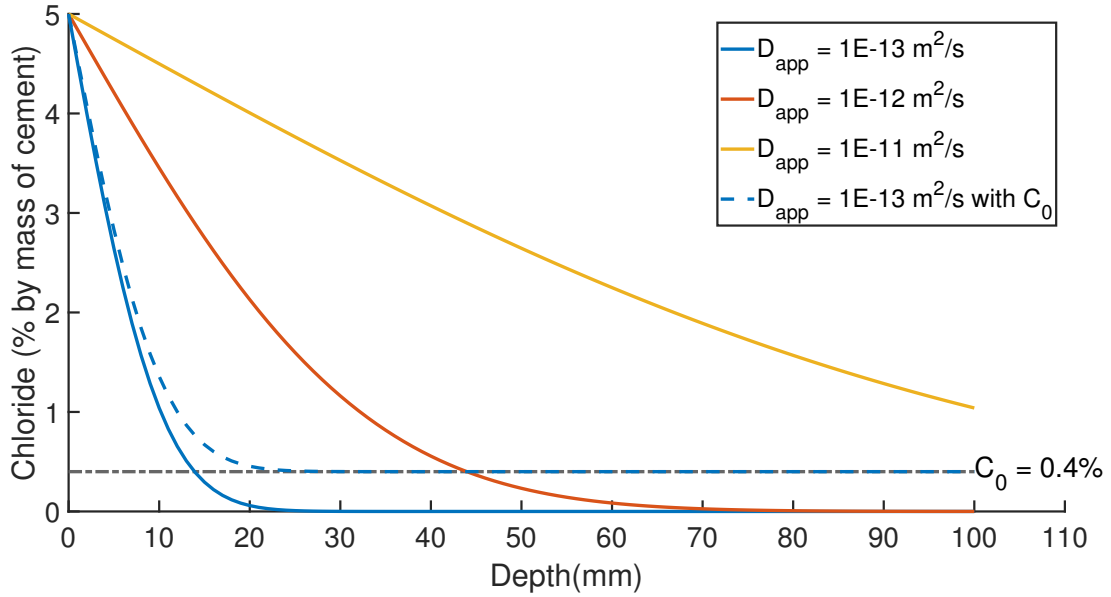
Figure 3.11: Examples of profiles of chloride ions diffusion in concrete for various apparent diffusion coefficient, with or without an initial chlorides concentration.

Equation 3.27 does not consider the ions binding to concrete's pore walls. Consequently, the mass balance equation needs to be modified to account for such binding. For an infinitesimal concrete volume, the equation is as follows [Nilsson et al., 1996]:

$$\frac{\partial C_t}{\partial t} = \frac{\partial C_f}{\partial t} + \frac{\partial C_b}{\partial t} = -\frac{\partial F}{\partial x} \rightarrow \frac{\partial C_f}{\partial t} = -\frac{\partial F}{\partial x} - \frac{\partial C_b}{\partial t} \tag{3.28}$$

where C_t represents the overall concentration of chlorides per concrete unit area, C_f and C_b denote the concentrations of free chlorides and bound chlorides, respectively.

By incorporating Fick's first law (Equation 3.15) to the mass balance equation (Equation 3.28), using a diffusion coefficient that varies accordingly to several parameters, a mass balance equation can be derived for a given volume of concrete [Nilsson et al., 1996]:

$$\frac{\partial C_f}{\partial t} = \frac{\partial}{\partial x}\left(D(t,T,RH,C_f)\frac{\partial C_f}{\partial x}\right) - \frac{\partial C_b}{\partial t} \tag{3.29}$$

with $D(t,T,RH,C_f)$ being the diffusion coefficient that relies on the concentration of free-chloride ions in the solution, the saturation degree of the porous system, the time, and the temperature, as stated in Equation 3.19.

An additional approach to consider regarding the binding of chloride ions in concrete according to Fick's second law (Equation 3.21) is by means of defining the binding capacity of concrete (Equation 3.14) [Xi & Bažant, 1999]:

$$\frac{\partial C_f}{\partial C_t}\frac{\partial C_t}{\partial t} = \frac{\partial C_f}{\partial t} = \frac{\partial C_f}{\partial C_t}\frac{\partial}{\partial x}\left(D\frac{\partial C_f}{\partial x}\right) = \frac{\partial}{\partial x}\left(\frac{D}{1+\frac{\partial C_b}{\partial C_f}}\frac{\partial C_f}{\partial x}\right) \tag{3.30}$$

where the concentrations are expressed per volume of the material. It is possible to convert them into concentration per volume of the solution by incorporating the water content of the porous system (w_e) [Isgor, 2001, Han, 2007, Chen & Mahadevan, 2008, Yuan et al., 2009, Fu et al., 2010, Guzmán et al., 2011]:

$$\frac{\partial C_f}{\partial t} = \frac{\partial}{\partial x} \left(\frac{D}{1 + \frac{1}{w_e} \frac{\partial C_b}{\partial C_f}} \frac{\partial C_f}{\partial x} \right) = D_{app} \frac{\partial^2 C_f}{\partial x^2} \tag{3.31}$$

which yields the apparent diffusion coefficient D_{app}:

$$D_{app} = \frac{D}{1 + \frac{1}{w_e} \frac{\partial C_b}{\partial C_f}} \tag{3.32}$$

In the study of chloride binding by means of binding isotherms, the use of the Freudlich isotherm changes the apparent diffusion coefficient [Chen & Mahadevan, 2008]:

$$C_b = K_b\, C_f^n \longrightarrow \frac{\partial C_b}{\partial C_f} = K_b\, n\, C_f^{n-1} \longrightarrow D_{app} = \frac{D}{1 + \frac{K_b\, n\, C_f^{n-1}}{w_e}} \tag{3.33}$$

This apparent coefficient of diffusion varies generally between 10^{-13} m^2/s and 10^{-10} m^2/s, depending on the specific properties of the concrete and its exposure conditions to chlorides. The pore structure of the concrete, which relates to the water-to-cement ratio, compaction, curing, and the existence of cracking, significantly influences this coefficient. Furthermore, the apparent diffusion coefficient is dependent on the composition of the concrete, including factors such as the type of cement used [Bertolini et al., 2004].

3.4.3.3 Two Dimensional Diffusion

Until now, it was presumed that diffusion took place only along one dimension. Fick's second law, in unsteady state and for a two-dimensional chloride diffusion, can be expressed as follows [Xiao et al., 2012, Ying et al., 2013b, Morga & Marano, 2015]:

$$\frac{\partial C_f(x,y,t)}{\partial t} = D_{app} \left(\frac{\partial^2 C_f(x,y,t)}{\partial x^2} + \frac{\partial^2 C_f(x,y,t)}{\partial y^2} \right) \tag{3.34}$$

Following the same assumptions as used in Fick's second law in one dimension (Equation 3.25), an analytical solution can be obtained in two dimensions [Ying et al., 2013b, Wu et al., 2020]:

$$C_f(x,y,t) = C_s \left[1 - \operatorname{erf}\left(\frac{x}{2\sqrt{D_{app}\, t}} \right) \operatorname{erf}\left(\frac{y}{2\sqrt{D_{app}\, t}} \right) \right] \tag{3.35}$$

Expressed in cylindrical coordinates (ρ, θ, z), Fick's second law becomes [Morga & Marano, 2015]:

$$\frac{\partial C_f}{\partial t} = D_{app} \left[\frac{1}{\rho} \frac{\partial}{\partial \rho} \left(\rho \frac{\partial C_f}{\partial \rho} \right) + \frac{1}{\rho^2} \frac{\partial^2 C_f}{\partial \theta^2} + \frac{\partial^2 C_f}{\partial z^2} \right] \tag{3.36}$$

which is applicable for axially symmetric cylindrical components, where diffusion takes place in the radial direction:

$$\frac{\partial C_f}{\partial t} = D_{app} \left(\frac{1}{\rho} \frac{\partial C_f}{\partial \rho} + \frac{\partial^2 C_f}{\partial \rho^2} \right) \tag{3.37}$$

3.4.4 Migration

In addition to diffusion, ion transport can also arise from migration caused by charge imbalances. These imbalances originate from either an external electric field or differences in the diffusion coefficient among different ionic species [Glasser et al., 2008, Liu et al., 2015]. The movement of cations and anions within the pore solution generates an internal electric field that enhances the velocity of ions with low diffusion coefficients, while decelerating those with higher diffusion coefficients, and simultaneously ensures electro-neutrality [Samson et al., 2000, Samson & Marchand, 2007, Glasser et al., 2008, Shi et al., 2012]. The flux of ionic species within the multi-phase pore solution can be determined using the Nernst-Planck equation [Tang, 1996, Samson & Marchand, 1999, Glasser et al., 2008, Spiesz et al., 2012, Liu et al., 2015, Ukrainczyk & Koenders, 2016]:

$$\frac{\partial C}{\partial t} = \frac{\partial}{\partial x}\left(D\ \frac{\partial C}{\partial x}\right) + \frac{\partial}{\partial x}\left(D\ C\ \frac{z\ F}{R\ T}\frac{\partial \Phi}{\partial x}\right) \tag{3.38}$$

where z represents the charge number of the ionic species under consideration, F is Faraday's constant (equal to $9.64846\ 10^{-4}\ \mathrm{C/mol}$), R is the ideal gas constant (equal to $8.3143\ \mathrm{J.mol/K}$) and T [K] is the absolute temperature. Lastly, Φ denotes the electrochemical potential [V].

The electrochemical potential is responsible for maintaining the electroneutrality in the pore solution [Glasser et al., 2008, Ukrainczyk & Koenders, 2016]. If the electochemical potential is determined by internal charge imbalances, the nonlinear Poisson equation can be utilised [Samson & Marchand, 1999, Samson & Marchand, 2007, Glasser et al., 2008, Liu et al., 2015]:

$$\frac{\partial^2 \Phi}{\partial x^2} = -\frac{F}{\varepsilon_0\ \varepsilon_r}\ \sum_{k=1}^{N} z_k\ C_k \tag{3.39}$$

where k represents the kth ionic species and N represents the total number of ionic species present in the pore solution. ε_0 denotes the permittivity of a vacuum, which is equal to $8.854\ 10^{-12}\ \mathrm{C/(Vm)}$, and ε_r denotes the relative permittivity of water at temperature T. For example, at 298K, the relative permittivity of water is 78.3 $\mathrm{C/(Vm)}$. This equation is valid under the assumption that ions in the pore solution travels much more slowly than the electromagnetic signal [Samson & Marchand, 1999].

Complexation reactions occur within the aqueous phase to ensure electroneutrality [Samson et al., 2000, Glasser et al., 2008]. An example of this is the formation of $\mathrm{Ca(OH)^+}$ from $\mathrm{Ca^{2+}}$ and $\mathrm{OH^-}$. The migration of ions in the pore solution may be slowed down by accounting for these reactions through a reaction term.

Currently, many models overlook the migration caused by electrochemical potentials and electrical coupling between multiple ions. This may be accurate when studying a solution that is not highly charged. However, in concrete, the pore solution is highly concentrated in ions, the electrochemical potential term may thus not be negligible compared to diffusion [Glasser et al., 2008].

3.4.5 Convection-Diffusion of Chlorides Ions

The transportation of chloride ions was initially thought to be solely conducted by means of diffusion. However, later on, migration was also taken into account. Both of these transport

mechanisms are the only ones relevant for saturated concrete, where diffusion is the prevailing process. However, when examining wetting and drying cycles, diffusion and migration are no longer the sole mechanisms involved. Capillary suction plays a significant role in transporting chloride ions when concrete is not fully saturated, as documented in several studies [Ye et al., 2012, da Costa et al., 2013, Wu et al., 2017].

During the wetting stage, chloride ions enter the concrete's pore network through the combined effects of diffusion and capillary suction. As the concrete dries, the water at the surface evaporates, resulting in the formation of a chloride salt and chloride flows exiting the pore system. The dissolution of the salt during the subsequent wetting stage leads to a high chloride concentration gradient that accelerates the ingress of chloride. It has been demonstrated that the chloride concentration rises with increasing duration of the drying-wetting cycles [Wu et al., 2017].

To accurately illustrate the transportation of chloride ions in the porous structure of concrete, a convection-diffusion model is essential (without migration being taken into account at this phase). The convection term can be expressed using the flux rate [Guzmán et al., 2011, da Costa et al., 2013]:

$$q = \frac{\partial}{\partial x} \left(C_f \ D_{RH} \ \frac{\partial RH}{\partial x} \right) \tag{3.40}$$

where RH represents the relative humidity, D_{RH} denotes the apparent diffusion coefficient that potentially accounts for the relative humidity, temperature and hydration time, C_f signifies the free-chloride concentration, and q refers to the flux rate.

The overall free-chloride flow can be determined by merging the diffusion and convection equations [Guzmán et al., 2011]:

$$\frac{\partial C_f}{\partial t} = D \ \frac{\partial^2 C_f}{\partial x^2} + D_{RH} \ \frac{\partial^2 RH}{\partial x^2} \ \frac{\partial C_f}{\partial x} \tag{3.41}$$

where D_{RH} is dependent on the relative humidity through the Van Genuchten's relationship [Ye et al., 2012]:

$$D_{RH} = D_{RH,ref} \ \sqrt{S_w} \ \left(1 - \sqrt[m]{S_w} \right)^m \quad \text{with} \quad 0 < m < 1 \tag{3.42}$$

where S_w denotes the saturation degree of the porous system.

As discussed in Section 3.3.5, this convection-diffusion model exhibits a maximum phenomenon. To address this, it is possible to utilise Fick's second law by scaling the "zero" of the x-axis at the location of the maximum and setting the new external surface concentration value to match the maximum chloride concentration [Andrade et al., 2015].

3.5   Impact of the Recycled Concrete Aggregates

This study examines the impact of replacing natural aggregates with recycled concrete aggregates. Previous research has investigated this substitution, and the literature provides a general summary.

It is widely acknowledged that recycled concrete aggregates (RCA) are composed of natural aggregates and mortar paste that adheres to them. This paste has higher porosity and water absorption than the natural aggregates, which enhances the transport properties of the recycled concrete. It is evident in this context that the higher the volume fraction of RCA in the concrete, the higher the effective diffusion coefficient, because of the higher ratio of adherent old mortar [Xiao et al., 2012, Ying et al., 2013a, Hu et al., 2018, Qi et al., 2018]. In fact, Qi et al. (2018) found a 31.9% increase in the diffusion coefficient at a replacement level of 100% [Qi et al., 2018].

The composite behaviour of concrete is a crucial aspect to consider. Concrete composed of natural aggregates can be seen as a three-phased material, including aggregates, mortar paste and the interfacial transition zone (ITZ) between them. However, the introduction of recycled concrete aggregates expands this to a five-phased material, consisting of aggregates and old adherent mortar, the ITZ between them, and new mortar with the ITZ between it and the RCA. In concrete composed of natural aggregates, these aggregates exhibit greater resistance to ion transport compared to the other two phases. Consequently, natural aggregates are commonly considered impermeable [Liu et al., 2015]. This is not the case when using recycled concrete aggregates, as the adhered old mortar from the RCA and the interfacial transition zone cannot be regarded as impermeable.
Additionally, incorporating a new ITZ significantly impacts the diffusion coefficient. It has been found that the diffusion coefficient of the interfacial transition zone is 4 to 15 times higher than that of bulk cement paste. This finding is dependent on the concrete's water-to-cement ratio and porosity [Ollivier et al., 1995, Liu et al., 2015], as other authors have found the opposite when the new mortar paste is rather compact [Thomas et al., 2013].

Furthermore, the recycled concrete aggregates could be a source of chloride ions, if contaminated [Debieb et al., 2010, Diotti et al., 2020]. The initial concentration would then not be null and the time to initiate the corrosion would be reduced.

Finally, the replacement of natural aggregates with recycled concrete aggregates was found to enhance the concrete's binding capacity, specifically the physical adsorption binding [Ying et al., 2013a, Qi et al., 2018].

3.6 Conclusion

This chapter concludes the literature review of this thesis. Over this chapter, the reader has learned about the degradation process that is chloride-induced corrosion of the reinforcement. Several theoretical aspects of this phenomenon have been detailed, including the binding of chloride ions, the concept of a threshold value, and the maximum phenomenon observed during drying and wetting cycles.

Once the theoretical knowledge was acquired, the modelling aspect was presented. Firstly, the state of the art introduced the advancements in complexity of the models developed to account for chloride ingress in concrete. Several models were presented for steady and unsteady state diffusions, migration and convection of chloride ions, as well as for the binding of said ions.

Finally, a brief literature review on the impact of substituting natural aggregates with recycled concrete aggregates on chloride ingress was presented.

65

2

EXPERIMENTAL PROGRAMME

4

EXPERIMENTAL ANALYSIS

Contents

4.1   Introduction

The primary objective of this research is to characterise the influence of substituting natural aggregates with recycled concrete aggregates in concrete, with a focus on durability. To achieve this objective, an experimental programme is employed. First, the concrete compositions developed are introduced. Subsequently, a focus is placed on the origin and properties of the recycled concrete aggregates, as they represent the key elements of this work. The complete experimental plan is then presented. This encompasses the evaluation of water and chloride transfer properties, which are assessed in terms of porosity, intrinsic water permeability and water retention curves, as well as chloride diffusion coefficients.

4.2   Experimental Concrete Compositions

Several concrete mixtures have been produced and examined in this study with the aim of characterising the microstructure of concrete. It is well-established that chloride ingress is heavily influenced by the porous structure of concrete, which is affected by numerous factors including the composition and mixing process. Each composition is identical to the others except for one component. In total, four mixes are created:

1. NAC: A micro-concrete comprising natural 2/7 aggregates of limestone origin;

2. RAC: The same micro-concrete created with recycled concrete aggregates. The particle size distribution has been reconstructed to resemble that of the natural aggregates. The volume fraction of the recycled concrete aggregates is the same as that of the natural aggregates;

3. E-M: A mortar composed of natural 0/2 Rhine sand;

4. E-CP: A plain cement paste that does not include any additional aggregates.

More information on each composition can be found in the Appendix A for reproducibility purposes, and the underlying thread for each composition is thoroughly explained and supported.

4.3   Origin and Properties of the RCA

The Recycled Concrete Aggregates used in this study were procured from the University of Liège's Construction Materials Laboratory. These RCA were supplied through the research project Interreg North-West Europe SeRaMCo (Secondary Raw Materials for Concrete Precast Products), and a paper is available on the matter [Hubert et al., 2023]. Several concrete compositions were formulated and blended in the laboratory for this investigation. The specimens were subsequently crushed at the research centre "Centre Terre et Pierre" (CTP) in Tournai, prior to being returned to the university for further analysis.
This section outlines the decision-making process behind the selection of these particular RCAs, in addition to providing a summary of their characteristics.

4.3.1 Origin of the Recycled Concrete Aggregates

In the SeRaMCo project, five concrete compositions were created in the laboratory and subsequently crushed using two different techniques: an impact crusher and a jaw crusher. This thesis focuses on the analysis of three compositions, each differing in their constituents:

- OC1.0: "Reference" concrete, which served as the primary composition and reference for the others;

- OC1.2: "Sandstone" concrete, which is made from sandstone aggregates;

- OC2: "Low Cement" concrete, which has a lower quantity of cement but same water-to-cement ratio.

The Table 4.1 shows their compositions and the properties of the concrete specimens obtained before crushing.
The sole distinguishable factor that could impact our decision-making is that OC1.2 displays a lower density compared to the other two compositions. This discrepancy may be attributed to greater porosity, the quantities of materials remaining equal between all compositions. This can be verified by the lower compressive strength offered by the sample.

4.3.2 Properties of the Recycled Concrete Aggregates

The RCA properties are presented in Table 4.2, while their granulometric curves are illustrated in Figure 4.1.

The properties of the RCA produced vary depending on the type of crusher used. It is evident that the jaw crusher produces particles with a higher global flakiness index, resulting in particles that are flatter than those produced by the impact crusher. This difference is also evident in their mean shape ratio. For concrete production, it is important to restrict such particles. Therefore, aggregates from the impact crusher are preferable.

There is little variance in water absorption among the different types of crusher. Typically, the impact crusher exhibits a lesser water absorption compared to the jaw crusher, yet the disparity is insignificant. However, there lies a distinction amongst the compositions, with OC1.2 showing the highest WA amongst the three, followed by OC1.0 and OC2, respectively. Furthermore, the water absorption of the aggregates is directly correlated to the particle size of the aggregates, the smaller particles displaying a higher water absorption.

Finally, there are no significant variations in Particle Size Distribution between the compositions. Nevertheless, the jaw crusher generates smaller particles compared to the impact crusher, which leads to the leftward shift of the curve.

Based on the parameters outlined, the selected composition for our Recycled Concrete Aggregates is the OC1.2 produced by the impact crusher.

Name	Reference OC1.0	Sandstone OC1.2	Low Cement OC2
Aggregate's Nature	Limestone	Sandstone	Limestone
Cement Type	CEM I 52.5	CEM I 52.5	CEM I 52.5
Cement Quantity $[\mathrm{kg/m^3}]$	400	400	320
Sand 0/4 $[\mathrm{kg/m^3}]$	604.9	604.9	664.4
Aggregates 2/7 $[\mathrm{kg/m^3}]$	368.8	368.8	405.1
Aggregates 7/14 $[\mathrm{kg/m^3}]$	345	345	379
Aggregates 14/20 $[\mathrm{kg/m^3}]$	433.5	433.5	476.2
Efficient Water $[\mathrm{kg/m^3}]$	224.2	224.2	180.6
W/C Ratio	0.56	0.56	0.56
Volume of Cement Paste $[\mathrm{dm^3/m^3}]$	351.2	351.2	282.2
Density $[\mathrm{g/cm^3}]$	2.35	2.31	2.36
Compressive Strength [MPa]	56.0±2.4	52.7±2.5	56±6.4

Table 4.1: Original concrete compositions manufactured in the laboratory and their properties.

Name	OC1.0		OC1.2		OC2	
Crusher Type	Jaw	Impact	Jaw	Impact	Jaw	Impact
Global Flakiness Index [%]	14	8	13	6	11	7
Shape Ratio (L/E) 4/8	3.62	2.77	3.62	3.01	3.44	3.04
Water Absorption 0/4 [% mass]	11.75	10.96	12.47	11.58	8.9	7.92
Water Absorption 4/6.3 [% mass]	8.18	-	7.14	-	-	-
Water Absorption 6.3/8 [% mass]	7.72	7.15	8.58	8.12	7.02	6.27
Water Absorption 8/12.5 [% mass]	6.9	-	8.14	-	-	-
Water Absorption 12.5/20 [% mass]	7.09	6.92	7.95	6.7	6.39	6.03
Water Absorption 20/25 [% mass]	6.9	7.65	6.53	6.83	6.96	6.11

Table 4.2: Properties of the RCA obtained from the compositions OC1.0, OC1.2 and OC2.
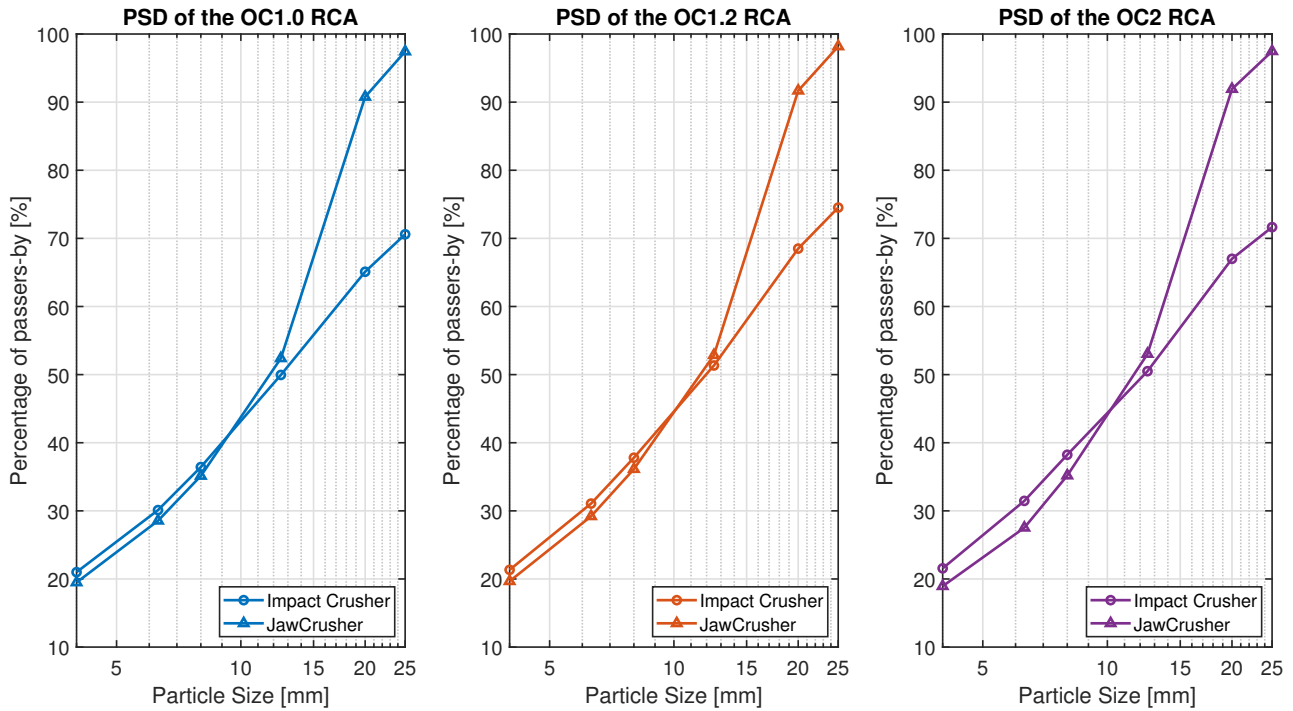
Figure 4.1: Particle Size Distribution (PSD) of the RCA produced from the three compositions OC1.0, OC1.2 and OC2.

4.3.3 Further Investigations

4.3.3.1 Water Absorption, Porosity and Densities of the RCA

The experiments conducted in this thesis necessitated a significant quantity of RCA. Regrettably, the amount of exploitable OC1.2 aggregates was insufficient. It should be reiterated that only minor fractions were utilised as the resulting concretes are categorised as "microconcretes". To increase the availability of aggregates, larger sizes were returned to the crushing centre where they underwent further grinding in the same impact crusher and using the same methods as in the initial process. After three rounds of crushing, the resulting size fractions (<2mm, 2-8mm, and above 8mm) were sent back to the university, usable for this research.
The RAC mixture will consist of 50% "old" aggregates (crushed only twice) and 50% "new" aggregates (crushed thrice). The water absorption, initial water content, and density of these aggregates must therefore be re-evaluated to adjust the initial composition and compare the characteristics of different crushing levels.

In accordance with EN 1097-5 and EN 1097-6 standards, measurements were obtained for the initial water content, oven-dried, apparent and saturated densities, as well as water content at 24 hours. These results are presented in Table 4.3 for both the "old" and "new" aggregates. It should be noted that the initial water content is not presented as it is not an intrinsic parameter and is dependent on storage conditions. In addition to these parameters, porosity is calculated using the equation below, which employs ρ_{rd} as the oven-dried particle density (ratio of the oven-dried mass and the volume it occupies in water, including water accessible voids) and ρ_a as the apparent particle density (ratio of the oven-dried mass and

the volume it occupies in water, excluding water accessible voids):

$$n = 1 - \frac{\rho_{rd}}{\rho_a} \qquad (4.1)$$

Size	WA24 [% mass]		Apparent Density [kg/m³]		Oven-dried Density [kg/m³]		Saturated Density [kg/m³]		Porosity [% volume]	
	Old	New	Old	New	Old	New	Old	New	Old	New
2/4	11.4	7.9	2676.1	2683.8	2052.3	2215.5	2285.4	2389.9	23.3	17.4
4/5	9.5	5.4	2653.3	2647.2	2117.4	2313.5	2319.3	2439.5	20.2	12.6
5/6.3	8.2	4.3	2661.0	2719.3	2182.7	2435.1	2362.4	2539.6	18.0	10.4
6.3/8	7.5	3.4	2624.5	2681.2	2192.1	2460.0	2356.9	2542.5	16.5	8.3

Table 4.3: Properties of the "old" and "new" aggregates obtained following the standard EN 1097-6.

It can be observed that the RCA subjected to a third crushing stage exhibit lower water absorption, reduced porosity and increased density as compared to the other samples, with values similar to the ones of Katz (2003) [Katz, 2003]. In fact, these RCA possess a comparable oven-dried particle density to that of the natural aggregates used in their parent concrete mix. This observation supports the notion that the more an aggregate undergoes crushing stages, the more liberated it becomes. It may be argued that an increased number of grinding steps leads to an increase in micro-cracks within the adherent mortar paste, which in turn raises water absorption rates. However, this finding was not observed in our research.

4.3.3.2 Cement Content of the Recycled Concrete Aggregates

The cement content of recycled concrete aggregates needs to be determined to ascertain the quantity of adherent mortar attached to the natural aggregates: the higher the cement content, the lower the properties of the concrete. The method developed by Zhao et al. (2022) involved dissolving the aggregates for one hour in a solution of salicylic acid (14 grams of salicylic powder dissolved in 80mL of methanol) after crushing them into a fine powder using a ring crusher [Zhao et al., 2022]. As our aggregates consist of sandstone, there is no possibility of dissolution of the natural aggregates.
After the complete dissolution process, the sample undergoes filtration with a glass filter. Subsequently, the weight of the remaining powder of natural aggregates is measured to determine the mass of dissolved cement.

The cement content is shown in Figure 4.2. As previously noted, the recycled concrete aggregates that underwent a third crushing stage contained significantly less cement than the initial recycled aggregates. In addition, existing literature highlights that cement content tends to be greater in finer recycled aggregates compared to coarser ones [Limbachiya et al., 2000, Katz, 2003, de Juan & Gutiérrez, 2009]. This observation was also confirmed in our study.
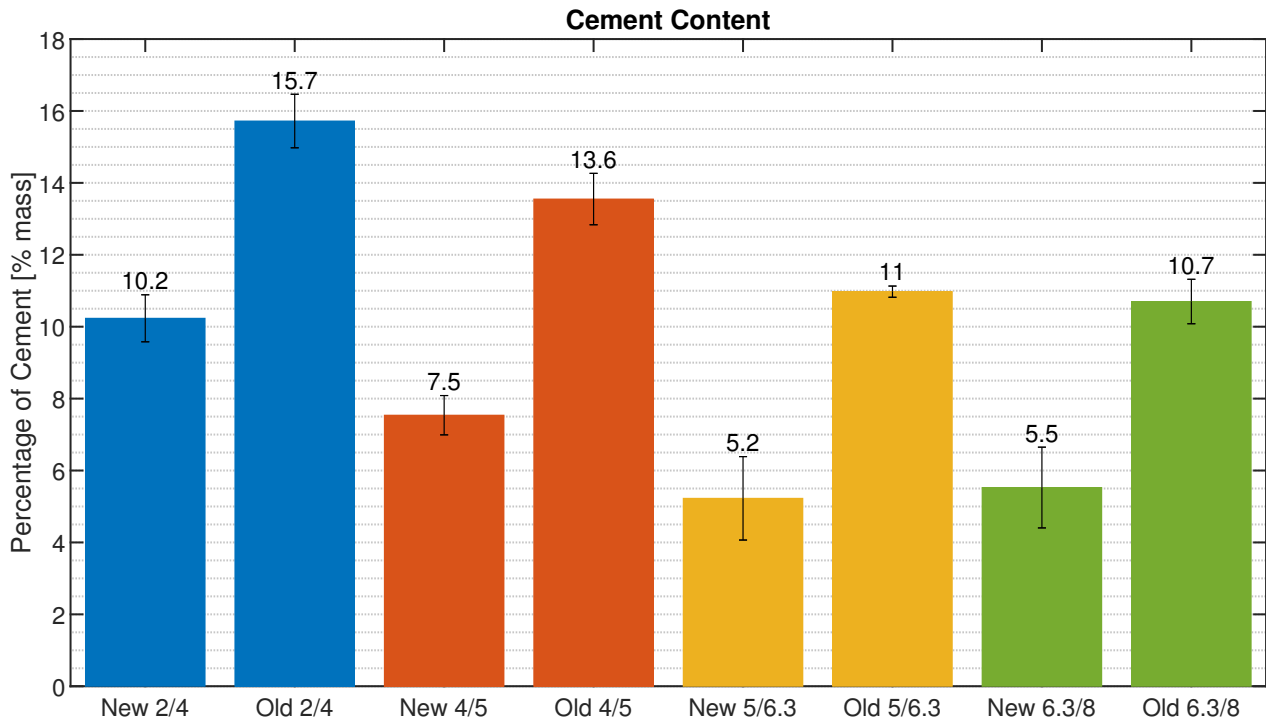
Figure 4.2: Cement content of the recycled concrete aggregates OC1.2.

4.4 Experimental Plan

The proposed experimental design facilitates a comprehensive understanding of concrete and results in macroscopic properties for all four compositions. However, in the comparison of these compositions, it is important to take into account only those differences which are caused by microscopical changes in the addition or substitution of a constituent.

Initially, a Water Absorption by Immersion (WAI) (NBN B 15-215:2018) test has been performed to analyse the dry and humid densities of our compositions and gain insight into their water absorption and porosity. However, it is essential to note that these values only indicate the porosity accessible to water.

Additionally, the ease of fluid percolation within the porous structure of the materials was investigated. The intrinsic permeability of porous media is determined through a water permeability experiment (NBN EN ISO 17892-11:2019). The media's interaction with its environment, through static sorption and desorption experiments, is also important to be determined. The results of these experiments can be interpreted as Water Retention Curves (WRCs), which establish the relationship between the saturation level of the porous system and external environmental factors, including relative humidity and temperature, via the suction term.

Moreover, experiments focused solely on the chloride transfer properties of the concrete's microstructure are conducted, alongside the moisture-related experiments. Experiments to determine chloride diffusion under steady-state and transient conditions are performed to characterise the ingress of chloride into the porous structure of concrete. The results of these tests provide diffusion coefficients that will be applied in the modelling section of this research.

Finally, a conduction experiment is conducted to gauge the electrical resistance of our concrete, which can be transformed to a resistance to penetration of chloride ions inside the porous structure.

4.4.1 Water Absorption by Immersion

The Water Absorption by Immersion (WAI) experiment provides information about the water absorption, porosity, and humid and dry densities of the tested compositions. The Belgian standards NBN B 15-215:2008 (which deals with water absorption in concrete) and NBN EN 772-4 (which concerns densities and porosity in masonry) dictate the procedure, which are equivalent to the ASTM C 642-97 "Standard Test Method for Density, Absorption, and Voids in Hardened Concrete".

The samples used are square plates with sides measuring 100×100mm and a thickness of approximately 10mm, sawed from a larger concrete specimen. Each composition should contain a minimum of five pieces.
The samples must be weighed twice: firstly when they are saturated and secondly after drying. Saturation is achieved through immersion in a water container. All faces of the sample must be surrounded by at least 5mm of water, and the sample must remain immersed for at least 48 hours. The sample is considered saturated when its mass does not vary by more than 0.1% over a 24-hour period. Under saturated conditions, the sample is weighed twice: firstly, submerged in water to obtain the saturated mass (m_{sat}), and secondly, in air to obtain the humid mass (m_{humid}). The sample is then dried in an oven at a temperature of 105°C until a constant mass is achieved, which may take at least 72 hours. The mass obtained after drying is the dry mass (m_{dry}).

The water absorption (abbreviated as WA [% mass]) and the water-accessible porosity (marked as n_w [% volume]) can be calculated using the following equations:

$$\text{WA} = \frac{m_{humid} - m_{dry}}{m_{dry}} \times 100 \tag{4.2}$$

$$n_w = \frac{m_{humid} - m_{dry}}{m_{humid} - m_{sat}} \times 100 \tag{4.3}$$

The final two pieces of information are the dry and humid bulk densities, denoted as ρ_d and ρ_h respectively. These values are obtained through adaptation of the NBN EN 12390-7:2019 and NBN EN 772-4 standards:

$$\rho_d = \frac{m_{dry}}{V_{sample}} = m_{dry} \quad \times \frac{\rho_w}{m_{humid} - m_{sat}} \tag{4.4}$$

$$\rho_h = \frac{m_{humid}}{V_{sample}} = m_{humid} \times \frac{\rho_w}{m_{humid} - m_{sat}} \tag{4.5}$$

4.4.2 Water Permeability

Water permeability is a critical characteristic of concrete, which is defined as the fluid's ability to enter and move through the porous medium.

To measure the water permeability, a triaxial cell is used as per the standard NBN EN ISO 17892-11:2019. The samples utilised are cylindrical in shape, measuring approximately

100mm in diameter and 100mm in height. Initially, they are saturated as they are stored in a damp chamber during curing and then in a bucket filled with water before the testing. The sample is wrapped in a waterproof membrane along its height, facilitating unidirectional flow. Porous discs are positioned on both the upper and lower sides of the sample, enabling water movements. Following this, the sample is placed into the triaxial cell, and water is discharged from the top to the bottom of the sample. The discharge rate is controlled to maintain a constant pressure difference of 2 kPa. This technique is identified as the constant-head method. As concrete is not very malleable, the larger pores on the sample's side are filled with plaster to decrease the possibility of micro-perforation of the waterproof membrane.

Once the inflow discharge is equal to the outflow discharge, the saturated conductivity can be determined based on Darcy's law under the assumption of a permanent flow in saturated porous media [Dassargues, 2017]. The equation for calculating the saturated hydraulic conductivity is as follows:

$$K_{sat} = \frac{Q_w}{i \times A} = \frac{Q_w}{A} \times \frac{H}{\Delta h} \tag{4.6}$$

The water-saturated conductivity (K_{sat}) is measured in meters per second, the discharge (Q_w) is measured in cubic meters per second, the hydraulic gradient (i) is dimensionless, and the cross-sectional area of the member (A) is measured in square meters. The hydraulic gradient is calculated by dividing the hydraulic head (Δh, in meters) by the height of the sample (H, in meters).

The discharge is not measured directly. Instead, the volume of water passing through the sample is recorded at regular intervals and the discharge is calculated by dividing the volume by the time elapsed.

This water-saturated conductivity value is temperature-dependent and will be converted to a standard value at 10°C:

$$K(10°\text{C}) = \frac{Q \times H}{(P_{int} \times 10.19) \times A} \frac{1}{0.7 + 0.03 \times T} \tag{4.7}$$

where H [m] is the height of the sample, P_{int} [bar] is the internal pressure and is converted to pressure head [m] through the coefficient 10.19, and T [°C] is the temperature of the environment, i.e. water. Once the conductivity has been calculated, it is possible to obtain the intrinsic permeability [m²]:

$$k_{int} = K(10°\text{C}) \times \frac{\mu_w}{\rho_w \, g} \tag{4.8}$$

with μ_w [Pa.s] the dynamic viscosity of water, ρ_w [kg/m³] the density of water and g the gravitational acceleration [m/s²].

4.4.3 Static Sorption and Desorption

Sorption and desorption isotherms and water retention curves can be obtained through static experiments using a technique called the vapour control method. This method is based on the premise that a hygroscopic material in contact with humid air absorbs or releases vapour depending on its water content until it reaches a state of equilibrium. This state of equilibrium is attained when the partial vapour pressure and temperature of both the ambient medium and the pore space are equivalent [Kowalski, 2003].

The vapour control technique relies on the imposition of a constant relative humidity on a sample, which is done through the use of saline solutions in this work: the type and concentration of the saline solution determines the relative humidity, in combination with the temperature which also influences the RH. The saline solution is placed in the same hermetically sealed chamber as the studied sample (Figure 4.3) [Pap et al., 2018b, Hubert, 2018].

Water exchange between the sample and saline solution happens through vapour transfer. The sample is subjected to a specific suction when equilibrium is reached [Delage et al., 1998]. Thus, this method is known as a suction control method. To achieve different relative humidity levels, we can use various saturated saline solutions, as done in this study, or different concentrations of the same product [Delage et al., 1998].

Four square plates measuring 100×100mm, with a thickness of approximately 10mm, are inserted into each chamber for each composition. Prior to the experiment, the samples used for static sorption are dried until a constant mass is achieved. Conversely, saturated samples are required for static desorption and are therefore taken directly from the humid chamber where they were curing. Each plate is weighed carefully before insertion into the chamber.

Figure 4.3: Left: Chambers used for the static sorption and desorption experiment, with the RH and temperature probe and the samples inside. Right: sensor housing displaying the measures for the four probes used.

Approximately once a week, the samples undergo weighing and the relative humidity and temperature of their chambers are recorded using hygrometric sensors. These chambers are situated in a controlled environment room (with 60% RH and temperature of 21°C) to maintain consistency. The weighing process is terminated when the sample's mass is deemed constant.

Five chambers, each filled with a different saline solution, are used for sorption and desorption to ensure better control and interpretation of results. The saline solutions selected,

along with their intended relative humidity targets, are detailed in Table 4.4. The selection criteria was to cover the entire possible relative humidity range.

The Kelvin law embodies the relationship between suction, relative humidity, and temperature, as depicted in the following equation [Hubert, 2018]:

$$p_c = p_a - p_w = -\frac{\rho_w\, R\, T}{M}\, \ln(RH) \tag{4.9}$$

The constant of ideal gases, R, is equal to $8.3143\ \mathrm{J.mol/K}$ and M refers to the molar mass of water, which is $18.016\ \mathrm{g/mol}$, while ρ_w indicates the density of water. In addition, the temperature T [K] and relative humidity RH [-] are also utilised.

Based on the assumed temperature of $21^\circ\mathrm{C}$ and intended relative humidity, it is feasible to calculate a target suction. If the target RH is 0%, which is unattainable, the desired suction is infinite. However, for a realistic value of 6%, the corresponding water vapour pressure is -381MPa.

Chamber id.	Saline solution	Target RH [%]	Target suction [MPa]
1 and 1'	KCl	90	-14.3
2 and 2'	NaCl	75	-39.1
3 and 3'	$Ca(NO_3)_2$	56	-78.7
4 and 4'	$MgCl_2$	35	-142.5
5 and 5'	Silica salt	0	∞

Table 4.4: Saline solutions used for the static sorption and desorption experiments.

Once the relative humidity of each chamber has stabilised and the mass of each plate is constant, the experiment will conclude. The mean water content will then be calculated for each composition and RH, to obtain the water retention curves of each composition. The water content requires the dry mass of each plate, which will need to be dried in a heat chamber at $105^\circ\mathrm{C}$ after the experiment (except for the one used in static sorption, of course).

The water retention curve, discussed in Section 2.3.2, shows how the saturation degree changes in response to suction. This curve is then used to calibrate the Van Genuchten model for modelling in this thesis.

4.4.4 Chloride Diffusion

The final three experiments diverge from the preceding ones by concentrating on chloride ion ingress. Steady-state and unsteady-state chloride diffusion will be analysed for all compositions. Furthermore, a conduction experiment will yield the electrical resistance of our concrete, which can subsequently be correlated to the resistance to the penetration of chloride ions inside the porous structure of the concrete.

4.4.4.1 Diffusion under Steady-State

The steady-state experiment investigates the effective diffusion coefficient of chloride ions in concrete, denoted as D_{eff}.

The samples comprise cylinders measuring 80mm in diameter and 20mm in height. To ensure that diffusion alone is responsible for chloride ingress, the samples will be fully saturated in a lime solution, with no contribution from capillary suction. In order to prevent the pH of the pore solution from becoming excessively acidic, a lime solution is employed in lieu of water.

The samples are used in the assembly of diffusion cells (Figure 4.4), which are sealed between two compartments containing two diverse solutions, similar to those of Page et al. (1981) [Page et al., 1981]. The first compartment comprises a saturated lime ($Ca(OH)_2$) solution with a concentration of 3g/L, whilst the other contains an aqueous solution of sodium chloride ($NaCl$) with a concentration of 3M, additionally to the previous lime solution.
Both chambers are constructed using cylindrical Plexiglas tubes with a 6.2cm inner diameter. The tubes are sealed at both ends that are not in contact with the sample using a Plexiglas plate. A hole is present at the surface of both chambers for removing part of the solution during measurements.
The sample chambers have been attached to the specimen securely and with waterproofing using Araldite glue. The area of the sample not contained within the chambers has been coated with an epoxy resin to ensure complete sealing.
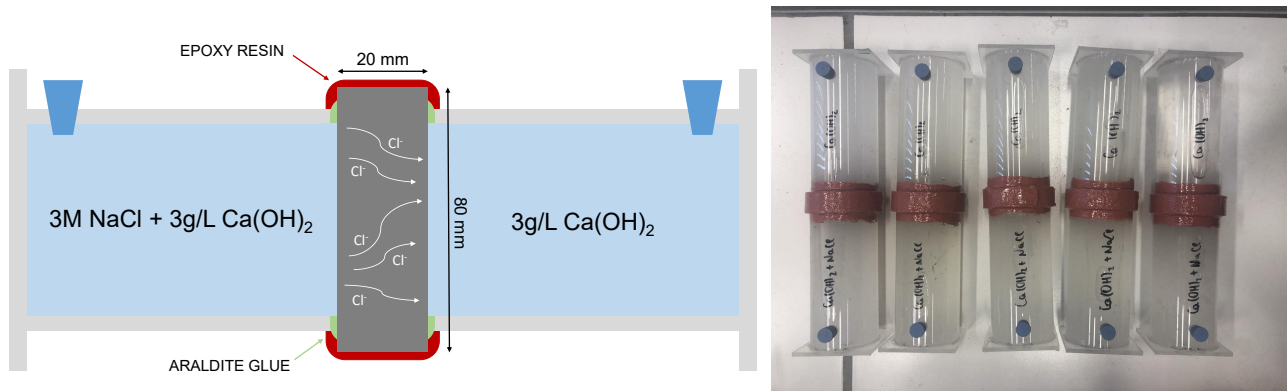
Figure 4.4: Experimental devices for the diffusion under steady-state.

Once a week, 10mL of solution is sampled in the first chamber, that only contains the lime solution initially. Potentiometric titration is used to determine the chloride concentration and the amount of chloride ions that have passed through the sample after a specific time period. After each sampling, 10 mL of solution must be added back to the cell to maintain equal volume between both compartments, thus ensuring a relatively constant concentration gradient. Of course, the added solution must contain the same chloride concentration as that taken for the potentiometric titration.

The amount of chloride ions present in the sampled solution at a specific time t_i is equal to the product of the chloride concentration $C_{2,i}$ and the sampling volume $V_{s,i}$. Similarly, the amount of chloride ions that remains in the sampling compartment at that same time is equal to the product of the same concentration $C_{2,i}$ and the remaining volume of the solution, that is, $(V_i - V_{s,i})$. Thus, the total amount of chlorides that has permeated through the sample by the time t_i is equivalent to:

$$Q_i = C_{2,i} \times V_{s,i} + C_{2,i} \times (V_i - V_{s,i}) = C_{2,i} \times V_i \tag{4.10}$$

The effective diffusion coefficient is calculated from the ion flow that reaches a steady-state. The constant flow parallel to the direction of ion diffusion is derived from the first law of Fick:

$$J = \frac{D_{eff}}{e}(C_1 - C_2) \tag{4.11}$$

where D_{eff} represents the effective diffusion coefficient ($[\mathrm{m^2/s}]$), e denotes the sample width ($[\mathrm{m}]$), C_1 refers to the chloride concentration in the saturated compartment initially ($[\mathrm{kg/m^3}]$) whilst C_2 corresponds to the chloride concentration in the compartment where sampling occurred.

An alternative method of expressing the ionic flow is through this equation [Page et al., 1981]:

$$J = \frac{V_2}{A_2}\frac{dC_2}{dt} \tag{4.12}$$

in which V_2 represents the volume of the solution in the second chamber and A_2 represents the area of that chamber.

By integrating the two aforementioned equations over time, starting from the initial ingress of chlorides into the second chamber (t_0) and ending at the conclusion of the experiment (t), the subsequent equation can be derived:

$$\int_{t_0}^{t}\left(\frac{D_{eff}}{e}(C_1 - C_2)\right)dt = \int_{t_0}^{t}\left(\frac{V_2}{A_2}\frac{dC_2}{dt}\right)dt$$

$$\ln\left(1 + \frac{C_2}{C_1 - C_2}\right) = \frac{D_{eff}\ A_2\ (t - t_0)}{e\ V_2} \tag{4.13}$$

Finally, it is worth noting that when the chloride concentration in the second chamber is lower than that in the first chamber ($C_2 \ll C_1$), which is always the case, one can express it as follows:

$$C_2 = C_1\ \frac{D_{eff}\ A_2\ (t - t_0)}{e\ V_2} \tag{4.14}$$

which is the Taylor expansion of $\ln(1 + x) = x$ about $x \simeq 0$.

The effective diffusion coefficient of chloride ions in concrete can then be determined:

$$D_{eff} = \frac{V_2}{A_2}\frac{C_2}{(t - t_0)}\frac{e}{C_1 - C_2} \tag{4.15}$$

4.4.4.2 Diffusion under Unsteady-State

The test for chloride diffusion can also be carried out under transient conditions, following the guidelines of the NBN EN 12390-11 "Testing hardened concrete - Part 11: Determination of the chloride resistance of concrete, unidirectional diffusion". It consists of determining an apparent diffusion coefficient (D_{app}) from the profile of the total chloride concentration in the sample.

All compositions are subjected to testing, including 2-3 samples per composition. The samples are cylindrical in shape with a diameter of 80mm and a thickness of 50mm. It

should be noted that the samples are first soaked in a lime solution to ensure diffusion of the ions and no other convective movement. Areas that will not be in contact with the chloride solution will be coated with an epoxy resin to guarantee a one-dimensional infiltration of the chloride ions. The specimens are subsequently submerged in a saline solution containing $NaCl$ at a concentration of 165±1 g/L. After this, they are placed in a closed chamber where the temperature is kept constant at 23°C. The procedure is illustrated in Figure 4.5.
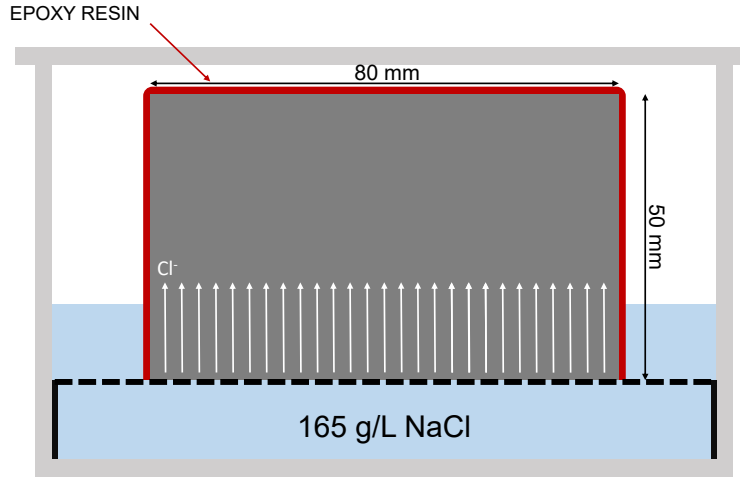
Figure 4.5: Experimental system for the diffusion under unsteady-state.

Sampling is conducted on a set schedule to determine a chloride profile within a sample. This involves grinding the sample perpendicular to the exposed surface at various depths in order to determine a chloride profile within the sample from the powder obtained [Poulsen, 1995]. The powder is oven-dried at a temperature of 105°C for minimum 12 hours. The powder is subsequently weighed, etched with nitric acid (HNO_3) to isolate the overall chloride quantity, incorporating both free and bound chlorides. Furthermore, the chloride concentration can be determined using the potentiometric titration "$AgNO_3$ SOL" method. A concentration profile illustrating the corresponding chloride concentration at each sample depth can be presented graphically by linking the data points.

Initially, the objective of the experiment is to determine the apparent diffusion coefficient of our compositions. Our hypothesis is that this coefficient is insensitive to changes in concentration. Fick's second law is then used to approximate the unidirectional ingress of chloride ions in our sample:

$$\frac{\partial C}{\partial t} = D_{app} \frac{\partial^2 C}{\partial x^2} \tag{4.16}$$

Then, in accordance with the same hypothesis as presented in Section 3.4.3.2, this equation may be formulated as follows [Poulsen, 1995]:

$$C(x,t) = C_i - (C_s - C_i) \times \text{erf}\left(\frac{x}{2\sqrt{D_{app}\,t}}\right) \tag{4.17}$$

where C_s is the surface concentration and C_i is the initial concentration in the sample.

However, this analytical solution may be too distant from reality, given the numerous hypotheses performed. Direct and inverse modelling would thus prove a more suitable method through which to derive the apparent diffusion coefficient from the experiment.

4.4.5 Conduction

The aim of the conduction experiment is to gauge the electrical current passing through the sample over a period of time. This allows the determination of the total penetration charge for each sample. It can then be used to estimate the chloride ion permeability of our materials according to the standard ASTM C 1202-05: "Standard Test Method for Electrical Indication of Concrete's Ability to Resist Chloride Ion Penetration".

The cylindrical samples employed have a diameter of 100mm and a height of 50mm. One cylinder is employed for each composition, which is subsequently coated with epoxy resin on its lateral surface. Prior to beginning the experiment, they are immersed in water to ensure saturation, utilising vacuum water absorption in accordance with the NBN B 24-213 standard.

The samples are inserted between two cells filled with distinct solutions. The initial cell is filled with a solution of $NaCl$ at a 30g/L concentration while the second cell contains a solution of $NaOH$ at a 12g/L concentration. The sample makes contact with the cells via a metal grid and is subsequently sealed with a rubber o-ring.
Next, the cells are connected to a generator that produces a voltage of 30V. The standard suggests using a 60V voltage, however our cells aren't equipped with temperature probes and this higher voltage would increase the "Joule effect", generating heat and altering the equations to be used. Therefore, we use a lower voltage to decrease the temperature rise inside the sample and the solutions employed.
The cell containing the $NaOH$ solution links to the positive terminal, whereas the negative terminal attaches to the other cell. An ammeter is connected to the two terminals to measure the electric current intensity flowing through the sample, induced by the potential difference. We correct the readings according to the Ohm's Law due to the reduced voltage, which is divided by two. Therefore, the intensity is multiplied by two during our analysis.
The experiment lasts for six hours at a constant voltage, and measurements are taken every 300 seconds. Figure 4.6 shows a representation and a picture of the setup.
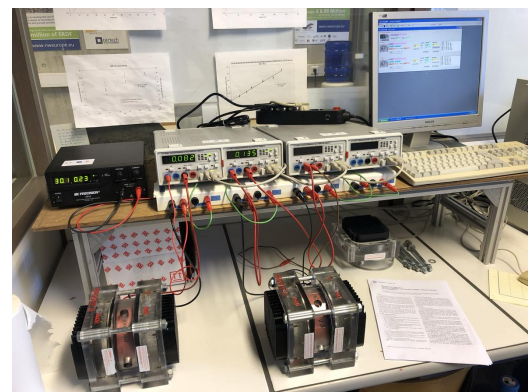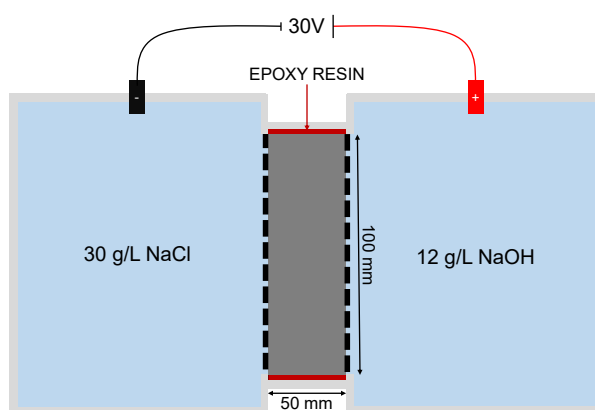
Figure 4.6: Electrical conductivity measurement (ASTM C 1202-05).

The overall electric charge that has passed through the sample, denoted as Q [C], can be calculated through the integration of results (intensity over time). One method for performing this integration is to use the trapezoidal rule (with one point every 30 minutes as specified in

the standard, which will need to be adjusted for our circumstances):

$$Q_{initial} = 900 \times \left(I_0 + 2 \times \left(\sum_{i=30}^{300} I_i \right) + I_{360} \right) \tag{4.18}$$

where I_0 represents the current (measured in amperes) immediately after the voltage application, and I_i represents the current measured at time i (in minutes).

The law is based on a sample with a diameter of 95mm. As our samples have a diameter of 100mm, it is necessary to modify the total electric charge using to the following equation:

$$Q_{diameter} = Q_{initial} \times \left(\frac{95}{100} \right)^2 \tag{4.19}$$

A final adjustment is then made to account for the decreased voltage utilised. In accordance with the Ohm law ($V = R \times I$) and assuming equal resistivity, when the voltage is doubled, the current passing through the sample is also doubled. Henceforth, it can be concluded that:

$$Q_{voltage} = 2 \times Q_{diameter} \tag{4.20}$$

This overall electrical charge ($Q_{voltage}$ after the two adjustments) that has passed through the sample can be associated with several classes of chloride permeability using the Table 4.5 [Whiting, 1981].

Chloride permeability	Charge passed [Coulombs]
High	>4000
Moderate	2000-4000
Low	1000-2000
Very low	100-1000
Negligible	<100

Table 4.5: Chloride permeability class regarding the total electric charge flowing through a sample in a conductivity experiment (from [Whiting, 1981]).

4.5 Conclusion

Throughout this chapter, several compositions used in our research were presented, along with multiple experiments that aim to better characterise the transfer of liquid, air, and pollutants (namely chloride ions) in concrete made from natural and recycled aggregates. The methodology used in each experiment was outlined, which allows for easy reproducibility and alleviates any doubts that may arise during analysis of the results.

5

EXPERIMENTAL RESULTS

Contents

5.1   Introduction

The aim of the experiments conducted in this study is to obtain the intrinsic properties of our materials, thus promoting a greater comprehension of the effects of Recycled Concrete Aggregates. This chapter outlines the outcomes obtained during this experimental phase and draws comparisons with findings from relevant literature.

5.2   Properties of Water Transfer

First, we will study the properties that characterise water transfer. Our interest lies in the experiments on water absorption by immersion, permeability, and static sorption and desorption.

5.2.1   Water Absorption by Immersion

The first experiment analysed is the Water Absorption by Immersion. The recorded outcomes are presented in both Figure 5.1 reflecting densities and Figure 5.2 indicating water absorption and open porosity.
Besides the dry and saturated densities obtained following the experiment's completion, the densities of the demoulded samples are also presented. However, the density of the E-CP composition could not be measured after demoulding as it was not possible to determine the sample's volume due to air bubbles formed during the mixing process. Additionally, the theoretical densities calculated from the composition designs are presented.
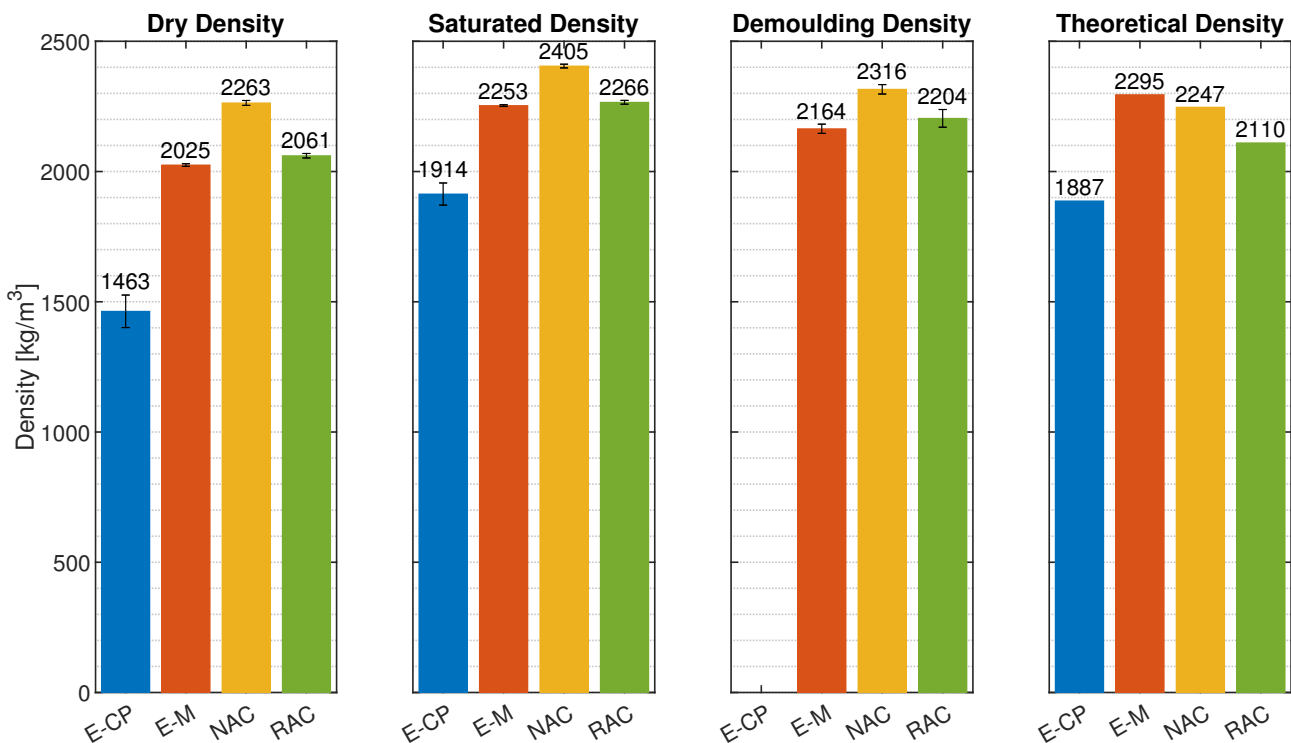
Figure 5.1: Saturated and dry densities obtained from the Water Absorption by Immersion experiment, as well as densities obtained after demoulding the samples and densities obtained theoretically, based on the compositions.

Firstly, comparison of the theoretical densities suggests that denser materials result in a denser composition. As a result, the mortar (E-M) is denser than the concrete made from natural aggregates (NAC) due to sand being denser than aggregates. Moreover, the density of the concrete made from recycled concrete aggregates (RAC) is less than that of the NAC due to the former's aggregates being less dense than the latter's ones. However, materials are not the only factor affecting density; porosity also plays a significant role. As a result, the density of cement paste (E-CP), which is much more porous than the other compositions, is smaller than their respective densities.

The difference between the theoretical and demoulding densities raises some questions. The NAC and RAC have a higher density than anticipated, which may result from a slight excess and loss of water during mixing. Conversely, the E-M composition is lighter than expected. This phenomenon may be attributed to minor segregation while being mixed, ultimately resulting in the moulds being filled with a composition of lower density than anticipated.

Finally, the demoulding densities provide sufficient information as the dry and saturated densities do not offer additional insights, and the trends between compositions remain constant. It is noteworthy, however, that the E-CP exhibits a more significant increase in density when transitioning from its dry to saturated state, owing to its greater water absorption, as depicted in Figure 5.2.
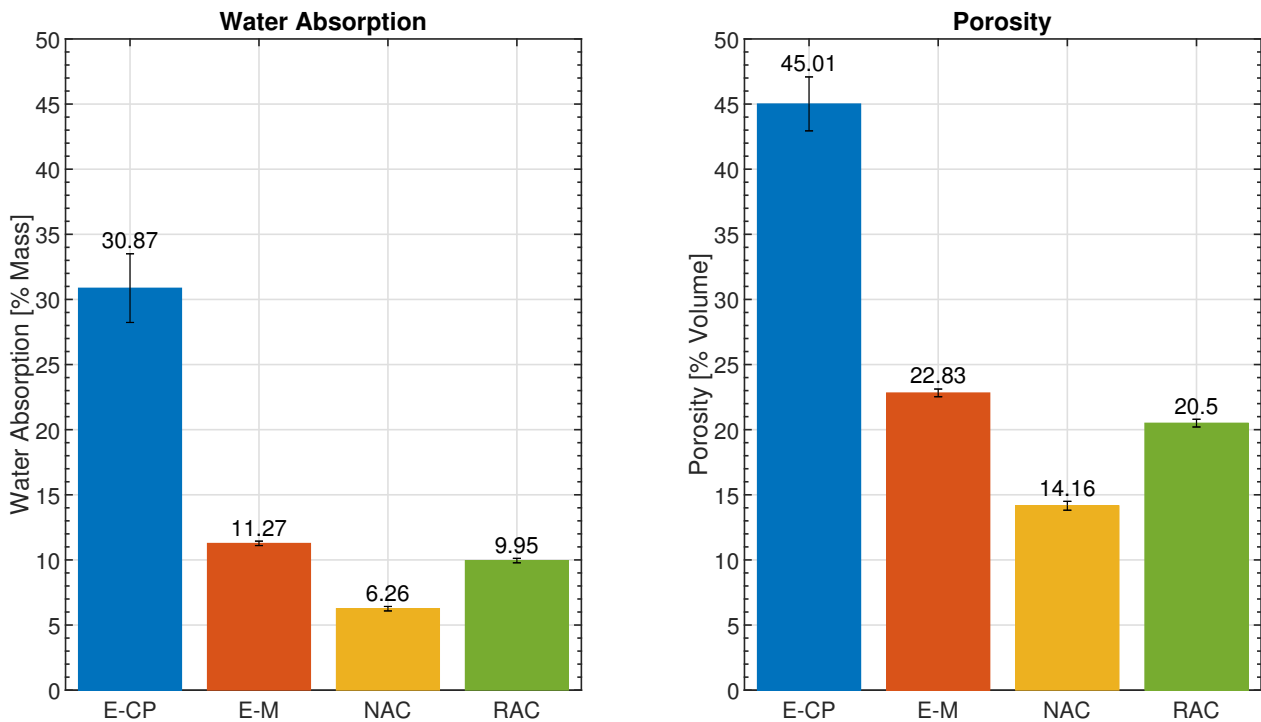
Figure 5.2: Porosity and water absorption obtained from the Water Absorption by Immersion experiment.

The compositions can be compared in terms of water absorption and water-accessible porosity, which are correlated parameters. The more continuous the granular skeleton, the less porous the material. Consequently, the concretes exhibit lower porosity than the mortar, whereas the mortar itself has less porosity than the cement paste. Furthermore, the content

of adhering mortar in RAC elevates its porosity and water absorption, leading to results that are more akin to those of E-M than NAC.

The water absorption of the two types of concrete, NAC and RAC, depends on the water absorption of their respective aggregates. There should therefore be a similar difference in water absorption (adjusted for the mass of aggregates incorporated into the composition) between the concretes (specified as $\Delta WA_{\text{NAC-RAC}}$) and their aggregates (specified as $\Delta WA_{\text{NA-RCA}}$):

$$\begin{cases} \Delta WA_{\text{NAC-RAC}} = WA_{\text{RAC}} - WA_{\text{NAC}} = 9.95 - 6.26 = 3.69\% \\ \Delta WA_{\text{NA-RCA}} = WA_{\text{RCA}} - WA_{\text{NA}} = 3.62 - 0.61 = 3.01\% \end{cases} \tag{5.1}$$

A variation of 3.69% in the concrete seems to be in a close proximity to the variation of 3.01% in the aggregates. Hence, it is possible to conclude that the majority of the observed differences between the two compositions is caused by the substitution of aggregates, which also alters the ITZ properties along with others, presumably giving rise to a small gap of 0.68%.

It is also feasible to compare the water absorption of the mortar components in NAC and RAC with the water absorption of the equivalent mortar (E-M). To do so, the water absorption of the respective aggregates must be subtracted from the water absorption of the concretes to determine the water absorption value of the mortar phase. This value must be corrected for the volume fraction it occupies.

The water absorption by natural and recycled aggregates in their respective concrete mixtures is as follows:

$$\begin{cases} m_{NA} \times WA_{\text{NA}} = 1111 \times 0.61\% = 6.78\text{kg} \\ m_{RCA} \times WA_{\text{RCA}} = 945 \times 8.08\% = 76.35\text{kg} \end{cases} \tag{5.2}$$

The water quantity absorbed by the aggregates should be divided by the theoretical density of their respective concrete to obtain the theoretical water absorption of the aggregates. This value can then be subtracted from the water absorption of the corresponding concrete to determine the water absorption solely attributable to the mortar paste:

$$\begin{cases} WA_{\text{mortar of NAC}} = WA_{\text{NAC}} - WA_{\text{NA inside NAC}} = 6.26 - \dfrac{6.78}{2247} \times 100 = 5.95\% \\ \\ WA_{\text{mortar of RAC}} = WA_{\text{RAC}} - WA_{\text{RCA inside RAC}} = 9.95 - \dfrac{76.35}{2110} \times 100 = 6.33\% \end{cases} \tag{5.3}$$

Finally, water absorption is adjusted for the proportion of mortar paste contained in the concrete mixture, assuming the concrete would be entirely composed of mortar:

$$\begin{cases} WA_{\text{NAC}} = 5.95\% \text{ for } \dfrac{2247 - 1111}{2247} \times 100 = 50.55\% \longrightarrow WA = 11.77\% \text{ for } 100\% \text{ of mortar} \\ \\ WA_{\text{RAC}} = 6.33\% \text{ for } \dfrac{2110 - 945}{2110} \times 100 = 55.21\% \longrightarrow WA = 11.46\% \text{ for } 100\% \text{ of mortar} \end{cases} \tag{5.4}$$

This is close enough to the E-M's 11.27% water absorption. The disparity could be attributed to the ITZ's presence in the concrete, which raises water absorption in contrast to plain mortar.

5.2.2 Water Permeability

The water permeability experiment determines the intrinsic permeability of the material, which refers to the ease at which water can percolate through the porous medium under study. The results are presented in Figures 5.3 and 5.4.

Figure 5.3 presents the experimental measurements carried out, depicting the increase in the volume of water passing through the porous medium over time. The data points used to calculate the intrinsic permeability are depicted in black. Additionally, Figure 5.4 displays the measured intrinsic permeability for each composition tested.
The results show that the most permeable material is the mortar (E-M), followed by the cement paste (E-CP). It may appear unusual as the water absorption and porosity of the cement paste are higher than those of the mortar. Nevertheless, the mean pore size of the cement paste may be less than that of the mortar paste [Zhu et al., 2019], which could reduce the intrinsic permeability.
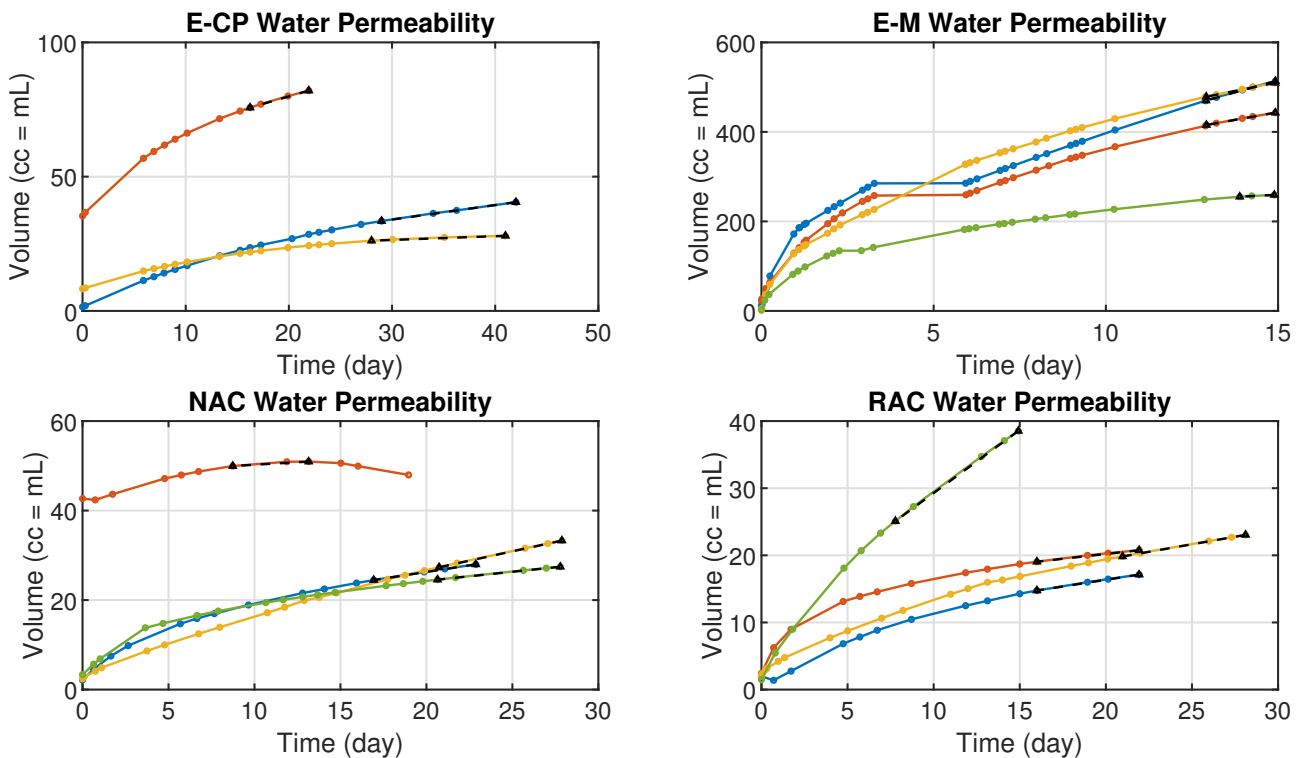
Figure 5.3: Results from the water permeability measurements, each color representing a different sample.

The intrinsic permeability of both concretes is quite comparable, with the concrete composed of natural aggregates (NAC) exhibiting lesser permeability than the concrete made of recycled aggregates (RAC). This observation appears to be logical, as RAC is more porous and the quality of the mortar paste encasing the aggregates may be inferior to that of NAC.
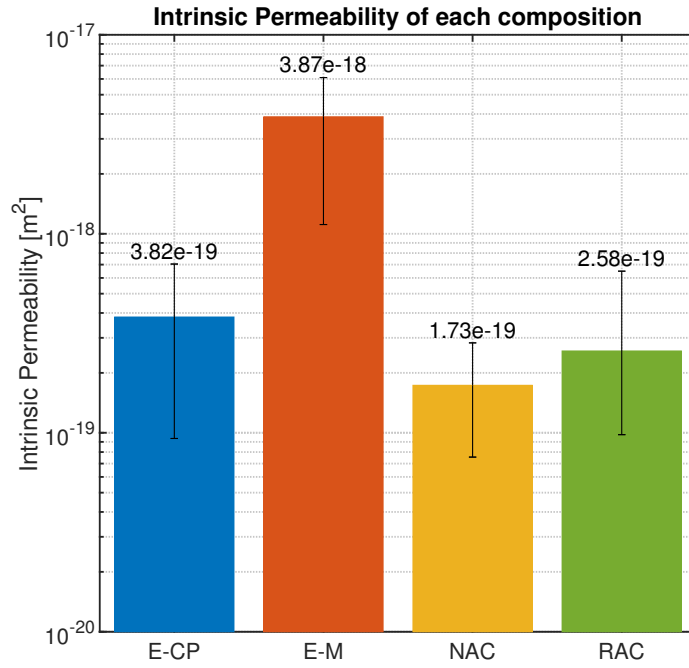
Figure 5.4: Comparison of the intrinsic water permeability of each composition.

5.2.3 Static Sorption and Desorption

The static sorption and desorption experiment enables characterisation of water and gas exchanges between the environment and the porous system studied. It utilises the vapour technique, or controlled suction technique, as previously explained.
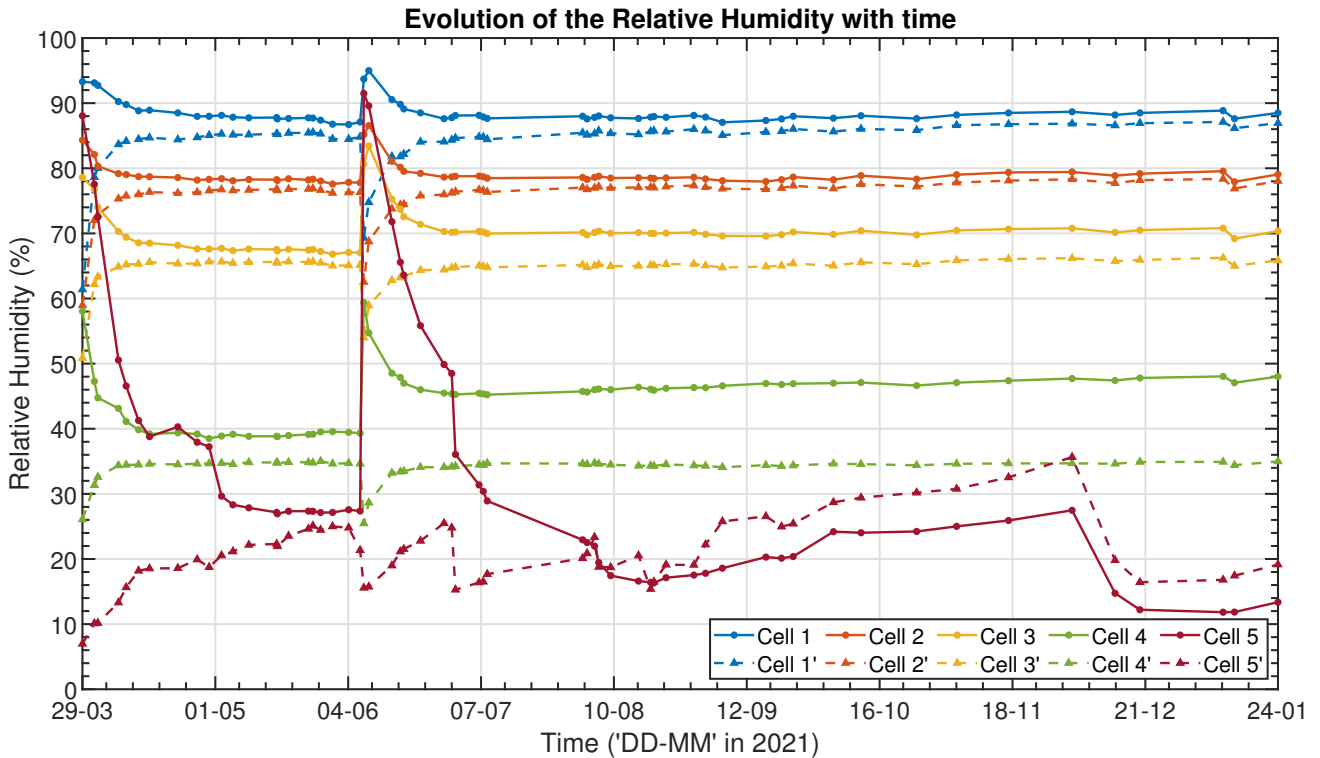
Figure 5.5: Evolution of the Relative Humidity inside each chamber.

The evolution of relative humidity (RH) inside each climatic chamber with time is depicted in Figure 5.5. The aim of this experiment is to achieve a steady Relative Humidity (RH) in each chamber, which will enable the samples to reach their equilibrium water content with the surrounding environment.

The E-CP and E-M compositions were mixed prior to the NAC and RAC, their experimental phase being separated. The abrupt alterations in RH experienced by all the chambers in June occurred due to the substitution of samples, with the NAC and RAC ones being either fully dehydrated or completely saturated.

Figures 5.6 and 5.7 (as well as B.5 and B.6 in the Appendix B, for the E-CP and E-M correspondingly) display the Water Retention Curve (WRC) derived from the analysis of outcomes obtained from the static sorption and desorption test.

The water retention curves were determined by fitting the Van Genuchten model to the experimental data. The two parameters that require calibration are α_{vG}, which represents the air-entry pressure of the porous material, and n_{vG}, which relates to the slope of the curve. A lower air-entry pressure corresponds to an earlier onset of desaturation of the medium. It has been reported in the literature that the model parameter n_{vG} is dependent on the pore structure of the material, which exhibits little variation between sorption and desorption [Likos et al., 2014].

The analysis outcomes, for each composition, are presented in Table 5.1.
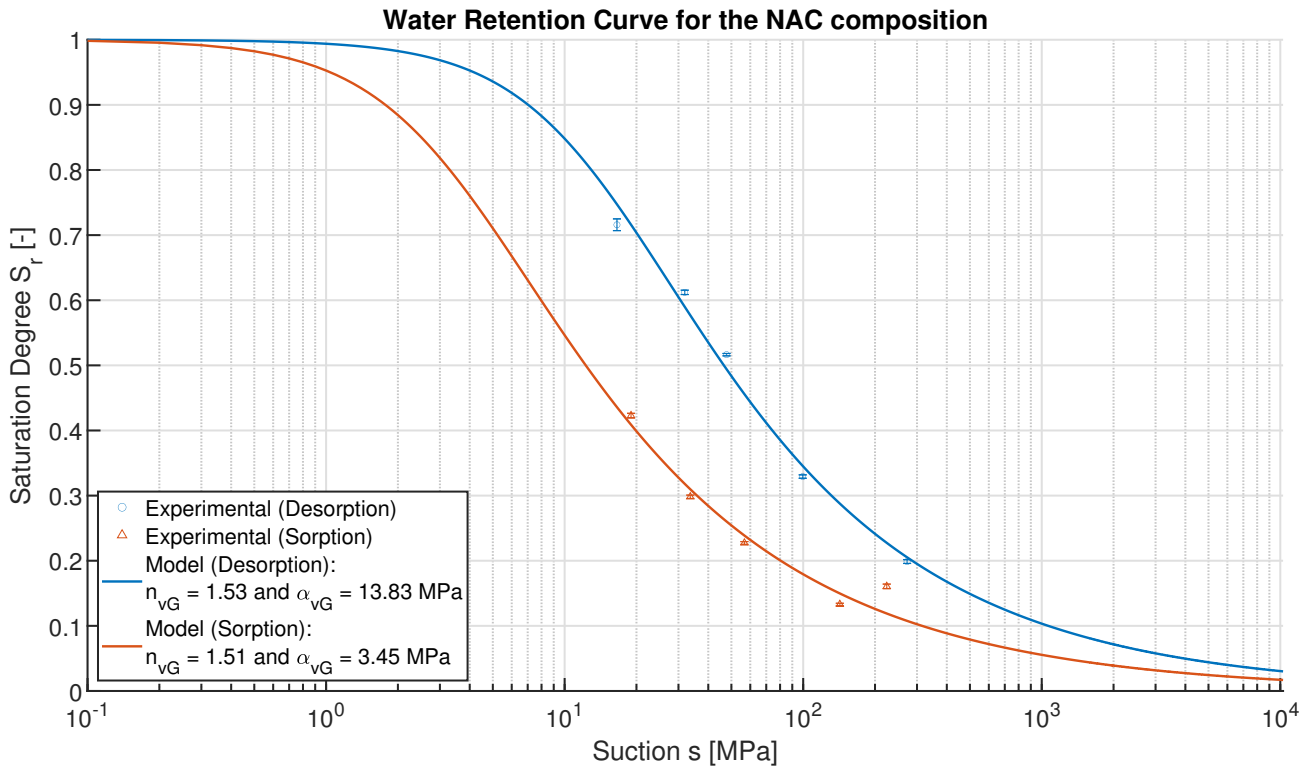
Figure 5.6: Water Retention Curve for the NAC composition, based on the results from the static sorption and desorption experiment, and using the Van Genuchten's model.
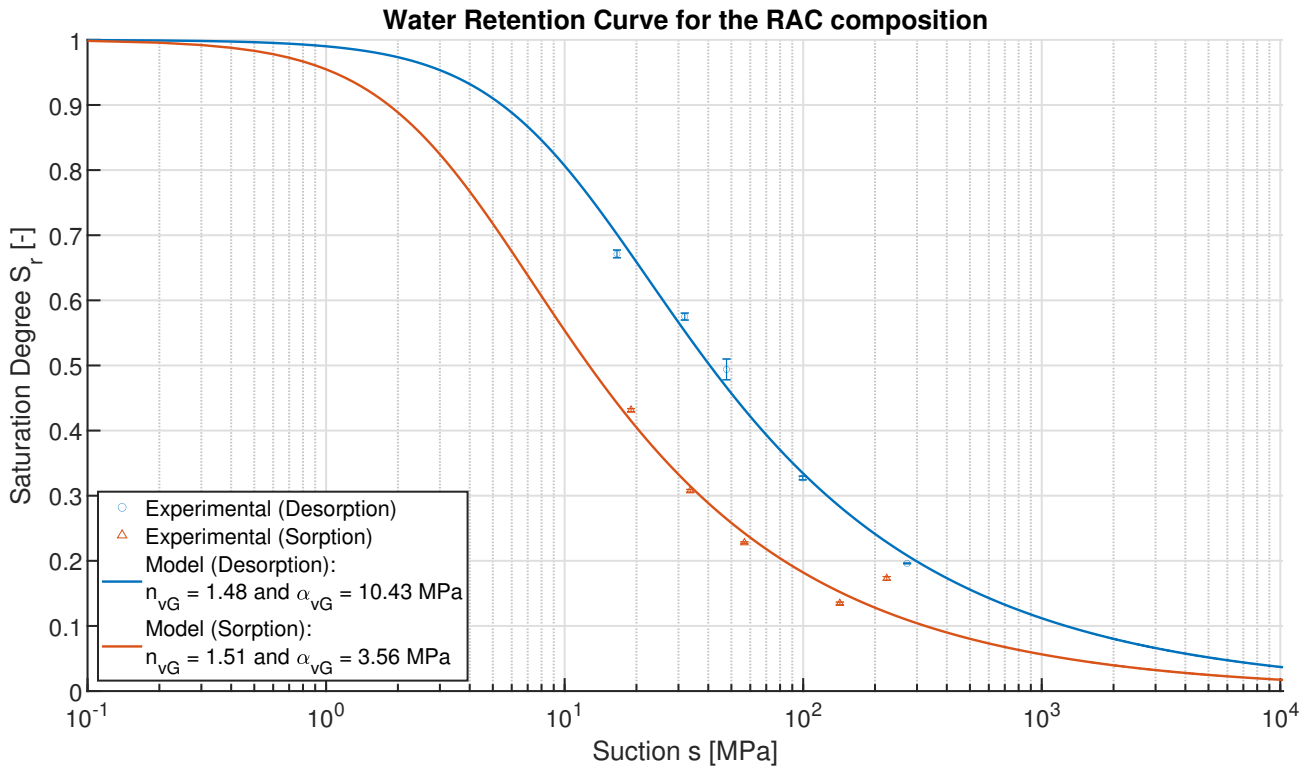
Figure 5.7: Water Retention Curve for the RAC composition, based on the results from the static sorption and desorption experiment, and using the Van Genuchten's model.

Composition	Desorption		Sorption	
	n_{vG} [-]	α_{vG} [MPa]	n_{vG} [-]	α_{vG} [MPa]
E-CP	1.51	10.95	1.50	3.84
E-M	1.51	11.55	1.49	2.75
NAC	1.53	13.83	1.51	3.45
RAC	1.48	10.43	1.51	3.56

Table 5.1: Results from the Static Sorption and Desorption experiment.

Firstly, the desorption results were analysed for all the compositions. The air-entry pressure was found to be smallest for RAC, increasing with E-CP and E-M before reaching a maximum for NAC. This pressure is primarily linked to the pores' size in the medium. The smaller the pores, the larger the air-entry pressure and the latter the water can escape the porous medium. When comparing the two types of concrete, it can be observed that the concrete made from recycled aggregates undergoes desaturation before the one made from natural aggregates.

During sorption, the curve reading is reversed in comparison to desorption, resulting in a decrease in suction. Therefore, the higher the air-entry pressure and the faster the medium begins its sorption. The biggest air-entry pressure is observed in the E-CP, followed by the RAC and NAC. Finally, the E-M has the smallest air-entry pressure. It would be more logical to maintain consistency between sorption and desorption orders. This is because

smaller pores lead to late desorption and early sorption due to the stronger capillary suction in smaller pores.
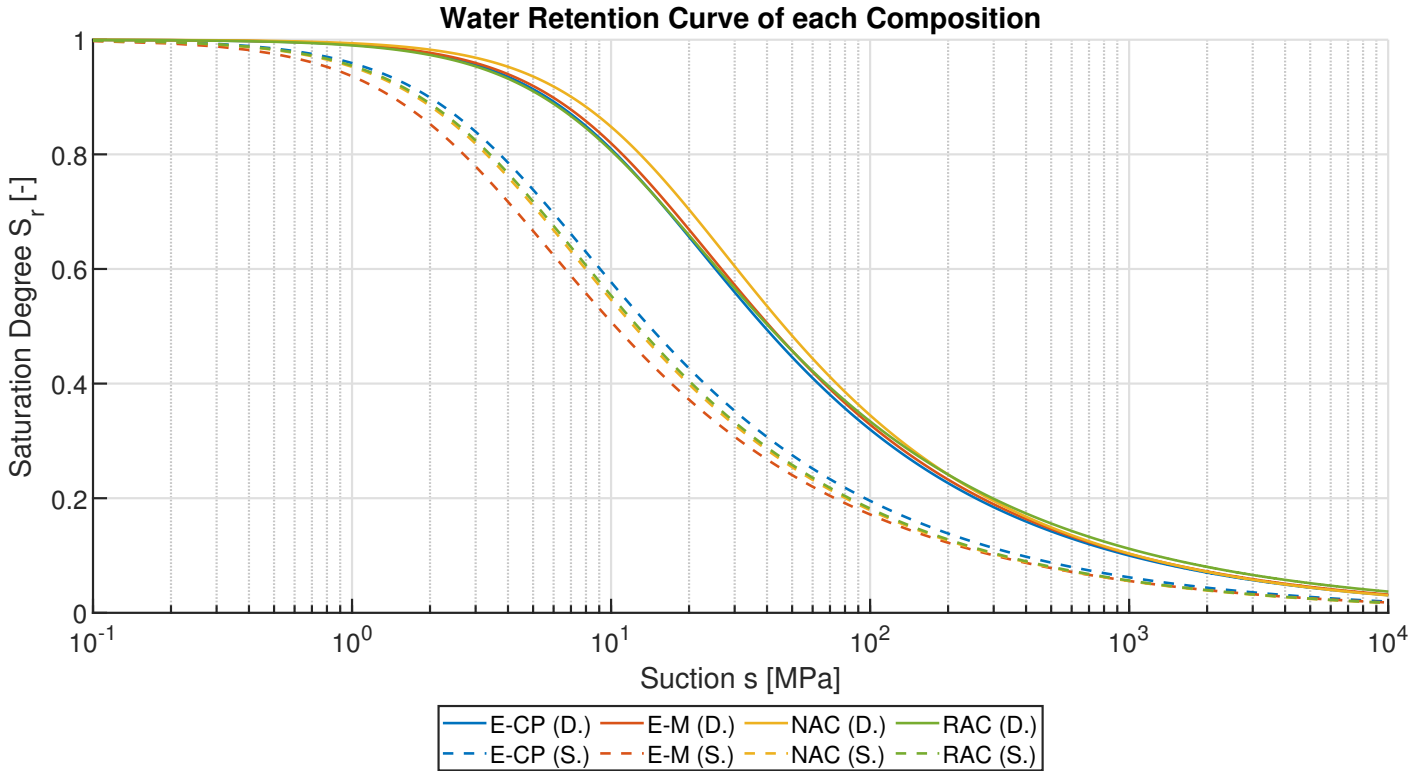
Figure 5.8: Water Retention Curve of each composition, based on the results from the static sorption (dashed lines) and desorption (solid lines) experiment, using the Van Genuchten's model.

Figure 5.8 presents the complete WRC, facilitating a clear comparison. Focusing on the concretes, it is apparent that the NAC is usually positioned outside of the RAC curves, indicating that it will desaturate later than the RAC at the same level of suction. This suggests that the porosity of the NAC consists of smaller pores than that of the RAC. Conversely, it could be argued that the sorption air-entry pressure is lower in the NAC in comparison to the RAC, indicating slightly larger pores in the NAC. However, the values are closely aligned with each other, with a somewhat indistinct difference.

One aspect of the water retention curves that has yet to be mentioned is the reduction in relative permeability once a porous material desaturates. When desaturation occurs and the water body is no longer continuous within the porous matrix, the permeability invariably decreases. This decrease in both the degree of saturation and permeability creates a blocking zone, reducing exchanges and isolating the surface of the material from its interior.

5.2.4 Study of the Hysteresis of the Water Retention Curve

As explained in Section 2.3.2, the degree of saturation of a porous material is highly dependent on its wetting and drying history, with the water retention curve exhibiting hysteresis [Bear & Verruijt, 1987]. It was therefore decided to investigate this hysteresis phenomenon by attempting to observe it in the laboratory and then find a model to replicate it. Since the main wetting and drying retention curves of our model are based on the Van Genuchten model [Van Genuchten, 1980], the hysteresis model has to be compatible and therefore the

one proposed by Zhou et al. (2012) was chosen [Zhou et al., 2012].

Without going into too much detail, the model proposes to model the hysteresis of the WRC based on the properties of the main WRC, i.e. the air-entry pressure α_{vG} and the slope of the curve n_{vG}, with the use of a fitting adimensional parameter b, always positive, which influences the slope of the scanning curve. The closer it is to zero and the closer the hysteresis curve is to the main curve, while the larger it is and the more horizontal the hysteresis curve becomes [Zhou et al., 2012].

Of course, the two main scanning curves act as limits for the hysteresis curves: they define boundaries that must never be crossed. The model used to represent the hysteresis is described in more detail in the modelling aspect of this thesis, in Section 6.3.5.

No. of the hysteresis	Starting RH	Chamber 1	Chamber 2	Chamber 3	Chamber 4
1	0%	91.60%	80.30%	45.74%	92.78%
2	0%	80.84%	45.31%	39.37%	92.78%

Table 5.2: Paths chosen to observe the hysteresis phenomenon experimentally, with two hysteresis in parallel.

To study the hysteresis phenomenon, the first step is to observe it experimentally. Several samples, the same as those used in previous sorption and desorption experiments, were dried in an oven to remove all moisture from their porous systems. They were then placed in specific climatic chambers, the same ones used in the previous experiment. After 3 months, the sample's saturation degree is stabilised under its environmental conditions (relative humidity and temperature), and the samples can then be moved to another chamber. The goal is to saturate, desaturate, and resaturate the samples to observe a hysteresis. The path followed for the E-M, NAC, and RAC (four samples each) is specified in Table 5.2.

The experiment employed the same samples as the previous static sorption and desorption experiment. However, the samples were stored in the hallway for approximately one year. The analysis revealed a significant discrepancy between the hysteresis and the previous results of water retention curves (Section 5.2.3), particularly the sorption curve. It was therefore decided to redo the entire experiment to observe the change in the WRC and potentially justify it due to inadequate storage leading to carbonation of our samples. Figure 5.9 shows the initial WRCs for E-M, NAC, and RAC in dashed lines and the new ones, after the hysteresis, in solid lines. The sorption curves are completely different, while the desorption curves are somewhat similar.

The experimental results analysis using the Van Genuchten model is presented in Appendix B, in Figures B.7, B.8, and B.9 that correspond to E-M, NAC, and RAC, respectively. The values of the corresponding parameters are displayed in Table 5.3.
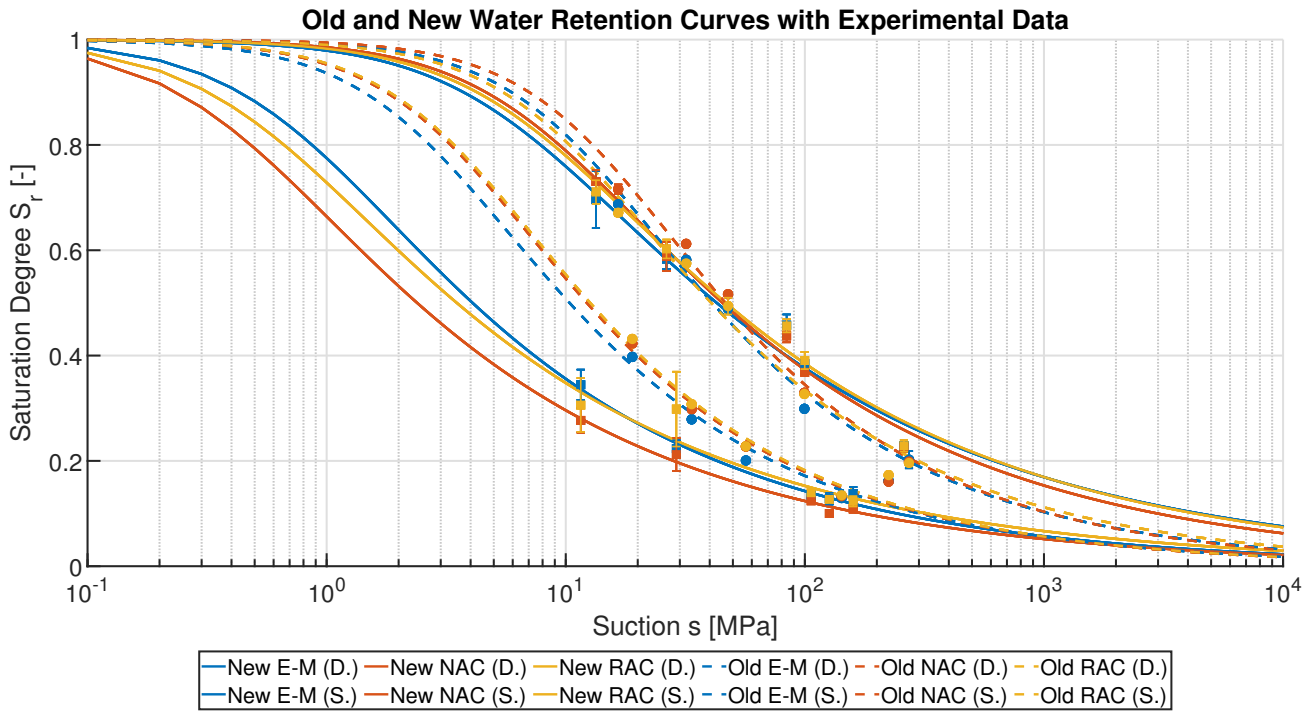
Figure 5.9: Initial (old) and new Water Retention Curves for the all composition, based on the results from the static sorption and desorption experiments (with data shown with markers), and using the Van Genuchten's model.

Based on the newer water retention curves, which are more appropriate for the samples at the time of the hysteresis experiment, the hysteresis phenomenon was observed and quantified based on the model of Zhou et al. (2012). This is shown in Figure 5.10 for the E-M, NAC and RAC.

Firstly, for some hysteresis, the starting point is slightly higher than expected, as it should be on the main wetting retention curve. This is because the fit is partially imprecise, some standard deviations are observed in our experimental results and therefore not all points are exactly on the main curves. For both hysteresis it was decided to use a separate value of b in order to best fit the experimental results with our model and to observe if the difference in the parameter is significant or not. Overall, the model proposed by Zhou et al. (2012) [Zhou et al., 2012] tends to represent the hysteresis phenomenon with sufficient accuracy.

Finally, it could be observed that the difference in the water retention curves obtained through the Van Genuchten model for the new and old sorption and desorption experiments may only be due to the fitting, as shown in Figure 5.9. Therefore, the Van Genuchten model was refitted to our experimental results using both the old and new data sets. Figures 5.11, 5.12 and 5.13 represent the E-M, NAC and RAC, respectively. The desorption results appear to be correct, and therefore, one water retention curve could be used for both the new and old experiments. However, for sorption, the fitting is less precise, as indicated by the R² value, especially for the NAC. Further investigation is necessary to determine the cause of the shift in the sorption water retention curve compared to the desorption curve, which remained unchanged over time.
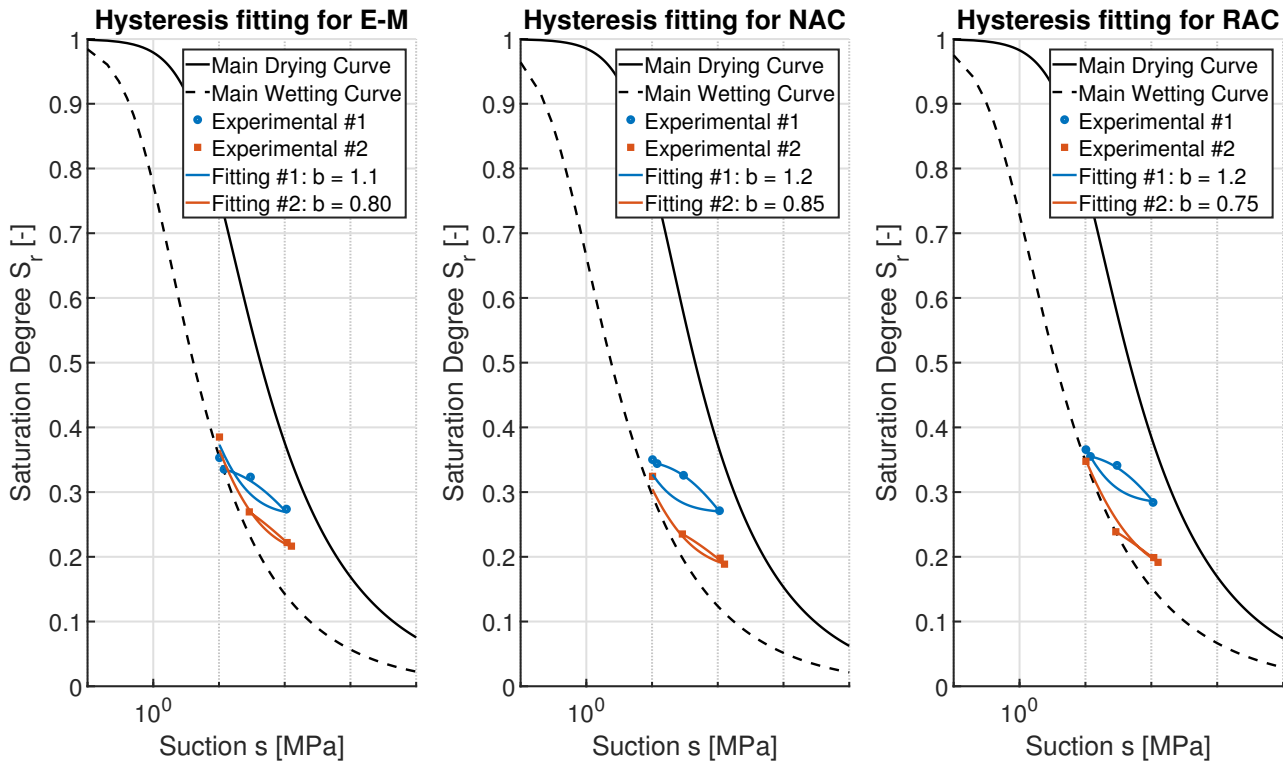
Figure 5.10: Fitting of the hysteresis for the E-M, NAC and RAC, based on the model by Zhou et al. (2012) [Zhou et al., 2012].

Composition	E-M		NAC		RAC	
	n_{vG} [-]	α_{vG} [MPa]	n_{vG} [-]	α_{vG} [MPa]	n_{vG} [-]	α_{vG} [MPa]
1st Sorption	1.49	2.75	1.51	3.45	1.51	3.56
1st Desorption	1.51	11.55	1.53	13.83	1.48	10.43
2nd Sorption	1.4	0.77	1.38	0.41	1.36	0.54
2nd Desorption	1.35	6.23	1.39	8.16	1.36	7.2
Hybrid Sorption	1.39	0.94	1.37	0.74	1.63	5.11
Hybrid Desorption	1.41	8.44	1.45	10.51	1.41	8.46

Table 5.3: Results from the Static Sorption and Desorption experiments for the hysteresis: 1st experiment, 2nd one and hybrid solution from both data sets.
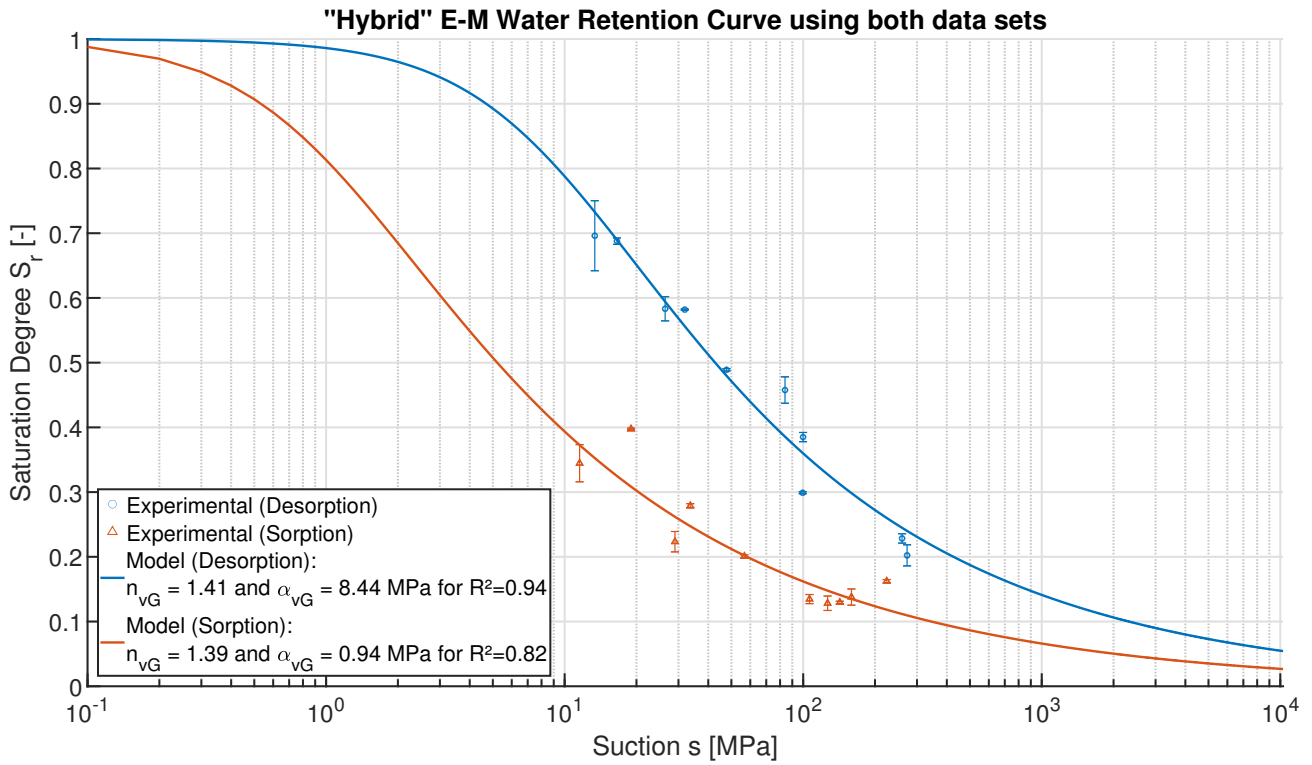
Figure 5.11: Water Retention Curve for the E-M composition, based on the results from both the new and initial static sorption and desorption experiments, and using the Van Genuchten's model.
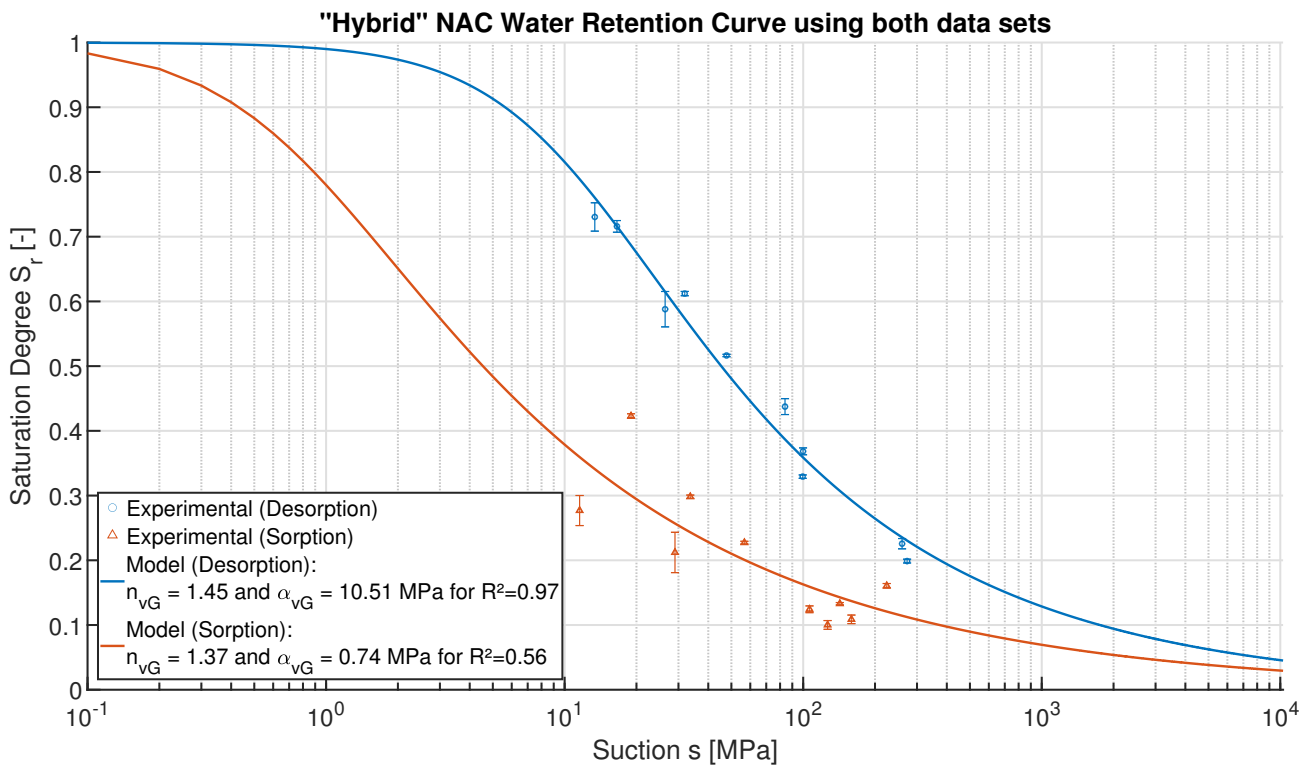
Figure 5.12: Water Retention Curve for the NAC composition, based on the results from both the new and initial static sorption and desorption experiments, and using the Van Genuchten's model.
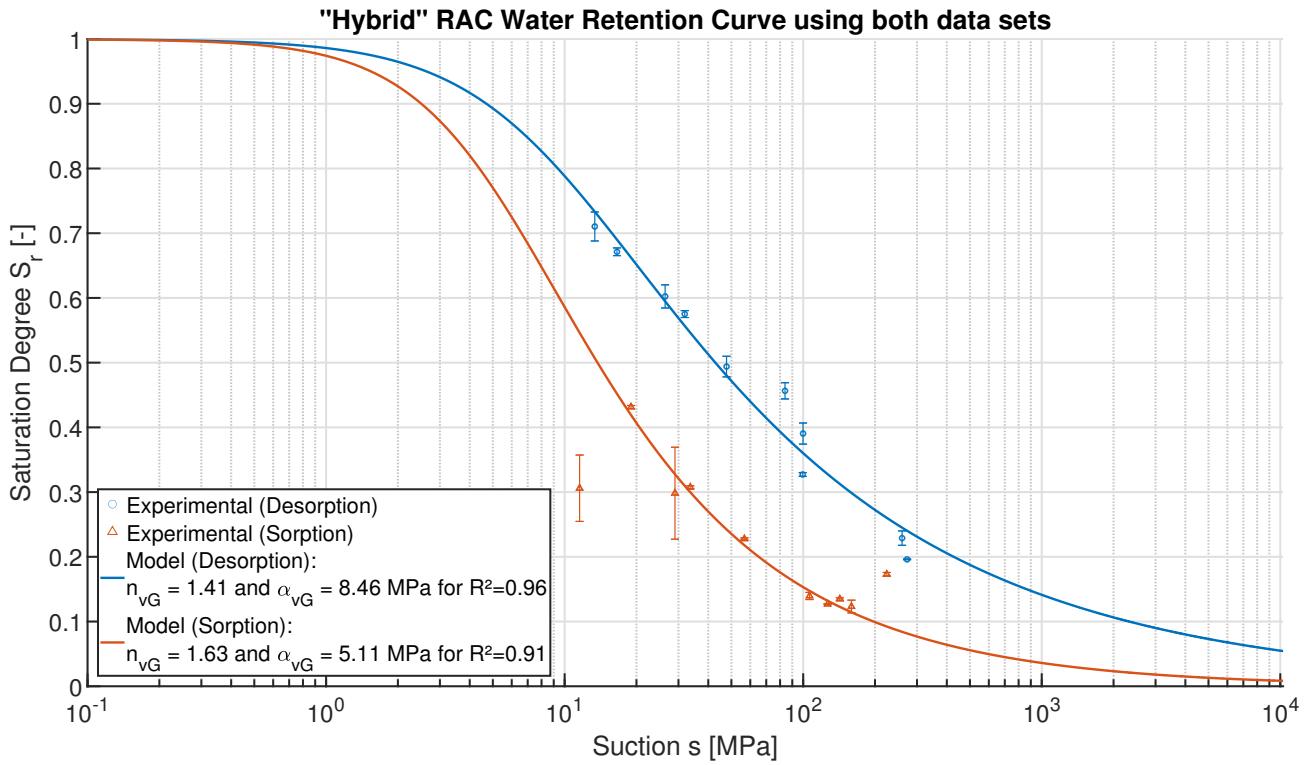
Figure 5.13: Water Retention Curve for the RAC composition, based on the results from both the new and initial static sorption and desorption experiments, and using the Van Genuchten's model.

Table 5.3 presents the results for the first, second, and hybrid sorption and desorption water retention curves fitted with the Van Genuchten model. The air-entry pressure decreased for all compositions between the first and second experiments, which may be attributed to carbonation. The samples were stored in simple cardboard boxes in the hallway and were only one centimetre thick. This is shown in Figure 5.14: there is carbonation of the surface of the sample, but the carbonation front did not reach the centre of the sample.
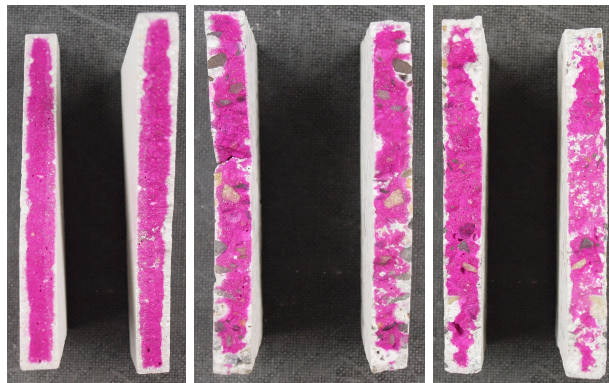
Figure 5.14: Samples used in the hysteresis experiment, sprayed with phenolphthalein to showcase the carbonation. From the left: E-M, NAC and RAC.

5.3 Properties of Chloride Transfer

5.3.1 Chloride Diffusion under Steady-State

Samples of each composition have undergone one-dimensional steady-state diffusion of chloride ions. One of the cells, initially free of chloride ions, was subjected to regular sampling of 10mL of solution over several days, during which its chloride content was analysed. Results are displayed in Figure 5.15, with the tangent dash-line serving as a guide to estimate the compositions' diffusion coefficient.
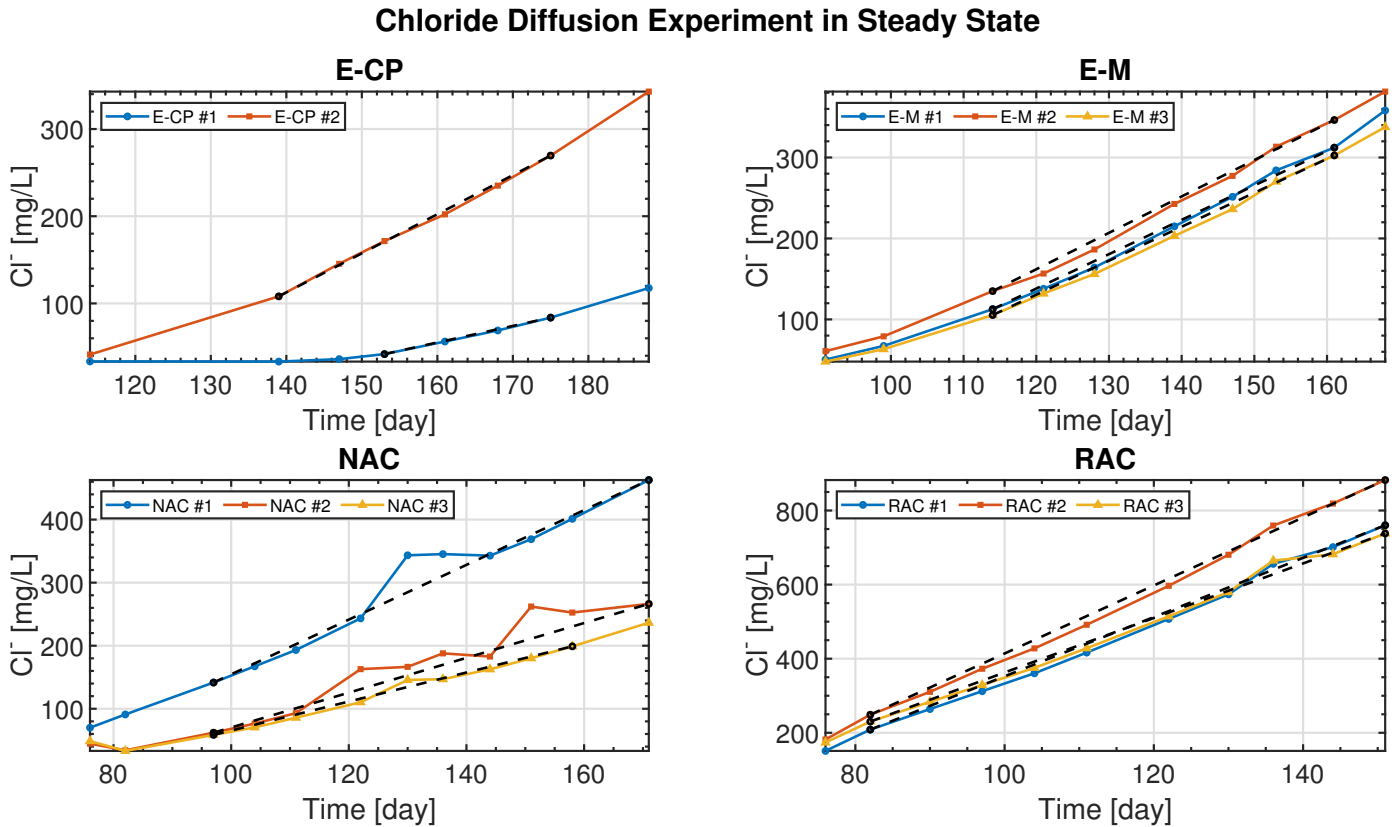
Figure 5.15: Experimental results from the chloride diffusion under steady-state experiment: evolution of the chloride content with time.

The chloride diffusion coefficients determined are shown in Figure 5.16. The highest value for the diffusion coefficient is obtained for recycled aggregate concrete (RAC), followed by the mortar (E-M) and cement paste (E-CP), whereas the lowest value is found in concrete made from natural aggregates (NAC). However, it can be seen that the standard deviations of diffusion coefficients are smaller for E-M and RAC than for the other two. It is logical to anticipate that a material with higher porosity would exhibit a higher chloride diffusion coefficient. However, the chloride adsorption phenomenon could lower the diffusion coefficient, particularly in materials with higher cement content.
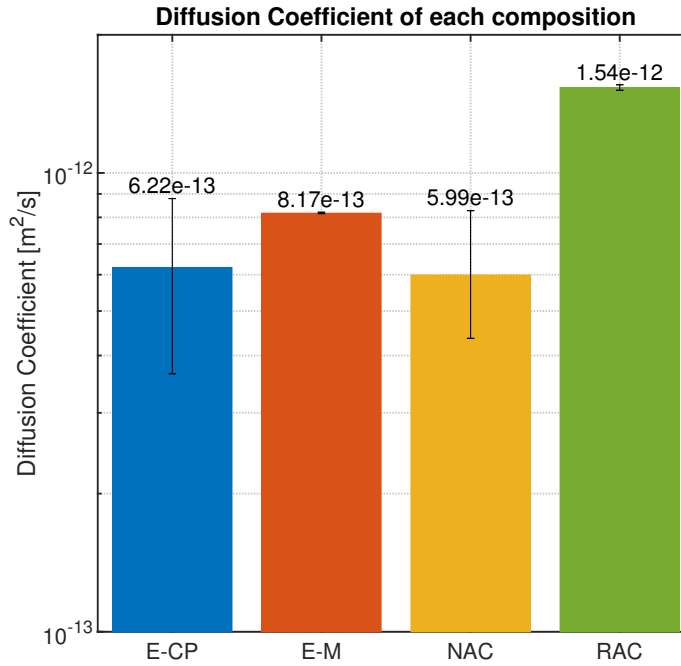
Figure 5.16: Mean diffusion coefficient obtained from the chloride diffusion under steady-state.

5.3.2 Chloride Diffusion under Unsteady-State

In this study of chloride diffusion under unsteady-state conditions, samples were immersed in a chloride ion solution for a predetermined period. Subsequently, the samples were ground to enable titration of the resulting powder, thereby determining the chloride content at several depths from the exposed surface. Results are presented in Figures 5.17 and 5.18, illustrating the chloride content as a percentage of total mass and binder mass, respectively, at different depths. Measurements were conducted at three time points: 15, 29, and 91 days. In addition to the experimental findings, the chloride threshold of 0.4% of binder mass, necessary to determine the depth at which steel reinforcements start to corrode according to code, is represented for each mix.

A differentiation needs to be made regarding the mass employed for the mass percentage of chloride content. In experimental procedures, data is acquired per mass of ground material, which is the total weight of the mixture. Nonetheless, according to the standard, the critical chloride content is expressed as a percentage of the mass of the binder. Hence, when presenting information, either the experimental outcomes or the chloride limit must be adjusted to ensure unit consistency.
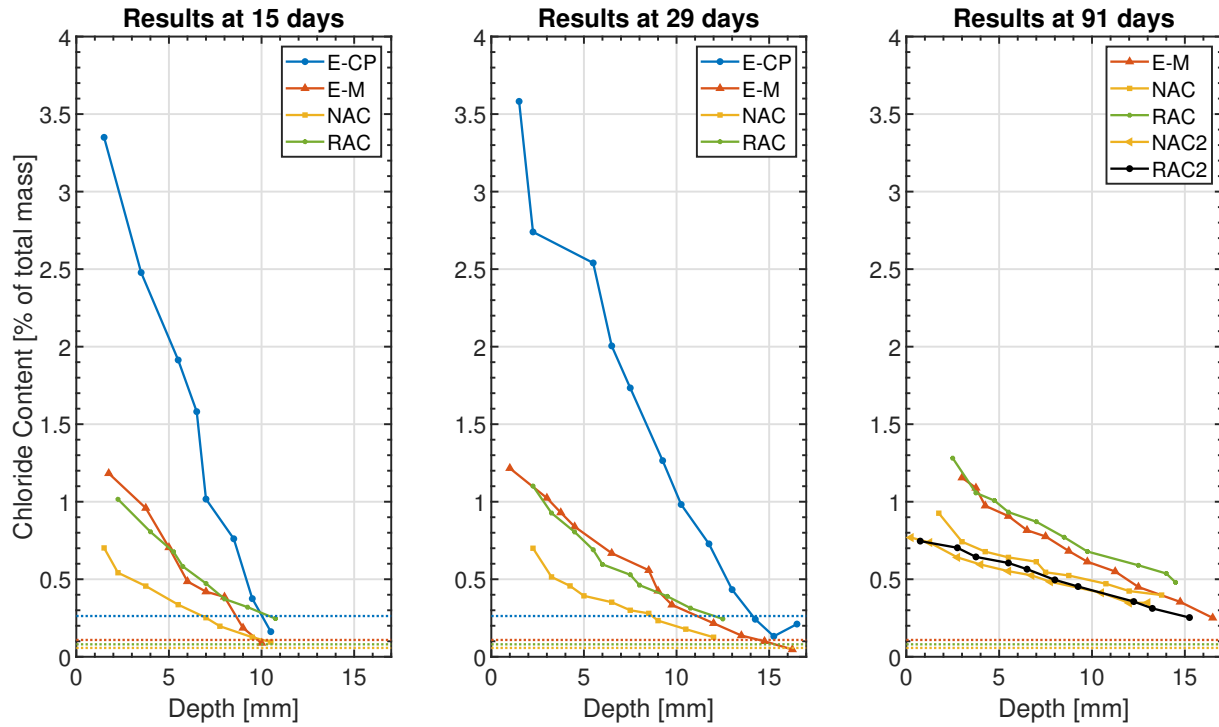
Figure 5.17: Results from the Chloride Diffusion under Unsteady-State experiment: evolution of the chloride content with respect to time and depth.
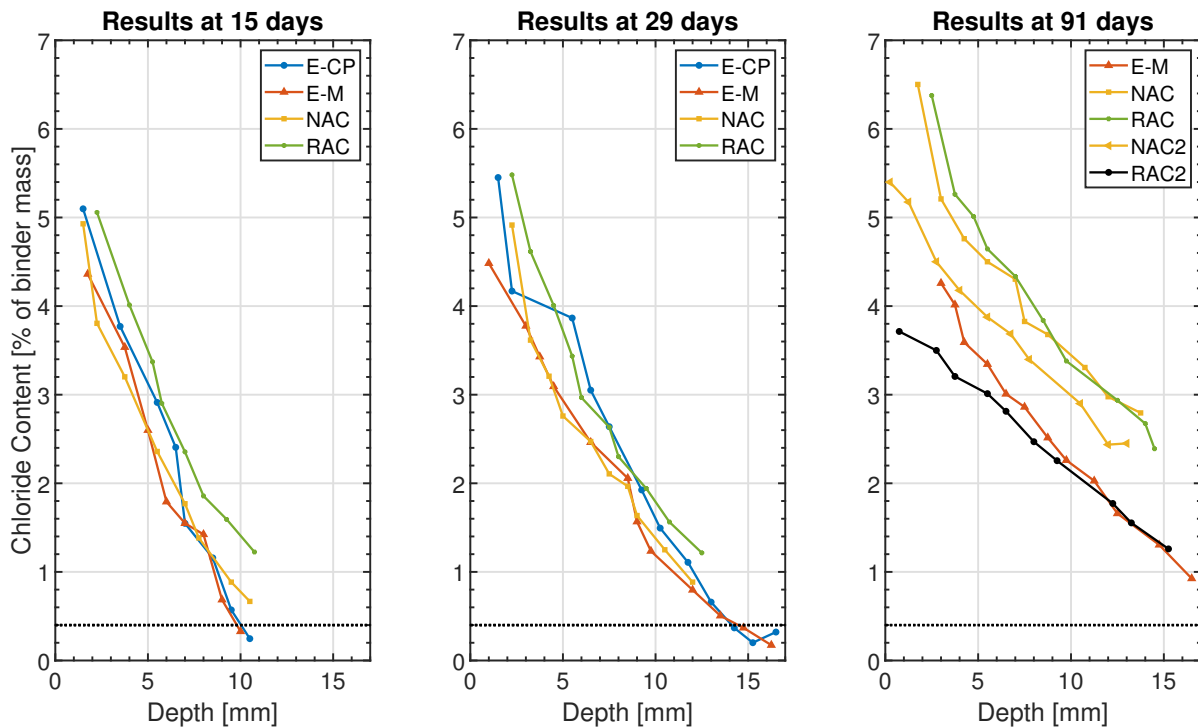
Figure 5.18: Results from the Chloride Diffusion under Unsteady-State experiment: evolution of the chloride content with respect to time and depth. The results have been corrected relatively to the mass of binder of each composition.

The chloride content is expressed as a percentage of the total mass in Figure 5.17. Thus, it appears reasonable that compositions with higher porosity have a greater chloride content.

The E-CP exhibits the highest concentration, followed by the E-M and RAC, and finally the NAC. Please note that the outcomes differ from those in steady-state.

Over time, the concentration of chloride on the surface increases until it reaches equilibrium with the solution, and the slope decreases due to an increase in concentration inside the sample.

On Figure 5.18, the percentage of binder mass is used to express the chloride content. Hence, all compositions are shifted inside the same spindle since the applied conditions are the same. Moreover, it should be noted that chloride ions are assumed to diffuse only inside the porous matrix paste. The sand and aggregates are impervious: therefore, only the cement content is permeable to chloride ions.

However, one composition partly follows this rule: the RAC. The cement content attached to the recycled concrete aggregates has been considered to adjust the chloride content regarding the mass of the binder.

Figures 5.19 to 5.22 illustrate the analyses conducted on the experimental findings for each composition. The surface concentration (C_s) and the apparent diffusion coefficient (D_{app}) are determined using Fick's second law, assuming an initial chloride content of zero. The equation below is fitted to the experimental points:

$$C(x,t) = C_s \left(1 - \text{erf} \left(\frac{x}{2\sqrt{D_{app}\, t}} \right) \right) \tag{5.5}$$

Table 5.4 presents a summary of the outcomes. The calculation of the depth at which the chloride content reaches 0.4% of the binder mass is included, in addition to the aforementioned parameter.

Composition	E-CP		E-M			NAC			RAC		
Time [day]	15	29	15	29	91	15	29	91	15	29	91
D_{app} [E-11 m^2/s]	1.63	1.51	1.71	1.43	0.92	1.81	1.44	2.93/1.58	2.46	1.65	1.78
C_s [% total mass]	4.15		1.45			0.78			1.27		
$X_{0.4\%t.m.}$ [mm]	12.1	16.2	11.9	15.1	21.5	12.3	15.2	38.4/28.2	14.8	16.9	31.1

Table 5.4: Apparent diffusion coefficient, surface concentration and threshold depth for each composition, obtained from the Fick analysis of the experimental results.

The diffusion coefficient is related to the slope of the curve. It is expected to decrease with time and this pattern is noted in the cement and mortar paste. Nonetheless, the two types of concrete examined do not follow this expected trend. Moreover, the variations observed within the same composition at different times are not particularly significant. When comparing the compositions, it is apparent that the diffusion coefficient of the RAC is the highest at 15 days, followed by the NAC, E-M, and lastly the E-CP. Although this result is unexpected, it is important to take into account the surface concentration when comparing diffusion coefficients. After 29 days, the RAC is still the most diffusive composition, followed by the E-CP, NAC, and lastly the E-M. The order of these compositions remains the same for the results obtained at 91 days.

Another area for comparison between our compositions is the surface concentration, which is determined by the level of chloride in the solution (3 mol of NaCl) and properties of the material, such as its porosity and dry density:

$$C_s[\%] = 106 \, [\text{kg/m}^3 \, \text{Cl}^-] \, \frac{n \, [\% \text{ volume}]}{\rho_d \, [\text{kg/m}^3]} \quad (5.6)$$

The E-CP mixture has the highest surface concentration among the four, owing to its greater porosity. The E-M and RAC exhibit similar levels of surface concentration, while the NAC has the lowest concentration, as anticipated. It should be mentioned that the surface concentration values were determined through fitting, and they all surpass the values calculated by Equation 5.6. One possible explanation is that the WAI may have underestimated the porosities that were calculated. Table 5.5 displays the experimental and theoretical values for both the porosity and surface concentration.

Mixture	Theoretical		Experimental		Difference
	C_s [% total mass]	n [% volume]	C_s [% total mass]	n [% volume]	
E-CP	3.34	45.6	4.15	56.7	+24.3%
E-M	1.18	22.6	1.45	27.8	+22.8%
NAC	0.67	14.4	0.78	16.65	+16.7%
RAC	1.06	20.7	1.27	24.8	+19.8%

Table 5.5: Comparison of the theoretical and experimental (obtained by fitting) surface concentrations.

Another interesting piece of information is the distance from the exposed surface at which the chloride content is equal to a threshold of 0.4% of the binder mass. This information is a combination of the two discussed above: the apparent diffusion coefficient and the surface concentration. Indeed, a greater surface concentration but a smaller apparent diffusion coefficient could still results in a deeper threshold position. The opposite could also happen. Indeed, if we compare the results at 15 days, the RAC is the worst composition, followed by the NAC, the E-CP and finally the E-M. At 29 days, the RAC is still the worst but followed by the E-CP, the NAC and finally the E-M. Finally, at 91 days, the NAC and RAC are competing for the worst position, depending on the experimental data set used.
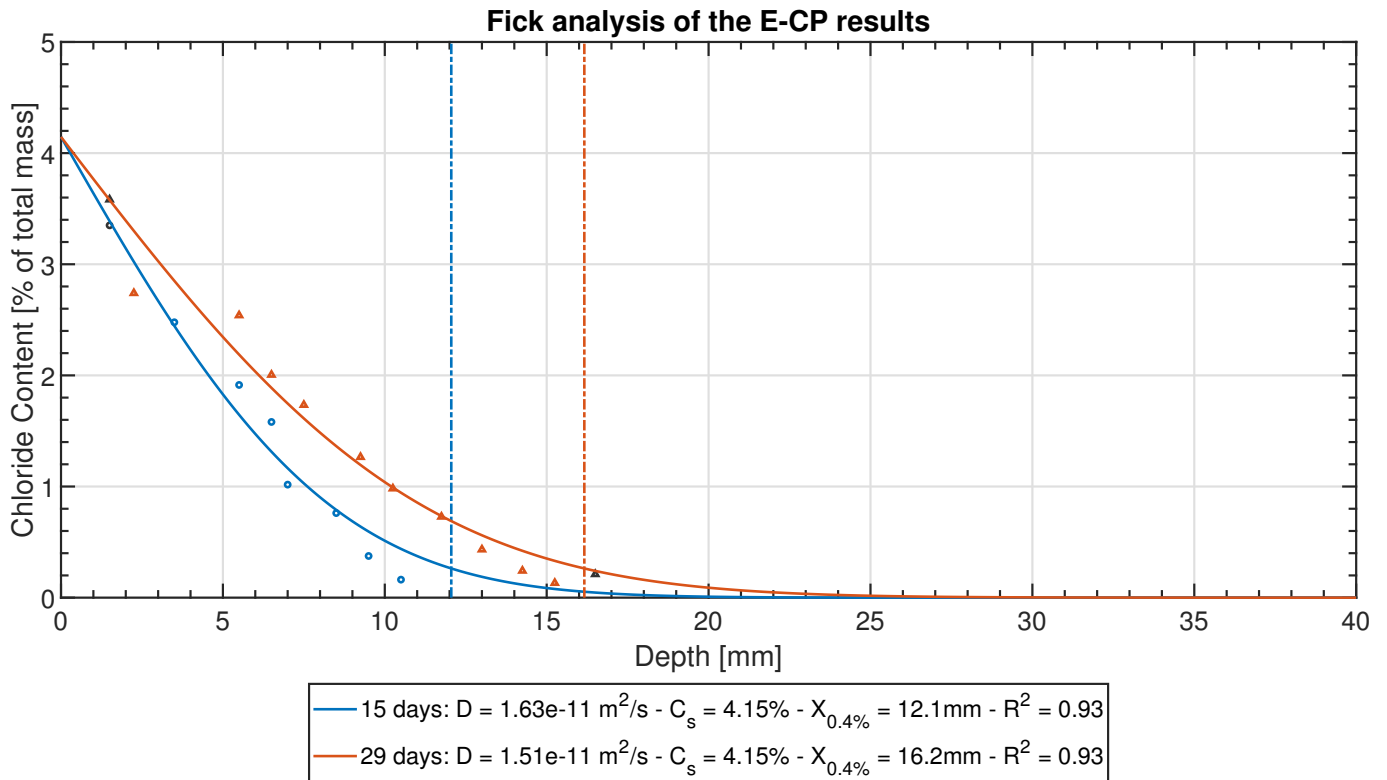
Figure 5.19: Analysis of the results for the E-CP: Fick's second law applied to determine the diffusion coefficient and the surface concentration.
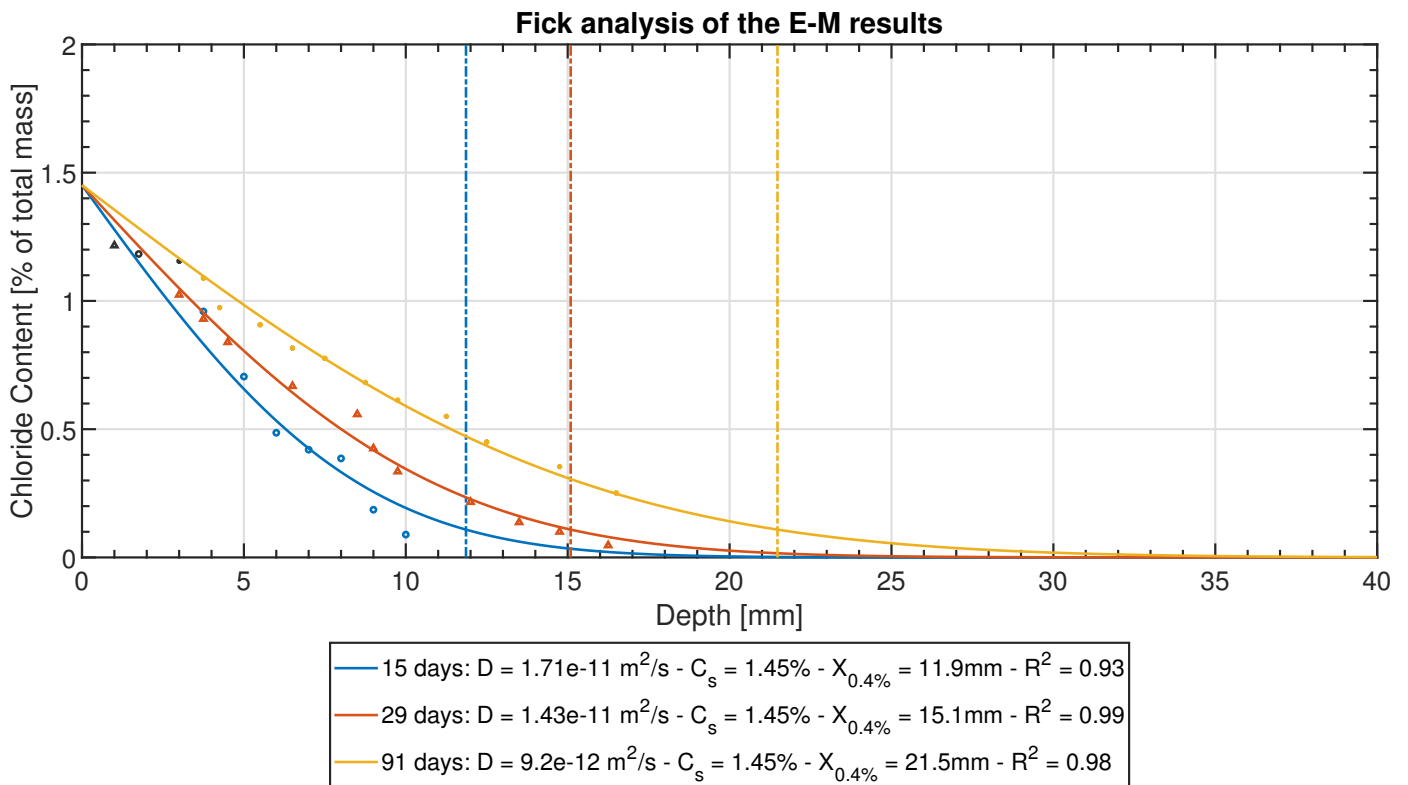
Figure 5.20: Analysis of the results for the E-M: Fick's second law applied to determine the diffusion coefficient and the surface concentration.
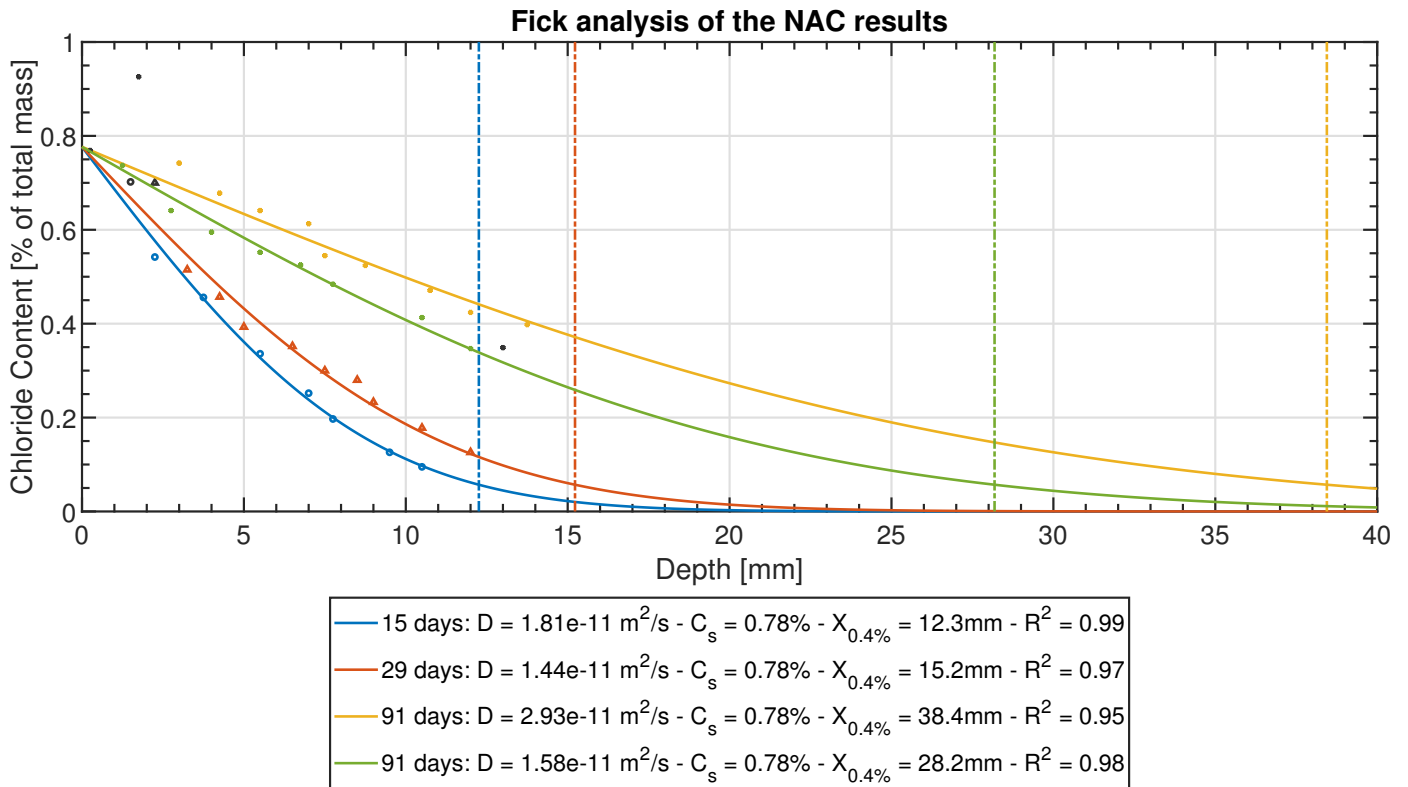
Figure 5.21: Analysis of the results for the NAC: Fick's second law applied to determine the diffusion coefficient and the surface concentration.
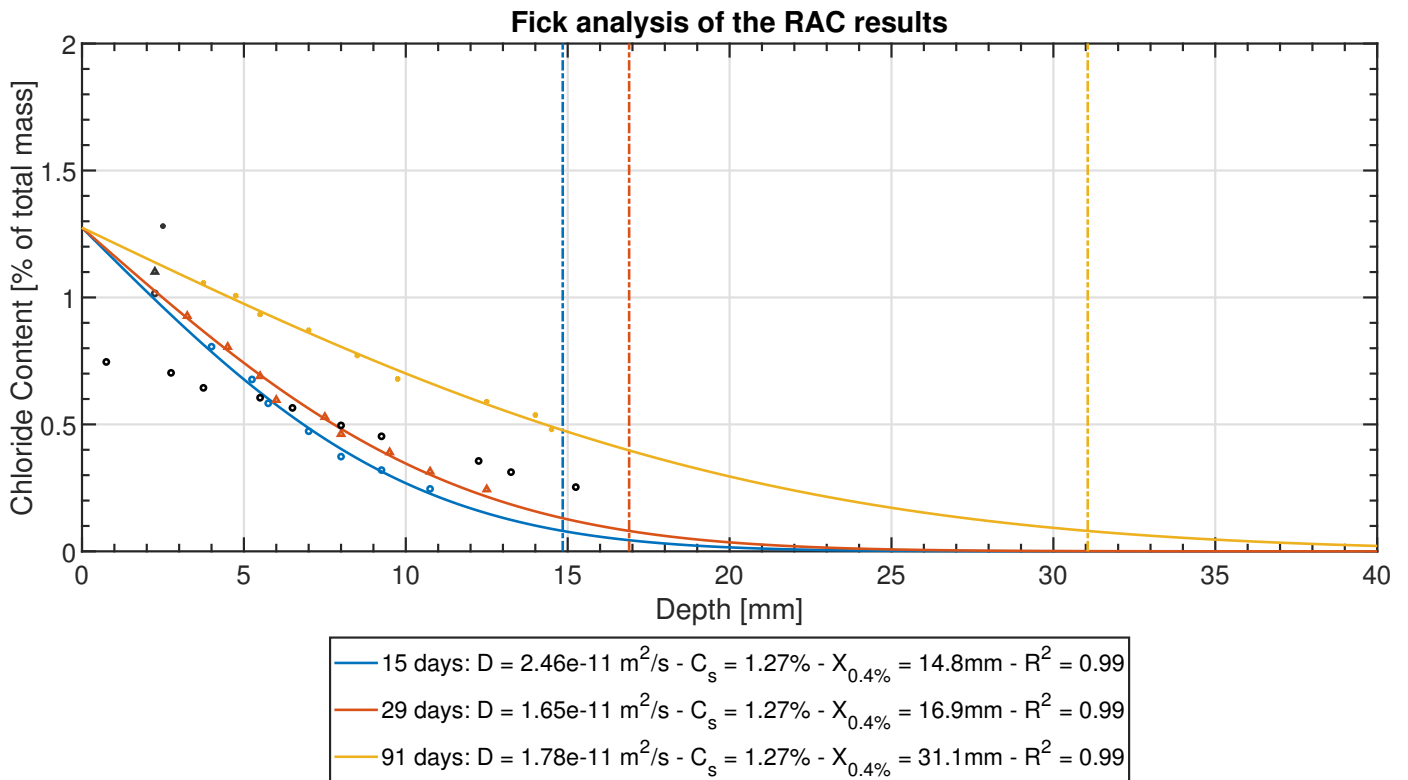
Figure 5.22: Analysis of the results for the RAC: Fick's second law applied to determine the diffusion coefficient and the surface concentration.

5.3.3 Chloride Adsorption Isotherms

For the investigation of chloride diffusion in an unsteady-state, the materials were ground into a fine powder before being titrated with an acidic solution to determine the concentration of chloride ions within the material. This acidic solution has the ability to dissolve any adsorbed chlorides, resulting in a concentration value that reflects the total chloride ions present, including both free and adsorbed forms.

The surplus powder, which was not used during the titration procedure, can be placed in water to dissolve only the free chlorides. This method allows for the determination of the concentration of free chloride ions present in our material, with the concentration of adsorbed chloride ions being subtracted from the total. Figure 5.23 displays the results obtained from this experiment.
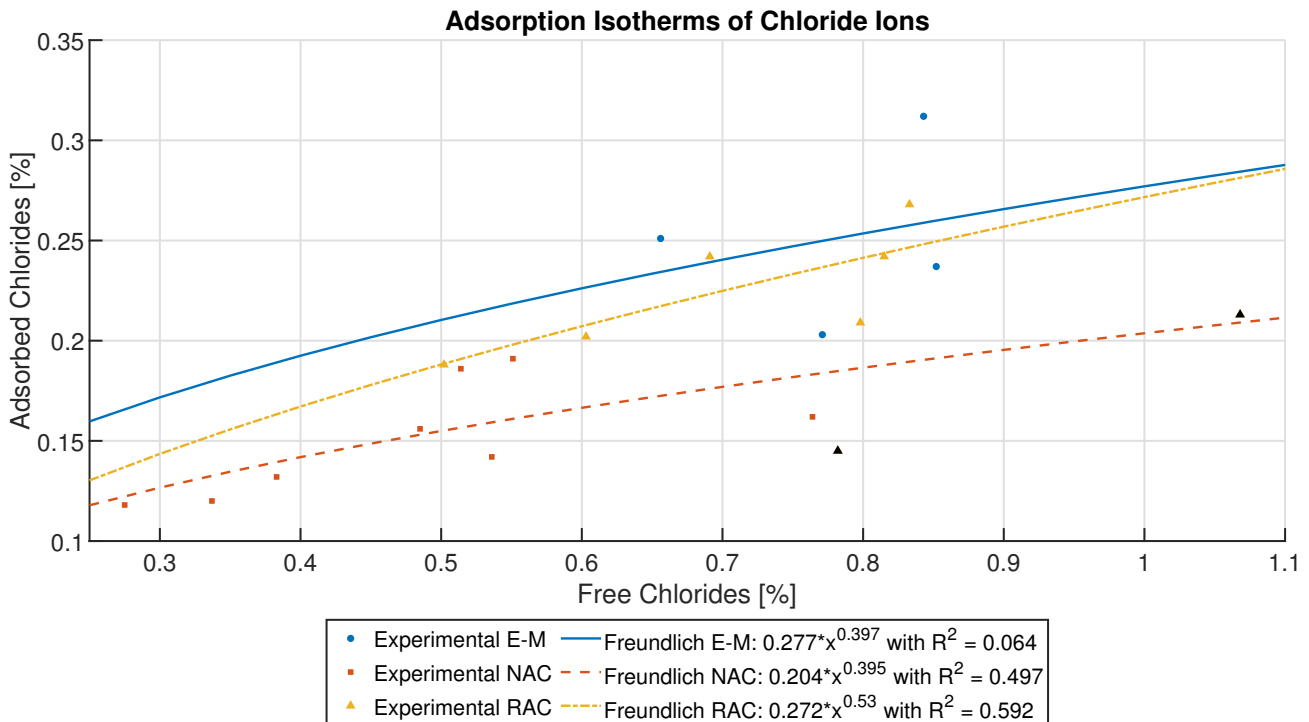
Figure 5.23: Chloride Adsorption Isotherms obtained with our chloride diffusion experiment under unsteady state.

The adsorption isotherms, which relate the amount of adsorbed chloride ions to the amount of free chloride ions, have been fitted with a Freundlich isotherm whose equation is [Yuan et al., 2009, Baroghel-Bouny et al., 2011, Spiesz et al., 2012]:

$$\text{Adsorbed Chlorides} = a \times \text{Free Chlorides}^{b} \tag{5.7}$$

Unfortunately, as can be seen in Figure 5.23, the results are not really meaningful. In fact, the value of R^2 obtained by fitting is about 50% for the NAC and 60% for the RAC. For E-M the results are even worse with a R^2 of 6%.

Focusing on the two concrete compositions, it appears that the RAC exhibits a greater adsorption phenomenon than the NAC. This could be attributed to the higher mortar content and the more intricate microstructure resulting from the substitution of aggregates.

5.3.4 Conduction

The experiment on conduction performed on our compositions gives qualitative results in terms of sensitivity to the diffusion of chloride ions. The temporal evolution of the intensity of the electric current passing through the sample is shown in Figure 5.24 for each composition. In terms of a qualitative perspective, the mortar (E-M) is more vulnerable to the penetration of chloride ions than the two concrete compositions. It is evident that the permeability of chloride ions is higher in concrete composed of recycled aggregates (RAC) compared to that made from natural aggregates (NAC), which was expected. Moreover, the RAC is more similar in current intensity to the E-M than the NAC, perhaps owing to its augmented paste content from the aggregate replacement.
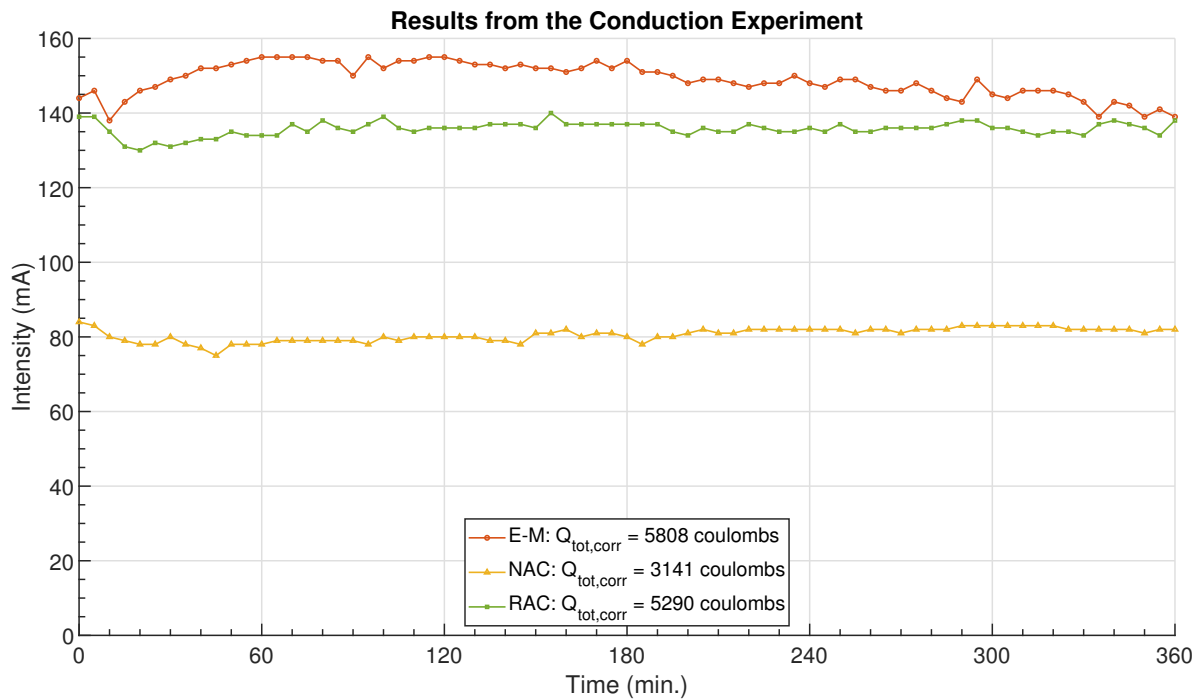
Figure 5.24: Results of the conduction experiment: evolution of the intensity with time and total charge passed.

The total charge that has passed through each sample can be compared quantitatively using Table 4.5. However, this table lacks precision, making the quantitative analysis less valuable than the qualitative one. The results in Table 5.6 align with the qualitative assessment, as the E-M and RAC compositions exhibit a high permeability class, while the NAC composition falls within a moderate permeability class.

Sample	Charge passed [Coulombs]	Chloride Permeability Class
E-M	5808 (>4000)	High
NAC	3141 (2000-4000)	Moderate
RAC	5290 (>4000)	High

Table 5.6: Comparison of the results from the conductivity experiment with the chloride permeability class from [Whiting, 1981].

5.4   Conclusion of the Experimental Results

The fundamental characteristics of our materials, as established by our complete experimental design, are presented in Table 5.7 underneath.

Property	E-CP	E-M	NAC	RAC
Dry Density [kg/m^3]	1463	2025	2263	2061
Saturated Density [kg/m^3]	1914	2253	2405	2266
Water Absorption [% Mass]	30.87	11.27	6.26	9.95
Porosity [% Volume]	45.01	22.83	14.16	20.50
Intrinsic Permeability [E-19 m^2]	3.82	38.7	1.73	2.58
n_{vG} (Desorption) [-]	1.51	1.51	1.53	1.48
n_{vG} (Sorption) [-]	1.50	1.49	1.51	1.51
α_{vG} (Desorption) [MPa]	10.95	11.55	13.83	10.43
α_{vG} (Sorption) [MPa]	3.84	2.75	3.45	3.56
Hysteresis b_1 [-]	-	0.8	0.85	0.75
Hysteresis b_2 [-]	-	1.1	1.2	1.2
D_{eff} [E-13 m^2/s]	6.22	8.17	5.99	15.4
D_{app} (29 days) [E-11 m^2/s]	1.51	1.43	1.44	1.65

Table 5.7: Summary of the experimental properties to be used for the modelling part of this thesis.

The general outcome of the experiment demonstrates that replacing natural aggregates with recycled concrete aggregates leads to a 59% increase in concrete's water absorption and a 45% increase in its porosity. Other research has found a similar ratio, up to two-to-one, for water absorption, which corroborates these results [Limbachiya et al., 2000, Thomas et al., 2013, Pedro et al., 2014a]. Furthermore, its intrinsic permeability rose by 49%.

In accordance, once again, with previous studies [Gonzalez & Etxeberria, 2014, Pedro et al., 2014a, Xuan et al., 2017, Qi et al., 2018, Russo & Lollini, 2022], the effective diffusion coefficient related to chloride ion diffusion exhibited a remarkable increase of 157%, while the apparent diffusion coefficient only rose by 15%. Additionally, the electrical conductivity of concrete also showed an increment of 40%.

Finally, the concrete with recycled aggregates exhibits a water retention curve which indicates the enhanced water exchange with the surroundings during both sorption and desorption processes. For a given material, the values of n_{vG} are similar for both sorption and desorption.

Multiscale Modelling of Chloride Ingress

6

MULTISCALE MULTIPHASIC MODELLING

Contents

6.1 Introduction

Once the experimental phase of this thesis has been completed, the second primary objective of this work is the development of a model that encompasses the material heterogeneities of concrete. This will enable a better understanding of the effect of that substitution. In this context, a multiscale model represents the optimal approach. The definition of a second smaller scale that accurately represents the aggregates in concrete would allow for an easier sensitivity analysis and change of parameters than a single scale model, where a new experimental campaign would be required for every change of aggregates.

This chapter presents the theoretical framework for the multiscale multiphasic modelling conducted in this research. It begins with an introduction to multiscale modelling, specifically the Finite Element Square Method (FE²) used in this work. The model's constitutive equations for water, gas, and chloride flows are then presented for both the mesoscale and macroscale. Additionally, the model accounts for the hysteresis of the Water Retention Curves, which is also presented in this section. Then, this section focuses on modelling the Representative Volume Element (RVE). Finally, the code is parallelised using OpenMP.

6.2 Finite Element Square (FE^2) Method

6.2.1 Introduction to Multiscale Modelling

The heterogeneity of concrete is well known: its constituents range from nanometre-sized pores to centimetre-sized aggregates [Garboczi & Bentz, 1998]. The addition of recycled concrete aggregates enhances this heterogeneity by increasing the number of different materials present. This is the reason why it is computationally impossible to model the entire microstructure of concrete.

One solution is to homogenise its properties over some spatial scale, using a sort of global-local analysis. Multiscale modelling, combined with numerical homogenisation techniques, has been developed to allow homogenisation of the properties at a smaller scale, to be scaled up later, and to keep the computational cost acceptable [Nilenius et al., 2013, Nilenius et al., 2014, Marinelli et al., 2016, Desrues et al., 2019, Bertrand, 2020]. Two material scales are therefore used in this approach:

- Macroscale: the material is assumed to be homogeneous and the constitutive laws must therefore represent the overall behaviour of the material. Mixture theory (Section 2.3) is often used to introduce multiple phases (e.g. liquid water and water vapour) percolating through the porous medium [Bowen, 1980, Bear & Verruijt, 1987]. Models based on this single scale have a disadvantage: any change in the microstructure (e.g. a change in constituents) requires a new experimental campaign to update the homogenised properties of the material.

- Mesoscale: the entire material structure is represented in the model, including the heterogeneities (e.g. aggregates). It is often composed of voids, aggregates, a mortar matrix and interfacial transition zones [Xiong et al., 2020]. Each constituent has its own constitutive equations and set of properties. A model could be based solely on this scale, which would increase the accuracy of the response, but the computational cost is quite high and is therefore not appropriate for metre-scale engineering structures.

Several homogenisation techniques have been developed in the literature, either analytical [Bensoussan et al., 1978] or numerical [Smit et al., 1998, Massart et al., 2006]. The homogenisation technique implemented in this model is considered as numerical homogenisation: it is formally called the unit cell method, based on the concept of the Representative Volume Element (RVE) [Smit et al., 1998, Kouznetsova et al., 2001, Özdemir et al., 2007, Marinelli et al., 2016]. This RVE represents the mesoscale, the volume that must contain all the required material heterogeneities. The material properties and behaviour at the macroscale are then obtained from the modelling of this RVE [Smit et al., 1998, Kouznetsova et al., 2001, Özdemir et al., 2007, Samson & Marchand, 2007, Marinelli et al., 2016, Bertrand, 2020].

Numerous multiscale numerical tools have been developed in recent years. In civil engineering, where real-scale engineering problems are studied, the continuum approach of the Finite Element Method is highly appropriate for the macroscale. For the mesoscale, several options are available, which range from Finite Element Methods [Marinelli et al., 2016, Bertrand, 2020] to Discrete Element Methods [Nitka et al., 2011, Desrues et al., 2019]. The former approach is more appropriate when studying couplings, such as chemo-thermo-hydraulic couplings, as opposed to the latter, which is better suited for solid mechanics and the intricate behaviour of granular materials, including friction, dilatancy, and anisotropy. Therefore, we have opted to utilise the FE^2 method, also referred to as FEM-FEM, to develop our model, as the durability of concrete is dependent on the flow of water and gas, amongst other.

A specificity of the FEM at the macroscale is that the material properties and behaviour are only known at the macroscopic integration points, due to the homogenisation of the RVE results [Smit et al., 1998, Kouznetsova et al., 2001]. In fact, the integration points of the discretised homogenised macrostructure are bound to a RVE and the finite element computations are performed for each RVE independently, assuming a periodicity of the microstructure near the integration point.

The developed model is a multi-physics FE^2 model, accurately representing water and gas flow, as well as advection and diffusion of chloride ions within a porous system, such as concrete. In the multiscale approach, appropriate averages over the mesoscale must replace macroscopic phenomenological quantities of interest, including storage terms and flow quantities. The constitutive equations, namely Darcy's and Fick's laws among others, are used at the mesoscale. In addition, homogenisation and localisation equations are employed to derive the macroscopic flows based on the phenomenological quantities of interest at the mesoscale. This process demands a significant space and time scale separation between the mesoscale and macroscale: the diffusion problem must be solved under steady-state conditions at the mesoscale [Özdemir et al., 2007].

The numerical double-scale method employed in this thesis can be summarised by four iterative steps performed on each Gaussian point of the macroscale mesh until the two scales converge [Massart et al., 2006, Özdemir et al., 2007, Nilenius et al., 2014, Bertrand, 2020]:

1. Localisation: the macroscale boundary conditions are localised at each gauss point and transformed into gradients and mean values (e.g. water and gas pressures, chloride concentration, ...), which are passed on as mesoscale boundary conditions;

2. Resolution of the mesoscale boundary value problem by finite element analysis;

3. Homogenisation: the fluxes obtained at each mesoscale integration point are homogenised to obtain a unique value per macroscale Gauss point;

4. Resolution of the macroscale boundary value problem by finite element analysis.

This iterative process is represented in the Figure 6.1.
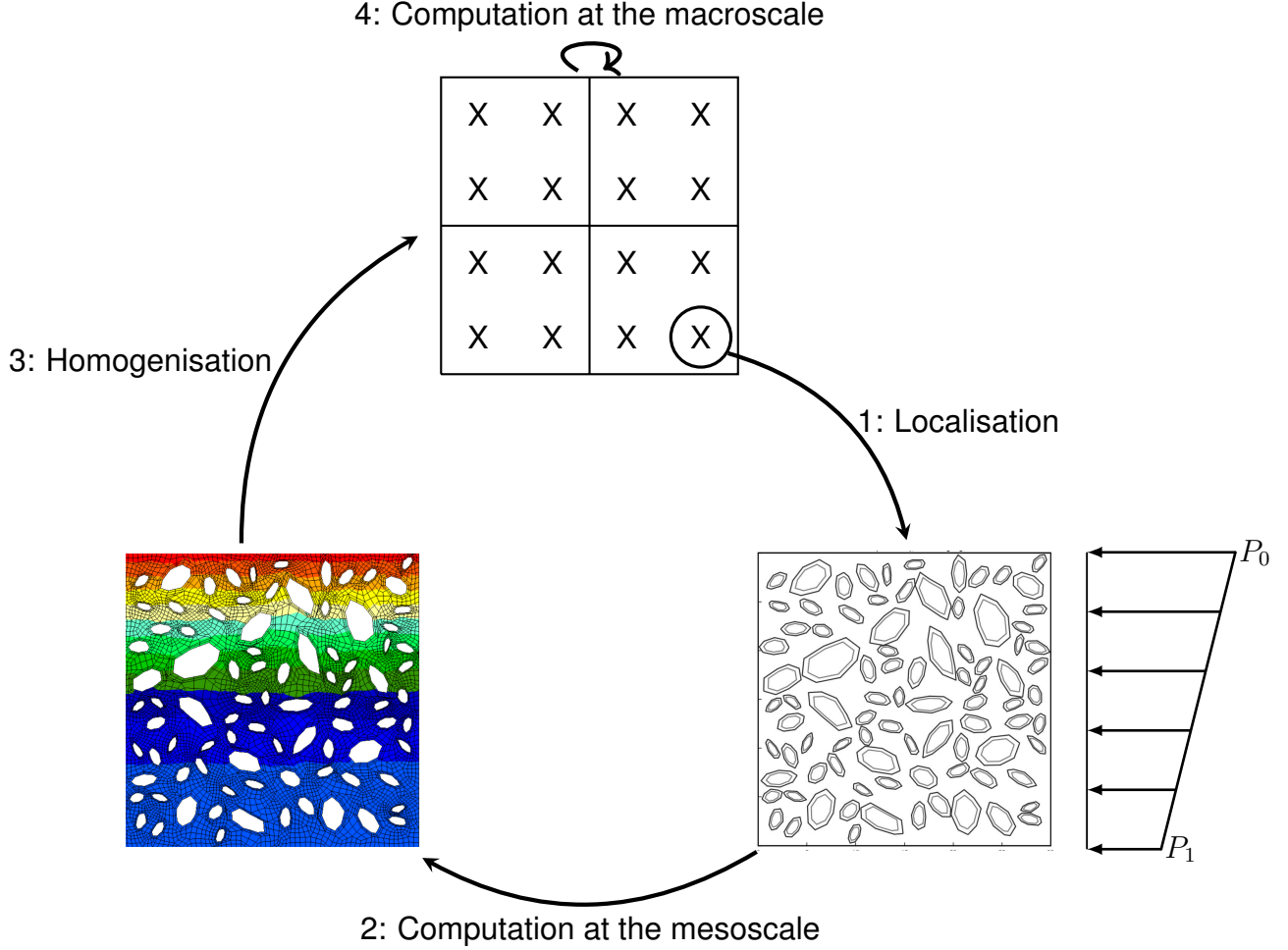
Figure 6.1: Representation of the iterative process performed on each Gauss point of the mesh during the multiscale computation.

6.2.2 General Multiscale Formulation

The multiscale modelling approach couples a subscale, referred in this work as the mesoscale, and a macroscale. The macroscale component ϕ^M and the subscale component ϕ^s of each scalar field ϕ are added together while the subscale portion defines the fluctuations of the total scalar field [Özdemir et al., 2007, Nilenius et al., 2013, Nilenius, 2014, Bertrand, 2020]:

$$\phi(x, \bar{x}) = \phi^M(x, \bar{x}) + \phi^s(x) \tag{6.1}$$

On the boundaries of the Representative Volume Element, denoted as Γ, the subscale component ϕ^s is considered to be zero, leading to $\phi = \phi^M$. Therefore, we can utilise a Taylor expansion to establish the macroscale scalar field. Within the macroscale continuum, the expansion can be restricted to its first order using the homogenisation technique's assumption of a linear variation of ϕ^M inside the RVE:

$$\phi^M(x, \bar{x}) \approx \bar{\phi}(\bar{x}) + \bar{g}(\bar{x}) \times (x - \bar{x}) \quad \forall x \in \Omega \tag{6.2}$$

where $\bar{x}$ represents the centre of the RVE, and $\bar{g}$ denotes a gradient that is defined by:

$$\bar{g}(\bar{x}) = \text{grad } \bar{\phi}\,(\bar{x}) \tag{6.3}$$

The Taylor expansion is illustrated in Figure 6.2 for a 1D RVE. Equation 6.2 represents the localisation step performed in the FE² algorithm, as depicted in Figure 6.1.

In the subscale, it is not always certain that the scalar field will exhibit continuity. As a result, the higher order terms of the Taylor expansion are significant and cannot be ignored. To account for changes in material properties, a fluctuation field $\phi^f = \phi^s$ is thus substituted [Özdemir et al., 2007, Nilenius et al., 2013]:

$$\begin{aligned}\phi(x, \bar{x}) &= \phi^M(x, \bar{x}) + \phi^f(x)\\ &= \bar{\phi}(\bar{x}) + \bar{g}(\bar{x}) \times (x - \bar{x}) + \phi^f(x)\end{aligned} \tag{6.4}$$
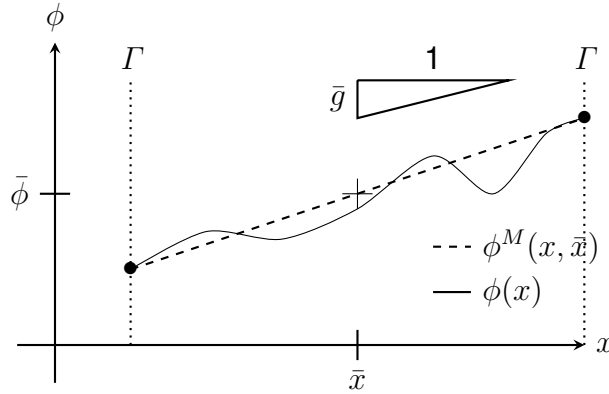
Figure 6.2: Illustration of the Taylor expansion limited to its first order, for a 1D RVE domain Ω (modified from [Nilenius et al., 2014]).

However, it is essential that both the macroscale and the subscale components of the scalar field are identical at all points on the macroscale. Hence:

$$\bar{g}(\bar{x}) \times (x - \bar{x}) + \phi^f(x) \ll \bar{\phi}(\bar{x}) \tag{6.5}$$

where the concept of separation of scales arises. It is required that the subscale's characteristic length (l_c^s) is negligible compared to the macroscopic field's characteristic fluctuation length (L_c^M) [Kouznetsova et al., 2002, Özdemir et al., 2007, Bertrand, 2020].

$$l_c^s \ll L_c^M \tag{6.6}$$

First-order homogenisation techniques require the verification of this assumption. If it is unverified, the local macroscale gradients cannot determine the boundary conditions of the subscale.

The transition from the subscale back to the macroscale, namely numerical homogenisation as depicted in Figure 6.1, necessitates the transfer of the flux. Under stationary conditions, the mass balance equation writes [Özdemir et al., 2007, Nilenius et al., 2013, Bertrand, 2020]:

$$\boldsymbol{\nabla} J = 0 \quad \text{in } \Omega \tag{6.7}$$

where J is the homogenised flux and Ω is the domain occupied by the RVE, where the material heterogeneities are embedded.

The scalar field division and first-order homogenisation thus enable the determination of the volume average $\bar{J}$ of the flux within the RVE:

$$\bar{J} = \frac{1}{|\Omega|} \int_\Omega J(x) \, d\Omega \tag{6.8}$$

that is the macroscale flux.

6.2.3 Finite Element Formulation

This section presents the finite element formulation and the spatial and temporal discretisation schemes used in this thesis. For more information on the discretisation of the equilibrium equations, see the work of Collin (2003) [Collin, 2003].

The isoparametric elements of the Serendipity type are used for both the macroscale and mesoscale. These elements can be seen in Figure 6.3. The geometry and discretised fields, including water and gas pressure, chloride concentration and temperature, are defined by their nodal values using N interpolation functions [Martin-Perez et al., 2001, Collin et al., 2002]. The elements are expressed in the local coordinate plane (ξ, η), which simplifies their analytical expression and volume integration [Collin et al., 2002].

Each node has six degrees of freedom (DOF): X and Y positions, water and gas pressures, chloride content and temperature. However, this thesis does not consider the mechanical nor the thermal aspects, so the two mechanical and the thermal DOFs are fixed for all nodes.
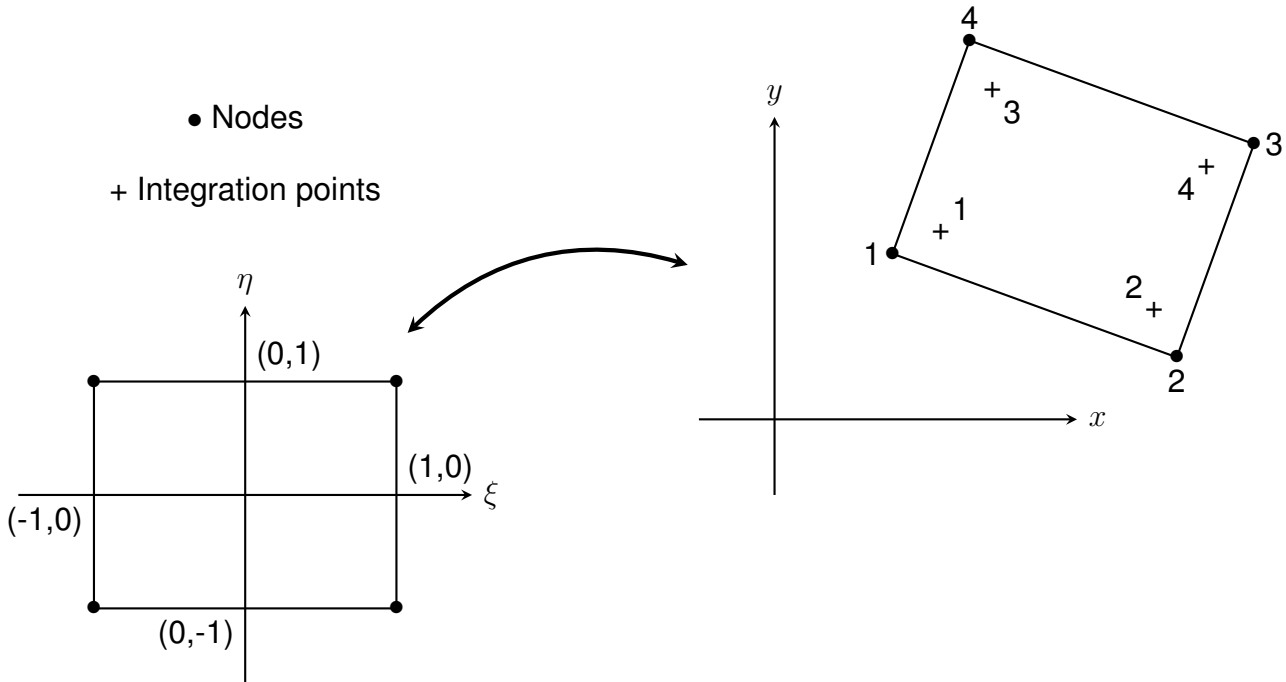
Figure 6.3: Isoparametric element with 4 nodes and 4 Gauss points.

The coordinates, displacements, velocities, pressures, and temperature of the element are expressed as a function of their nodal values using the same interpolation functions [Collin

et al., 2002]:

$$x_i = N_L \, X_{L,i} \quad \text{and} \quad p = N_L \, P_L \tag{6.9}$$

for example, where L ranges from 1 to the number of nodes in the element (4 in this case).

Apart from the spatial discretisation, the temporal discretisation intervenes directly in the problem by defining time steps, i.e. temporal finite elements. A time step is defined by two moments, which we denote as A and B. We assume that the DOF vary linearly over the time step, whether at any point or at a node [Collin, 2003]:

$$t = (1 - \theta) \, t^A + \theta \, t^B \tag{6.10}$$

$$DOF_i = (1 - \theta) \, DOF_i^A + \theta \, DOF_i^B \tag{6.11}$$

where θ ranges from 0 to 1, and DOF_i represents one of the six DOF presented before.

Henceforth, the derivative of the degree of freedom with respect to time is reduced to a pattern similar to that of finite differences:

$$\frac{d \, DOF_i}{dt} = \frac{DOF_i^B - DOF_i^A}{t^B - t^A} = \frac{\Delta DOF_i}{\Delta t} \tag{6.12}$$

To ensure that the balance equations are respected throughout the entire time step, we use the weighted residue method with a time-varying weighting function. This function is chosen to be reduced to a collocation. The value of θ is based on this collocation and the precision and stability it can achieve. The implicit scheme (θ = 1) and Galerkin scheme (θ = 2/3) are the most commonly used schemes for this purpose [Collin, 2003].

6.3 Constitutive Equations of the Model

The multiscale model has been created to cater for both saturated and unsaturated scenarios. At the macroscale, three degrees of freedom, i.e. water pressure, gas pressure and chloride concentration, are defined and used as boundary conditions. Afterwards, gradient and mean values of aforementioned degrees of freedom are conveyed to the RVE for every Gauss point. Based on these localised boundary conditions, a value of the water pressure, gas pressure and chloride concentration is assigned to each integration point of the subscale. The boundary value problem at the subscale can then be resolved.

6.3.1 Mesoscale Water Flows

The mass balance equation of liquid water inside the porous matrix of concrete, in a fixed and underformable system, under the hypothesis of steady-state, is:

$$\frac{\partial}{\partial x_i} (\rho_w \, v_i^w) = 0 \tag{6.13}$$

where ρ_w is the water density [kg/m³] and v_i^w is the fluid flow rate per unit area [m/s].

The first factor of the Equation 6.13, that is the water density, varies with the mean water pressure:

$$\rho_w = \rho_{w0} \times \left(1 + \frac{P_{w,average} - P_{w0}}{\chi_w} \right) \tag{6.14}$$

where ρ_{w0} [kg/m³] is the initial density of liquid water, $P_{w,average}$ [Pa] is the mean pressure at the macroscale integration point and P_{w0} [Pa] is the initial pressure inside the porous structure (pressure at which ρ_{w0} was calculated). This relation is also dependent on the fluid bulk modulus, noted χ_w [Pa] (at 20°C, $\chi_w = 2 \ 10^9$ Pa).

The second factor of the Equation 6.13 expresses the liquid water flow. The Darcy's law is used to describe this movement of liquid water inside the porous medium. Under the hypothesis of a homogeneously permeable medium, in presence of gravitational forces, the fluid flux and the gradient of water pressure are directly proportional:

$$v_i^w = -\frac{k_{int} \ k_{rel,w}}{\mu_w} \left(\frac{\partial P_w}{\partial \ x_i} + \rho_w \ g_i \right)$$
(6.15)

where k_{int} [m²] is the intrinsic permeability of the porous matrix and $k_{rel,w}$ [-] is the water relative permeability, μ_w [Pa.s] is the dynamic viscosity of water and $(\partial P_w)/(\partial x_i)$ is the gradient of water pressure. The gravity term is only accounted for along the y-axis, with $\vec{g}$ [m/s²] the vector that accounts for the gravitational acceleration. In two dimensions, $\vec{g}$ is equal to $[0, -9.81]$.

The relative permeability $k_{rel,w}$ is dependent on the degree of saturation of the porous matrix (noted $S_{r,w}$), as pores filled by air reduce the sectional area available to water flow [Collin et al., 2002]. It is theoretically equal to 0 in perfectly dry conditions, or equal to 1 in saturated conditions. The empirical equation used to express this relative permeability is the one of Van Genuchten [Van Genuchten, 1980]:

$$k_{rel,w} = \sqrt{S_{r,w}} \times \left(1 - \left(1 - S_{r,w}^{1/m_{VG}} \right)^{m_{VG}} \right)^2$$
(6.16)

where $S_{r,w}$ [-] is the degree of saturation in liquid water of the porous medium and m_{VG} [-] is a model parameter associated to the curvature of the water retention curve [Fanara et al., 2022]. The degree of saturation is also obtained by an empirical equation from Van Genuchten [Van Genuchten, 1980]:

$$S_{r,w} = S_{res} + (S_{sat} - S_{res}) \left(1 + \left(\frac{s}{\alpha_{VG}} \right)^{n_{VG}} \right)^{-m_{VG}}$$
(6.17)

where n_{VG} [-] is another model parameter related to the rate of desaturation of the porous system (equal to $1/(1-m_{VG})$) and α_{VG} [Pa] is the air-entry pressure. Two other parameters, S_{res} [-] and S_{sat} [-] are, respectively, the residual saturation of the medium (often equal to 0) and the maximum saturation of the medium (often equal to 1). Finally, the suction s [Pa] is the matrix suction defined as the difference between the gas pressure and the liquid water pressure:

$$s = p_g - p_w$$
(6.18)

6.3.2   Mesoscale Gas Flows

The mass balance equation of gaseous air inside the porous matrix of concrete, under the same hypothesis as for the water, is:

$$\frac{\partial}{\partial \ x_i} \left(\rho_g \ v_i^g \right) = 0$$
(6.19)

where ρ_g is the air density [kg/m³] and v_i^g is the gas flow rate per unit area [m/s].

The first term of the Equation 6.19, that is the gas density, varies with the mean gas pressure of the matrix:

$$\rho_g = \rho_{g0} \times \left(\frac{P_{g,average}}{P_{g0}} \right) \tag{6.20}$$

where ρ_{g0} [kg/m³] is the initial density of gaseous air, $P_{g,average}$ [Pa] is the mean gas pressure at the macroscale integration point, and P_{g0} [Pa] is the initial gas pressure inside the porous structure (pressure at which ρ_{g0} was computed).

The second factor of the Equation 6.19 expresses the gaseous air flow. The Darcy's law is also used to describe this movement of gaseous air inside the porous medium. Under the same assumptions as for the liquid water, the gas flux writes:

$$v_i^g = -\frac{k_{int}\, k_{rel,g}}{\mu_g} \left(\frac{\partial P_g}{\partial x_i} + \rho_g\, g_i \right) \tag{6.21}$$

where k_{int} [m²] is the intrinsic permeability of the porous matrix and $k_{rel,g}$ [-] is the gas relative permeability. The term μ_g [Pa.s] is the dynamic viscosity of the gas and $(\partial P_g)/(\partial x_i)$ is the gradient of pressure.
The gravity term is only accounted for along the y-axis, with $\vec{g}$ [m/s²] the vector that accounts for the gravitational acceleration. In two dimensions, $\vec{g}$ is equal to $[0, -9.81]$.
The relative permeability of gas is computed with the same equation as for the relative permeability of water based on the principle that the porous matrix must be completely filled with water and gas. Therefore the addition of the degree of saturation of liquid water and the one of gaseous air must be equal to one [Van Genuchten, 1980]:

$$k_{rel,g} = \sqrt{1 - S_{r,w}} \times \left(1 - S_{r,w}^{1/m_{VG}} \right)^{2\, m_{VG}} \tag{6.22}$$

A component of dissolved air could be taken into account in the model, as well as a component of water vapour [Collin et al., 2002]. However, at this stage in the development of the model, these two species have not been implemented.

6.3.3 Mesoscale Chloride Ingress

The balance equation of the chloride ions is:

$$\frac{\partial}{\partial x_i}(v_i^c) = 0 \tag{6.23}$$

where v_i^c [m/s] is the chlorides flow rate per unit area.

The chlorides flow rate can be caused by an addition of three phenomena: advection, dispersion and diffusion [Biver, 1993, Nagesh & Bhattacharjee, 1998, Ababneh et al., 2003, Baroghel-Bouny et al., 2011, Liu et al., 2015, Wu et al., 2017, Chen et al., 2019, Di Pillo & Todisco, 2020]. The first one is a movement of the chlorides inside water due to water flows. The second one is due to the irregularity of the porous system, causing a local variation of

the concentration. The last one is due to a gradient of concentration inside the fluid itself. One can therefore write:

$$v_i^c = v_i^{\text{advection}} + v_i^{\text{diffusion+dispersion}}$$
$$= C_M \, v_i^w - D \, \frac{\partial \, C_m}{\partial \, x_i} \tag{6.24}$$

where C_M [-] and C_m [-] are, respectively, the concentration in chloride ions at the macroscale and mesoscale integration points, v_i^w [m/s] is the water velocity obtained with Darcy's law and D [m^2/s] is the diffusion and dispersion coefficient, obtained experimentally. The contribution due to convection is calculated at the macroscale, based on the homogenised water flows, as explicited in Equation 6.27. This is due to the hypothesis of this model, which postulates that the mesoscale problem is solved under steady-state conditions. The solution of the boundary value problem with diffusion and convection at the mesoscale would create oscillations and not converge due to the incompatibility of the diffusion and convection boundary conditions. In order to achieve convergence, and in accordance with the steady-state hypothesis, the convection of chloride ions is solved at the macroscale.

6.3.4 Homogenised Macroscale Response

The constitutive equations explained above for the mesoscale solution are solved following a fully coupled finite element scheme, with analytical stiffness matrices. The mesoscale fluxes are thus obtained as a solution of the boundary value problem solved. They are then homogenised numerically: the fluxes of each mesoscale integration point are summed proportionally to their relative area. The homogenised flow, after being transmitted to the macroscale point of integration, is used to calculate the macroscale internal fluxes.

The mass balance equations for the multiple species (water, gas and chloride ions) occupying the pore space of the macroscale are the following, respectively:

$$\frac{\partial}{\partial x_i} \left(\rho_w \times v_{i,\text{homogenised}}^w \right) + \frac{\partial S_w}{\partial t} = 0 \tag{6.25}$$

$$\frac{\partial}{\partial x_i} \left(\rho_g \times v_{i,\text{homogenised}}^g \right) + \frac{\partial S_g}{\partial t} = 0 \tag{6.26}$$

$$\frac{\partial}{\partial x_i} \left(C_M \times v_{i,\text{homogenised}}^w + v_{i,\text{homogenised}}^c \right) + \frac{\partial S_c}{\partial t} = 0 \tag{6.27}$$

where one recognizes the spatial variation of the flux and the temporal variation of the storage, for each species. The homogenised water, gas and chloride ions fluxes are obtained through the spatial homogenisation of the flux computed at the mesoscale, proportionally to the relative surface of the RVE, as explained hereabove. The storage terms, on the other hand, are computed by calculating the total mass of each species over the RVE, at each given time. For the chloride ions, the coupling between the water flows and the chloride advection is expressed at the macroscale, by multiplying the homogenised water flows and the mean macroscale concentration in chloride ions.

The elementary stiffness matrix of the macroscale problem is obtained through the classical perturbation method [Özdemir et al., 2007, Nitka et al., 2011, Marinelli et al., 2016, Bertrand, 2020], unlike that of the mesoscale which is analytical. The gradients and mean values of

water and gas pressure, as well as chloride concentration, are perturbed in sequence, after which the stiffness matrix is computed for the macroscale based on these perturbations:

$$K_{i,j} = \frac{\mathsf{Flux}_{i,\mathsf{perturbated}} - \mathsf{Flux}_{i,\mathsf{original}}}{\mathsf{Perturbation}_j} \tag{6.28}$$

The method is time-consuming since it necessitates solving mesoscale calculations ten times. Nevertheless, it is imperative to obtain a consistent tangent operator as the problem is highly non-linear.

6.3.5 Hysteresis of the Water Retention Curve

The Water Retention Curve expresses the evolution of the saturation degree with suction, accounting for unsaturated conditions as shown in Equations 6.22, 6.16 and 6.17 for the relative permeability of gas, water, and the water saturation degree respectively. The empirical model employed is the Van Genuchten model [Van Genuchten, 1980]. As a reminder, the saturation degree is expressed according to this equation:

$$S_e = S_{res} + (S_{sat} - S_{res})\left(1 + \left(\frac{s}{\alpha_{vG}}\right)^{n_{vG}}\right)^{-m_{vG}} \quad \text{with} \quad m_{vG} = 1 - \frac{1}{n_{vG}} \tag{6.29}$$

where n_{vG} [-] is an adimensional model parameter related to the rate of desaturation of the porous system and m_{vG} [-] is another adimensional model parameter related to the curvature (slope) of the water retention curve. The last model parameter, denoted α_{vG} [Pa], is related to the air-entry pressure [Fanara et al., 2022]. Finally, one can see the maximum saturation S_{sat} [-] and the residual saturation S_{res} [-], as well as the suction s [Pa].

The concept of suction was introduced in Section 2.3.2 where the concept of water retention curve was explained. The phenomenon of hysteresis was also introduced: depending on the evolution trend of the environmental conditions, that is either sorption or desorption, the water retention curve is not identical [Bear & Verruijt, 1987]. Two phenomena can explain this hysteresis: the ink-bottle effect, where water re-entering narrow pores requires a local increase in suction, and the raindrop effect, due to the difference in contact angle between an advancing and a retreating interface [Bear & Verruijt, 1987]. Depending on the history of the material, an infinity of paths can be defined, in between the two main scanning curves.

Various methods for defining hysteresis have been described in the literature [Kool & Parker, 1987, Kohgo, 2008, Zhou et al., 2012]. Zhou et al. (2012) proposed a method for the Van Genuchten model [Zhou et al., 2012]. The main scanning curves of the water retention curves, as defined by Equation 6.29, can be written specifically for the drying curve (with a suffix d) and for the wetting curve (with the suffix w), according to that model:

$$S_{ed} = S_{res} + (S_{max} - S_{res})\left[1 + \left(\frac{s}{\alpha_d}\right)^{n_d}\right]^{-m_d} \tag{6.30}$$

$$S_{ew} = S_{res} + (S_{max} - S_{res})\left[1 + \left(\frac{s}{\alpha_w}\right)^{n_w}\right]^{-m_w} \tag{6.31}$$

The scanning curves (suffix s) are then defined by [Zhou et al., 2012]:

$$\frac{\partial S_{ew,s}}{\partial s} = \left(\frac{s_w}{s}\right)^b \left(\frac{\partial S_{ew}}{\partial s}\right) \quad \text{with } s_w = \alpha_w \left(S_e^{-1/m_w} - 1\right)^{1/n_w} \tag{6.32}$$

$$\frac{\partial S_{ed,s}}{\partial s} = \left(\frac{s_d}{s}\right)^{-b} \left(\frac{\partial S_{ed}}{\partial s}\right) \quad \text{with } s_d = \alpha_d \left(S_e^{-1/m_d} - 1\right)^{1/n_d} \tag{6.33}$$

where the parameter b [-] is defined as a fitting parameter, always positive. It influences the gradient of the scanning curve, the closer it gets to zero and the closer the hysteresis curve is to the main curve, while the greater it is and the more horizontal the hysteresis curve gets [Zhou et al., 2012].

The final saturation degree may then be obtained thanks to the derivative defined above and the increment in suction (ds) applied:

$$S_e^t = S_e^{t-1} + \left(\frac{\partial S_{e,s}}{\partial s} \right) \times ds \tag{6.34}$$

Of course, the two main scanning curves act as limits for the hysteresis curves: they define boundaries that may never be crossed. The saturation degree therefore depends on the history of the material, as well as on the increment of suction applied.

An example of main wetting and drying water retention curves, along with hysteresis curves for several values of b, is shown in Figure 6.4.
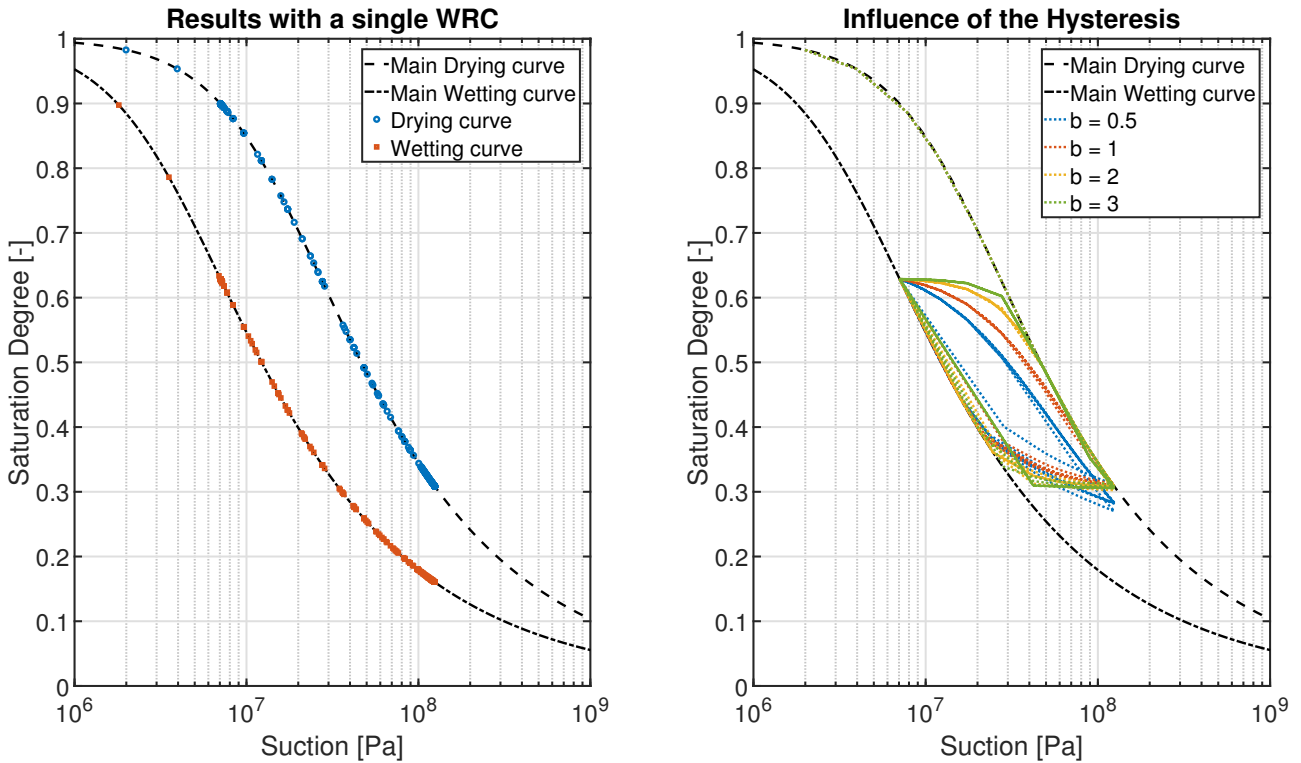
Figure 6.4: Example of main water retention curves along with hysteresis curves for several values of parameter b.

6.3.6 Boundary Layer Model

To model the mass transfer between a reinforced concrete member and its environment, following real environmental conditions, the boundary layer model is introduced (through the existing law FMIVP in Lagamine). The water content at the exchange surface of the model is assumed to be in equilibrium with the partial pressure of water vapour in the air. The vapour flux between the sample and its environment, denoted $\bar{q}$, is then assumed to be proportional

to the difference between the vapour density of the ambient air ($\rho_{v,air}$) and the vapour density of the exchange surface of the sample ($\rho_{v,surf}$) [Gerard et al., 2010]:

$$\bar{q} = \alpha_{b.l.m.}(\rho_{v,surf} - \rho_{v,air}) \qquad (6.35)$$

where $\alpha_{b.l.m.}$ is the mass transfer coefficient that characterises the transfer properties of the surface, and depends on the water saturation degree of the boundary layer. The mass transfer coefficient is assumed to be maximum when the boundary layer is saturated, and decreases with desaturation [Gerard et al., 2010].

The mass transfer coefficient can be determined from drying kinetics experiments, specifically during the Constant Rate Period (CRP) [Idso et al., 1974, Kowalski, 2003, Yiotis et al., 2006, Lehmann et al., 2008]. This is the period when the liquid connections between the exchange surface and the hearth of the medium are sustained and high enough to produce vapour at the exchange surface faster than it is withdrawn by the ambient air. The value of the drying rate during this period is indeed linked to the capacity of the ambient air to evaporate the water from the surface of the porous medium:

$$\alpha_{b.l.m.} = \frac{\bar{q}_{CRP}}{\rho_{v,surf} - \rho_{v,air}} \qquad (6.36)$$

where the vapour density of the drying air is known because the temperature and relative humidity are controlled during a drying experiment, and the vapour density of the exchange surface is also known because it is assumed completely saturated during that period.

The boundary conditions applied to the sample are smoothed through the use of the mass transfer coefficient. This is because the vapour pressure of the ambient air is not directly applied to the exchange surface, but rather penalised by the coefficient $\alpha_{b.l.m.}$. As there was no convective drying experiment performed in this work, the value of the mass transfer coefficient is taken from previous experiments, equal to 1.99E-3 [m/s] [Fanara, 2020].

6.4 Modelling of the Representative Volume Element

The mesoscale, key element of the multiscale formulation, is modelled by a Representative Volume Element (RVE). For this research, where our focus is on aggregate substitution, this RVE must represent a slice of concrete whose scale is similar to the samples used for the experimental campaign. This means that the RVE is made up of a homogenised mortar paste (with homogenised properties) filled with impervious aggregates and, for recycled concrete aggregates, an adherent homogenised mortar paste [Xi & Bažant, 1999]. Other studies would also place the ITZ between the aggregates and the mortar paste, and between the aggregates and the adherent mortar paste for RCA [Sun et al., 2011, Ying et al., 2013a, Nilenius et al., 2013, Liu et al., 2015, Hu et al., 2018, Tian et al., 2019, Xiong et al., 2020, Jin et al., 2022, Li & Song, 2022]. For the time being, our model does not account for the ITZ due to two reasons. Firstly, it is extremely challenging to accurately characterise this phase in itself, and therefore its introduction into the model could potentially introduce further uncertainty. Secondly, the incorporation of the ITZ would result in a more complex model, with no appreciable increase in accuracy, particularly in the absence of a comprehensive experimental characterisation.

The parameters in the mesoscale equations are inherent material properties. These properties are only related to a single phase, within either the adherent mortar or the new mortar

matrix, depending on the location of the integration point at the mesoscale. At the macro-scale, however, the material is considered as a composite represented by a single homo-genised phase. Thus all its properties are averaged effective properties.

The mesoscale is defined with a characteristic length of the order of several centimetres, while the macroscale has a characteristic length of the order of several metres, to respect the principle of separation of scales. In instances where convection represents the primary mode of chloride ingress, it may become necessary to refine the mesh in the vicinity of the boundary conditions to enhance the convergence of the simulation. Consequently, the di-mensions of the finite elements at the macroscale may be too similar to the dimensions of the RVE, rendering it impossible to respect the aforementioned principle.

Multiple ways of generating a RVE are available, including image analysis [Tian et al., 2019, Zhou et al., 2019, Pourebrahimi et al., 2023] and algorithm development [Nilenius et al., 2013, Nilenius et al., 2014, Holla et al., 2021, Jin et al., 2022]. The former method enables the creation of a relatively precise concrete slice based on an image, whereas the latter relies purely on intrinsic features of the concrete mixture. For this study, an algorithm designed specifically for our model and based on that of Nilenius (2013) [Nilenius et al., 2013] or Holla (2021) [Holla et al., 2021] was employed to generate the RVE. The following section provides a detailed explanation.

6.4.1 RVE Generation Algorithm

The algorithm generating the RVE is presented in Figure 6.5. The process necessitates sev-eral intrinsic properties of the concrete mix, including the Particle Size Distribution (PSD) of the aggregates, the Surface Fraction (SF) of aggregates within the mix, and their Aspect Ra-tio (AR). These are introduced in the algorithm to generate a random slice of concrete, which aims to accurately represent the concrete produced in the laboratory, through achieving a maximum packing density for octagonal inclusions [Holla et al., 2021]. The requirements for such an algorithm are [Nilenius, 2014, Holla et al., 2021]:

- There must not be any overlapping of aggregates;

- The spatial distribution of aggregates is random;

- The packing density is maximised (to be equivalent to the laboratory concrete);

- The RVE boundaries are periodic.

The first step in the algorithm is to compute the area required for each interval of the particle size distribution. Based on the RVE size and the surface fraction of aggregates (that is, the volume of aggregate for one cubic metre of concrete), the required aggregate surface area can be determined. According to the particle size distribution, the total surface of aggregate is then distributed between the diameter intervals. Finally, the RVE is filled with aggregates from the largest diameter interval to the smallest. When an aggregate cannot be placed without exceeding the required area, then the interval is considered complete and a smaller one is filled.

The generation of the aggregate follows a random pattern. First, a random size is taken from the current diameter interval and used to generate an elliptical aggregate that meets the required aspect ratio. Next, the ellipse is degenerated into an octagon and all vertices are shifted slightly to emphasise the random aspect of the aggregate. Finally, this aggregate

is randomly placed inside the RVE. To ensure that the aggregates do not make contact with each other, a non-intersection criterion is evaluated to confirm their respective positions. If there is an intersection with aggregates already placed, the latest one is deleted and a new aggregate is created.

Once an aggregate is placed into the RVE, the surface fraction is updated, and we may move on to the final step, provided that the concrete slice created comes from Recycled Aggregate Concrete. This step involves modelling a recycled concrete aggregate as a natural aggregate with a surrounding layer of adherent mortar. The surface area of the mortar layer is equal to a specified percentage of the RCA. The process of generation of an aggregate can be seen in Figure 6.6.

After completing the entire RVE, it is meshed with the use of a different software from the University of Liege, namely gmsh [Geuzaine & Remacle, 2009]. Figure 6.7 presents an example of a generated and meshed RVE, which displays a blue mesh with properties of the homogenised mortar, an orange mesh with properties of the homogenised adherent mortar, and unmeshed, white impervious aggregates.
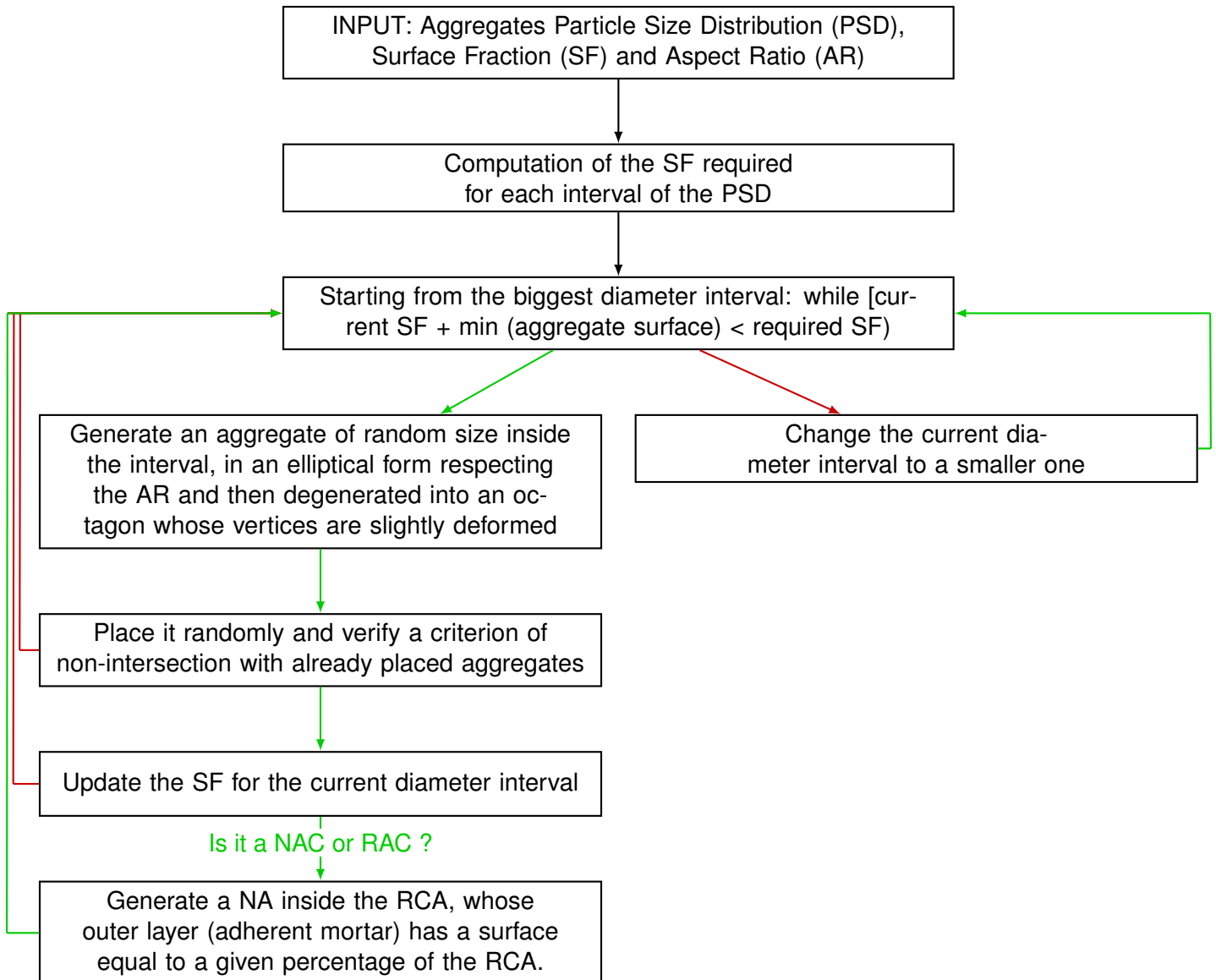
Figure 6.5: Algorithm generating the RVE.
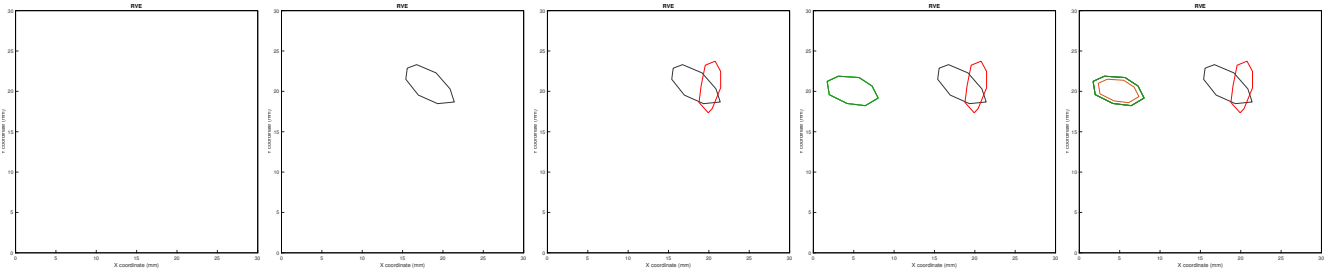
Figure 6.6: RVE generation: Steps of aggregate positioning and RCA creation.
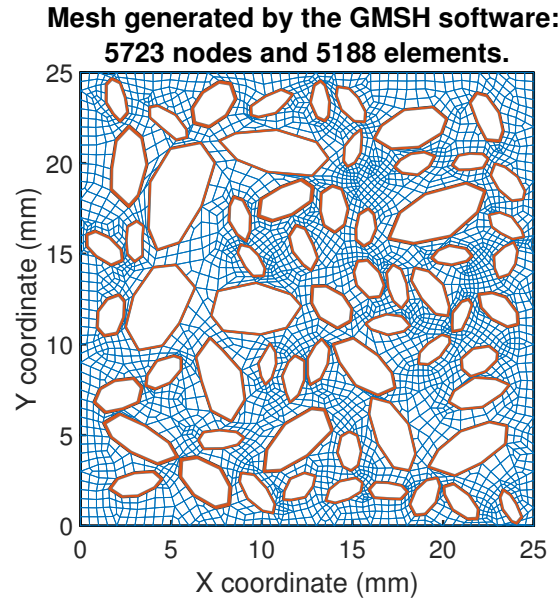
Figure 6.7: Example of a RVE generated with the algorithm developed and meshed with gmsh.

This algorithm, whilst robust, has several drawbacks based on underlying assumptions, including:

- The surface fraction corresponds to the volume fraction of aggregate. However, this is only partially correct due to the non-homogeneous distribution of aggregates in concrete. Consequently, not all sections possess an identical surface fraction.

- The distribution of particle sizes in the aggregates differs from that in a concrete slice. The aggregates are non-spherical, meaning their size and shape can vary depending on their orientation.

One way to reduce inaccuracies resulting from these hypotheses is through reverse modelling and verifying that the Representative Volume Element accurately replicates experiments conducted in the laboratory, for instance.

Another source of inaccuracy may come from the 2D aspect of the algorithm. Modelling concrete should indeed be performed using a three-dimensional model as it is highly heterogeneous and its 3D porous structure may create preferential paths in all directions. However, this approach requires greater computational power.

In this thesis, the two-dimensional approach is preferred, keeping in mind that other authors have compared 2D and 3D models, which yielded diffusivity coefficients up to 40% higher in 3D than in 2D [Nilenius et al., 2013, Nilenius, 2014, Pan et al., 2015, Tian et al., 2019, Jin et al., 2022, Li & Song, 2022]. The reason for this is easily explained by the restriction created in 2D, where the flow must bypass the aggregates in the plane. In contrast, in 3D, an out-of-plane solution is possible.

If one would like to learn more about the algorithm generating the RVE, it is summarised in Appendix C, as well as the meshing method and parameters used in gmsh [Geuzaine & Remacle, 2009].

6.4.2 Example of a RVE

The algorithm developed was used to model a RVE representing a slice of RAC of 25mm width, with a cement content respecting the one determined experimentally (see Section 4.3.3.2). It is presented in Figure 6.8, whose title gives many information:

- There is 63.4% of new mortar (for a surface fraction of aggregates equal to 36.6%) which is higher (respectively smaller) than what was required by the input, that is 58.9% of mortar (respectively 41.1% of aggregates). This is due to the unefficient packing of aggregates, as proven by the Particle Size Distribution in Figure 6.9. This means that the ratio of permeable mortar to impervious aggregates is higher, so the chloride content should be overestimated.

- In the 36.6% of Recycled Concrete Aggregates, there is 3.3% of adherent mortar paste and therefore 33.3% of Natural Aggregates inside the RCA. For a surface fraction focused only on the aggregates, this corresponds to approximately 9% of adherent mortar and 81% of NA, which corresponds to what was found in the cement content analysis of our aggregates (Figure 4.2).

- The mean aspect ratio for the RCA is equal to 2.1.
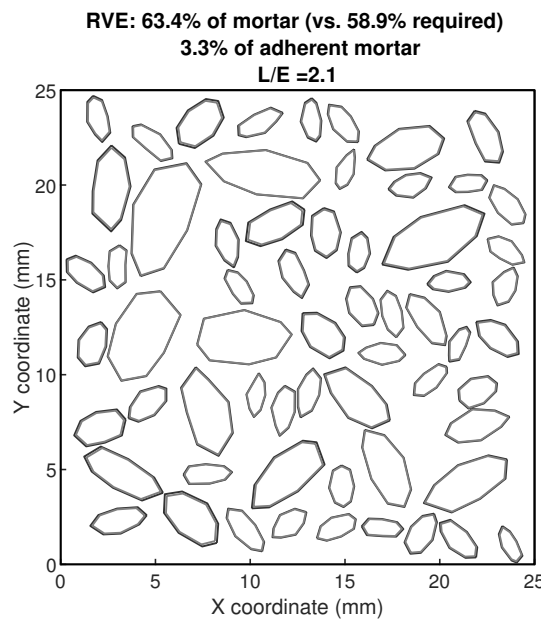
Figure 6.8: Representation of the sample achieved via the algorithm developed for the concrete with Recycled Concrete Aggregates.

The Particle Size Distribution (PSD) is represented in Figure 6.9, for the RVE as well as the theoretical curve. As mentioned previously, the PSD obtained is above the theoretical one, mainly due to the inefficient packing of the aggregates inside the RVE. It is indeed rather impossible to completely fill the area of the RVE with the corresponding required surface area of aggregates. It results in less aggregates area than anticipated and therefore a higher particle size distribution.

One can also remark that the difference between the two curves grows as the particle diameter increases. It is rather logical as it is easier to achieve the required surface fraction for smaller aggregates than for larger aggregates. Furthemore, the wider the RVE is and the closer the two curves will get, but the more computational power it will require.
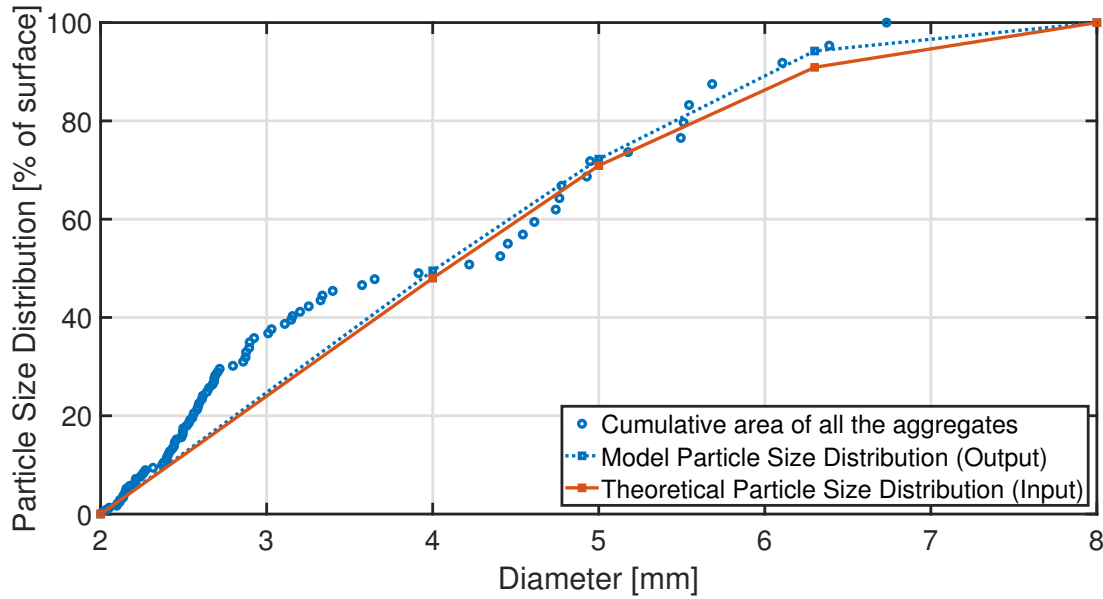
Figure 6.9: Comparison between the Particle Size Distribution in input vs. output, and the real curve accounting for all the aggregates placed.

The aspect ratio of our aggregates inside the RVE is supposed to be between 1.5 and 2.5, as required by the algorithm. This is demonstrated in Figure 6.10 where the histogram for all the aggregates inside the RVE is shown. The normal distribution fitted to this histogram also shows a maximum at the mean value of the aspect ratio, that is 2.1.
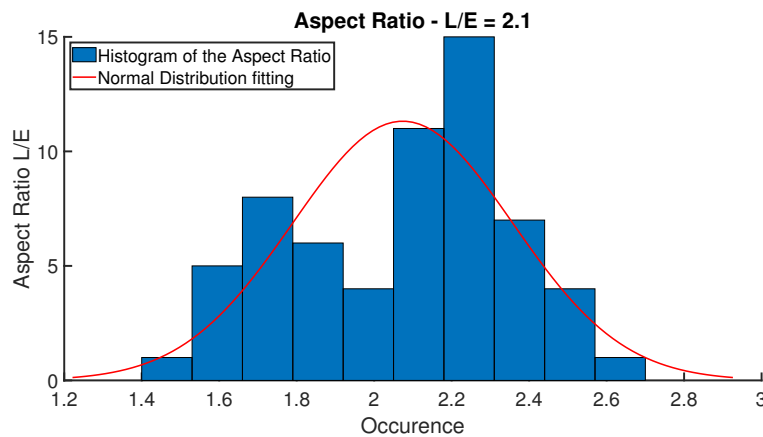
Figure 6.10: Histogram of the aspect ratio for the aggregates generated in the sample, and the normal distribution associated with it.

The sample generated through the algorithm must be meshed in order to be properly used as a RVE. It is done with the gmsh software [Geuzaine & Remacle, 2009] from the University of Liège. The 2D mesh is obtained with a Frontal-Delaunay algorithm for quads, with a simple mesh recombination algorithm applied to all surfaces and a subdivision algorithm ensuring that all the elements are quadrangles. The results for the example discussed is shown in Figure 6.11. The new mortar matrix and the adherent mortar matrix are shown in blue and orange, respectively, and may get different properties introduced into the model.
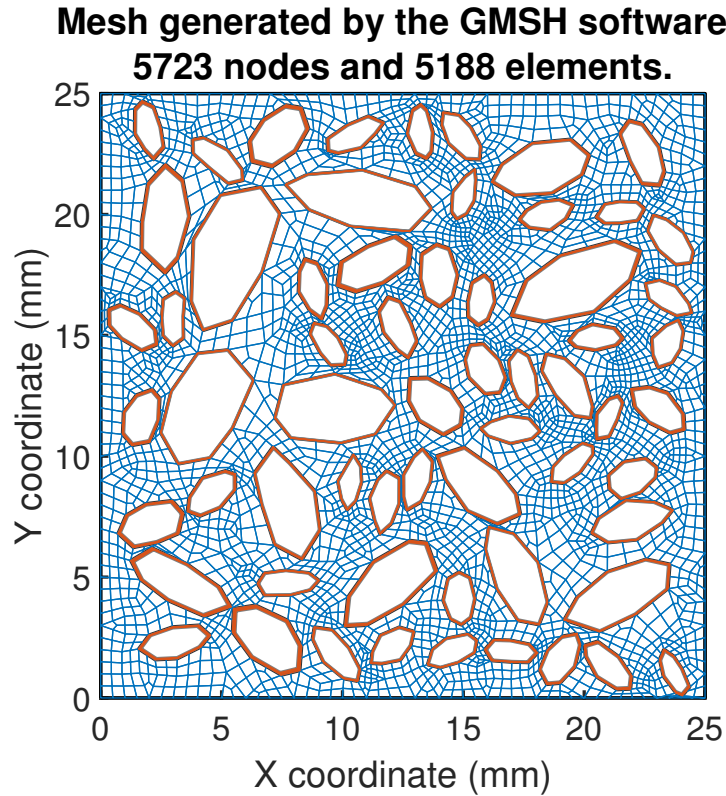
Figure 6.11: Mesh obtained after feeding the sample through the GMSH software.

The adherent mortar paste is always divided in two rings of elements. Then, around the aggregates, one may see that the mesh is more refined. It is due to the octagonal form of the aggregates that require many points and elements. Even though the sample is small, its complexity is therefore resulting in a high number of nodes and elements, which is not ideal for the multiscale modelling that we seek to perform on it, but required for precision purposes.

6.5 Parallelisation of Lagamine with OpenMP

As explained in Section 6.3.4, the multiscale model is computationally intensive, as the problem is solved several times at the mesoscale before being transferred to the macroscale, for each time step. To accelerate this process, it is necessary to parallelise the software: this has been done in this thesis using the OpenMP language [Desrues et al., 2019].
The aim of parallelisation is to enable the model to process one macroscale element per CPU thread. Therefore, the more threads a CPU has, the faster the modelling is performed, until other hardware limits are reached. To achieve this, several measures must be taken.

This section explains these measures, along with the Visual Studio parameters modified to account for parallelisation.

6.5.1 Mesoscale parallelisation

First, the mesoscale must be well suited to parallelisation. In fact, parallelisation means that any loop in the model can be run in any order. Therefore, a good measure is to ensure that any loop can be reversed and still give correct results. For a stiffness matrix obtained by perturbation, this means that the unperturbed case must be separated from the perturbation loop and run first. This reduces the risk of a race condition.

Potential failures may arise from local variable definitions, since all threads will be performing the same computation using the same variables. To avoid this, each variable of the mesoscale model must be defined locally in the elements instead of using modules. Modules should only be used for variables that must remain constant for all elements, such as macroscale parameters.

When defining local functions in the mesoscale, it is necessary to pass all variables as arguments. This measure mitigates the risk of local data being overwritten by other working threads.

Lagamine users may be accustomed to defining variables using 'IMPLICIT DOUBLE PRECISION', which automatically defines all variables as double precision floats, except those that are explicitly defined as integers. However, replacing this statement with 'IMPLICIT NONE' forces the user to precisely define each variable and throws an error when a variable is not correctly defined. This ensures that every local variable is well-defined before its use.

Finally, parallelisation requires a significant amount of memory as variables are defined multiple times, once for each thread. To prevent any issues with data management and erasure, it is necessary to use allocatable variables for the bigger ones.

6.5.1.1 Start of the Parallelisation Zone

To ensure that the mesoscale model is correctly defined and ready for parallelisation, it is recommended to first attempt parallelisation of the perturbation loop alone. If successful, modifications can then be made to the macroscale element for parallelisation.

At the mesoscale, parallelisation of the perturbation loop can be achieved by introducing the code lines below before the start of the loop. To achieve parallelisation, variables must be defined as SHARED, PRIVATE or FIRSTPRIVATE. When defined as SHARED, all threads can access the same variable in memory and modify it at any time, even though most of the time those variables are only to be read. When defined as PRIVATE, each thread will define the variable locally. When defined as FIRSTPRIVATE, each thread also defines a local variable that is based on and equal to a pre-existing variable with the same name outside the parallelisation zone.

The "!$OMP" indicates that the code must process the following directive as an OpenMP language. The "!$OMP PARALLEL" starts the parallelisation zone, which must end with "!$OMP END PARALLEL" at the end of the zone.

```
1  !$OMP   PARALLEL NUM_THREADS(NLOOP) DEFAULT(PRIVATE)    &
2  !$OMP   SHARED(...)   &
3  !$OMP   FIRSTPRIVATE(...)
4
5  !$OMP DO ORDERED SCHEDULE(DYNAMIC)
```

Then the "!$OMP NUM_THREADS(NLOOP)" sets the number of threads used to the number of iterations in the loop. In fact, there is no need to have more threads working than the number of iterations in the loop. Note that this is not useful if the parallelisation is on a macroscale, and that the maximum number of threads remains the number of threads in the CPU, minus one, which is the master thread.

Finally, the "!$DEFAULT(PRIVATE)" defines all variables as private by default. Then the other variables can be defined as shared or firstprivate as needed.

Finally, the "!$OMP DO ORDERED SCHEDULE(DYNAMIC)" starts the actual parallelisation process, which ends with "!$OMP END DO". The ORDERED statement forces the threads to work in the order defined in the loop, but this is not always verified. The SCHEDULE(DYNAMIC) then means that the software will manage the allocation of work to the different threads.

6.5.2   Macroscale parallelisation

At the macroscale, the parallelisation is the same as at the mesoscale, except that "DEFAULT(NONE)" is used and therefore all variables must be explicitly defined. In addition, "!$OMP CRITICAL" and "!$OMP END CRITICAL" are defined around critical statements and functions, such as when working on the stiffness matrix. This ensures that only one thread is working on the stiffness matrix at a time, as the work is additive for all threads.

6.5.3   Visual Studio Parameters

In Visual Studio, the integrated development environment (IDE) used to develop Lagamine, the initial parameters are only for sequential modelling. They need to be modified to account for and allow parallelised modelling. The parameters that require modification are presented below.

It is important to note that only the 'Release' version of Lagamine should be parallelised. In the 'Debug' version, parallelisation would make debugging impossible as the IDE may jump from thread to thread between two breakpoints, causing the data to change constantly.

In the 'Release' version, the following parameters require modification:

- Fortran:
  - General:
    * Multi-processor Compilation → Yes
  - Optimization:
    * Parallelization → Yes (/Qparallel)
  - Language:

            * Process OpenMP Directives → Generate Parallel Code (/Qopenmp)

      – External Procedures:

            * Calling Convention → C, REFERENCE (/iface:cref)

      – Libraries:

            * Runtime Library → Quickwin (/libs:qwin)

            * Use Intel Math Kernel Library → Parallel (/Qmkl:parallel)

- Linker:

      – System:

            * Heap Reserve Size → 268495456

            * Heap Commit Size → 268495456

            * Stack Reserve Size → 268495456

            * Stack Commit Size → 268495456

            * Enable Large Addresses → Support Addresses Larger Than 2GB (/LARGE-ADDRESSAWARE)

6.6 Conclusion

This chapter presented the multiscale model in detail, outlining its development and application. Firstly, the necessity of a multiscale model and the optimal formulation to achieve the aforementioned objective were discussed. Subsequently, the model was presented, from its constitutive equations to the algorithm that was developed to generate the representative volume element. Finally, the parallelisation of Lagamine was introduced. Although not a novel concept, it required a significant investment of time and resources to develop.

The following chapter will present the validation of the model and a sensitivity analysis of both the representative volume element and the hysteresis parameters.

7

NUMERICAL RESULTS

Contents

7.1 Introduction

Now that the multiscale model has been detailed, it is time to validate and use it. This chapter presents the numerical results of the multiscale model under various conditions. The model is validated under both saturated and unsaturated conditions using analytical, numerical, or experimental methods whenever possible. A sensitivity analysis is then performed on the Representative Volume Element by modifying its size and properties to study the effects of these modifications. Another sensitivity analysis is also performed on the parameters of the hysteresis of the water retention curve.

The multiscale model can be used in four configurations, depending on the value of the parameter 'KFLU', which are listed in Table 7.1. Using the last option (KFLU = 4) to model all of the mentionned cases is possible, but it increases the computation cost. Therefore, proposing multiple options is recommended.

KFLU	Water	Gaz	Pollutant	Unsaturated
1	X			No
2	X		X	No
3	X	X		Yes
4	X	X	X	Yes

Table 7.1: Type of modelling performed depending on the value of the parameter "KFLU"

7.2 Validation of the Model under Saturated Conditions

The validation process begins by focusing on saturated conditions, that is with KFLU=2. At first, the model's validation relies on an analytical solution obtained from Biver's work (1993), which is the most accurate method for validating a model. Subsequently, numerical validation is conducted using an established single-scale model built within the same software, which combines fluid transfer and pollutant transfer laws. Finally, the model's results are experimentally validated by comparing them with the diffusion experiment of chloride ions under unsteady-state conditions.

7.2.1 Analytical Validation

The literature has extensively studied the diffusion and advection of pollutants within a saturated porous system, with analytical solutions readily available. One such solution is the one used by Biver (1993) for a one-dimensional semi-infinite medium [Biver, 1993, Chen et al., 2019]:

$$C(x,t) = \frac{C_0}{2} \exp\left(\frac{ux}{2D}\right) \left[\exp\left(-x\frac{u}{2D}\right) \text{erfc}\left(\frac{x}{2\sqrt{Dt}} - \sqrt{\frac{u^2 t}{4D}}\right)\right.$$

$$\left. + \exp\left(x\frac{u}{2D}\right) \text{erfc}\left(\frac{x}{2\sqrt{Dt}} + \sqrt{\frac{u^2 t}{4D}}\right)\right] \tag{7.1}$$

where C_0 [-] is the limit state condition, u [m/s] is the fluid flow, D [m^2/s] is the diffusion coefficient and x [m] and t [s] are respectively the position and the time. Of course, if $u = 0$, then one recognises the Fick's second law solution.

Results of the analytical validation, for both the diffusion and advection of pollutants, are visible in Figure 7.1. The parameters are listed in Table 7.2, where the water flows u are obtained as follows:

$$u = -\frac{k_{int}}{\mu_w} \times \frac{\partial P_w}{\partial x} = -\frac{10^{-19}}{10^{-3}} \times \frac{105325 - 101325}{0 - 1} = 4 \times 10^{-11} \text{ cm/s} \qquad (7.2)$$

Case	C_0 [mg/ml]	D [cm^2/s]	u [cm/s]
$u \neq 0$	100	1E-8	4E-11

Table 7.2: Values of the parameters for the analytical validation of the model.
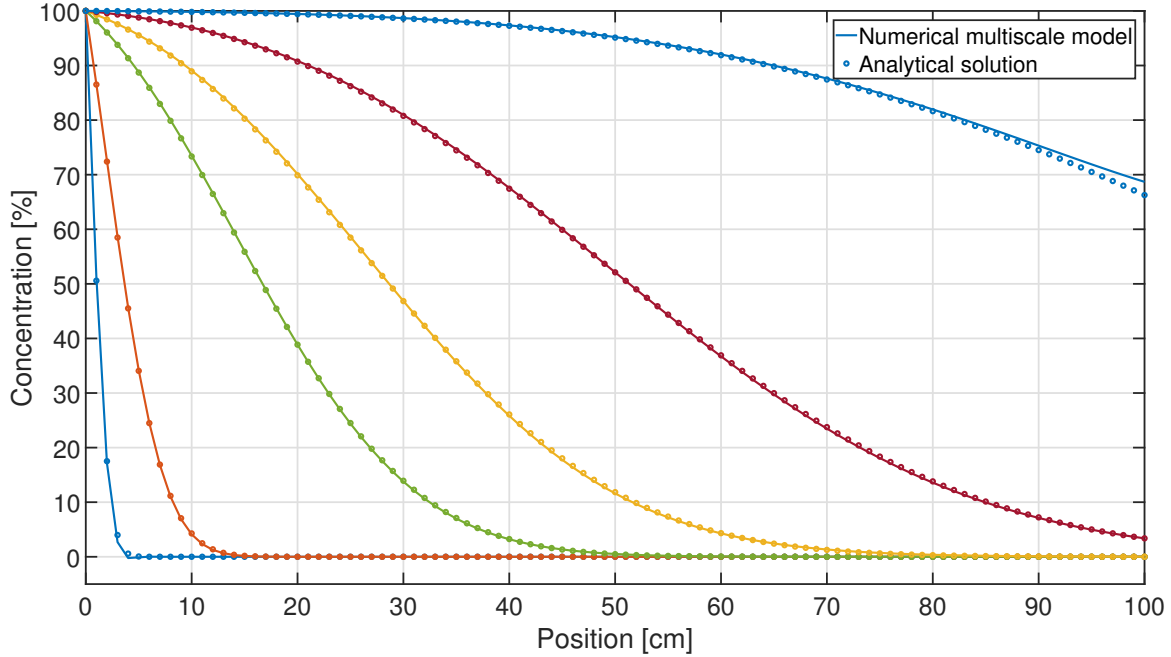
Figure 7.1: Analytical validation of the model for the diffusion and convection of chloride ions.

The numerical solution, shown as a solid line, closely matches the analytical solution, represented by the local data points. This validates the multiscale model for the diffusion and advection of a pollutant in a homogeneous and saturated porous medium. The simulation used a homogeneous RVE to replicate the analytical results. The diffusion of pollutants was also tested without fluid flows, and the results were accurate, as expected.

7.2.2 Numerical Validation

Previous research on pollutant diffusion in porous media has been conducted at the University of Liège. Within this context, several single-scale models were developed using the

LAGAMINE environment. Two laws, the WAVAT [Collin, 2003] and ADVEC [Biver, 1993] laws, are particularly useful for validating our multiscale model numerically. The WAVAT law is a thermo-hydraulic law that is used for fluid flows in both saturated and unsaturated conditions. On the other hand, the ADVEC law is a law for transporting pollutants that can be combined with the WAVAT law for the diffusion and advection of pollutants.

The comparison focused on both the diffusion and advection phenomena, and the results are shown in Figure 7.2. The RVE is again homogeneous. Initially, the water pressure is equal to the atmospheric pressure ($101325 \mathrm{Pa}$) and the chloride concentration is zero throughout the mesh. Then, from 0s. to 1E5s., the pressure and the chloride concentration vary linearly to reach a value of $105325 \mathrm{Pa}$ and 100 mg/ml respectively on the left boundary, while remaining constant on the right boundary. Finally, these conditions are kept constant until 1E10s.
The multiscale model, represented by a plain line, accurately fits the single-scale response, represented by square data points, at all times. The model is therefore validated both numerically and analytically.
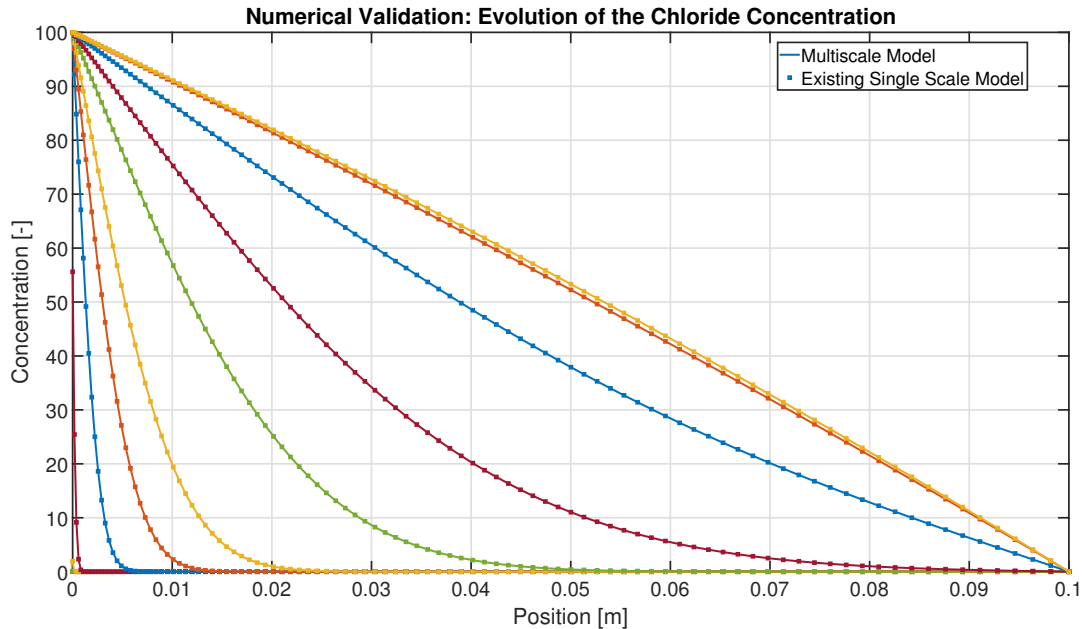
Figure 7.2: Numerical validation of the multiscale model for the diffusion and advection of a pollutant under saturated conditions.

Figure 7.3 represents the results of our multiscale model for an imposed water pressure 40 times greater than announced previously. Its goal is to show that once the chloride front has reached the right border, numerical oscillations appear. This is because to satisfy the boundary conditions, an infinite slope should appear on the last element, to go from one imposed boundary condition to the other, which is impossible in finite element models. It is also one explanation of our choice to model the chloride ingress due to convection at the macroscale and not at the mesoscale: the mesoscale problem being solved under steady-state, these oscillations would appear at all time, and therefore the model would not be accurate.
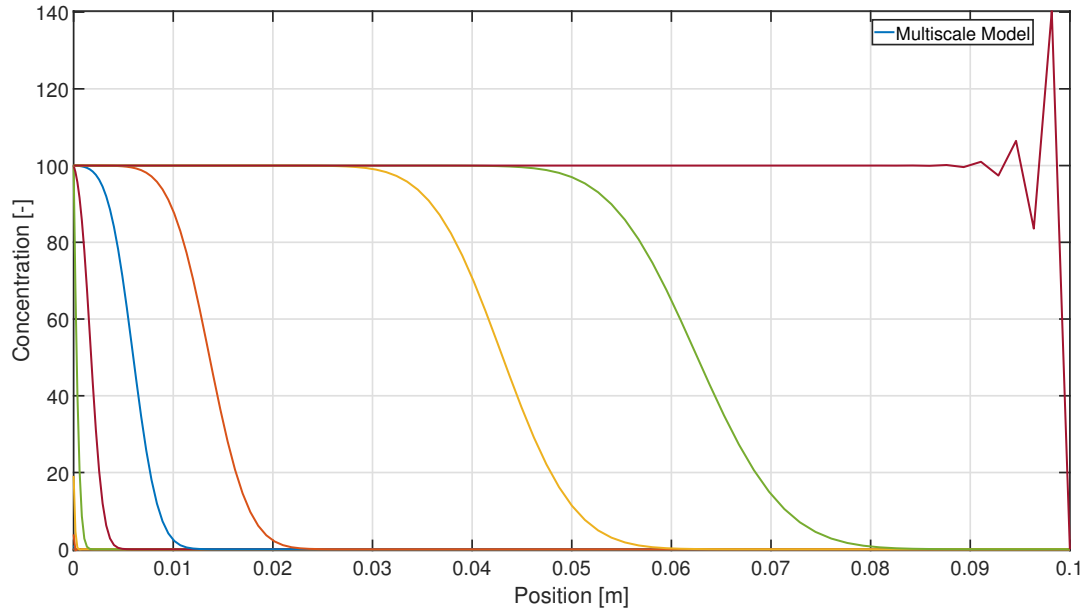
Figure 7.3: Numerical oscillations at the right border under greater water flows.

7.2.3 Experimental Validation

The multiscale model, now both analytically and numerically validated, was then compared with experimental results to assess its ability to accurately represent concrete results with mortar properties, through the use of the representative volume element. The unsteady state chloride diffusion experiment presented in Section 5.3.2 is an ideal case for this application. The experiment tested three compositions: an equivalent mortar (E-M), a concrete made from NA (NAC) and another from RCA (RAC). Several additional experiments were carried out to determine the necessary intrinsic parameters of the materials, including intrinsic water permeability, porosity and diffusion coefficient. The experimental intrinsic properties incorporated into the model are given in Table 7.3 and are taken from Chapter 5.
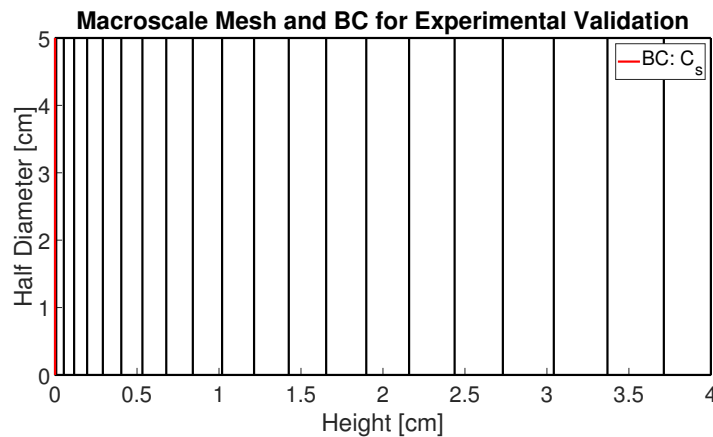
Figure 7.4: Macroscale mesh representing the experiment performed, with the Boundary Conditions applied according to Table 7.3. It is shown horizontally instead of vertically for visibility purposes. The diameter of the experimental sample is divided by two under axisymmetric conditions.

Property	E-M	NAC	RAC	E-M +30%
Intrinsic Permeability [m^2]	3.87E-18	1.73E-19	2.58E-19	5.02E-18
Porosity [% Volume]	22.83	14.16	20.50	29.68
Diffusion Coefficient [m^2/s]	1.43E-11	1.41E-11	1.65E-11	1.86E-11
C_s [-]		1.45	0.78	1.27

Table 7.3: Intrinsic properties of the E-M, NAC and RAC obtained experimentally and implemented in the constitutive laws of the multiscale model.

The macroscopic mesh that depicts the experimental sample, is shown horizontally in Figure 7.4 instead of vertically (as for the experiment), for visibility purposes. The boundary conditions are enforced at the bottom of the mesh (on the left in Figure 7.4), which allows for chloride ions to leach vertically (resp. horizontally) into the porous structure in a unidirectional manner. At the opposite side, both the water pressure and chloride content are free degree of freedoms. The sides perpendicular to the boundary conditions are considered impervious. The water pressure remains constant at atmospheric pressure to maintain a saturation degree of 100%. Additionally, the chloride concentration matches the surface concentration (C_s) value of the corresponding concrete, which is listed in Table 7.3. The mesoscopic meshes provided in Figure 7.5 depict sections of either NAC or RAC. For the latter, the cement content found in Section 4.3.3.2 is introduced into the RVE algorithm.
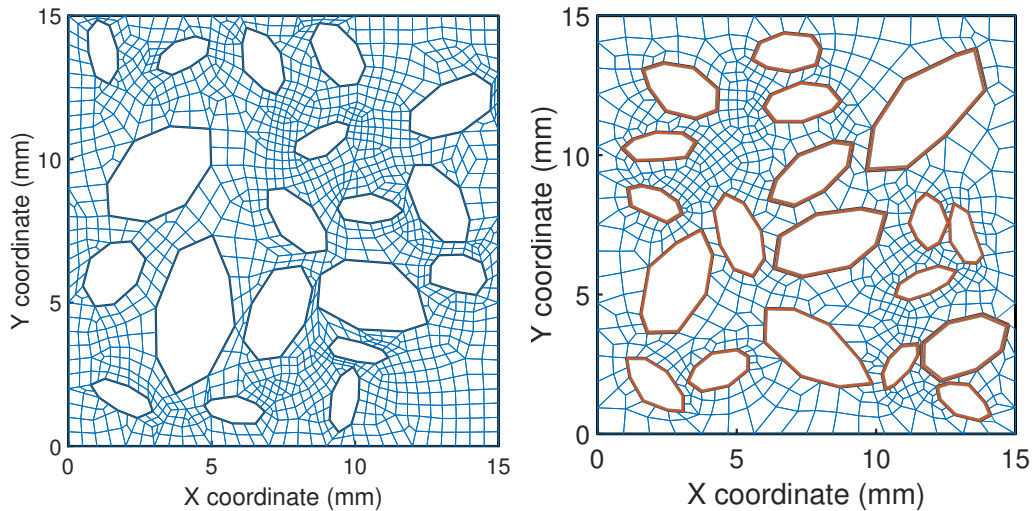
Figure 7.5: Mesoscale mesh representing the experiment performed.

The results of the experimental validation can be viewed in Figures 7.6 and 7.7 for the NAC and RAC, respectively. The data points in black represent the experimental results obtained over 15, 29 and 91 days of diffusion. We carried out various comparisons, starting with a RVE that was homogeneous and had properties equal to those of the NAC or RAC obtained during the experimental campaign (see Table 7.3). Figures 7.6 and 7.7 show the results for the homogeneous RVE, in straight lines. These lines represent the best fit of our model to the experimental results, owing to the time variation of the diffusion coefficient expressed experimentally, whereas our model requires a single value of the diffusion coefficient. Nonetheless, these findings are favourable when compared to the experimental results, particularly the 29-day results which yielded the diffusion coefficient used numerically.

143
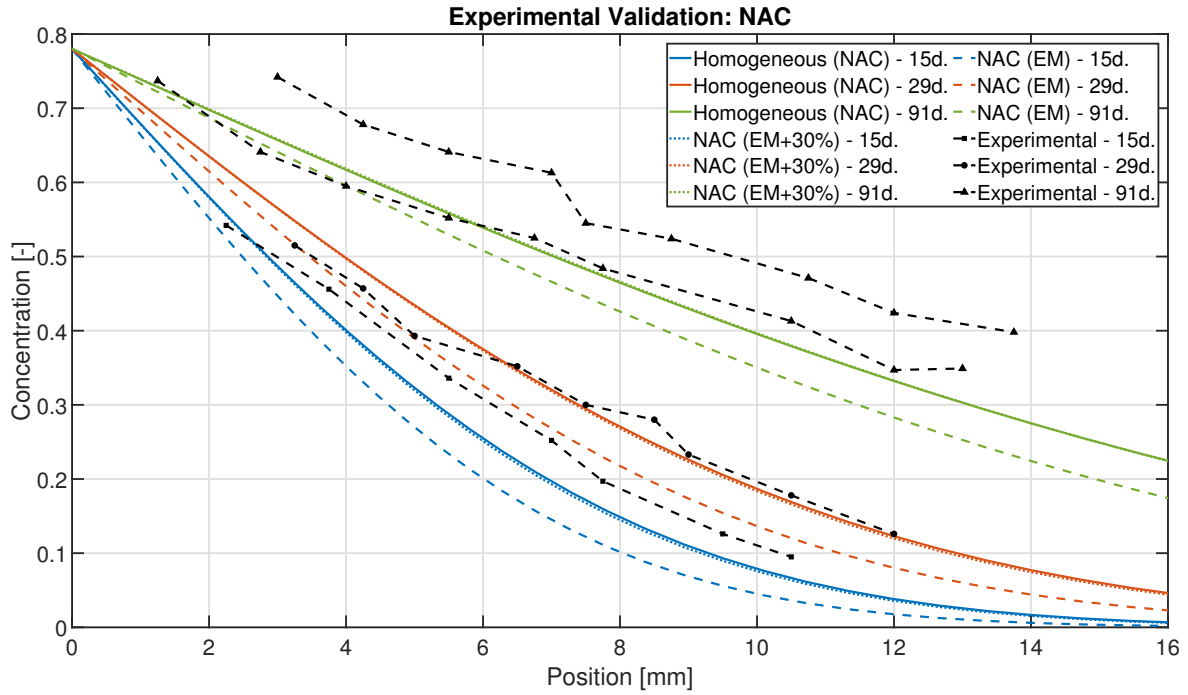
Figure 7.6: Experimental validation of the multiscale model for the NAC.

The RVEs depicted in Figure 7.5 were subsequently utilised, requiring the input of equivalent mortar paste (E-M) material properties as only the mortar is meshed in the RVE, the aggregates being impervious. The resultant responses, represented by a dashed line, is less precise than anticipated. However, accurate results are obtained by increasing the diffusive properties of the mortar paste by 30%, as shown by the dot lines. This is due to the two-dimensional aspect of our model in comparison to a 3D experiment. Such findings are in line with previous studies, which state that the diffusion can increase up to 40% when the model is in 3D instead of 2D [Nilenius, 2014].
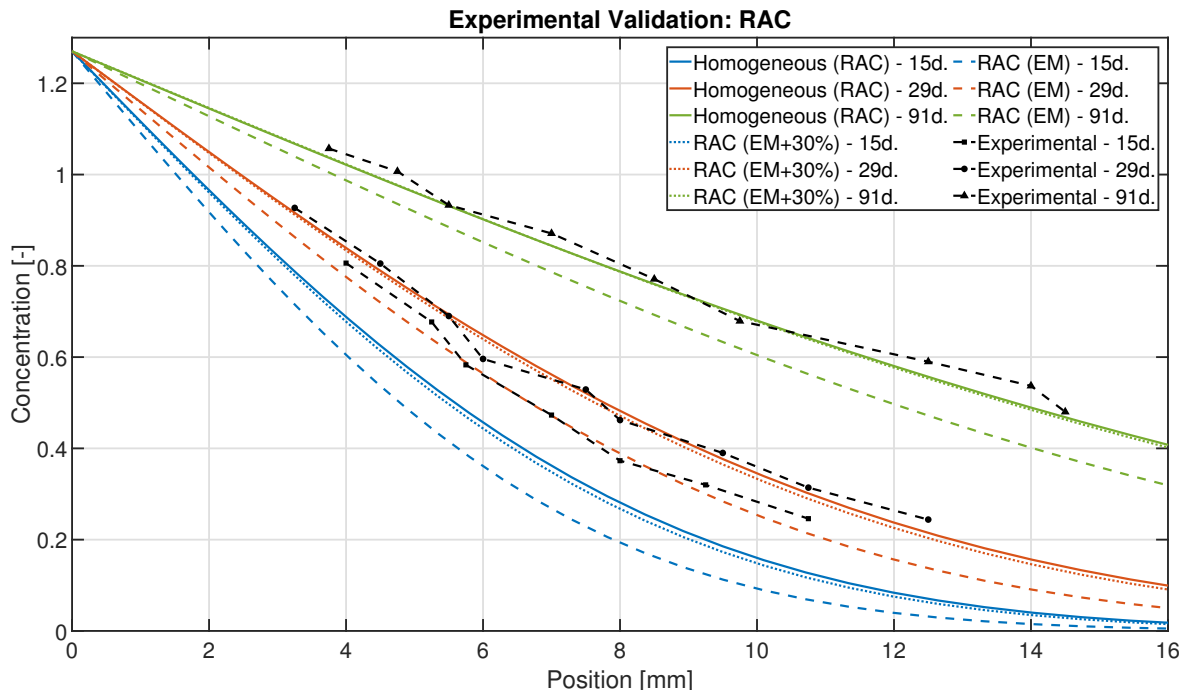
Figure 7.7: Experimental validation of the multiscale model for RAC.

For the RAC, it is possible that the properties of the adherent mortar paste differ from those of the plain mortar paste. However, obtaining these properties experimentally is impossible, except through the use of reverse modelling. Initially, all phases of the RAC RVE utilise the properties of the E-M composition, just like the NAC. The RVE is indeed what distinguishes the two concrete types. To enable a comparison between the NAC and RAC, the parameters have also been increased by 30%. However, it is also feasible to enhance the diffusivity of the cohesive mortar paste in accordance with relevant literature.

7.3   Validation of the Model under Unsaturated Conditions

Under unsaturated conditions (KFLU=4), the model exhibits significant non-linearity, making analytical validation difficult. Consequently, numerical validation was preferred, utilising established single scale models developed at the University of Liège [Biver, 1993, Collin et al., 2002]. The combination of WAVAT and ADVEC laws, which were developed using the LAGAMINE software employed for this multiscale model, enables the simulation of advection and diffusion of any pollutants within an unsaturated porous medium. A homogeneous RVE was necessary for comparing the responses. Initially, the medium has zero chloride concentration, and the gas and water pressures throughout are equivalent to the atmospheric pressure. Then, the boundary conditions are applied on the left border as shown in Figure 7.8. The water pressure varies cyclically from -124.39MPa to -6.96MPa, while the concentration of chloride ions rises to 100 and remains constant thereafter.
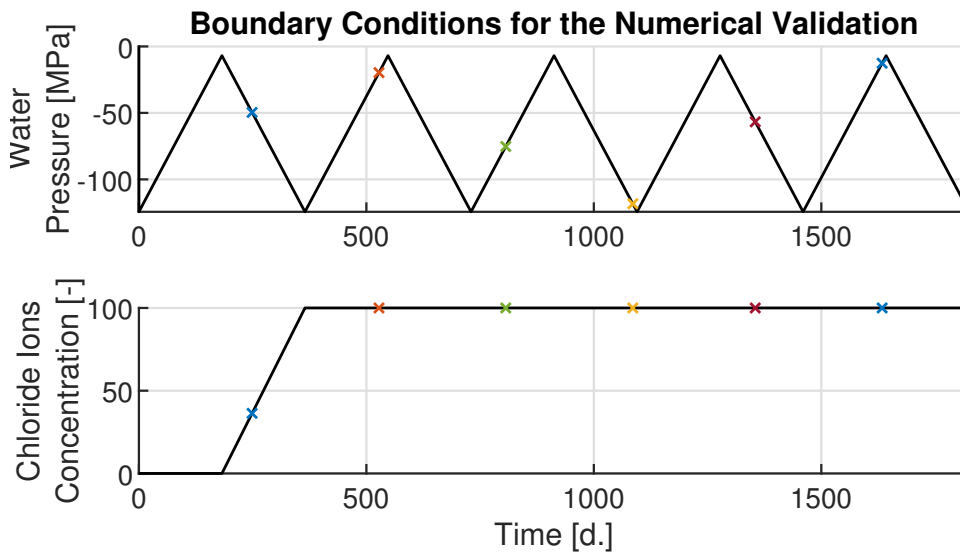
Figure 7.8: Boundary conditions of the validation under unsaturated conditions. Each marker corresponds to a time represented in Figures 7.9 and 7.10.

The outcomes of the numerical validation are illustrated in Figures 7.9 and 7.10, denoting the chloride concentration and water pressure, respectively. The time and boundary conditions displayed by markers in Figure 7.8 refer to the responses of Figures 7.9 and 7.10.
The outcomes of the recently developed multiscale model are shown with dashed lines and triangle markers, while the outcomes of the already validated single-scale model are illustrated with solid lines. It is evident that there is a satisfactory match between the two responses for both the water pressure and chloride concentration, indicating the confident validation of our model for chloride ion advection and diffusion within an unsaturated porous medium.
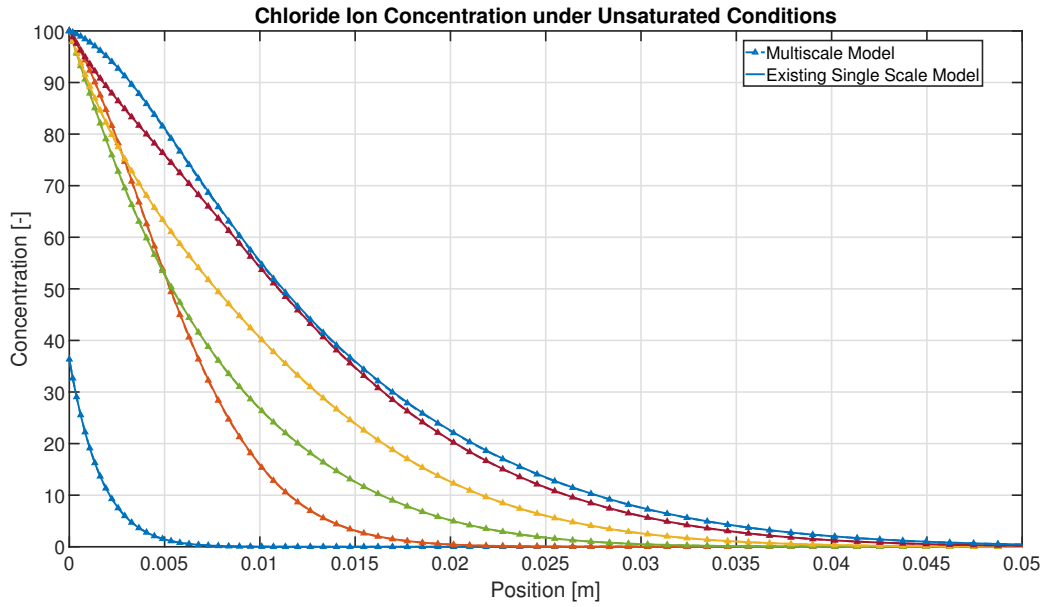
Figure 7.9: Numerical validation of the multiscale model under unsaturated conditions: results in terms of chloride ions concentration.
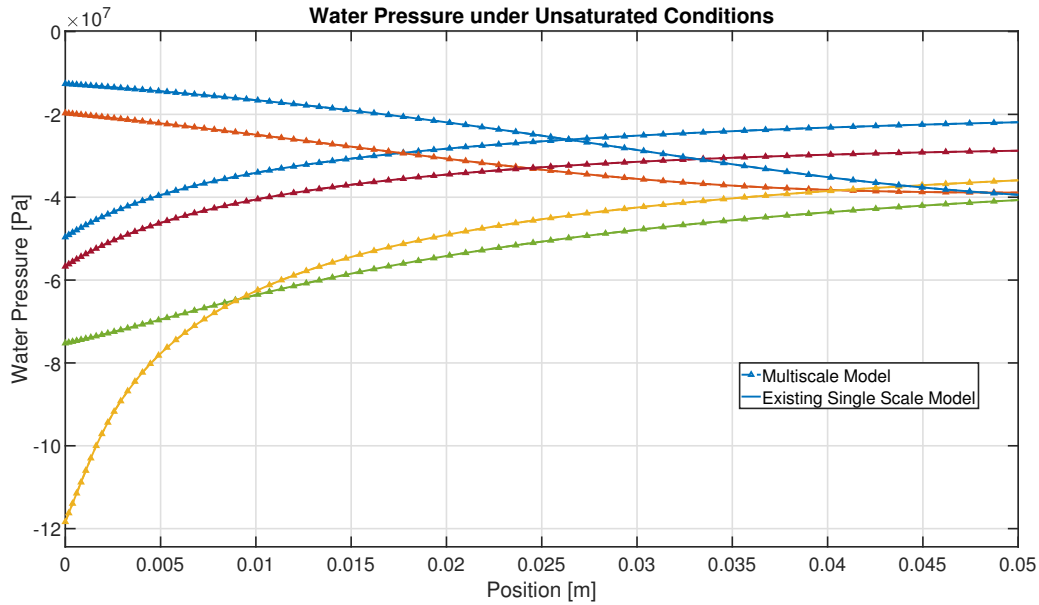
Figure 7.10: Numerical validation of the multiscale model under unsaturated conditions: results in terms of water pressure.

7.4 Sensitivity Analysis on the RVE

The previous chapter presented the multiscale model. The previous section aimed to validate this model under both saturated and unsaturated conditions. Now that the model is validated, it will be used for the first time in a sensitivity analysis of the RVE.
The influence of the size of the RVE is studied first, with the packing of aggregates varying with the space available. Finally, a study is conducted on the influence of the quantity of adherent mortar and its properties.

7.4.1 Influence of the RVE Size

The representative volume element represents a slice of concrete with a specific particle size distribution. As stated in Section 6.4.2, a smaller RVE may result in fewer aggregates being placed than required due to a lack of space and inefficient packing, which can lead to a higher diffusive surface.

To investigate this aspect, four RVEs of different sizes (10, 15, 20, and 25mm) have been generated for both NAC and RAC. They are represented in Figures 7.11 and 7.12, respectively, and were tested under the same conditions as to validate our model experimentally. The particle size distribution results can be found in Figure 7.13. The chloride content is presented in Figures 7.14 and 7.15 for the chloride profile at 19, 28 and 91 days, as well as for the mean value of chloride content at the end of the experiment (91 days), respectively.
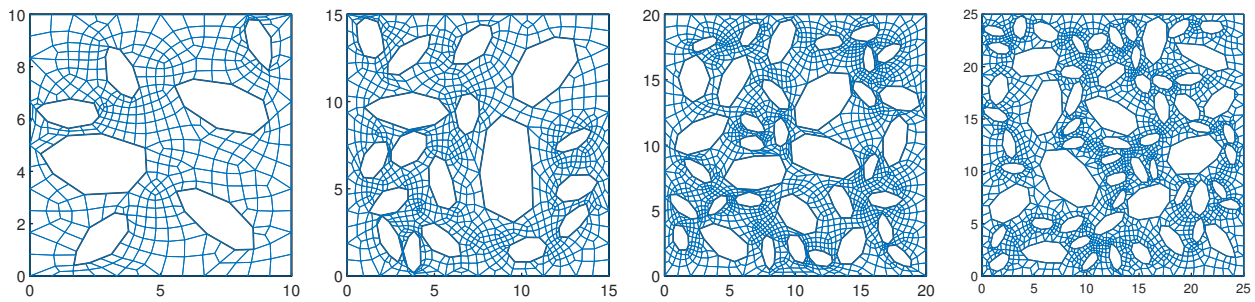
Figure 7.11: Mesh of the NAC RVEs used for the sensitivity analysis to the RVE size, from 10mm to 25mm sides.
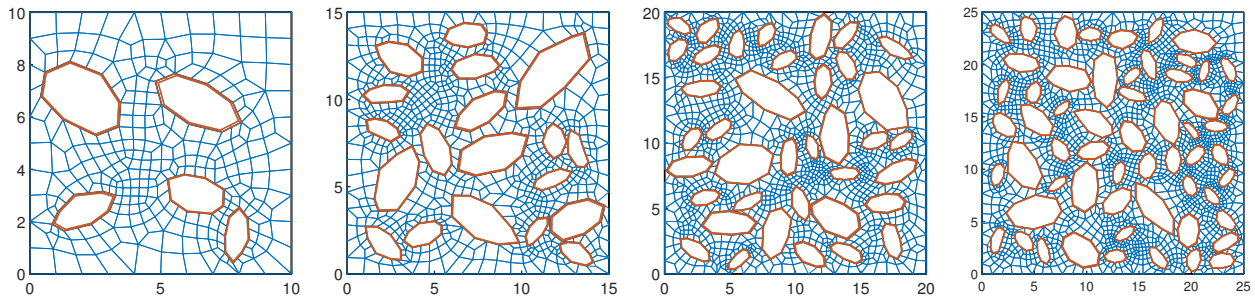
Figure 7.12: Mesh of the RAC RVEs used for the sensitivity analysis to the RVE size, from 10mm to 25mm sides.

Figure 7.13 confirms that the larger the RVE is, the closer the modelled particle size distribution is to the required distribution for both NAC and RAC. However, the difference appears to be greater in NAC than in RAC, with the latter proving more difficult to achieve the targeted particle size distribution.
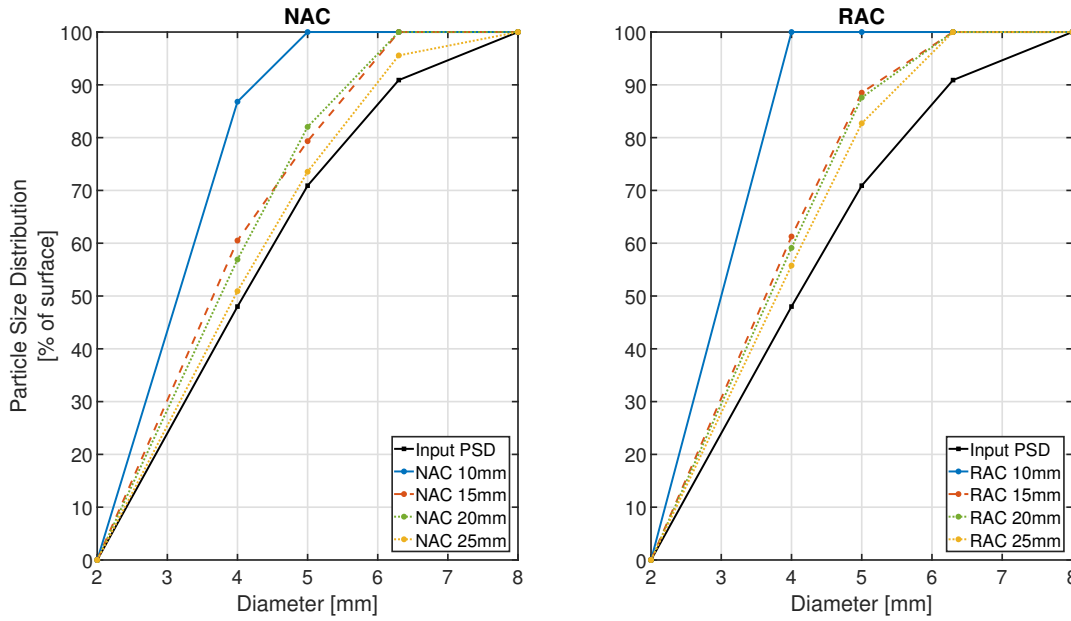
Figure 7.13: Influence of the RVE size on the Particle Size Distribution obtained numerically.
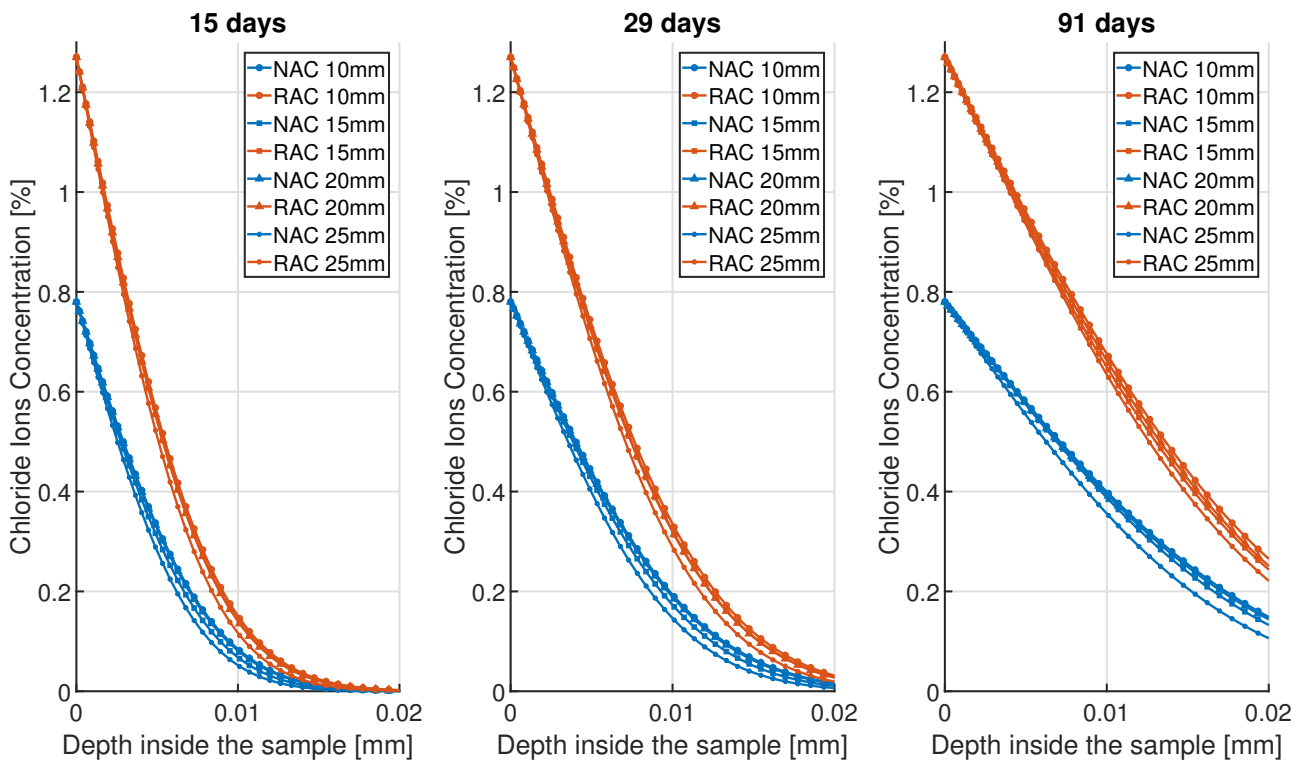
Figure 7.14: Influence of the RVE size on the chloride concentration profile under the conditions of the unsteady state diffusion experiment.

Figures 7.14 and 7.15 confirm that the chloride distribution profile stabilises as the RVE size increases. Additionally, a larger RVE size results in a smaller mean chloride concentration in the sample due to better aggregate packing, which reduces the overall diffusive surface and induces a lower concentration profile. However, it is important to consider that the size of the RVE directly affects the computation time, as demonstrated in Figure 7.16.
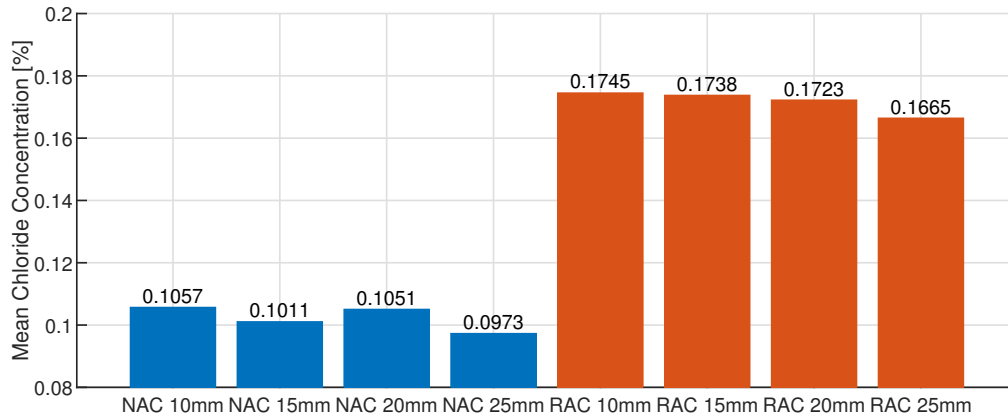
Figure 7.15: Mean value of the chloride concentration in the sample at the end of the experiment.

The computation time increases according to a power law with the number of nodes in the RVE. Therefore, a balance must be struck between computation time and the accuracy of the RVE and, consequently, the results. Hence, using a 15mm RVE is a suitable compromise. It overestimates chloride ingress to a negligible extent and significantly reduces computation time compared to a 25mm RVE.

The fitting curves in Figure 7.16 for NAC and RAC differ, which may be due to the type of fitting or insufficient data. Additionally, a third dashed line is presented, resulting from the same computation as the NAC analysis but with a KFLU of 4 instead of 2. The results for chloride ingress remain unchanged, except for the size of the computed DOF (from two to three), which significantly increases simulation time. This highlights the importance of using the best possible case to reduce computation time to the minimum necessary.
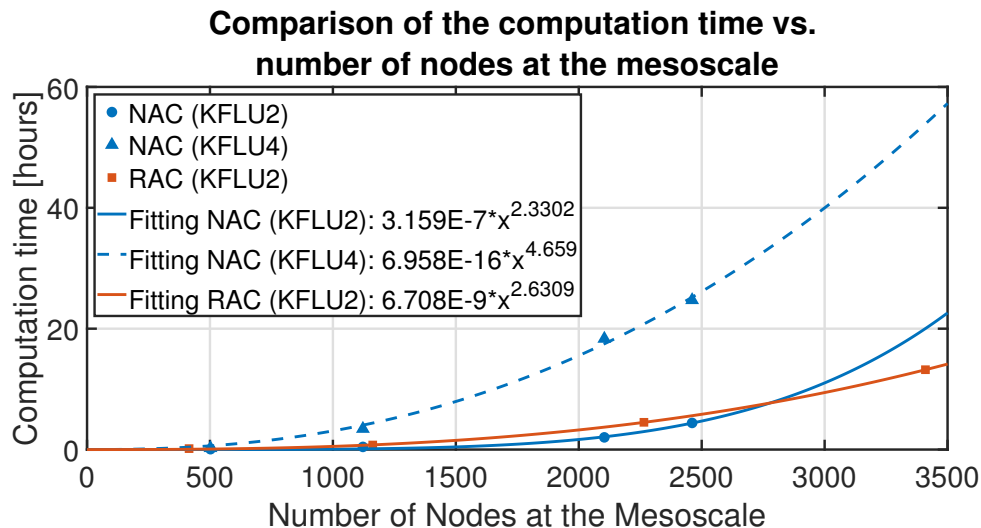
Figure 7.16: Influence of the number of DOF in the RVE on the computation time.

7.4.2 Influence of the RCA's Diffusion Coefficient

The diffusion coefficient is a crucial parameter related to recycled concrete aggregates. However, characterising the diffusive properties of the adherent mortar paste alone is difficult

or even impossible experimentally, making it an unknown in our multiscale model. Nonetheless, some authors found that the chloride diffusivity of old mortar is 0.2-5 times that of new mortar [Jin et al., 2022]. To characterise the sensitivity of our model to this intrinsic property, we conducted a sensitivity analysis on the diffusion coefficient of the RCA's adherent mortar paste, using the simulation described in Section 7.2.3.

Several diffusion coefficients were introduced into the same simulation while keeping all other parameters constant. The simulation used the representative volume element shown in Figure 7.17 and the properties were sourced from the E-M composition with a 30% increase as described in Section 7.2.3. The properties used are listed in Table 7.4.

Mortar Matrix's Properties				
Intrinsic Permeability [m^2]		5.03E-18		
Porosity [% Volume]		29.68		
Diffusion Coefficient [m^2/s]		1.85E-11		
Adherent Mortar's Properties				
Intrinsic Permeability [m^2]		5.03E-18		
Porosity [% Volume]		29.68		
Diffusion Coefficient [m^2/s] 1E-10	5E-10	1.85E-11	5E-11	1E-12

Table 7.4: Properties of the different phases for the sensitivity analysis of our model on the RCA's diffusion coefficient.

Mesh generated by the GMSH software: 1401 nodes and 1256 elements.
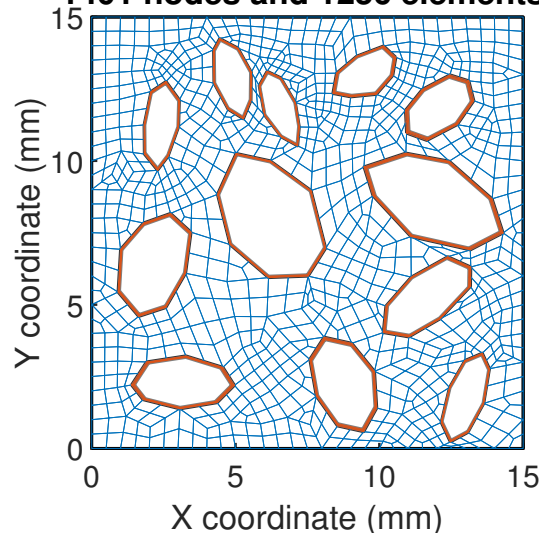
Figure 7.17: Mesoscale RVE mesh for the sensitivity analysis on the diffusion coefficient of the RCA's adherent mortar.

Figure 7.18 shows the chloride concentration profiles at 15, 29, and 91 days of diffusion for five different chloride diffusion coefficients. As expected, higher diffusion coefficients result

in higher chloride concentrations. Figure 7.19 displays the mean chloride concentration inside the sample for the defined days, relative to the defined diffusion coefficient.
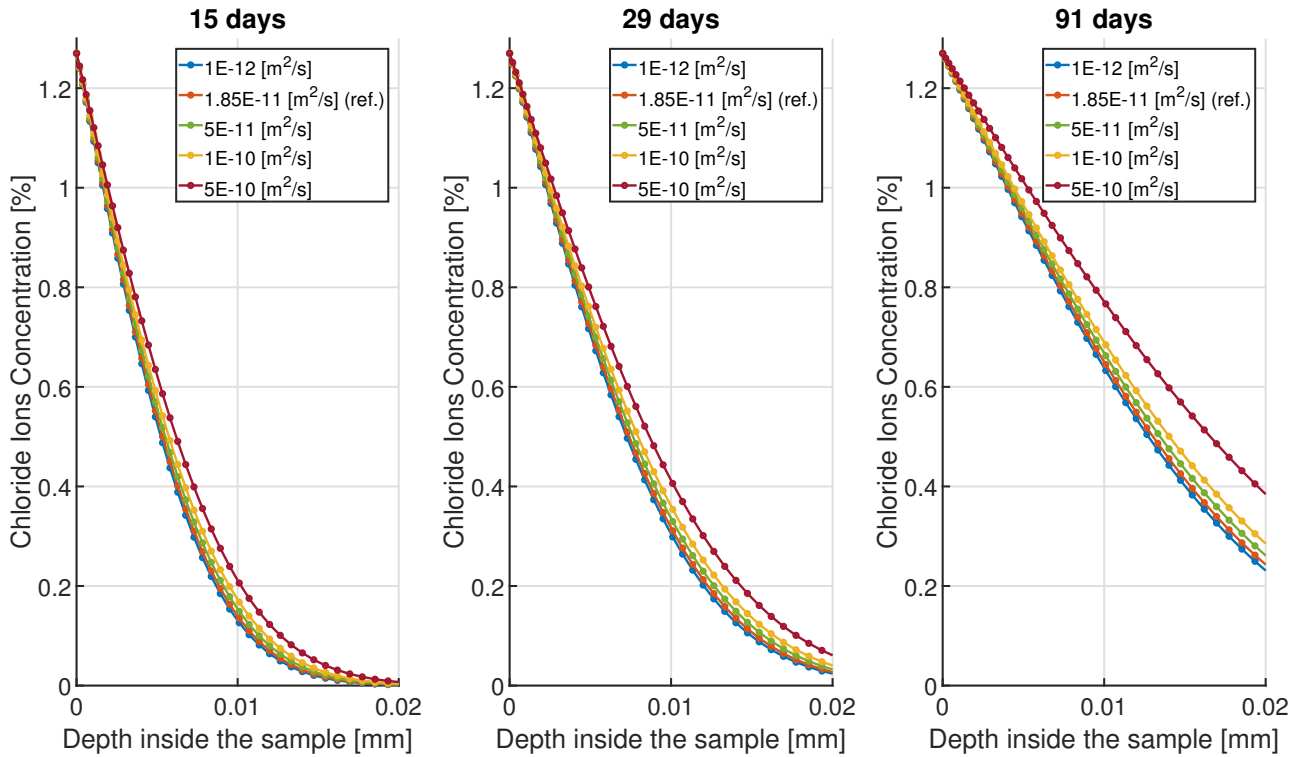
Figure 7.18: Chloride concentration profiles at 15, 29 and 91 days of simulation for different RCA's chloride diffusion coefficients.
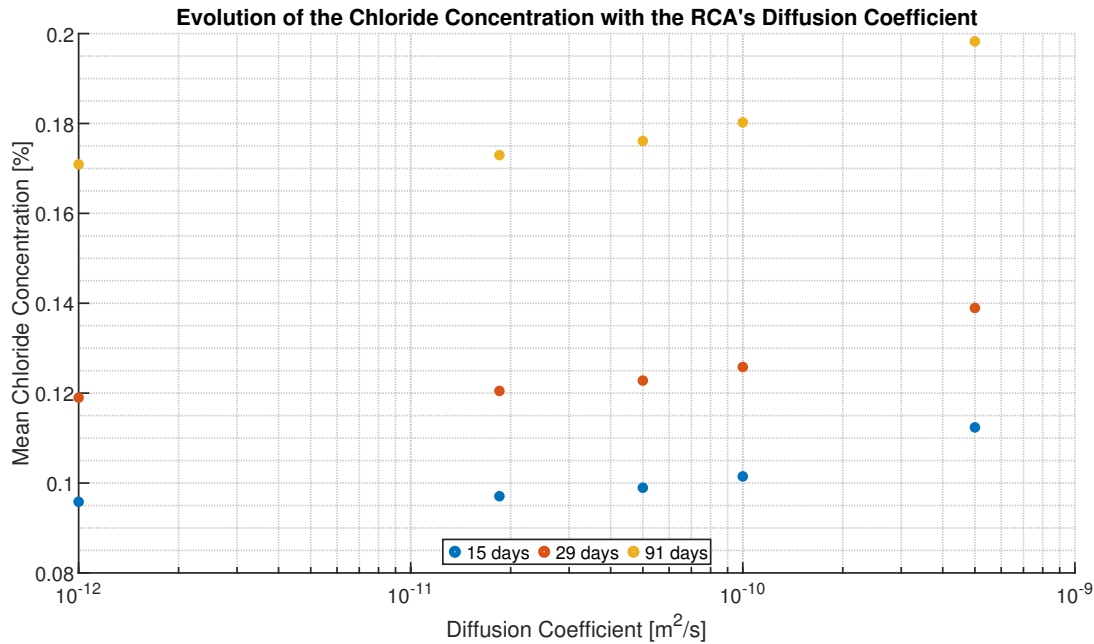
Figure 7.19: Evolution of the mean chloride content inside the sample with respect to the RCA's chloride diffusion coefficient.

It is clear that the relationship is not strictly linear, but rather follows a power law. Furthermore, the increase in mean chloride concentration is proportionally limited compared to the

rise in the chloride diffusion coefficient. This is supported by Table 7.5, which demonstrates that for a diffusion coefficient 27 times greater than the reference value, the chloride concentration is only 15% higher. The impact of the unknown diffusion coefficient of the RCA's adherent mortar on this model is thus considered limited. This is a positive aspect of our model as any errors would not completely invalidate the results. Furthermore, as the simulation runs for a longer period, the error tends to decrease.

Diffusion Coefficient [m²/s]	1E-12	1.85E-11 (Ref.)	5E-11	1E-10	5E-10
Diffusion Coefficient [% Ref.]	5.40	100	270.27	540.54	2702.70
Results at 15 days [% Ref.]	98.72	100	101.94	104.54	115.77
Results at 29 days [% Ref.]	98.75	100	101.91	104.41	115.31
Results at 91 days [% Ref.]	98.81	100	101.82	104.21	114.63

Table 7.5: The diffusion coefficients and mean chloride concentration at 15, 29, and 91 days expressed as percentages relative to the reference value.

7.4.2.1 Effective Diffusion Coefficient based on Relative Area of each Phase

Due to the nature of the multiscale model and the separation of time and space scales, mesoscale calculations are performed under the assumption of steady-state, as explained in Section 6.2.1. Under saturated conditions, the problem is somewhat linear. Therefore, one may question the necessity of a multiscale model and whether a single-scale model, using average diffusive properties over the relative area of each phase, is sufficient. This question will be investigated here.

Mortar Matrix's Properties					
Intrinsic Permeability [m²]	5.03E-18				
Porosity [% Volume]	29.68				
Diffusion Coefficient [m²/s]	1.85E-11				
Adherent Mortar's Properties					
Intrinsic Permeability [m²]	5.03E-18				
Porosity [% Volume]	29.68				
Diffusion Coefficient [m²/s]	1E-10	5E-10	1.85E-11	5E-11	1E-12
Average RVE's Properties					
Intrinsic Permeability [m²]	3.8178E-18				
Porosity [% Volume]	22.5271				
Diffusion Coefficient [m²/s]	1.607E-11	2.607E-11	1.404E-11	1.482E-11	1.360E-11

Table 7.6: Properties of the different phases for the sensitivity analysis of our model on the RCA's diffusion coefficient.

The Figure 7.17 shows the RVE used for the sensitivity analysis on the diffusive properties of the RCA. The RVE consists of 73.4% matrix mortar, 24.1% impervious recycled concrete aggregates, and 2.5% adherent mortar content. The following equation can be used to calculate an average diffusion coefficient:

$$D_{\text{average}} = 0.734 \times D_{\text{Mortar Matrix}} + 0.025 \times D_{\text{Adherent Mortar}} + 0.241 \times 0 \tag{7.3}$$

It should also be applied to the intrinsic permeability and porosity of each phase.

The simulations that were run for the sensitivity analysis on the RCA's diffusion coefficient were then repeated using a homogeneous RVE. This produces results similar to a single-scale model, with the average RVE properties mentioned in Table 7.6.
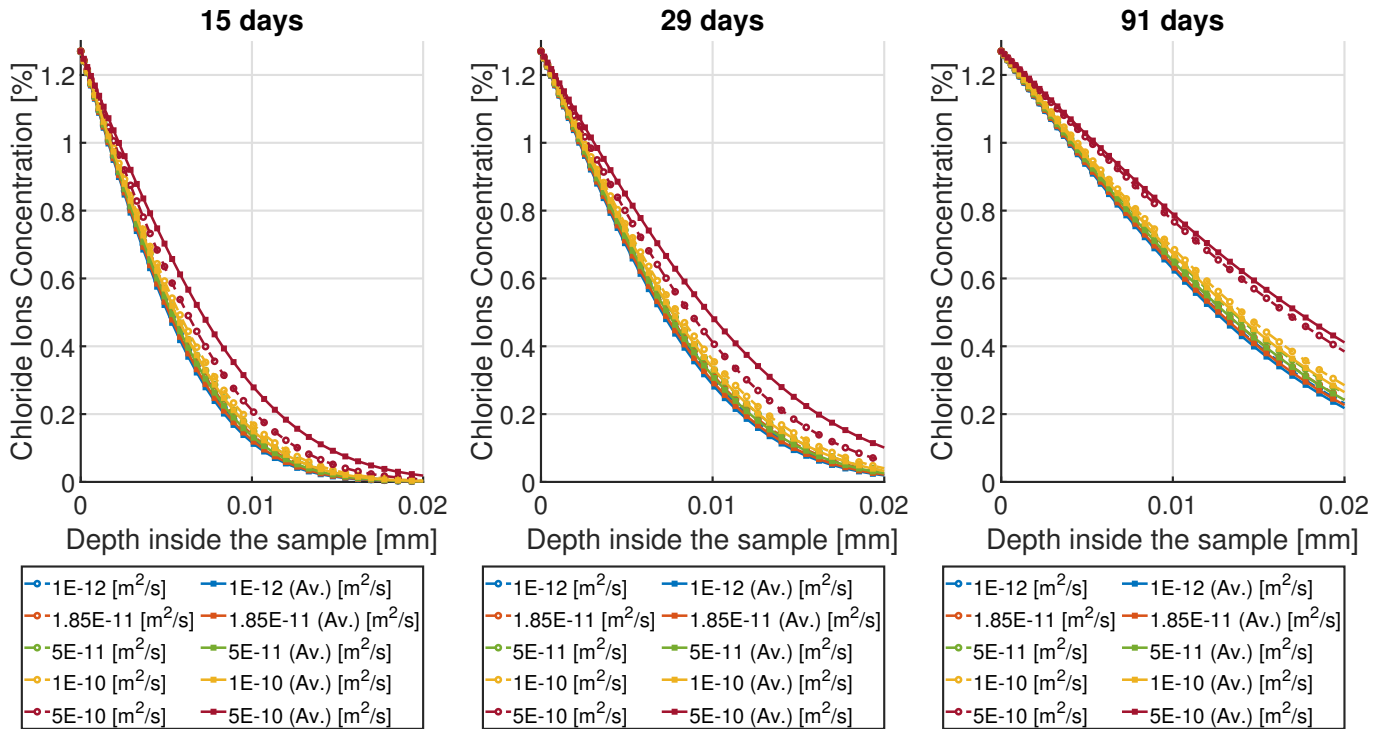
Figure 7.20: Chloride concentration profiles at 15, 29 and 91 days of simulation for different RCA's chloride diffusion coefficients, with a RVE or with average properties over the RVE.

Results of the analysis can be seen in Figures 7.20 and 7.21 in terms of chloride profile and mean chloride content inside the sample. It is evident that there are differences between the simulation with a RVE and the simulation without a RVE but with average properties. The reasons for these differences are various. The first issue is that the problem is not perfectly linear, while the second issue is related to the two-dimensional aspect of the representative volume element. In fact, with a RVE, the chloride flow is not only one-dimensional (as it is in the single-scale), but some fluxes are redirected due to the aggregates, which can slow the chloride ingress and induce flows along the y-axis, even though the boundary conditions are only along the x-axis.

This explanation could be valid for all tested diffusion coefficients except for the largest one. In this case, the mean chloride content increased instead of decreased after averaging the properties. This is because the averaged diffusion coefficient value is higher than the value of the mortar matrix's diffusion coefficient.
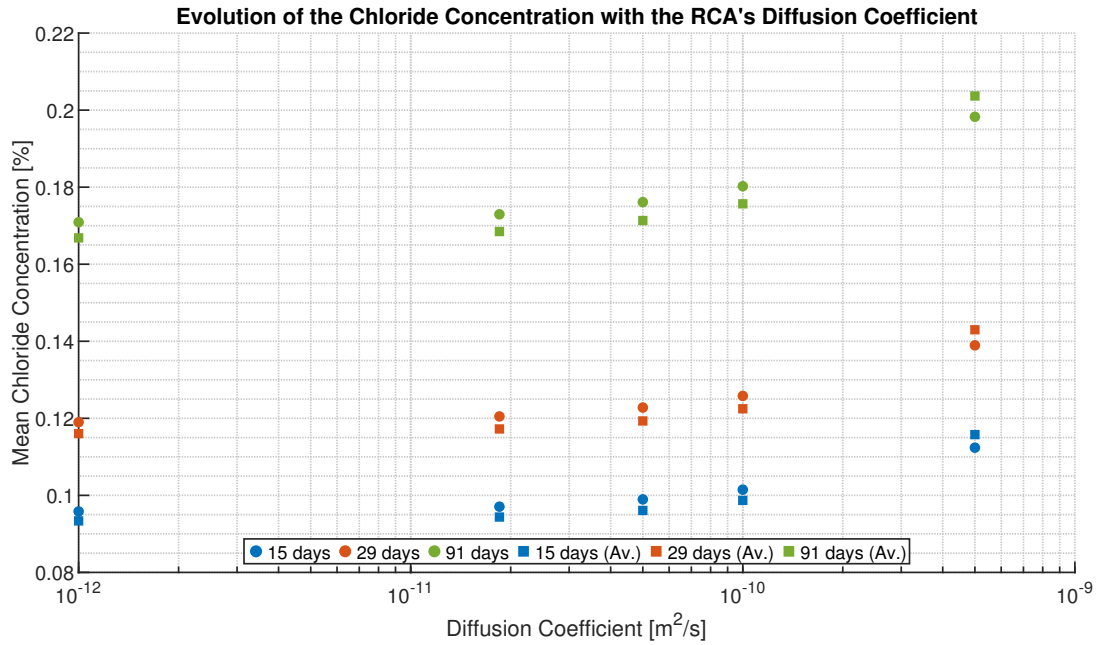
Figure 7.21: Evolution of the mean chloride content inside the sample with respect to the RCA's chloride diffusion coefficient, with a RVE or with average properties over the RVE.

7.4.3 Influence of the RCA's Cement Content

Another important parameter of the RCA is the adherent mortar content. The cement content of our recycled concrete aggregates was measured through the experiment described in Section 4.3.3.2, and is therefore known. However, the properties and quantities of adherent mortar in aggregates used in the industry can vary greatly. Therefore, a sensitivity analysis on the effect of the quantity of adherent mortar on our model's response is necessary. This will help predict whether determining the cement content for every batch of aggregates is critical or if a mean value could be used over time without any significant errors.

To conduct the sensitivity analysis, we will once again use the simulation of diffusion under unsteady-state, as described in Section 7.2.3. We will begin with a reference case, using the experimentally measured mortar content. We will then multiply this value several times and study the effects on the chloride content profile after 15, 29, and 91 days.
The results for the adherent mortar paste introduced into the RVE algorithm are presented in Table 7.7.

Simulation	Reference	Times 2	Times 3	Times 4	Times 7
Mortar paste (% overall surface)			66.3		
Adherent Mortar (% overall surface)	3.2	7.0	10.8	14.7	26.2
Adherent Mortar (% RCA' surface)	9.49	20.77	32.05	43.62	77.74

Table 7.7: Percentage of adherent mortar paste for all the simulations.
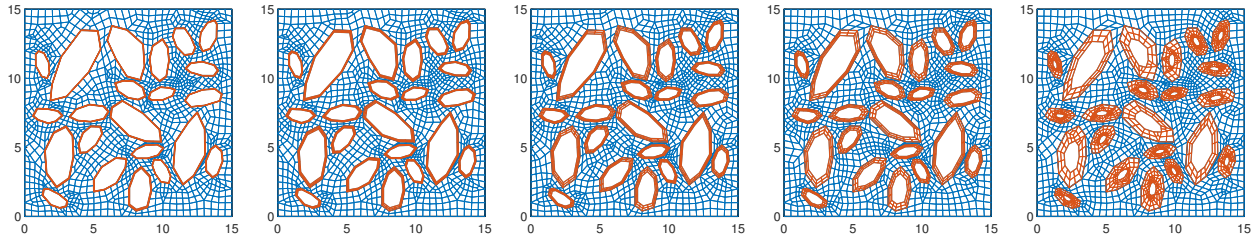
Figure 7.22: Mesh of the RAC RVEs used for the sensitivity analysis to the RCA's adherent mortar content.

Figure 7.22 displays the RVE used for each simulation, clearly showing the increase in adherent mortar content. Figure 7.23 presents the chloride profile for 15, 29 and 91 days of diffusion, for each RVE. The higher the adherent mortar content and the higher the chloride content is. This is supported by Figure 7.24, which shows the mean chloride concentration inside the sample at 15, 29, and 91 days for all RVEs. There appears to be a slight increase in mean chloride concentration with the increase in adherent mortar content, as expected.
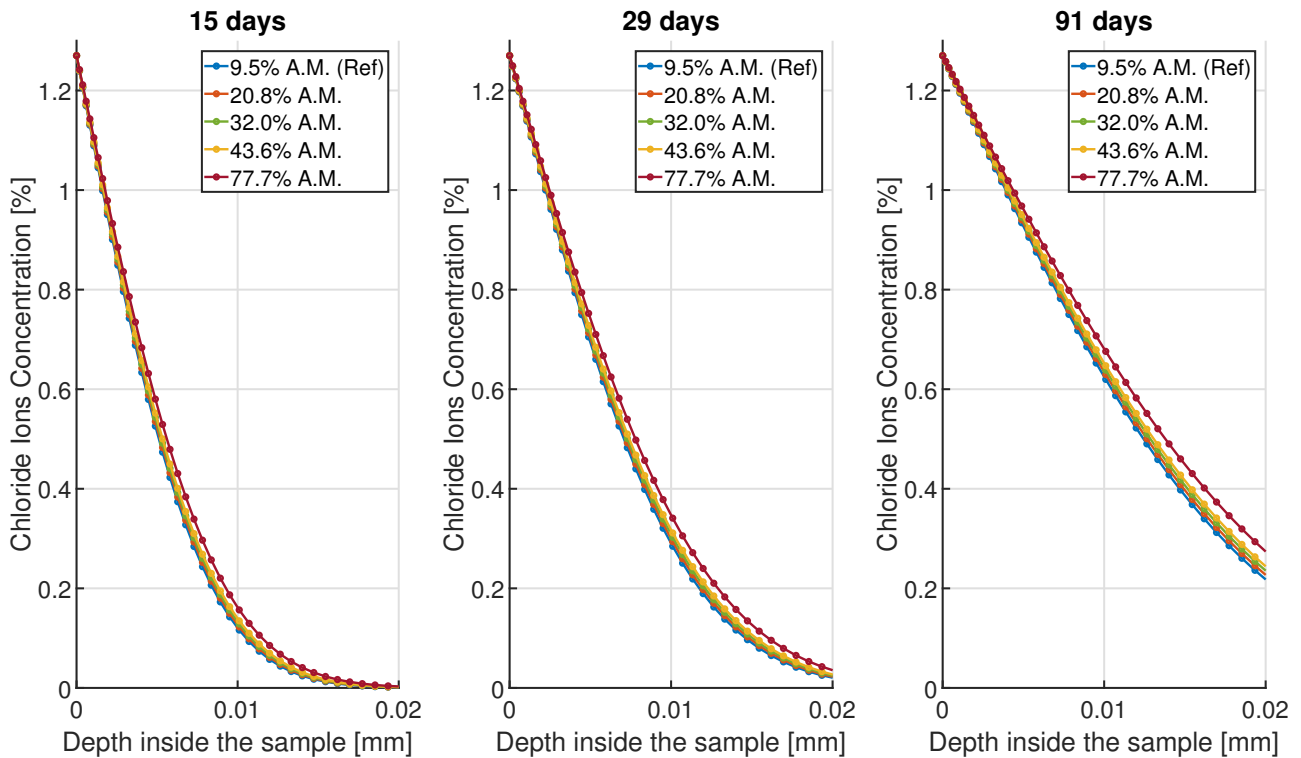
Figure 7.23: Chloride concentration profiles at 15, 29 and 91 days of simulation for different RCA's adherent mortar content.
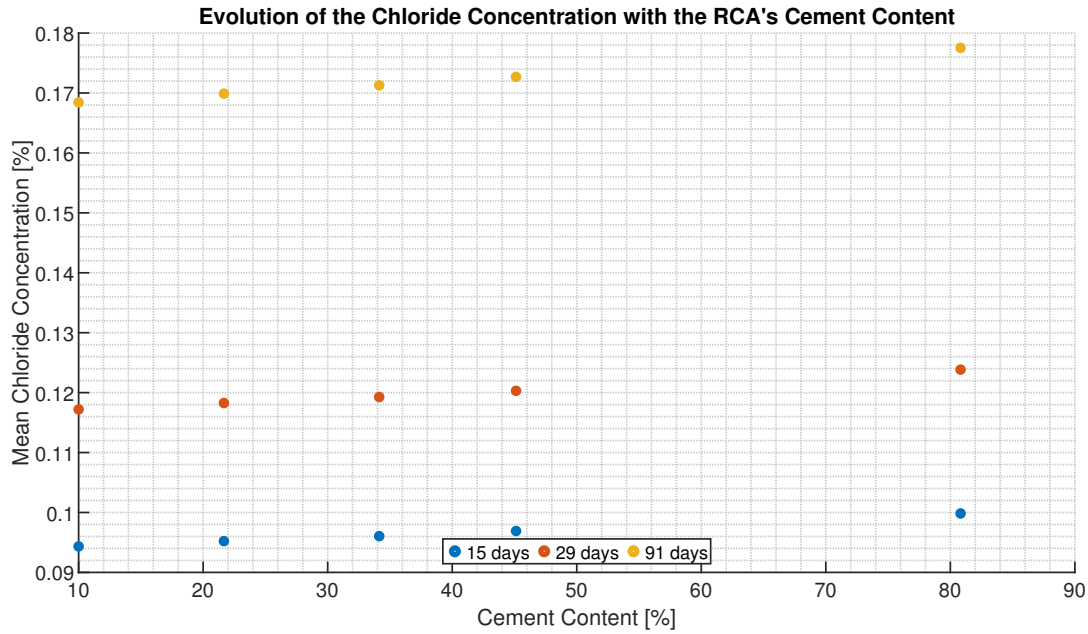
Figure 7.24: Evolution of the mean chloride content inside the sample with respect to the RCA's adherent mortar content.

Table 7.8 displays the relative percentage of adherent mortar and mean chloride concentration at 15, 29, and 91 days compared to the reference simulation. The results indicate that, for example, despite an increase of 118.7% in adherent mortar content (for the second RVE), the mean chloride concentration only increased by less than a percent.

Therefore, it appears that the quantity of adherent mortar content is not as crucial as one might expect. When the properties of the adherent mortar are equal to those of the plain mortar, the increase in chloride content appears to be negligible, even with a greater overall diffusive surface. The literature shows that cement content in recycled concrete aggregates can reach up to 50% for smaller aggregates [de Juan & Gutiérrez, 2009, Akbarnezhad et al., 2013, Florea & Brouwers, 2013]. Using this amount of adherent mortar content in our RVE would result in an approximate 3% increase in the mean chloride content, as our reference cement content would be multiplied by 5. The error in the mean chloride content due to the error in the adherent mortar content therefore seems acceptable in our model. However, if the diffusive properties of the adherent mortar were higher than those of the mortar matrix, the results may differ.

Simulation	Reference	Times 2	Times 3	Times 4	Times 7
Adherent Mortar (% Ref.)	100	218.7	337.5	459.4	818.7
Results at 15 days (% Ref.)	100	100.93	101.81	102.72	105.83
Results at 29 days (% Ref.)	100	100.91	101.76	102.65	105.66
Results at 91 days (% Ref.)	100	100.87	101.68	102.53	105.40

Table 7.8: Relative percentage of adherent mortar content and mean concentration at 15, 29 and 91 days compared to the reference simulation.

7.4.3.1 Influence of the Adherent Mortar Content with Increased Diffusive Properties

As stated in the previous sensitivity analysis on the adherent mortar content of the RCA, the small influence it has on the response of the model may be due to the properties of the adherent mortar that were taken equal to the one of the matrix mortar for that example. A new study was therefore performed by multiplying the intrinsic water permeability and the chloride diffusion coefficient by ten, while multiplying the porosity by two, for the adherent mortar.
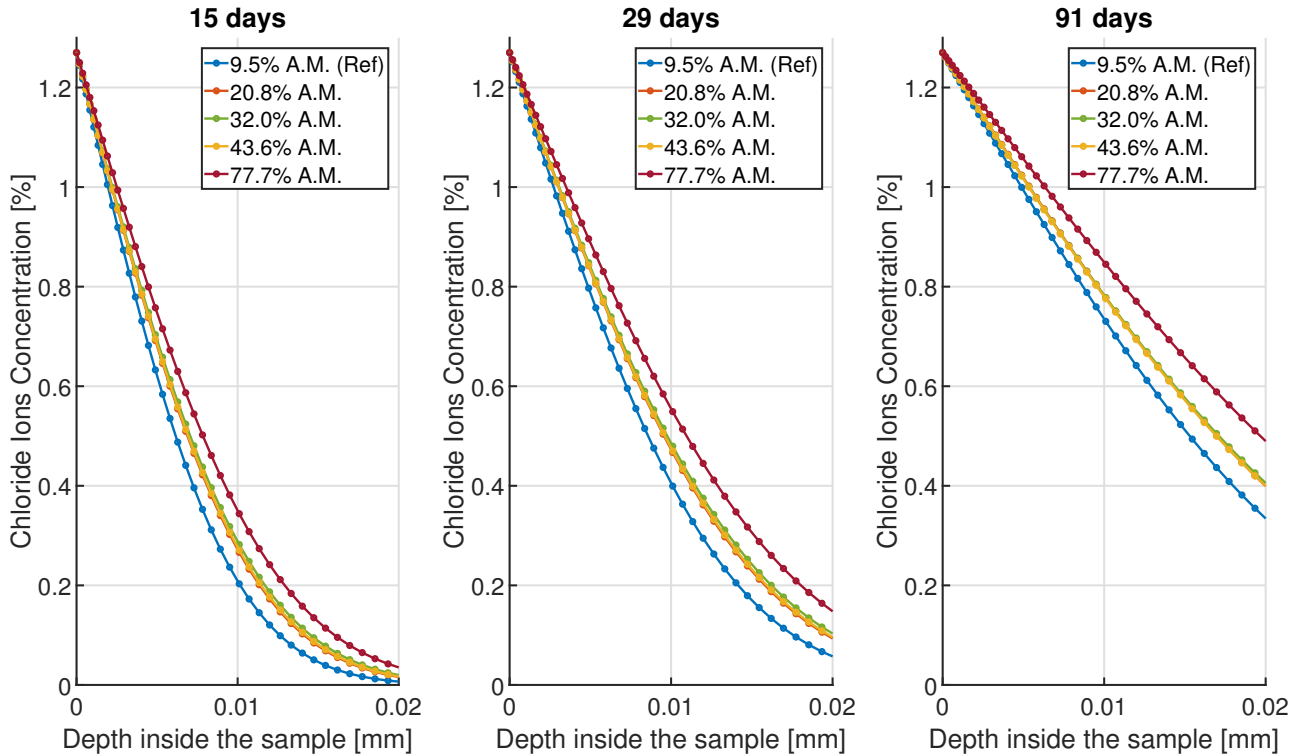
Figure 7.25: Chloride concentration profiles at 15, 29 and 91 days of simulation for different RCA's adherent mortar content, after increasing the properties of the adherent mortar.

Results are shown in Figures 7.25 and 7.26 in terms of chloride profile and mean chloride content over the sample, respectively. One can see that this time, as the diffusive properties are increased, the trend in between the simulations is clearer, with the chloride content increasing along with the adherent mortar content. In terms of percentage, as shown in Table 7.9, the increase in the mean chloride concentration stays limited, even with diffusive properties ten times higher than previously.

It can be observed that in the 'Times 4' simulation, the chloride content is lower than in the 'Times 3' simulation. This is difficult to explain as the RVE in this case has a higher mortar content, resulting in a larger diffusive surface area, with properties equal to all other simulations. The chloride content should be higher than that of the 'Times 3' case.
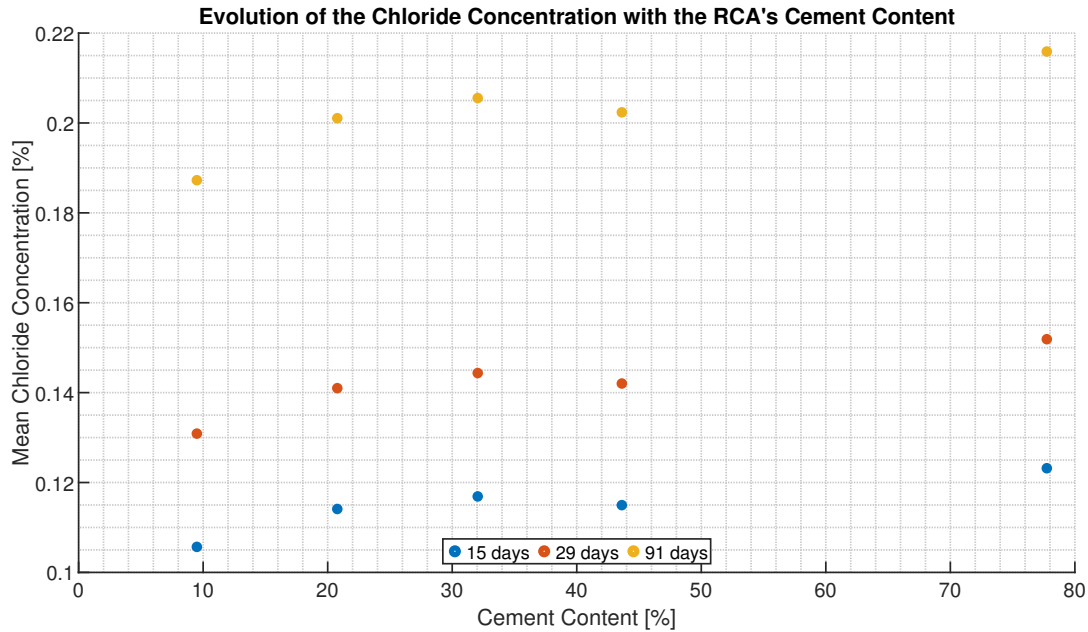
Figure 7.26: Evolution of the mean chloride content inside the sample with respect to the RCA's adherent mortar content, after increasing the properties of the adherent mortar.

Simulation	Reference	Times 2	Times 3	Times 4	Times 7
Adherent Mortar (% Ref.)	100	218.7	337.5	459.4	818.7
Results at 15 days (% Ref.)	100	107.97	110.62	108.78	116.56
Results at 29 days (% Ref.)	100	107.73	110.29	108.51	116.05
Results at 91 days (% Ref.)	100	107.37	109.76	108.07	115.29

Table 7.9: Relative percentage of adherent mortar content and mean concentration at 15, 29 and 91 days compared to the reference simulation, after increasing the properties of the adherent mortar.

7.4.3.2 Influence of the Adherent Mortar Content on the Overall RVE Porosity

It is known that the adherent mortar of the recycled concrete aggregates introduces a higher porosity into the concrete. It would therefore be appropriate to quantify this increase in porosity by calculating the total porosity in relation to the surface area of each component. In fact, the mortar matrix and the adherent mortar both have a porosity of 29.68%, which corresponds to the porosity obtained experimentally for E-M, increased by 30% as explained earlier in the experimental validation.

The total porosity is calculated and presented in Table 7.10. As a reminder, the experimentally obtained porosity for the RAC is equal to 20.5%, which is approximately what was found for the reference case with our experimentally determined cement content. By multiplying the adherent mortar content by 7, the porosity only increased by about 7%, which is quite acceptable for recycled concrete aggregates composed of 77.74% adherent mortar.

Simulation	Reference	Times 2	Times 3	Times 4	Times 7
Mortar paste (% overall surface)			66.3		
Adherent Mortar (% overall surface)	3.2	7.0	10.8	14.7	26.2
Adherent Mortar (% RCA' surface)	9.49	20.77	32.05	43.62	77.74
Overall Porosity (% Volume)	20.63	21.75	22.88	24.04	27.45

Table 7.10: Overall porosity of the RVE.

7.5   Influence of the Hysteresis Parameters

The implementation of the hysteresis of the water retention curve requires controlling several parameters. These include the parameter b, which influences the gradient of the scanning curve [Zhou et al., 2012], and the increment of suction ds.

The first parameter is obtained experimentally by fitting, although sorption and desorption experiments can be slow and laborious, particularly when observing hysteresis. Additionally, the experimental work in this research has demonstrated that a single value of b may not satisfy the same material, depending on its history. Therefore, it is crucial to understand the effect of this parameter b on our model's response to characterise its significance.
The second parameter, the increment of suction ds, is dependent on the time step of our numerical simulations and the applied suction increment. The model is more prone to error with larger time steps and/or suction increments. Navigation through the water retention curve and its hysteresis is achieved by calculating derivatives to the water retention curves, using the suction increment. Overshooting the correct degree of saturation is more likely with larger steps and the resulting greater interpolation.

The following two sections examine the impact of each parameter. As the mesoscale is composed of permeable mortar, the implemented mesoscale properties (porosity, intrinsic permeability, and chloride diffusion coefficient) are those of the E-M composition, multiplied by 1.3 to account for the difference between a 2D and 3D model. The water retention curve, however, is considered a macroscale property. The parameters implemented correspond to either NAC or RAC, depending on the mesoscale used. Figure 7.27 shows the two mesoscale representative volume elements modelled for the NAC and RAC used in this sensitivity analysis. The macroscale represents a 1D sample that is 10cm long (Figure 7.28).
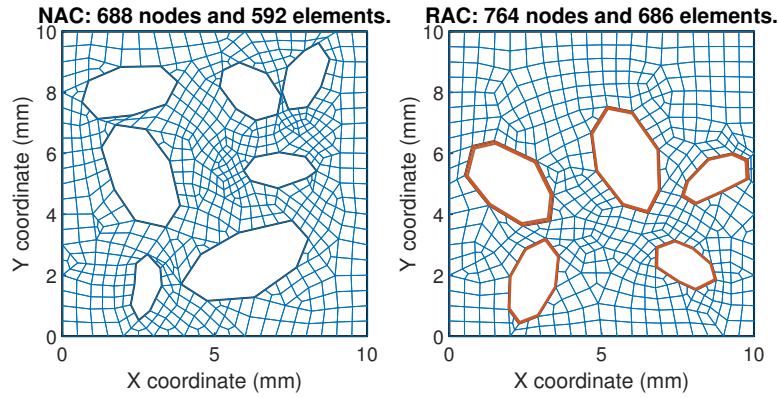
Figure 7.27: RVE representing the mesoscale of both NAC (left) and RAC (right), with properties of the E-M composition for the blue mortar phase (new mortar matrix) and the same properties for the orange mortar phase (adherent mortar of the RCA).
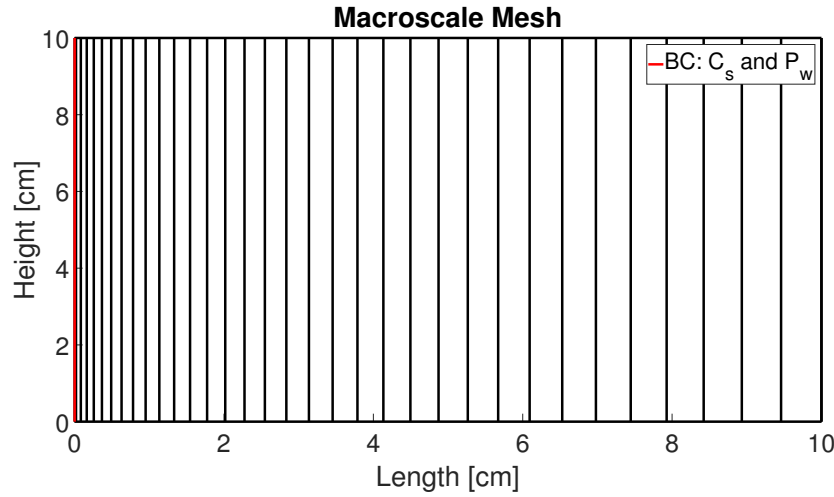
Figure 7.28: Macroscale mesh for the study of the influence of both the increment of suction and the parameter b on the hysteresis model.

7.5.1   Influence of the Increment of Suction

The increment of suction is the first parameter of the hysteresis model studied, and is considered the most important. A preliminary study was conducted using MATLAB, and the results are presented in Figures 7.29 and 7.30 (zoomed in). Figure 7.29 displays two solutions for the extremum values of b determined experimentally. Various suction increments were employed, with each boundary condition divided into 10, 100 or 1000 equal sub-increments. As shown, increasing the number of sub-increments results in a smaller suction increment (ds) and a more precise degree of saturation for a given suction. Figure 7.30 displays the same results, but with a closer view of the hysteresis section of the simulation. The variation in refinement results in a difference in the degree of saturation of the porous medium, even when the same suction value is applied as a boundary condition. The degree of difference may be significant, depending on the number of sub-increments applied.
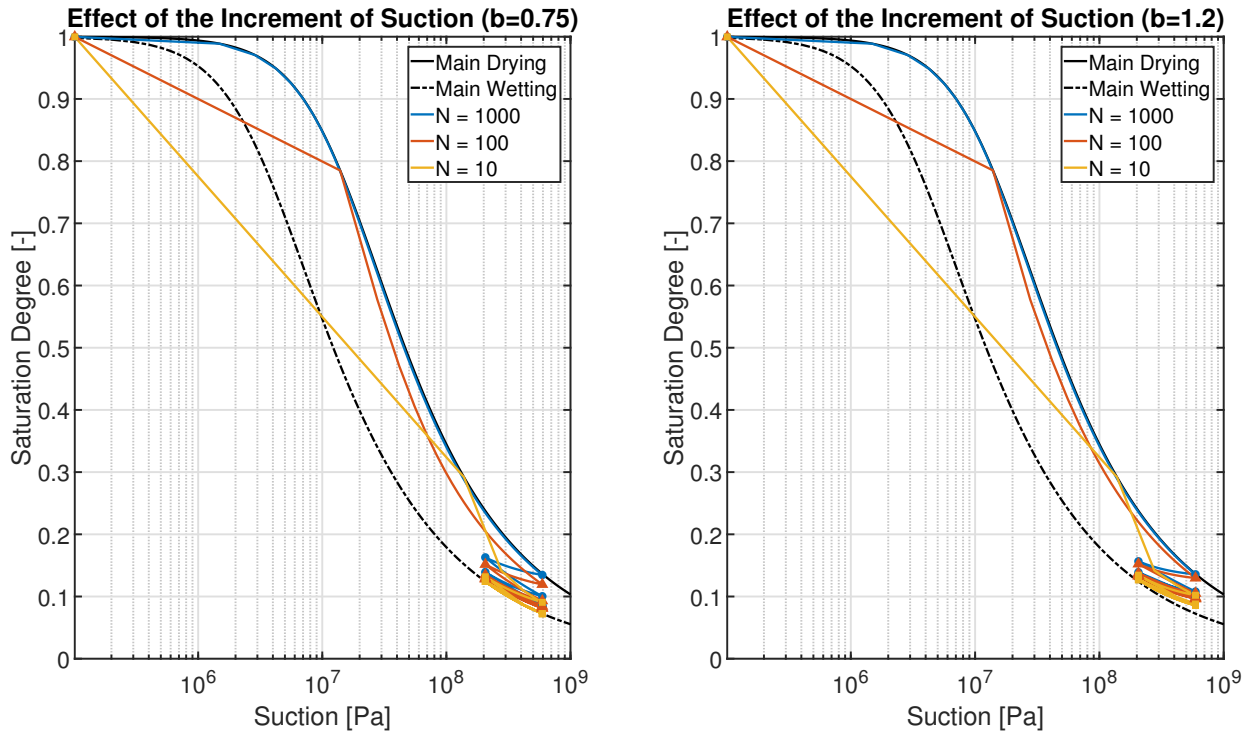
Figure 7.29: Effect of the increment of suction on the hysteresis model, for two limit values of b found experimentally. N is the number of sub-increments implemented.
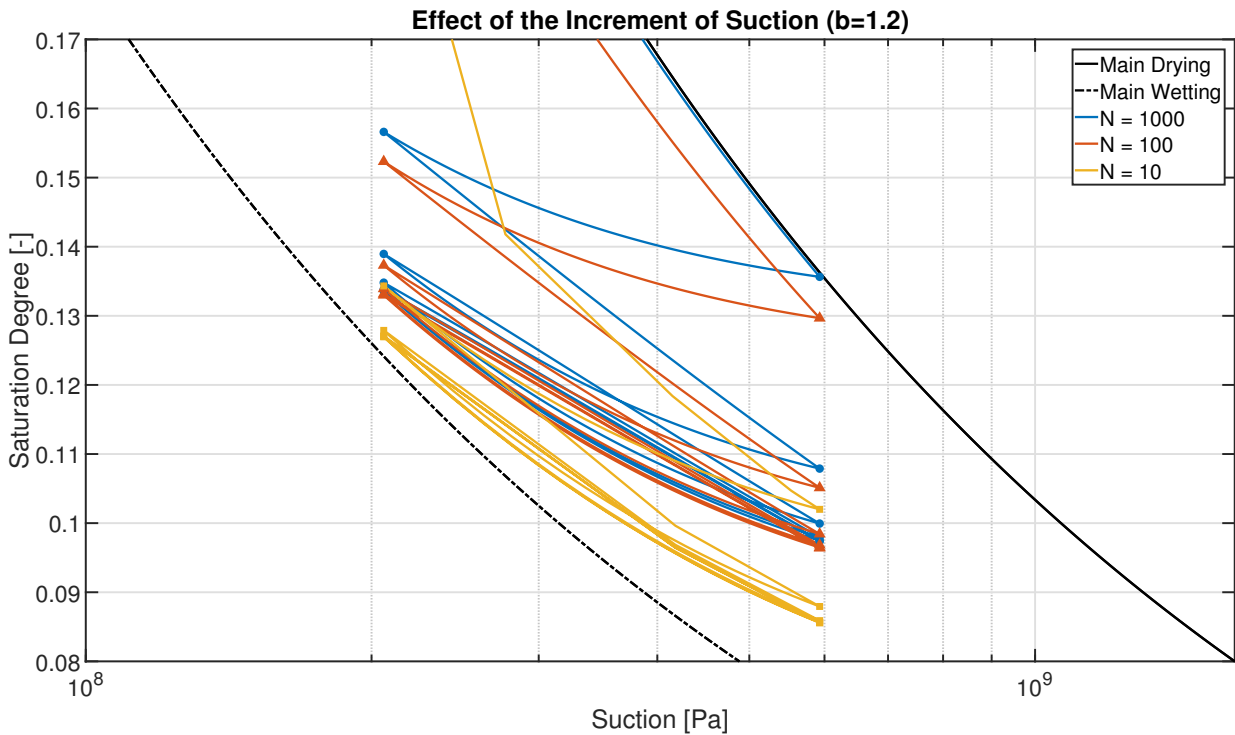
Figure 7.30: Zoom in of Figure 7.29 for $b = 1.2$. N is the number of sub-increments implemented.

A simulation was then performed using the developed multiscale model. The macroscale mesh and the boundary conditions are shown in Figures 7.28 and 7.31. The hysteresis was

defined with a sub-increment of suction equal to the air-entry pressure at the maximum, or even smaller by dividing it by an integer N. The results are presented in Figure 7.32. The sub-incrementation of the suction to navigate the hysteresis improved the accuracy of the results. Although there may be a slight difference between the shown curves, it is negligible at this point. The two vertical curves represent the suctions obtained through the boundary conditions. The conclusion is that to obtain accurate results from the hysteresis model, it is sufficient and necessary to impose a maximum increment of suction equal to the air-entry pressure.
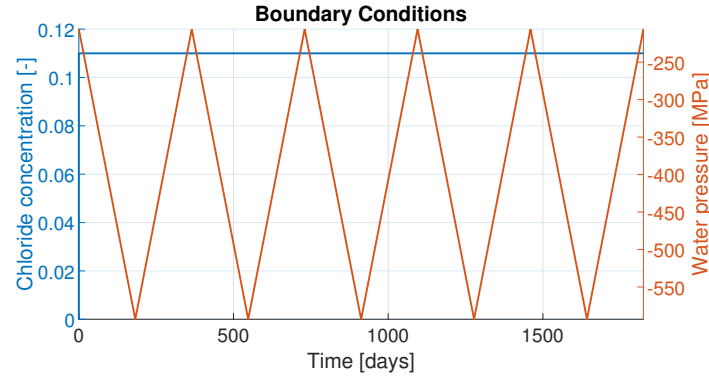
Figure 7.31: Boundary conditions for the study of the influence of the increment of suction on the hysteresis model.
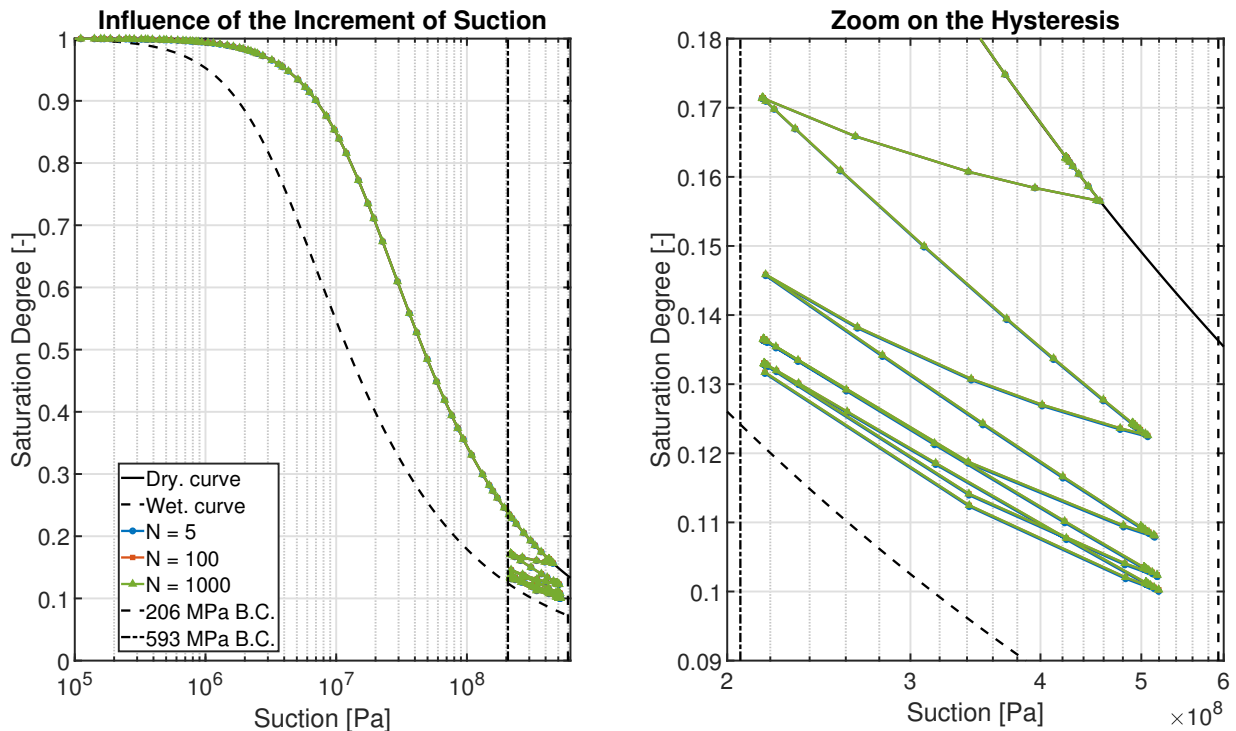
Figure 7.32: Influence of the increment of suction on a simulation in the multiscale model for $b = 1$. N is the number of sub-increments implemented.

7.5.2 Influence of Parameter b

The second parameter studied is b, a positive, dimensionless value that controls the slope of the hysteresis scanning curve. This curve ranges from parallel to the main water retention curve (b closer to zero) to horizontal (b closer to infinity). Figure 7.34 displays the results of our multiscale model for a NAC and RAC RVE, and for various values of b. Two simulations were conducted without the hysteresis of the water retention curve, using properties of the boundary drying or wetting curves.

The initial water pressure conditions inside the sample were equal to the atmospheric pressure. The pressure on the outside border is changed bi-annually to -2MPa and -200MPa for a period of ten years. Furthermore, the outside border is set to have a chloride content of 0.11 [-], while the inside of the sample is initially devoid of chloride. The macroscale mesh and the boundary conditions are shown in Figures 7.28 and 7.33.
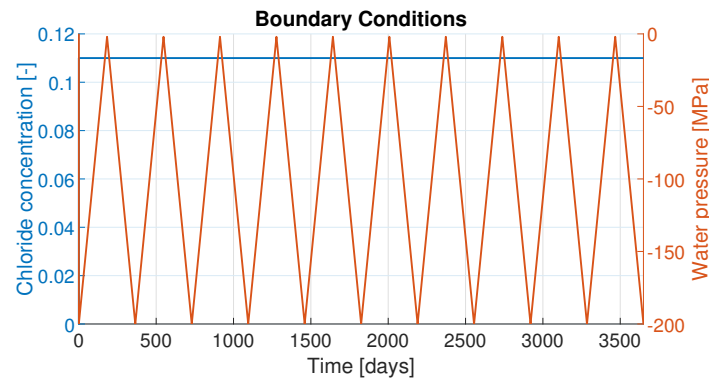
Figure 7.33: Boundary conditions for the study of the influence of the parameter b on the hysteresis model.
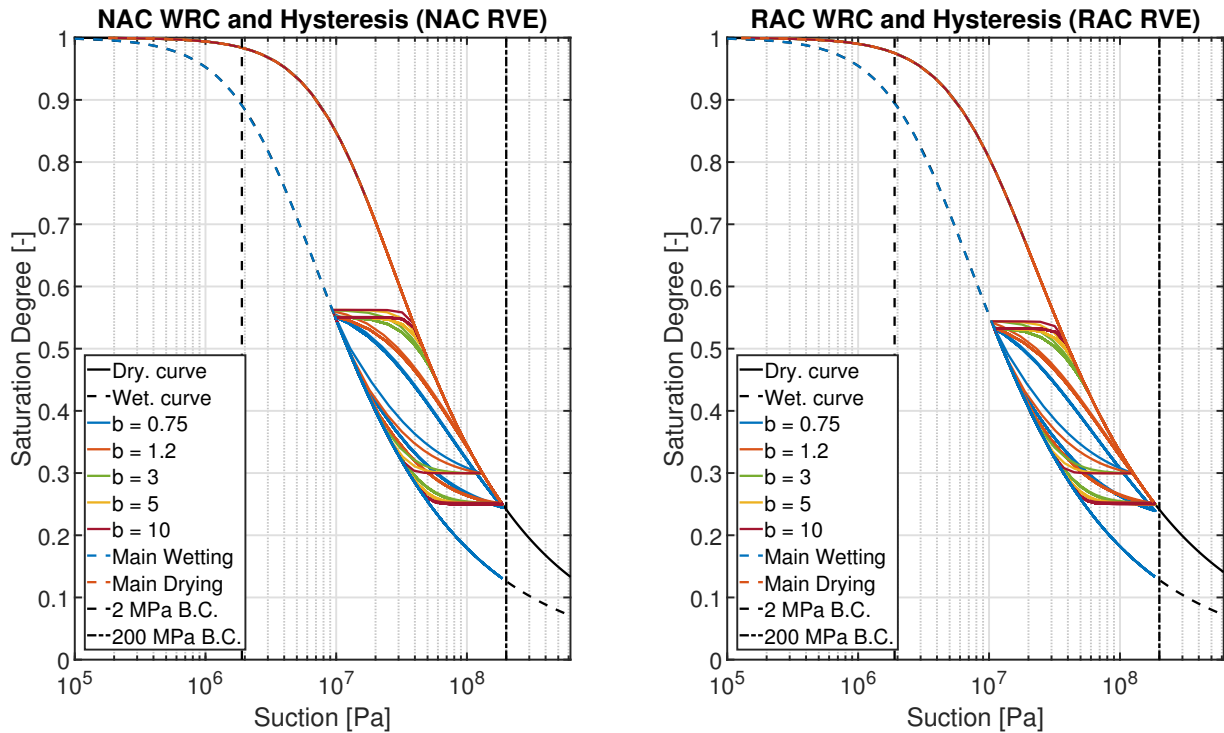
Figure 7.34: Influence of the parameter b on the hysteresis model: Water Retention Curves for the NAC and RAC.

The higher the value of b, the faster the hysteresis reaches the boundary curves. Additionally, the saturation degree throughout the NAC has a greater variation range than the RAC RVE.

This is confirmed by Figure 7.35, which shows the evolution of the saturation degree at the surface of exchange of the concrete for both the NAC and RAC. It is evident that the hysteresis curves approach the main boundary curves during both drying and wetting phases. The transition slope becomes more horizontal with an increase in the value of b, which relates to a faster convergence of the hysteresis curves to the boundary curves.
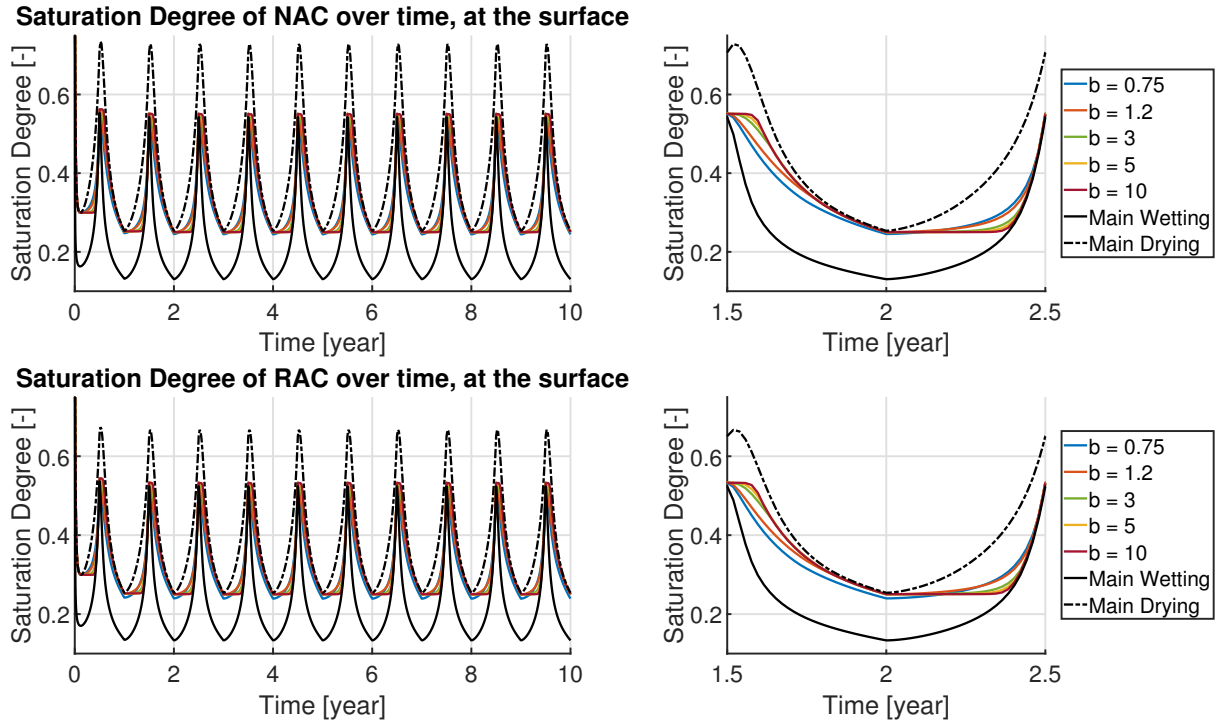
Figure 7.35: Influence of the parameter b on the hysteresis model: Water Saturation Degree of NAC and RAC at the surface over a ten-year period (left), with a focus on a specific year (right).

Figures 7.36 and 7.37 show the chloride content evolution at depths of 0cm, 2cm, 5cm, and 10cm inside the sample for both NAC and RAC over a ten-year period. Additionally, the results are presented in Figure 7.38 at a depth of 3cm only.

As the value of b increases, the variations between drying and wetting phases decrease and the water saturation degree evolves more linearly. Consequently, the chloride content tends to be higher for greater values of b, with a negligible difference for values of 3 and above. Using a higher value of b is therefore conservative due to the overestimation of the chloride content.

Furthermore, the impact of the boundary conditions is smaller at greater depth, the diffusion being predominant over the advection of chloride ions. At the surface, the difference between the values of b is negligible due to the applied boundary conditions.

Additionally, it may be concluded that higher saturation degrees and chloride contents are positively correlated, as supported by simulations without hysteresis. Indeed, the sample with the boundary drying curve consistently exhibits higher chloride content than the one with the boundary wetting.
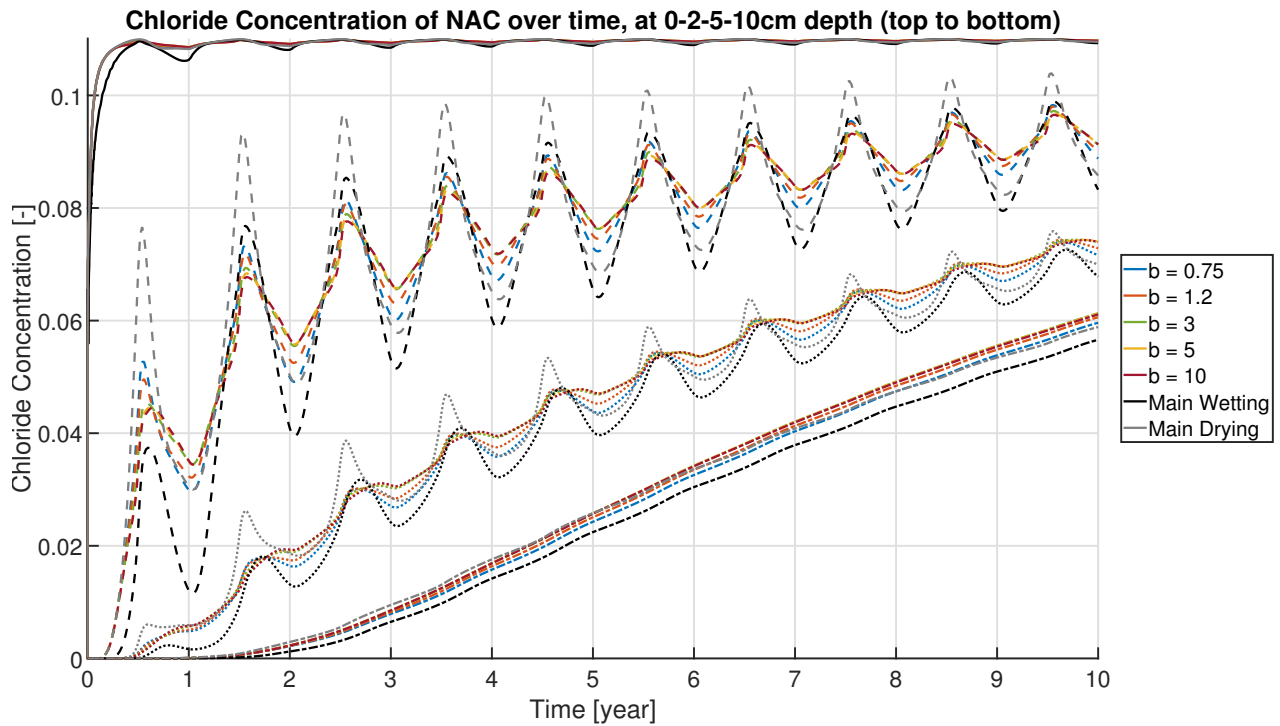
Figure 7.36: Influence of the parameter b on the hysteresis model: Chloride Content of NAC at 0, 2, 5 and 10cm depth over a ten-year period.
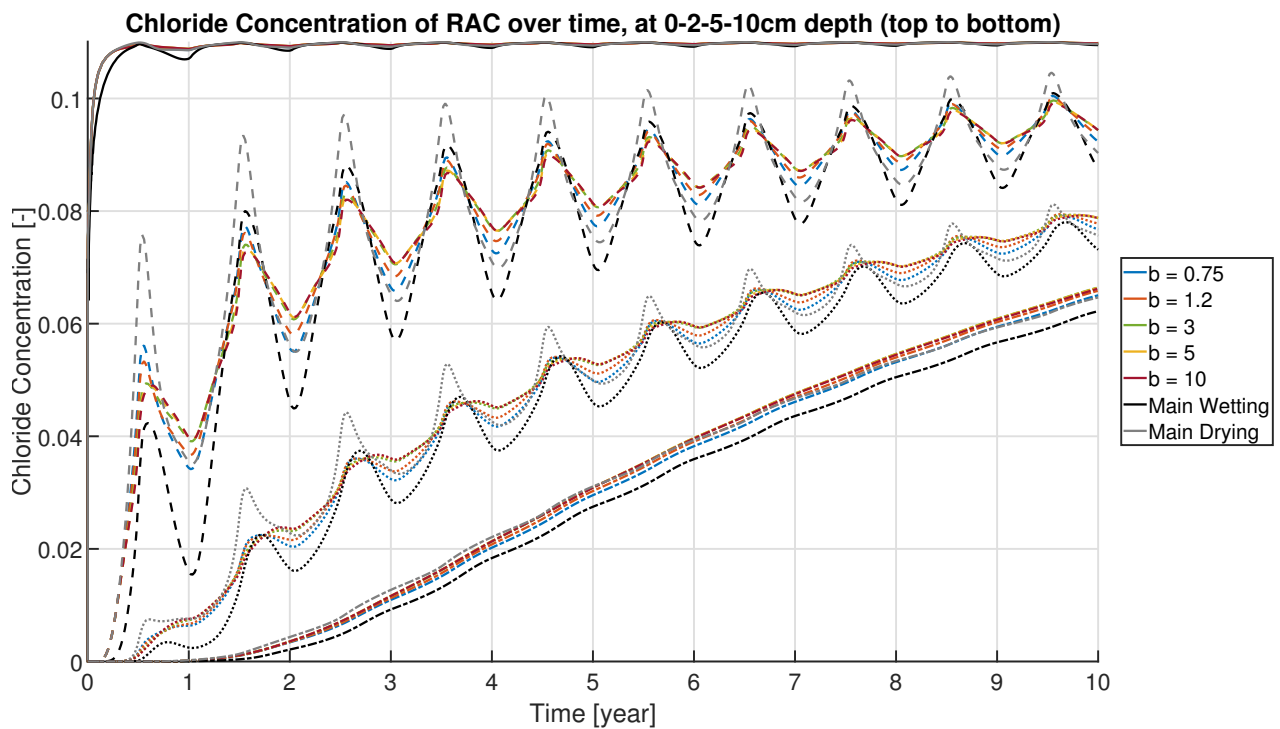
Figure 7.37: Influence of the parameter b on the hysteresis model: Chloride Content of RAC at 0, 2, 5 and 10cm depth over a ten-year period.
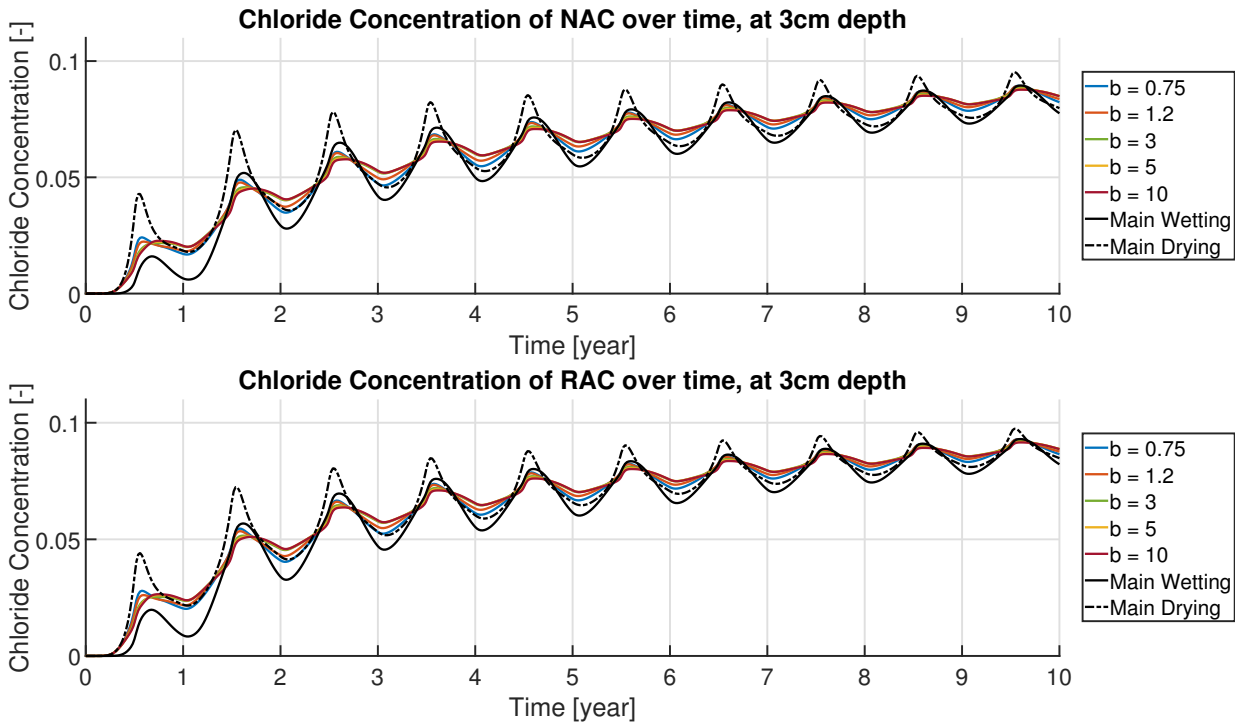
Figure 7.38: Influence of the parameter b on the hysteresis model: Chloride Content of NAC and RAC at 3cm depth over a ten-year period.
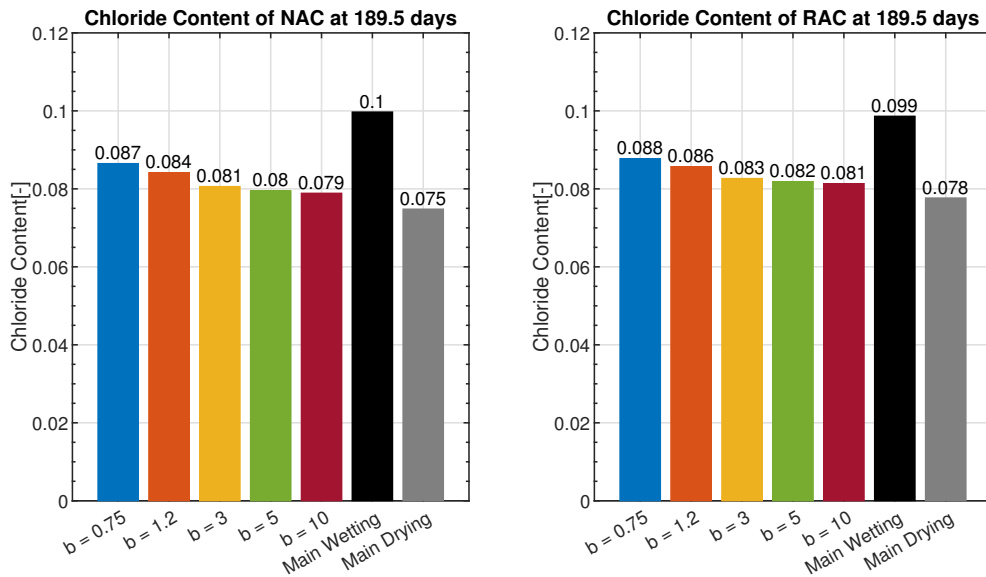
Figure 7.39: Mean chloride content of NAC and RAC over 2cm depth, at 189 days.

Figures 7.39 to 7.41 represent the mean chloride content for each value of b, from 0cm to 2cm depths, at different times. Figure 7.39 corresponds to the end of a wetting phase, while Figure 7.40 represents the end of a drying phase. It can be demonstrated that the greater the value of b, the smaller the variations in chloride content. Furthermore, after 10 years (Figure 7.41), the chloride content is indeed higher for higher values of b, although the difference is negligible.

Therefore, it is necessary to implement the hysteresis model to obtain accurate chloride

content values, as the results without hysteresis are greatly different. Furthermore, it is necessary to employ the correct value of b, which can be obtained through experimentation, to prevent overestimation of the chloride content within the sample. However, if experimental work is to be excluded, the error should not be significant, especially as the differences between several values of b tend to decrease with time.
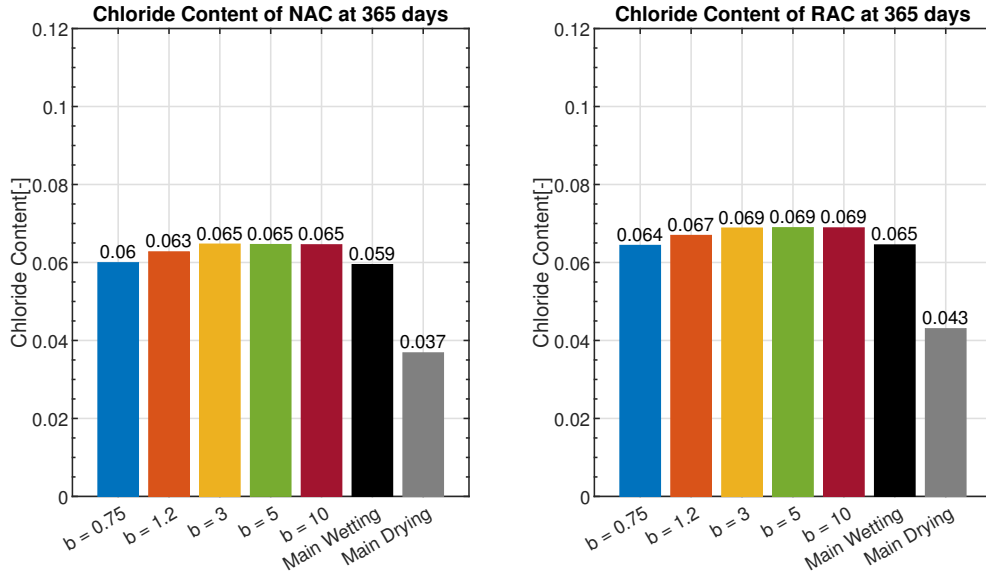
Figure 7.40: Mean chloride content of NAC and RAC over 2cm depth, at 365 days.
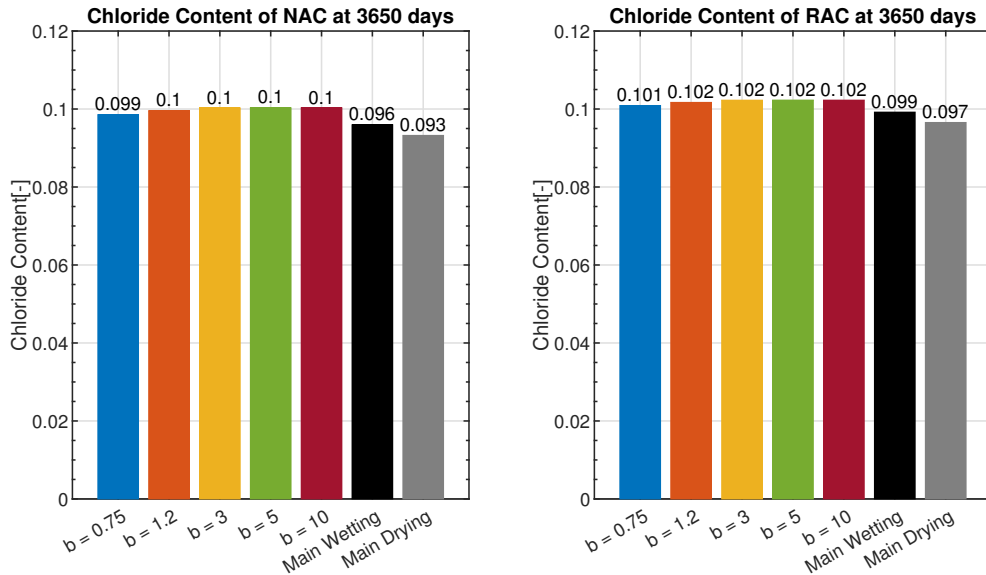
Figure 7.41: Mean chloride content of NAC and RAC over 2cm depth, at 3650 days.

7.6 Conclusion of the Numerical Results

This chapter and the previous one present the numerical multiscale model developed in this thesis. The model has been validated and used for a sensitivity analysis on the RVE and

water retention curves.

The validation process demonstrated that the model can accurately replicate analytical solutions under saturated conditions or numerical results of a simple-scale model under unsaturated conditions. The experimental validation has concluded that to reduce the 2D-3D errors, the porosity, diffusivity and permeability of the materials should be increased by 30%. Additionally, it has been demonstrated that the multiscale model can accurately represent the behaviour of concrete by using a RVE that represents concrete with the intrinsic properties of plain mortar.

A sensitivity analysis was then performed on the Representative Volume Element. It was concluded that the optimum RVE size to maximize accuracy while minimizing computation cost is 15mm. Lower sized RVEs are faster to compute but tend to overestimate the chloride content inside the sample.
When using RCA, the value of the diffusion coefficient of the adherent mortar paste does not play a significant role in chloride diffusion. Increasing the diffusion coefficient to 2700% resulted in only a 15% increase in chloride content after 91 days. The study also examined the effect of adherent mortar content, which showed that increasing the quantity of adherent mortar to 820% only led to a 5% increase in chloride content after 91 days. Furthermore, the total porosity of the RVE only increased by 3.4%, which is negligible compared to the initial 20.6%.
The study also examined the need for a Representative Volume Element, by comparing the results of our multiscale model with those of a single-scale model. The single-scale model had properties equivalent to the RVE properties averaged over the relative surface of each phase. The study concluded that the RVE is necessary to obtain accurate results. The single-scale model with averaged properties yielded a greater chloride content than the multiscale model. This could be due to the 2D aspect of the RVE and the non-linearities of the model, such as the spatial distribution of aggregates.

Finally, a sensitivity analysis was conducted on the parameters of the hysteresis of the water retention curve. The impact of the fitting parameter b on the water saturation degree was demonstrated, highlighting the need for calibration with experimental results. The study also examined the effect of the increment of suction and concluded that a maximum increment equal to the air-entry pressure resulted in greater numerical accuracy.

8

APPLICATION TO A REAL LIFE SCENARIO

Contents

8.1 Introduction

The aim of this study is, ultimately, to predict the effect of substituting natural aggregates with recycled concrete aggregates on the service life of a reinforced concrete structure. Once the experimental campaign is completed, and the numerical multiscale model is validated, it is possible to fulfill that objective.

Figure 8.1: Example of a maritime lock [Gärtner, 2022].

To investigate the difference in durability between natural aggregate concrete and recycled aggregate concrete, an application was developed using a realistic scenario. The study focused on a reinforced concrete lock wall in direct contact with salt water, which is the most critical environment in terms of chloride attack. An example of a maritime lock is shown in Figure 8.1.

8.2 Boundary Conditions and Parameters

The modelled maritime lock wall is in contact with water on both sides. Assuming symmetry in loading and response, the wall is divided into two parts in the model. Figure 8.2 shows the model of the lock wall, which is 1m wide (50cm in the model), 4m high above the water, and 2m deep below the water. Although a real lock wall would be deeper than this, the response is assumed to be constant under 2m of water. The wall has thus been cropped to reduce the time needed to run the simulations. A transition zone is defined between the hydrostatic and atmospheric conditions to smooth the gradient of the water pressure applied to the wall.
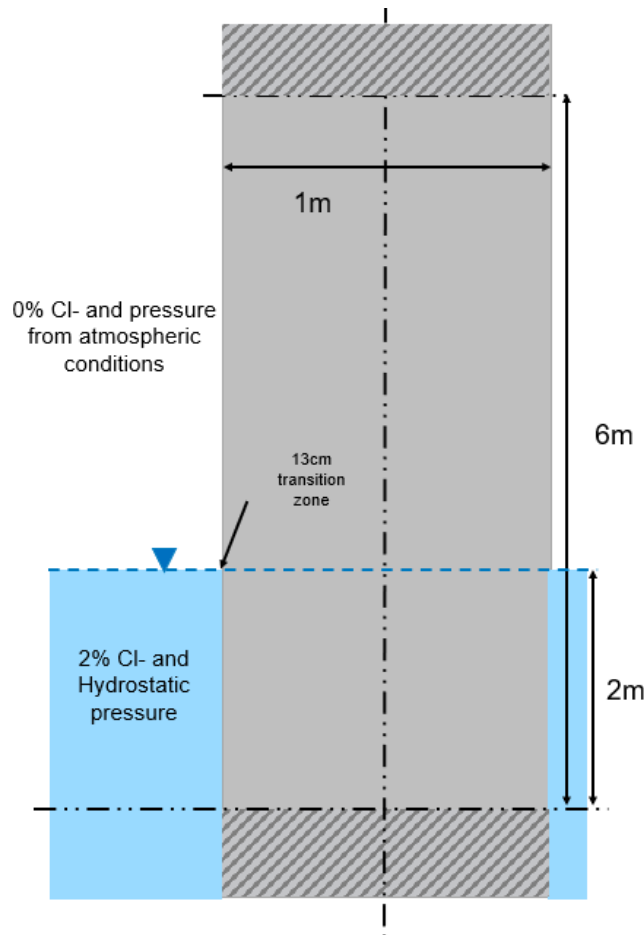
Figure 8.2: Representation of the lock wall modelled.

The environmental conditions are those of the study conducted by Zuquan et al. (2018) [Zuquan et al., 2018], and are shown in Table 8.1. The chloride concentration in salt water was chosen to be equal to 17g/L, or approximately 2% of the water density [Zuquan et al., 2018]. The chloride content was converted into a surface concentration using the subsequent equation:

$$C_s[\%] = 17 \, [\text{g/L Cl}^-] \, \frac{n \, [\% \text{ volume}]}{\rho_d \, [\text{kg/m}^3]} \tag{8.1}$$

resulting in a surface concentration of 0.11% for the NAC and 0.17% for the RAC.

The chloride concentration in the air was assumed to be 0%. In an ideal numerical simulation, the tides should be taken into account. However, due to the time consuming nature of such simulations, they were neglected in the simulation with concrete RVEs. However, their influence was studied with a homogeneous RVE.

The boundary conditions impose the water pressure, which is calculated to achieve a specific suction. This suction is determined by the relative humidity and temperature, as per Kelvin's law (Equation 2.14). Furthermore, the boundary layer model is also implemented to transfer the boundary conditions of the ambient air to the surface of exchange of the wall (see Section 6.3.6).

Month	Jan.	Feb.	Mar.	Apr.	May	Jun.	Jul.	Aug.	Sep.	Oct.	Nov.	Dec.
RH [%]	62.5	63.9	65.3	69.5	72.5	81.9	86.1	81.4	69.3	65.2	66.3	63.9
T [K]	273.4	275.4	279.3	284.6	290.1	293.9	297.9	298.8	295.4	289.6	282.2	276.0
P_w [MPa]	-59.3	-56.9	-55.0	-47.8	-43.0	-27.1	-20.6	-28.4	-50.0	-57.2	-53.5	-57.0

Table 8.1: Environmental conditions (temperature and relative humidity) applied to the pier, with the corresponding water pressure.

Two RVEs were used for this application: one representing the NAC and the other representing the RAC. Both RVEs have the same disposition of aggregates, whether natural or recycled, and the RAC has 2.3% of adherent mortar and 77.5% of new mortar. The RVEs are shown in Figure 8.3. It is worth noting that the size of the RVE, which is 10mm, was found to be suboptimal in our sensitivity analysis. However, because of the large size of the macroscale mesh and the associated computation time, it was decided to decrease the precision of the results in a safe manner, as the chloride content will be overestimated.
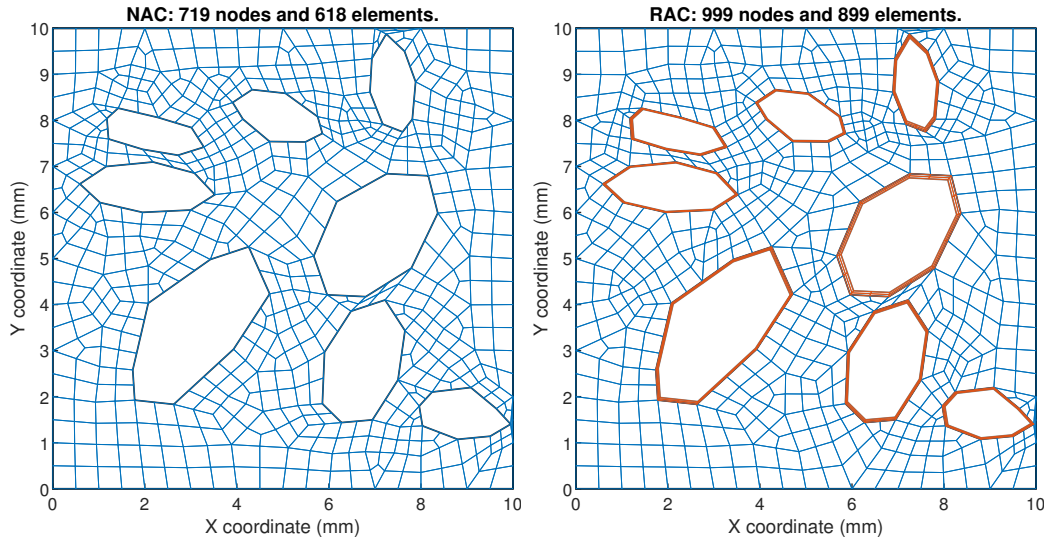
Figure 8.3: NAC and RAC RVE for the application.

According to the experimental validation, the properties of the E-M were used for both compositions, increased by 30%. However, the water retention curve is defined as a macroscale parameter in the model and was therefore defined based on the experimental results of the NAC and RAC, respectively. The parameters used in the model, for both RVEs, are provided in Table 8.2. The intrinsic properties of the adherent mortar of the RCA are equivalent to the properties of the plain mortar multiplied by 10 for the diffusivity and permeability coefficients and by 2 for the porosity. Theses values were decided to worsen the properties of the RCA and therefore increase the difference between the NAC and RAC.

Property	NAC	RAC	Adherent mortar of RCA
Intrinsic Permeability [m^2]	5.02E-18	5.02E-18	5.02E-17
Porosity [% Volume]	29.68	29.68	59.36
Diffusion Coefficient [m^2/s]	1.86E-11	1.86E-11	1.86E-10
n_{VG} Sorption [-]	1.51	1.51	-
α_{VG} Sorption [MPa]	3.45	3.56	-
n_{VG} Desorption [-]	1.53	1.48	-
α_{VG} Desorption [MPa]	13.83	10.43	-
b [-]	1.20	1.20	-
$\alpha_{b.l.m.}$ [m/s]	1.99E-3	1.99E-3	-

Table 8.2: Intrinsic properties of the NAC and RAC used in the application.

8.3 Results of the Application

8.3.1 Time to Equilibrium of the Water Pressure

Prior to introducing chloride ions into the lock wall, we conducted an investigation to determine the time required for our model to reach equilibrium with the environmental conditions, specifically regarding water pressure. These results allowed us to establish an initial condition for the water pressure inside the lock wall.

For this simulation, a mean water pressure of -46.3MPa is imposed, which is equivalent to the average water pressure over the year. Initially, the lock wall has an inside water pressure of 101325Pa, adjusted to account for gravity effects. The simulations are then run for 4000 years with the imposed water pressure. It is evident that the lock wall would be completely destroyed by that time. The objective is to determine the time it takes for external pressure to reach the wall's core and the initial conditions required for the model before introducing chloride ions.

Figure 8.4 shows the water pressure at the end of the 4000-years simulation for both the NAC and RAC. The left surface boundary conditions have propagated completely through the lock wall. Below two metres, the lock wall is not fully saturated due to the high suction imposed above that water level.
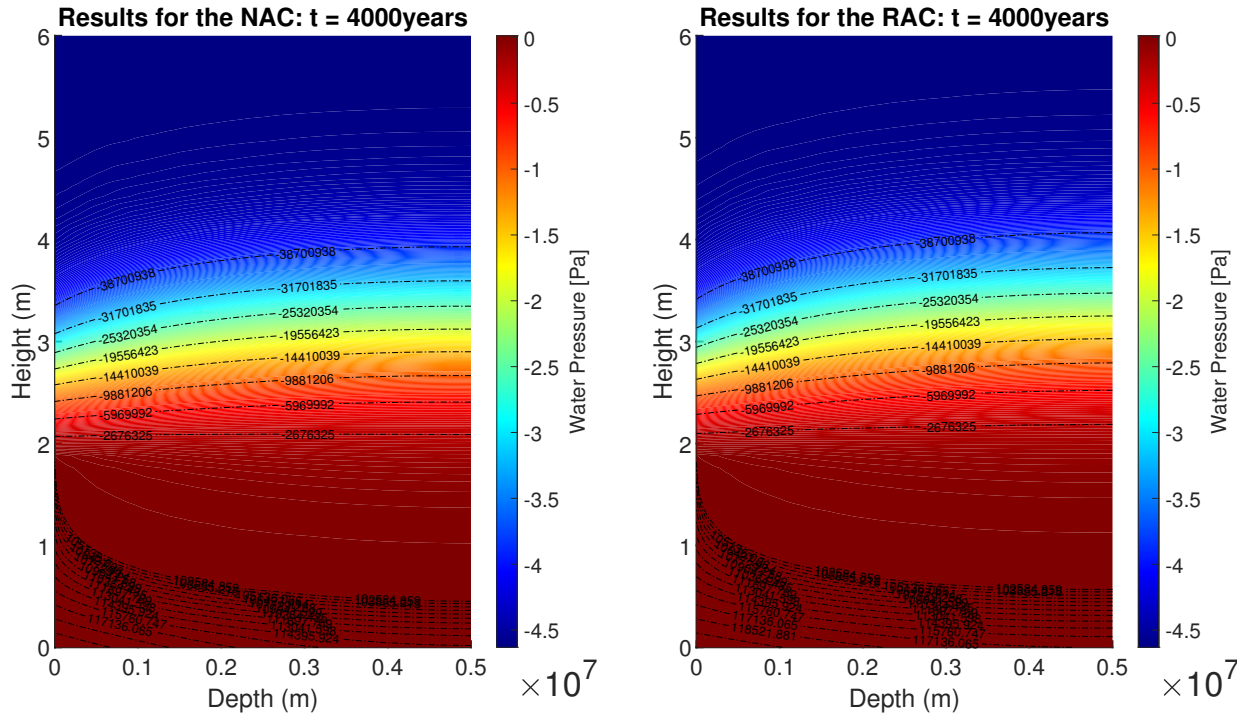
Figure 8.4: Water Pressure for the NAC (left) and RAC (right) after 4000 years.
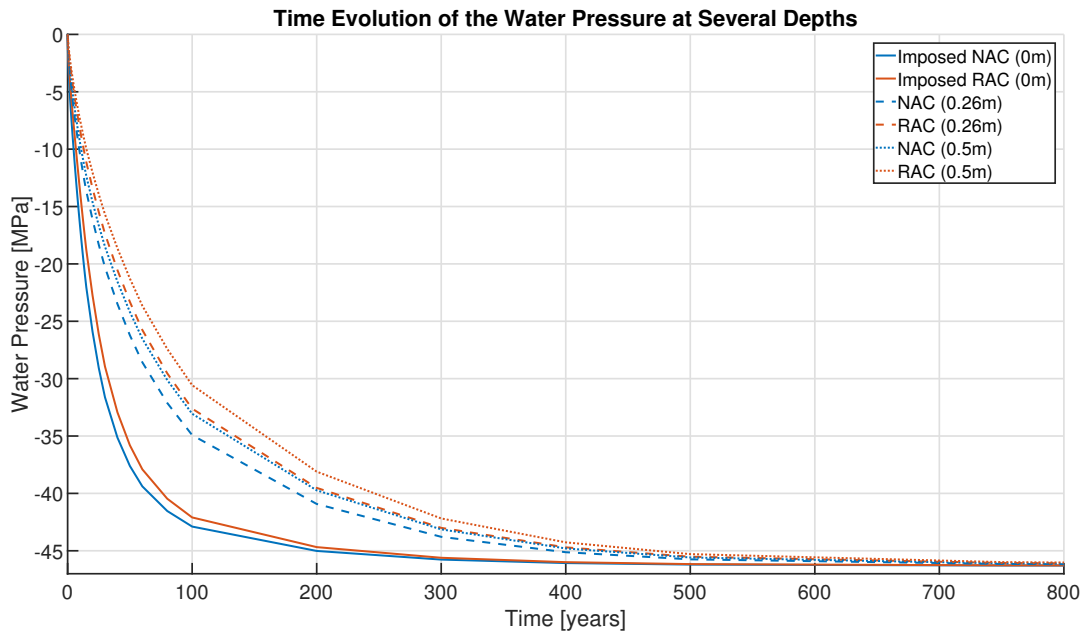
Figure 8.5: Evolution of the water pressure with time, at a given height (6m) and three distinct depths (0m, 0.26m and 0.5m) inside the lock wall, for the NAC and RAC.

Figure 8.5 shows the evolution of water pressure over time at a height of 6m and various depths (0m, 0.26m, and 0.5m) for both NAC and RAC. At 0m depth, the water pressures are determined by the boundary conditions and the boundary layer model. It is evident that it takes almost 300 years for the environmental conditions to reach the exchange surface of the lock wall. The time taken for water pressure to equilibrate increases as we move deeper into the lock wall, as expected. The NAC reaches equilibrium faster than the RAC due to

the different water retention curves of the materials. The RAC desaturates faster than the NAC, which limits moisture exchanges between the core of the wall and the ambient air by dropping its relative permeability.

According to the presented results, attempting to achieve an equilibrium in water pressure within the concrete lock wall appears illogical. Additionally, it is unlikely for a wall with a depth of 50 centimetres to reach equilibrium with its surroundings over its service life. This phenomenon is solely due to the evolution of relative permeability with the saturation degree of the porous medium. Due to the boundary conditions, the surface desaturates quickly, creating a low permeability zone. This zone can have a water permeability value as low as 5.02E-22 m², which decreases moisture exchange rates between the surface and the core of the wall.

For the application involving the introduction of chloride content, the wall will initially be saturated, as it is the case in reality after the curing of concrete.

8.3.2 Five Years Application with Chloride Ingress

Now that the initial conditions of our lock wall have been determined, the five-year application with chloride ingress can start. The boundary conditions in terms of water pressure and chloride content presented in the introduction will be used (Table 8.1).

Figure 8.6 presents the results for water pressure. The pressure within the NAC is observed to be lower than within the RAC. This result indicates that the NAC had a more significant moisture exchange with its surroundings, given its closer values to the applied boundary conditions than the RAC. The water saturation degree in Figure 8.7 confirms that it is lower in the NAC compared to the RAC, although very close.

These findings contradict expectations that the RAC would have higher rates of water and chloride exchange with its environment compared to the NAC, as suggested by previous experimental results. However, the RAC exhibits a tendency to desaturate at a more rapid rate than the NAC, as evidenced by its water retention curve. Consequently, the reduction in relative permeability resulting from desaturation may impede the exchange rates between the core of the concrete and its environment. This phenomenon is illustrated in Figure 8.8, where it is observed that the higher we are in the sample and the smaller the total water permeabilities of our materials are. Furthermore, the difference between the NAC and the RAC is observed to decrease with increasing depth. Furthermore, at higher depths, the water permeability is lower for the RAC than for the NAC, at proximity of the surface of exchange.
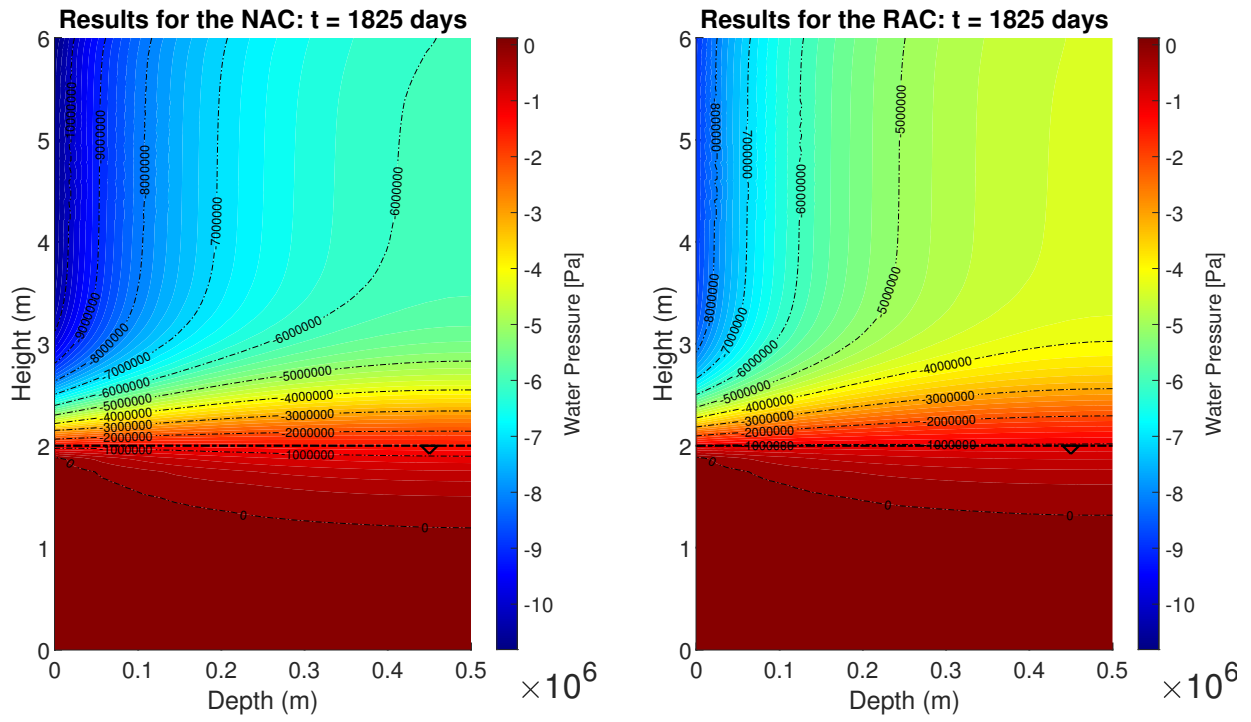
Figure 8.6: Water Pressure for the NAC (left) and RAC (right) after 1825 days.
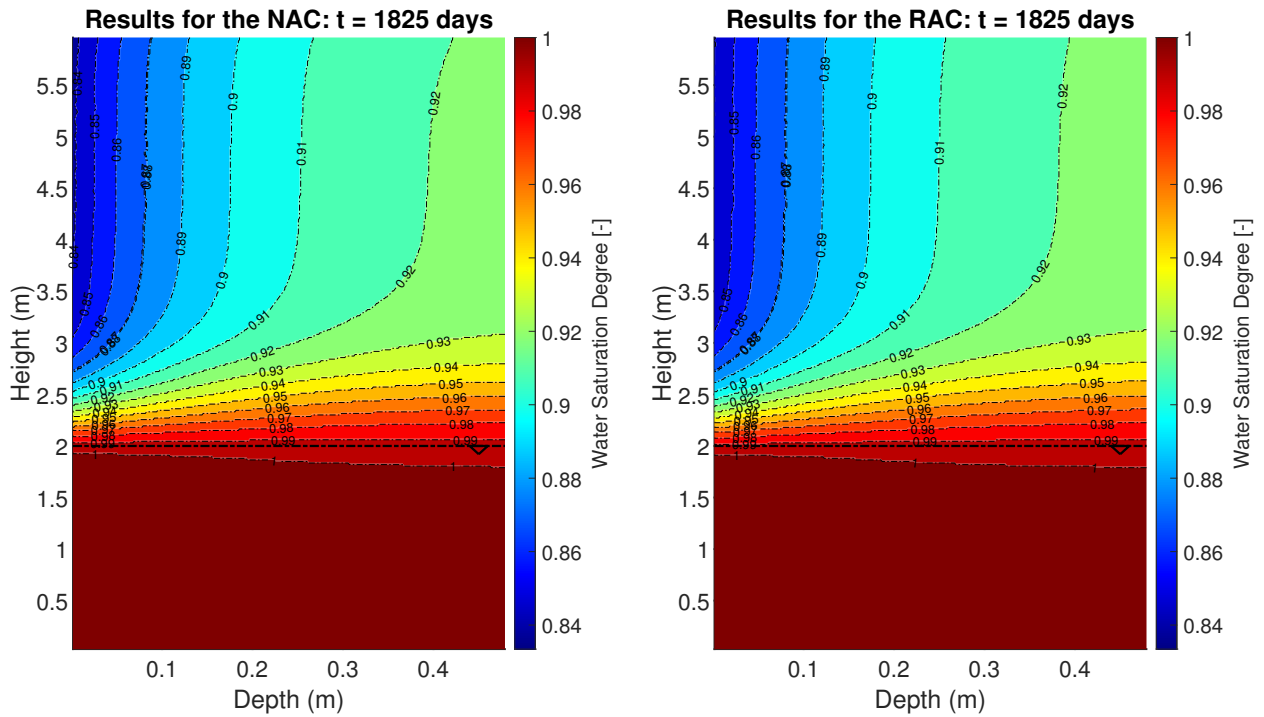
Figure 8.7: Water saturation degree for the NAC (left) and RAC (right) after 1825 days.
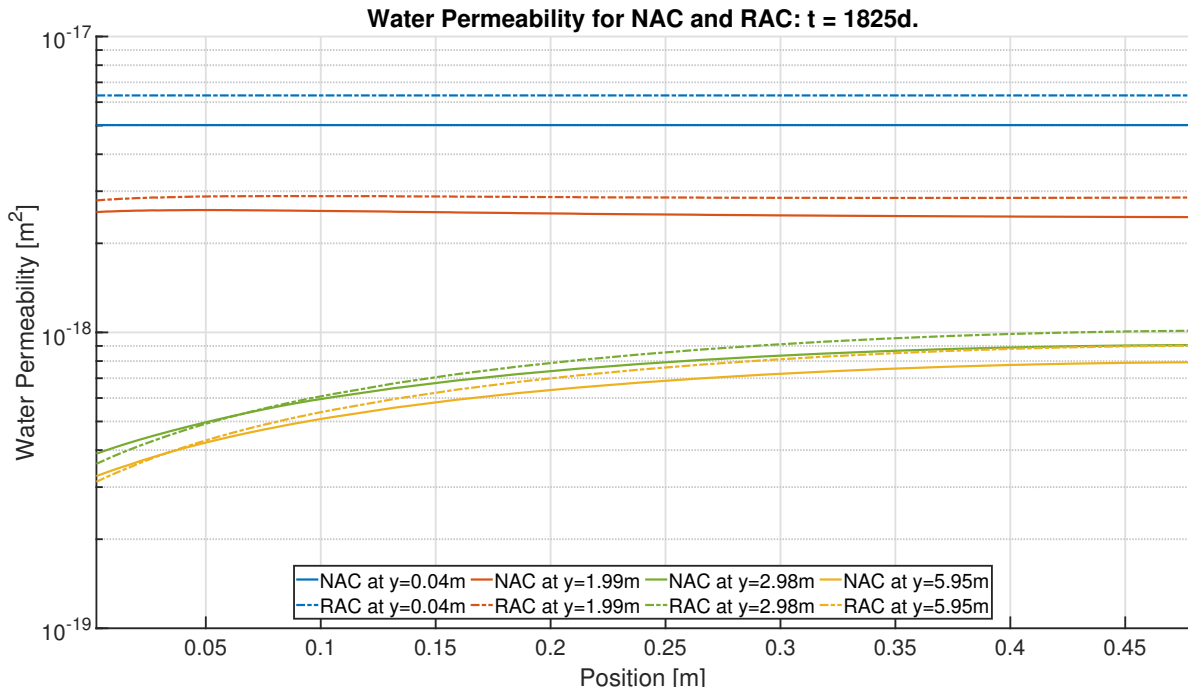
Figure 8.8: Evolution of the water permeability with depth for the NAC and RAC, at different height on the lock wall and at 1825 days.
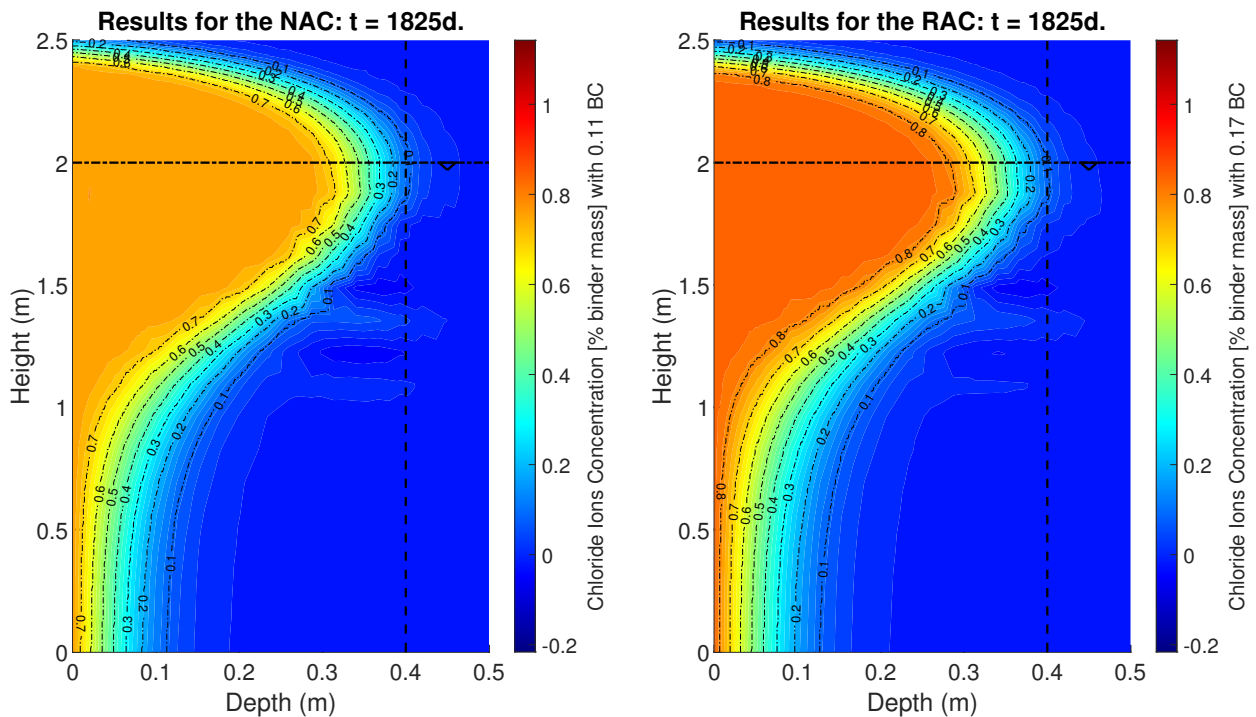
Figure 8.9: Chloride ions concentration for the NAC (left) and RAC (right) after 1825 days, expressed as a percentage of the binder mass.

Additionally, studying the chloride concentration (expressed as a percentage of the binder mass) in both concretes serves as an excellent indicator of the effects of unsaturated conditions. In unsaturated conditions, the chloride concentration of RAC is slightly higher than that of NAC, as illustrated in Figure 8.9. It is notable that the RAC also exhibits a higher chloride

content than the NAC at the bottom of the mesh, where both concretes are fully saturated. This can be attributed to the fact that the RAC is more diffusive. However, at the transition zone from hydrostatic to atmospheric conditions (at a height of 2m), the saturation degree of water reduces, and the phenomenon described above begins. Consequently, the chloride content of the NAC and RAC is comparable, despite the surface concentration being higher in the RAC than in the NAC.

Figure 8.10 displays the evolution of the chloride content for both concrete, through the depth of a sample and at a height of 2m. It confirms the findings above: the NAC and RAC have similar chloride content, except at their maximum value which is mainly due to the difference in boundary conditions. Otherwise, both chloride fronts move simultaneously, the one of the RAC being slightly shallower than the one of the NAC.

Figure 8.11 depicts the water pressure at a depth of 0.17m and through the height of the wall at distinct times. Firstly, at 0 days, it can be observed that the water pressure exhibits a downward slope due to the influence of gravity. Subsequently, upon imposition of the boundary conditions, the NAC experiences a more rapid loss of pressure than the RAC, reaching equilibrium with the external water pressure at a more rapid rate. The only explanation for this phenomenon is the water retention curve. Indeed, the RAC is presumed to exhibit greater permeability to water than the NAC. Consequently, it would be reasonable to anticipate the opposite observation. However, the aforementioned phenomenon, which links the saturation degree to the relative permeability, appears to reverse that tendency. This is corroborated by Figure 8.12, which is identical to Figure 8.11, but expresses the evolution of the saturation degree instead of the water pressure. The RAC consistently exhibits a greater saturation degree than the NAC.
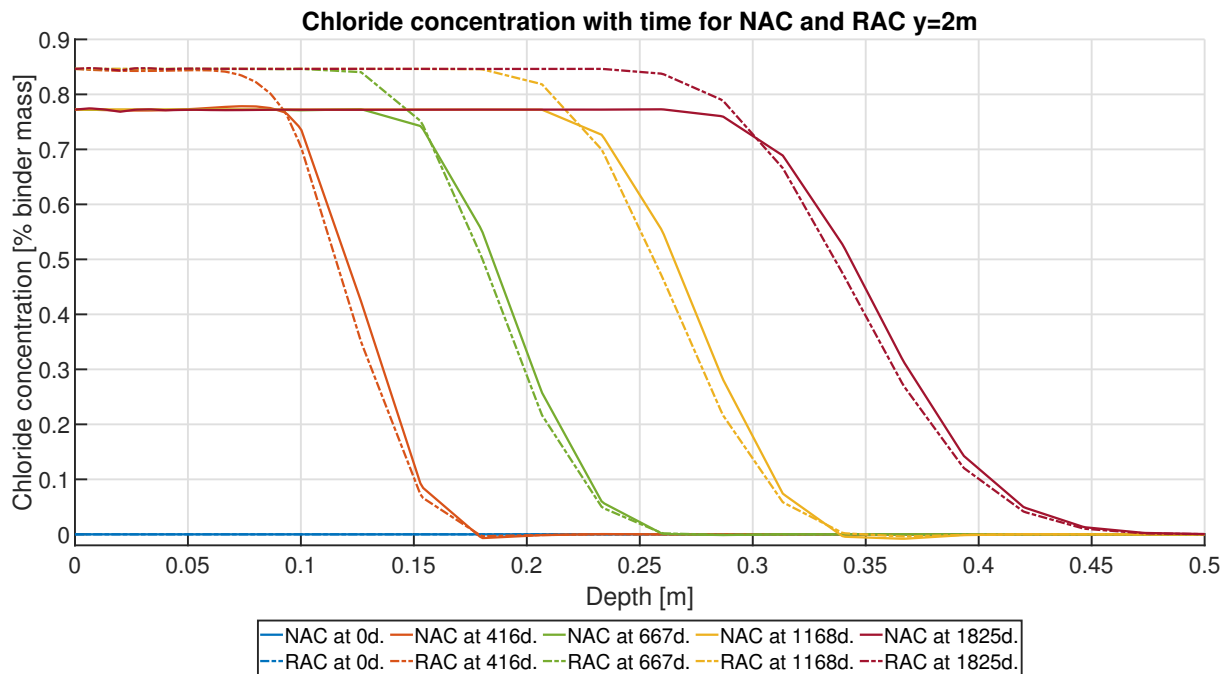
Figure 8.10: Evolution of the chloride content with time, for both NAC and RAC, at a height of 2m and throughout the depth of the wall.
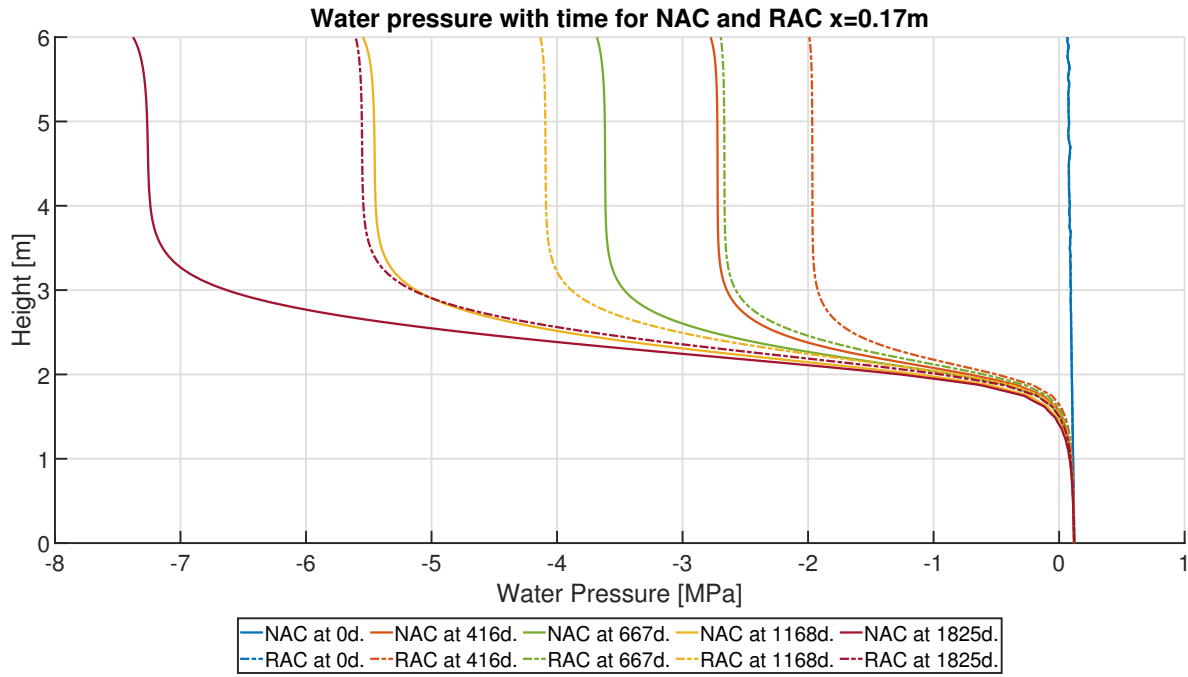
Figure 8.11: Evolution of the water pressure with time, for both NAC and RAC, at a depth of 0.17m and throughout the height of the wall.
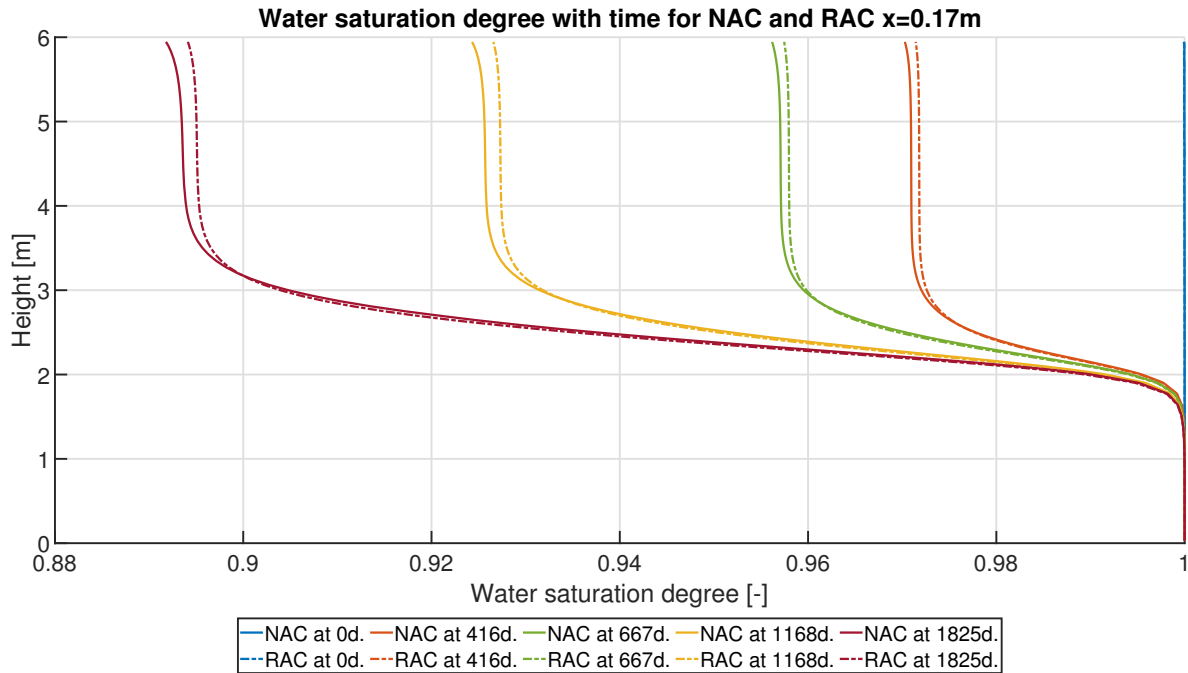
Figure 8.12: Evolution of the water saturation degree with time, for both NAC and RAC, at a depth of 0.17m and throughout the height of the wall.

Finally, Figure 8.13 represents the water retention curves of both concretes, as well as the relative permeability curves. Each data point represents a specific position and time. Firstly, it can be observed that the hysteresis does not appear to have any effect in this particular

application. Indeed, the minimum boundary condition in terms of water pressure is equal to -20.6MPa, while the water pressure inside the lock wall only reaches -10.8MPa. Consequently, if drying and wetting cycles occur, they are so insignificant that their hysteresis is not observed. Furthermore, it is readily apparent that the NAC exhibits a greater suction and a smaller saturation degree than the RAC.
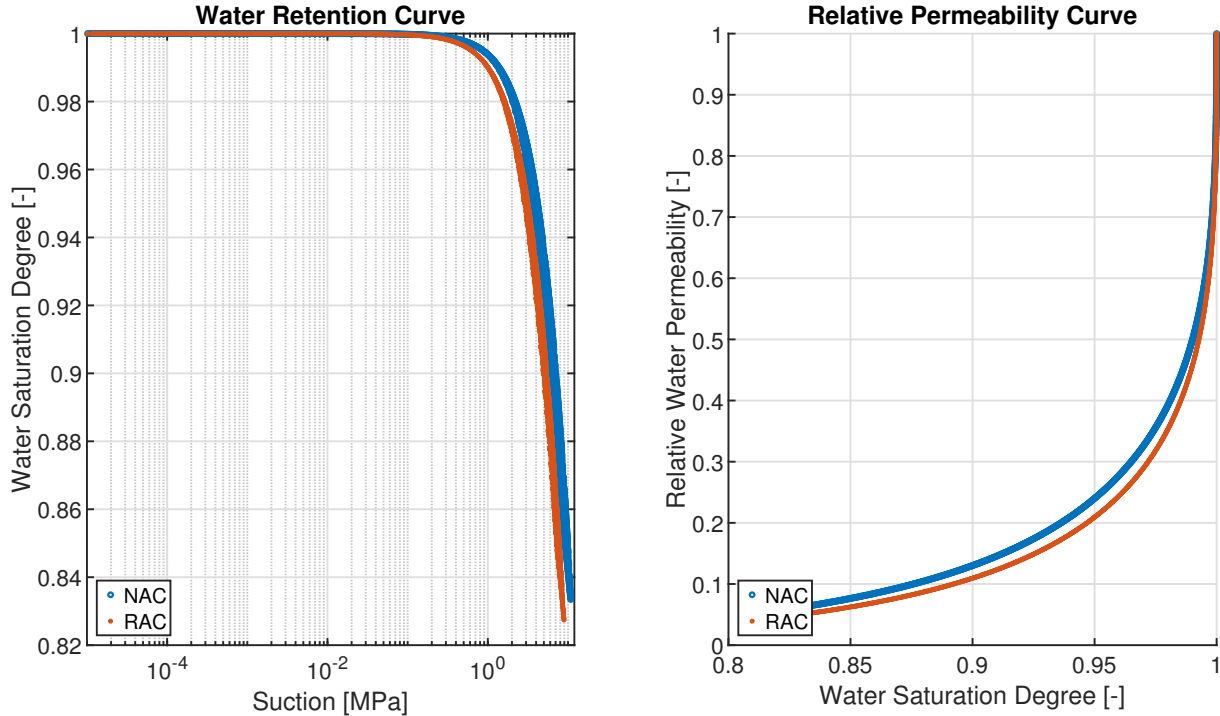
Figure 8.13: Water Retention Curves and relative permeability curves for the NAC and RAC.

8.3.3 Effect of the Tides

The application, which consists of a lock wall in a maritime area, is in reality subjected to tides, which were neglected in the primary simulation. However, determining the influence of these tides is crucial to ascertain the results found previously. In order to achieve this, a simulation was thus performed on the same macroscale mesh than the main application, but with a homogeneous RVE as time consumption would be too high. The properties are equivalent to the one of the NAC of the previous simulation, and the boundary conditions are also equivalent to the previous simulation, except for when the tides are high. The amplitude of the tide is equal to 2 metres, as detailed in Table 8.3. When the tides are high, the part of the wall between 2m and 4m is below the water level and hydrostatic pressure is applied. Otherwise, when the tides are low, this zone is subjected to the atmospheric pressure.

Time of the day [hours]	7	12	19	24
Height of the tide [m.]	0	2	0	2

Table 8.3: Amplitude of the tides at a given time of a day.

Figure 8.14 depicts the water pressure with and without tides, as observed after five years of simulation. In the absence of tides, the results are clearly analogous to those of the primary

simulation. However, when tides are included in the simulation, the transition zone between the atmospheric conditions and the constantly saturated conditions (under two metres of height) is greater and is as high as the amplitude of the tides. This is further illustrated in Figure 8.15, which depicts the water saturation degree. The same conclusions can be drawn with regard to the water pressure.

Upon examination of the chloride content, the results become more evident. This is illustrated in Figure 8.16. Firstly, it can be assumed that the chloride content in the tidal zone is negligible. It can be observed that the chloride front is less deep with the tides than without the tides, which seems to be at odds with expectations. This phenomenon is attributed to the transition zone between atmospheric and hydrostatic conditions, where the maximum effect is observed. The implementation of the tides reduces the water pressure gradient in that zone, thereby preventing the accumulation of chloride ions in that area. This results in a smaller and shallower front. Nevertheless, the maximum value of chloride content is identical in both scenarios.
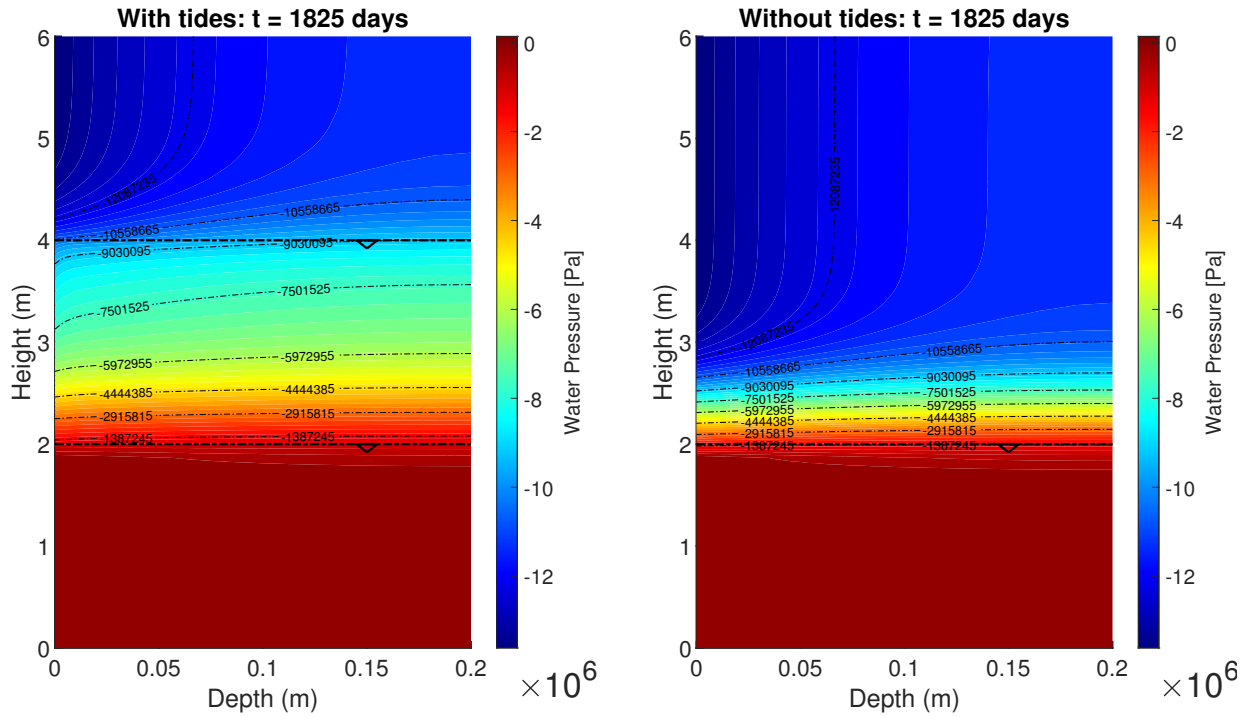
Figure 8.14: Influence of the tides on the water pressure.
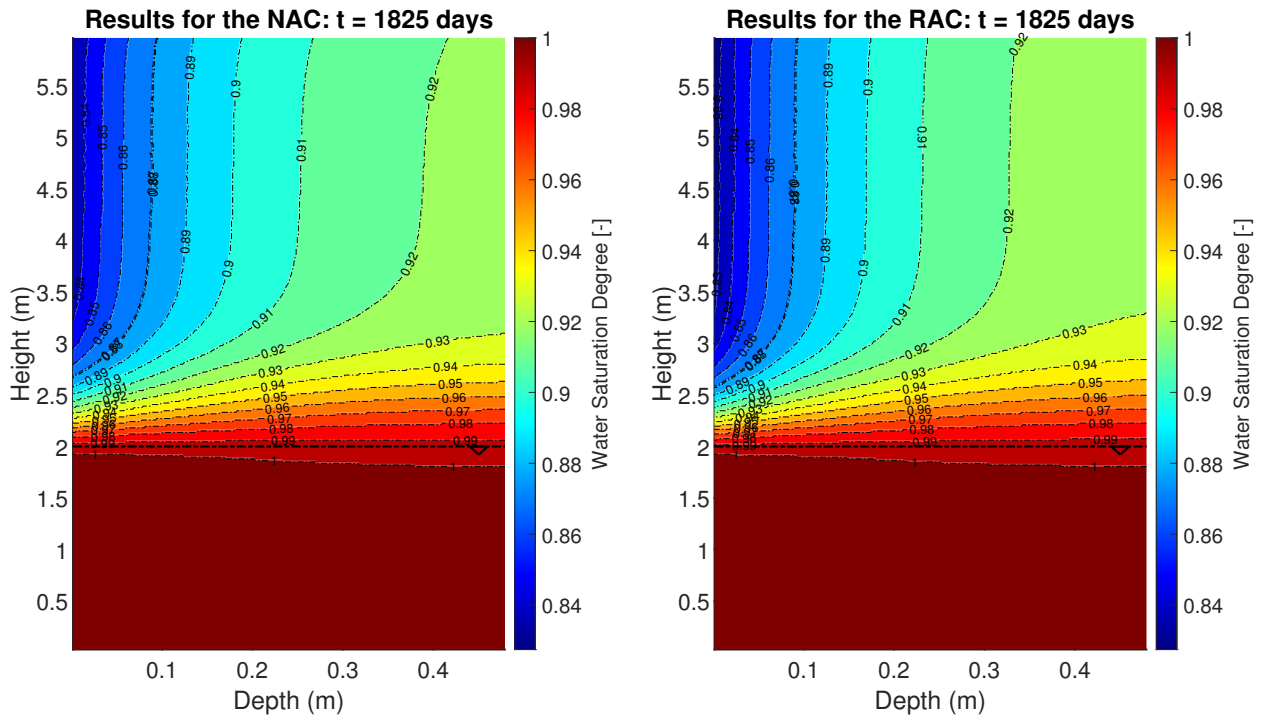
Figure 8.15: Influence of the tides on the water saturation degree.
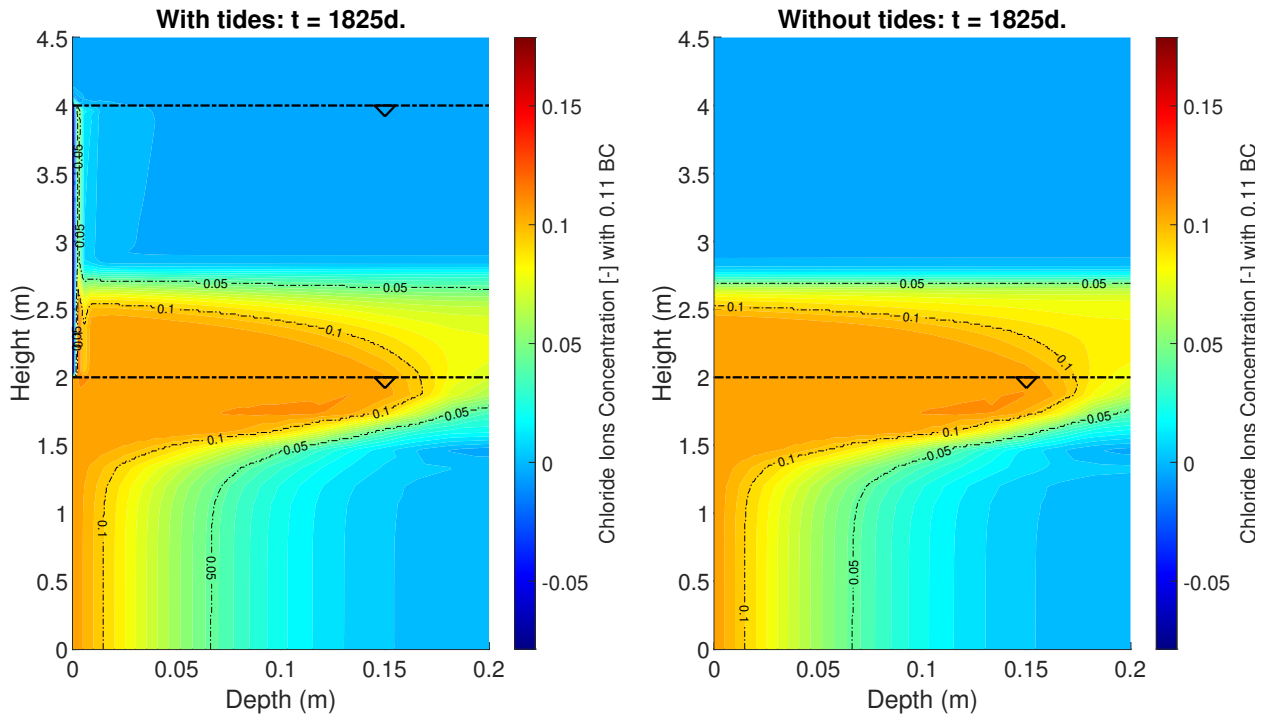
Figure 8.16: Influence of the tides on the chloride content.

8.4 Conclusion

The application has enabled us to gain a deeper insight into the impact of substituting natural aggregates with recycled concrete aggregates on the durability of a maritime lock. It

was demonstrated that, despite the RAC being more permeable, diffusive and porous than the NAC, when unsaturated conditions prevail, its chloride content is not appreciably higher than for the NAC.

The following observations may be discussed:

- There appears to be oscillations in the results, as illustrated in Figure 8.9. These oscillations are purely numerical and only appear in the evaluation of the chloride content, due to a convective flux that is higher than the diffusive flux, which tends to generate numerical oscillations. Over time, these oscillations dissipate and may be mitigated by performing smaller time steps or refining the mesh. Nevertheless, both of these options would considerably increase the computation time, and therefore they were neglected.

- The bell curve of our chloride profile may seem unrealistic. However, it appears directly at the interface between saturated and unsaturated conditions, and may be assimilated to the maximum phenomenon visible in Figure 3.7. Indeed, at the aforementioned transition, the water pressure may fluctuate in accordance with wetting and drying cycles, resulting in a maximum chloride content that is not observed at the surface but rather at a specific depth where the cycles cease. Moreover, the direction of the water flux is perpendicular to the lines of equal water pressures as depicted in Figure 8.6. Consequently, the chloride content therefore follows these water flows and concentrates when the saturation degree declines. If migration was accounted for in the model, the bell curve may not be as significant as to respect the electroneutrality conditions. It is indeed possible that the chloride ions diffusivity may be reduced [Samson et al., 2000, Ukrainczyk & Koenders, 2016]. Nevertheless, the water fluxes are more pronounced than the diffusive process, and it is possible that this may offset the reduction in diffusion [Samson & Marchand, 2007].

- The effect of the tide is to reduce the maximum phenomenon observed in the primary simulation. It is therefore considered safe to ignore these tides, as the chloride front obtained is deeper.

In conclusion, the evidence suggests that the substitution of NA by RCA may not have a significant detrimental impact on the durability of concrete. The extent of this impact is dependent on a number of factors, including environmental conditions and the properties of the concrete, the unsaturated conditions being in favour of the RAC.

185

PART

CONCLUSION

4

9

CONCLUSION

Contents

This manuscript concludes with an overall summary of the experimental campaign and numerical work. The original contributions of this thesis are then presented, with a focus on new numerical developments. Finally, perspectives for further studies are discussed, as well as industrial perspectives, this work being part of a F.R.I.A. grant.

As a reminder, this thesis aimed to address the following scientific question: **"How does the incorporation of Recycled Concrete Aggregates affect the durability of concrete in terms of chloride attacks?"**

Despite the inferior properties of RCA compared to NA, the substitution of aggregates was believed to have a non-negligible effect on the durability properties of concrete. This question was addressed through a dual experimental-numerical approach, and the main conclusions of this approach are presented hereafter.

9.1 General Conclusion

Experimental conclusion   Several materials were experimentally characterised throughout this research. The experimental programme is described in Chapter 4, and the results are presented in Chapter 5, as well as in Table 9.1 (which is identical to the one at the end of Chapter 5).
The aim of this comprehensive experimental characterisation was twofold: firstly, to observe the effect of substituting natural aggregates with recycled concrete aggregates on the transfer properties of water and chloride ions in concrete, and secondly, to obtain intrinsic properties of our materials to input into our numerical model.

The use of recycled concrete aggregates in concrete increases the material's overall porosity due to their inherent porosity. In correlation with the increase in water-accessible porosity, water absorption also increases by an amount equivalent to the absorption of the aggregates themselves.
The intrinsic water permeability also increases due to the substitution, possibly because of a greater interconnectivity of the pores, which can be correlated to the higher water-to-cement ratio of the RAC compared to the NAC. The effective water-to-cement ratio is the same for both materials. However, this assumes complete water absorption of the aggregates, which may not occur in reality. As a result, excess water may evaporate, leading to the creation of more capillaries. Another reason for the higher water permeability of RAC may be the creation of a larger Interfacial Transition Zone, which could be due to the use of recycled aggregates instead of natural aggregates.

Regarding the transfer of chloride ions, the diffusion coefficient of the RAC increased for both steady and unsteady-state diffusions. This is expected as the substitution of NA by RCA worsens all water transfer properties, and chloride ion transport is directly related to the water movements and water content inside the porous structure of concrete. Therefore, the overall ingress of chloride ions is increased due to this substitution. The electrical conductivity of the RAC is higher than that of the NAC, which increases the risk of corrosion.

When examining the water retention curves, it is evident that the air-entry pressure of the materials shows that the RAC has a larger maximum pore size than the NAC, as it saturates

(and desaturates) at a higher (respectively lower) suction value. However, it is important to note that this may not have a negative impact, as the faster desaturation leads to a rapid decrease in the relative permeability of the NAC, which reduces its ability to exchange water from the core of the structure to the surface.

Property	E-CP	E-M	NAC	RAC
Dry Density [kg/m^3]	1463	2025	2263	2061
Saturated Density [kg/m^3]	1914	2253	2405	2266
Water Absorption [% Mass]	30.87	11.27	6.26	9.95
Porosity [% Volume]	45.01	22.83	14.16	20.50
Intrinsic Permeability [E-19 m^2]	3.82	38.7	1.73	2.58
n_{vG} (Desorption) [-]	1.51	1.51	1.53	1.48
n_{vG} (Sorption) [-]	1.50	1.49	1.51	1.51
α_{vG} (Desorption) [MPa]	10.95	11.55	13.83	10.43
α_{vG} (Sorption) [MPa]	3.84	2.75	3.45	3.56
Hysteresis b_1 [-]	-	0.8	0.85	0.75
Hysteresis b_2 [-]	-	1.1	1.2	1.2
D_{eff} [E-13 m^2/s]	6.22	8.17	5.99	15.4
D_{app} (29 days) [E-11 m^2/s]	1.51	1.43	1.44	1.65

Table 9.1: Summary of the experimental properties to be used for the modelling part of this thesis.

Numerical conclusion   Alongside the experimental campaign, a multiscale numerical model was developed. The model was introduced in Chapter 6 and its validation and sensitivity analysis are presented in Chapter 7. The aim of this model is to predict the service life of a concrete member under realistic conditions. This was demonstrated in Chapter 8.

An algorithm was developed to model the mesoscale of our materials. This corresponds to a slice of concrete several centimetres in size, where only the mortar phases are meshed and the natural aggregates are impervious. The RVE was proven to be able to replicate experiments on concrete materials using properties of our experimental mortar. An adjustment was made for the 2D model versus 3D experiment. Increasing the transport properties by 30% was necessary to account for out-of-plane solutions, which are inherently neglected in a 2D model.

The model was validated through various means, and a sensitivity analysis was conducted on the Representative Volume Element. The analysis concluded that a 15mm RVE size was a suitable balance between efficiency and accuracy for the model. Additionally, the properties of the recycled concrete aggregates were investigated, including cement content and diffusion properties. Small errors in these properties would not significantly impact the accuracy of the model. In relation to the hysteresis model, it has been demonstrated that,

whenever possible, the value of the fitting parameter b should be obtained through an experimental campaign, as it has an impact on chloride ingress. However, that impact decreases with time, and therefore the possible error due to an incorrect value of b also decreases with time.

The service life prediction of a concrete member was conducted on a maritime lock wall under realistic environmental conditions, including temperature and relative humidity. Initially, a simulation was performed without chloride ingress for 4000 years to determine the time required for the member to be in complete equilibrium with its environment. The results showed that the core of the wall will never be in complete equilibrium with its environment during its service life.

To simulate chloride ingress, a saturated state, which is equivalent to the initial state of a concrete member after curing, was selected for beginning. The simulation ran for 5 years, providing information on the depth and time at which the chloride content exceeds the threshold chosen in this work (0.4% of the binder mass). Furthermore, it allows a clear comparison of the chloride profiles between the NAC and the RAC, allowing us to conclude on the effect of the substitution of aggregates on the durability of that lock wall.

It was determined that the chloride content is marginally higher in the RAC than in the NAC, which is a logical conclusion given that the diffusion coefficient, water permeability, and porosity of the RAC are all higher than those of the NAC. Moreover, the boundary conditions, in terms of surface concentration of chloride ions, are higher in the RAC than in the NAC. The detrimental effects of the substitution of aggregates are therefore relatively limited. This phenomenon can be attributed to the rapid desaturation of the porous system of the RAC in comparison to the NAC, which tends to achieve equilibrium between both concretes in terms of water permeability.

It is important to note that the properties used in this numerical application originate from our experimental programme, which studied a concrete manufactured from 100% recycled concrete aggregates. From an industrial perspective, it would not be economically viable to use a 100% substitution ratio, which would result in a more limited detrimental effect. Conversely, our aggregates were produced in a laboratory setting and are of superior quality in comparison to those produced industrially. Consequently, the two effects may be said to balance each other out.

9.2 Original Contributions

This thesis represents one of the first combination of experimental developments in the building materials team and numerical developments in the geomechanics team at the University of Liège. However, the experiments were not developed specifically for this thesis, and the numerical work is based on previous developments in the Lagamine software, including the unsaturated and coupled model by Collin (2003) [Collin, 2003] and Gerard (2011) [Gerard, 2011], the pollutant transport model by Biver (1993) [Biver, 1993], and the multiscale models by Marinelli (2013) [Marinelli et al., 2016], Van den Eijden (2015) [Van den Eijden, 2015], and Bertrand (2020) [Bertrand, 2020].

The principal experimental contributions of this work are as follows:

- The experimental study of the water retention curves and their hysteresis in concrete, made from natural or recycled concrete aggregates, was conducted through the use of

the vapour control method. The experiment is time-consuming and requires significant resources, but it allows for the calibration of the empirical numerical model and a better understanding of the impact of aggregate substitution on the water retention properties of concrete, which are intimately linked to its porosity.

- The study of chloride ions diffusion, in steady and unsteady state, in concrete made from recycled concrete aggregates, is relatively uncommon. The analysis has contributed to the advancement of scientific knowledge on chloride ingress in recycled aggregates concrete.

The main numerical contributions of this work include:

- The implementation of a hysteresis model that follows the Van Genuchten model for Water Retention Curves [Van Genuchten, 1980, Zhou et al., 2012]. Any Lagamine user can now easily implement this hysteresis into their simulations, which can increase the accuracy of many unsaturated flow models.

- The creation of an algorithm to generate a representative volume element that emulates a concrete slice. The corresponding files required for Lagamine to operate are also produced automatically, and the simulation are executed through a batch file.

- The development of a multiscale law that couples the transport of water and pollutants, specifically chloride ions in this case. This law can be applied to any porous material using the RVE and can accommodate multiple phases, provided they are porous.

- The parallelisation of the multiscale law and element using OpenMP. Initially, the Lagamine code was intended to be parallelised at the element scale, but this approach was not efficiently used and was not fully compatible with the developed multiscale laws. Therefore, a tedious task was performed to make our multiscale law capable of running parallel simulations.

9.3 Perspectives

9.3.1 Scientific Perspectives

The study of chloride ingress in concrete is complex. Further work may improve the accuracy of our model or account for other phenomena. These perspectives are detailed below.

Regarding the ingress of chloride ions, our model could be improved by introducing adsorption isotherms of chloride ions: this has the potential of decreasing the rate of ingress of chloride ions due to local adsorption. From this point of view, the experimental results were inconclusive in this work, and further investigations are necessary to characterise the adsorption capacity of our materials before introducing them into the model.
The ingress of chloride ions may also be slowed down by accounting for the migration of ionic species in the pore solution, as suggested in the literature [Samson et al., 2000].
Although these modifications may improve the accuracy of the model, they are difficult to verify experimentally. Furthermore, the model is currently considered safe as it overestimates the ingress of chloride ions.

In the context of degradation, additional processes, such as carbonation or alkali-aggregate reactions, could be incorporated into the model. It is widely acknowledged that degradation reactions interact, and including more degradation processes in a model can enhance the understanding of the service life of a structure. The corrosion reactions could be implemented and used to characterise the time required for corrosion initiation, considering parameters such as pH or ionic species concentrations.

A new degree of freedom, temperature, could also be added to the model. Although its effect may be negligible at the temperature at which regular recycled aggregates concrete is used, it is deeply linked to the transport phenomenon implemented in the model.

In terms of modelling the mesoscale, a 3D model could be developed to significantly increase accuracy and eliminate the need to increase the intrinsic properties of the mortar by 30%. However, it would increase the computation time significantly.

Another potential avenue of exploration is the creation of a database of representative volume elements, with varying cement content, transport properties of the adherent mortar, and substitution rates of the aggregates, among other parameters. This would aid in comprehending the crucial elements of the RVE that require control during the development of concrete from recycled aggregates. Additionally, it would facilitate the creation of a database from which concrete compositions could be extracted.

One final improvement regarding the RVE is that currently, all integration points of the macroscale share the same RVE. However, to increase the heterogeneity of concrete and make simulations more realistic, a different RVE could be used for each integration point. It would not significantly increase the computation time, but it would require more memory to run the simulations.

With regard to the time consumption of our simulation, a number of potential improvements may be considered. Firstly, the stiffness matrices obtained by perturbation could only be calculated at the initial iteration of each step and then maintained at a constant value throughout the remainder of the current step. This would result in a reduction in the overall time required for the simulation. Secondly, it is possible to run one iteration with a representative volume element, then to deduce homogenised properties from that simulation through regressive analysis, and finally to run a single-scale simulation with those homogenised properties.

In terms of application of the model, it could be applied to a road salt application instead of obtaining chloride ions from seawater. Papers such as Martin-Perez et al. (2001) [Martin-Perez et al., 2001] or Alsheet et al. (2018) [Alsheet & Razaqpur, 2018] could serve as references for the boundary conditions. The study of a bridge exposed to chloride attack by de-icing salt could then be carried out to compare the use of NAC or RAC.

It should finally be noted that the substitution rate of a concrete manufactured industrially may not reach 100% and that the quality of the recycled aggregates utilised may not be as high as those used in this study. It would therefore be of interest to study concrete made from industrial recycled concrete aggregates with a smaller substitution ratio.

9.3.2 Industrial Perspectives

This research is part of a F.R.I.A. grant, which has the objective of promoting research that is applicable to the Belgian industrial sector. The objective of this thesis was to promote the use of recycled concrete aggregates in buildings of greater value by ensuring that the durability of recycled aggregates concrete would be sufficient to meet the required standards.

The findings of this study indicate that the substitution rate of RCA in concrete may be increased in applications where concrete would be in contact with chloride ions. Moreover, the industrial sector may be able to predict the quality of concrete produced from their aggregates through the use of our model. In order to implement the aforementioned applications, it is necessary to conduct experimental characterisation of the industrial aggregates to be used. However, this process is already partially automated, as the aggregates must comply with established standards before being introduced into concrete.

PART

5

Appendices

A

Contents

A.1 Introduction

This appendix presents the experimental compositions designed for this research. Firstly, the materials used throughout all compositions are outlined, followed by a detailed explanation of each composition. The primary aim of this appendix is to ensure the reproducibility of the study, in addition to aiding comprehension of the variations in results between compositions. Four compositions were studied in this research to determine the influence of each concrete constituent. Firstly, a reference concrete was created using Natural Aggregates (NA), named NAC. Next, we obtained its analogue by substituting the NA with Recycled Concrete Aggregates (RCA), which resulted in the RAC. Afterwards, we decided to study the mortar paste (E-M) independently by removing any aggregate, and used the Concrete Equivalent Mortar method for design. Lastly, we analysed a plain cement paste (E-CP).

A.2 Materials

The materials utilised in this research are documented below:

- Water: tap water that meets the requirements of the NBN EN 1008 standard;

- Cement: CEM I 42.5 N from the CBR industry;

- Sand: 0/2 Rhine Sand;

- Aggregates:

  - Natural Aggregates (NA) are crushed limestone aggregates of fraction 2/7;

  - Recycled Concrete Aggregates (RCA) are aggregates derived from the OC1.2 composition (refer to Section 4.3). The Particle Size Distribution (PSD) of the RCA has been reconstituted from fractions 0/4, 4/6.3, and 6.3/8, to achieve a similar PSD to that of the natural aggregates. This has helped alleviate potential biases by mitigating one more variable.

The particle size distribution (PSD) of both the sand and aggregates, namely natural aggregates (NA) and recycled concrete aggregates (RCA), are illustrated in Figure A.1. As can be observed, the PSD of the two aggregate types varied considerably initially, necessitating reconstruction.
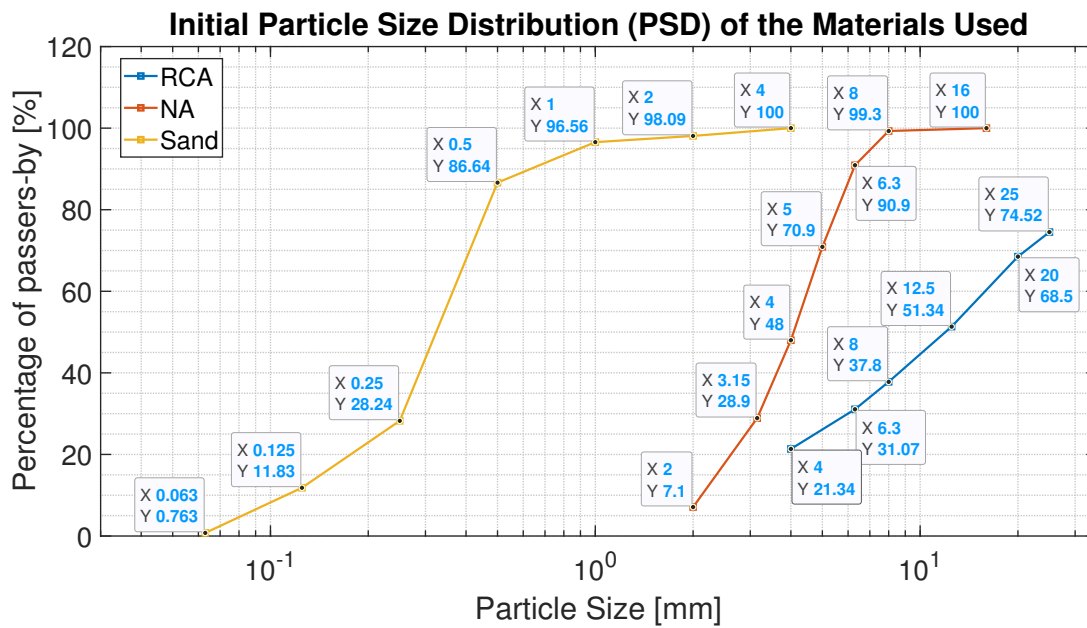
Figure A.1: Particle Size Distribution (PSD) of the Natural Aggregates (NA), Recycled Concrete Aggregates (RCA) and Rhine Sand used in the experimental compositions.

A.3 Concrete Compositions

A.3.1 NAC - Reference Concrete made from NA

The first composition displayed is the Natural Aggregates Concrete (NAC), which serves as the reference concrete and is created with natural aggregates. All other compositions stem from this one, making it particularly significant. The composition is determined using the NBN EN 206 guidelines for the water-to-cement ratio and amount of cement utilised, along with the Dreux-Gorisse [Dreux & Festa, 1998] method for determining the granular skeleton.

The NBN EN 206 is founded on various environmental classes that determine the suitability of concrete for its intended application. These classes are established on the severity of the environment (presence of pollutants, acids, etc.) and the probability of freezing or the existence of chloride ions. The contents of this research concentrate on the scrutiny of concrete in an environment afflicting it with chlorides, such as in the coastal region or adjacent to roads. However, it is essential to ensure that the porosity and permeability of our compositions are not too limited, as this could lead to modelling challenges and potentially reduce the differences between compositions with natural aggregate and recycled concrete aggregate.

Based on the given parameters, the selected concrete type is "T(0,50)" which is suitable for EE3, ES2 or EA2 environments:

- EE3: Humid interior or exterior environment, with a risk of freezing, contact with rainwater and/or projections of water (from a road, ...) but without any de-icing salts (this would require a T(0,45) concrete).

- ES2: Marine environment, not in contact with sea water but possibly in contact with marine air (up to 3km from the coast) and/or in contact with brackish water. There is

also a risk of freezing. However, to be in contact with sea water (immersed or in tidal zones) would require a T(0,45) concrete too.

- EA2: Moderately aggressive chemical environment.

A T(0,45) concrete may be more appropriate for direct exposure to chloride ions from sea water or de-icing salts. However, T(0,50) and T(0,45) have similar properties, and choosing T(0,50) would only slightly increase porosity, aiding our observations during both experimental and modelling phases.

Based on the concrete type selected, specifically T(0,50), the NBN EN 206 outlines the necessary criteria:

- Maximum water-to-cement ratio: 0.5 ;

- Minimum cement content: 320 kg per m^3 of concrete;

- Minimum compressive strength class: C30/37.

Therefore, to comply with the standard and produce concrete with appropriate strength and porosity, we opted for a cement content of 320 kg per m^3 of concrete, with a water-to-cement ratio of 0.5.

The subsequent stage involves the enhancement of the granular skeleton (Figure A.2). The Dreux-Gorisse approach has demonstrated effectiveness in this regard. The method entails:

- To begin, it is necessary to represent the Particle Size Distribution (PSD) of all the fractions of aggregate and sand utilised. For our investigation, we specifically examined the NA 2/7 and the Rhine Sand 0/2.

- Then, the curve O-A-B must be drawn. It is obtained by computing:

    - O : $O = (0.08; 0)$.
    - A : $A = \left(D_{max}/2; 50 - \sqrt{D_{max}} + K\right)$ where K is a coefficient determined by the level of vibration used for compaction, the type of sand (crushed or rolled), and the amount of cement. In our case, it was set at 2 (strong vibration, crushed aggregates, and a cement concentration of approximately $320\mathrm{kg/m}^3$).
    - B : $B = (D_{max}; 100)$.

- Finally, a line must be drawn between the 95% of passers-by from the sand and the 5% of passers-by from the aggregates. The point where this line intersects with the O-A-B curve reveals the percentage of sand in the mixture (by volume). In this case, we thus have 36.58% of sand and 63.42% of aggregates.
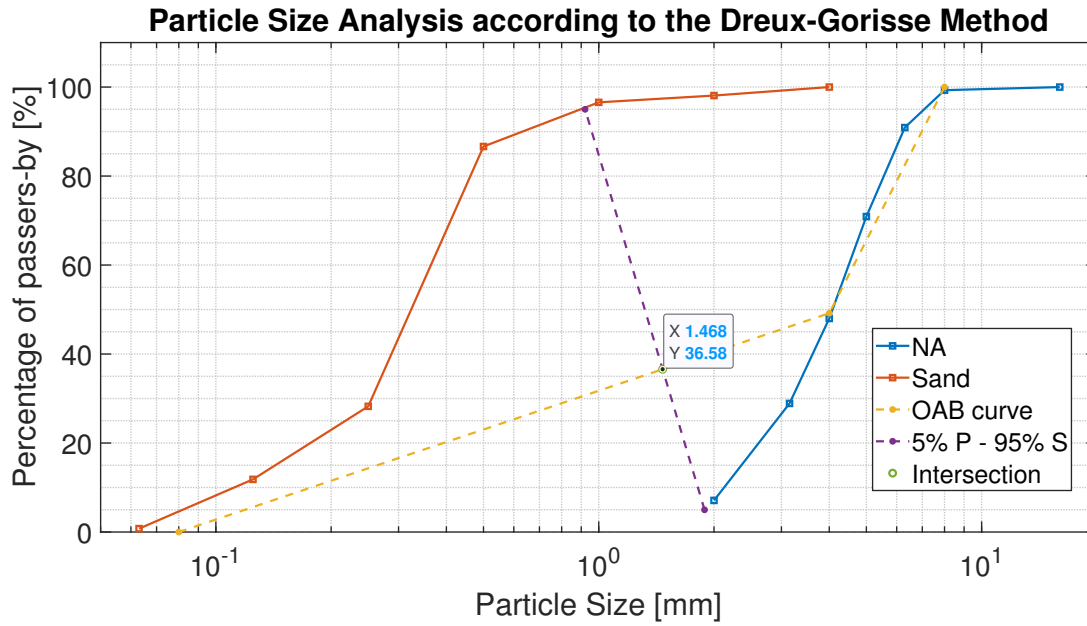
Figure A.2: Dreux-Gorisse method to improve the granular skeleton of the reference concrete composition.

Once the ratio of p/s has been determined, it is possible to calculate the values of p and s separately using a compacity coefficient γ:

$$\gamma = p + s + c = 0.783 \tag{A.1}$$

where γ is determined from a table and is dependent on the type of aggregates and sand (rolled sand and crushed aggregates), the consistency of the mix (soft) and the maximum size of the aggregates (D_{max}).

We then calculate the values of p and s using the following equations:

$$c = [C]/\rho_c = 0.1067 \tag{A.2}$$
$$p = 0.6342 * (\gamma - c) \tag{A.3}$$
$$s = 0.3658 * (\gamma - c) \tag{A.4}$$

and the required quantity of aggregates and sand can be calculated by multiplying the values of p and s with $\rho_p = 2590 \text{kg/m}^3$ and $\rho_s = 2600 \text{kg/m}^3$ respectively.

Now that the concentrations of all the materials utilised in our composition are known, we only need to adjust the water amount considering the sand and NA absorption, as well as their initial water content. The final composition of the reference concrete, denoted as NAC, is displayed in Figure A.3.

Composition of the NAC (W/C = 0.54)

643.169 kg/m^3

1111.008 kg/m^3

- Aggregates
- Water
- Cement
- Sand

320 kg/m^3

172.578 kg/m^3
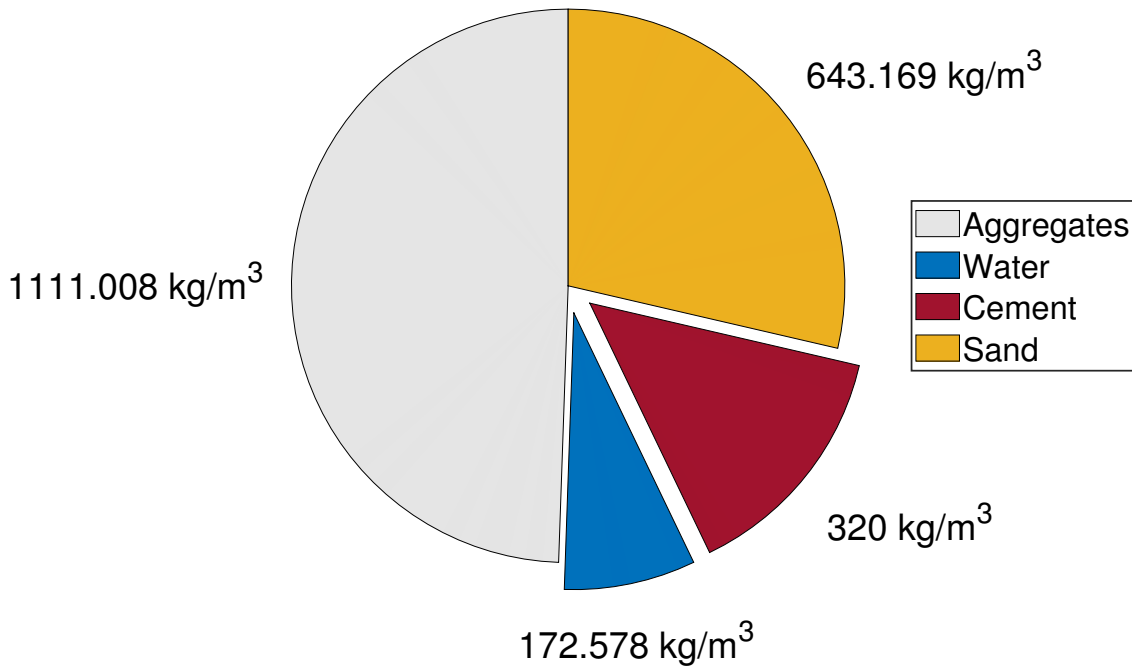
Figure A.3: Diagram illustrating the components of the NAC composition and their corresponding mass per cubic metre of concrete produced.

It is important to note that the Dreux-Gorisse approach necessitates an alteration in the water and cement content if the largest aggregate size is below 25mm. This adjustment is intended to ensure a fluid composition with high workability. Nevertheless, this amendment was not implemented in this case because it would result in an increase in the amount of cement to 358 $\mathrm{kg/m^3}$ (compared to 320 $\mathrm{kg/m^3}$). Failure to implement this correction results in concrete with a workability equivalent to a mixture with 290 $\mathrm{kg/m^3}$, which is qualified as poor workability.

However, to confirm that this alteration does not significantly affect our composition, a NAC with adjusted amounts of water and cement was tested in our laboratory, showing no noticeable difference in slump and workability.

Therefore, our original composition remained consistent throughout the research. It is important to note that the objective is to compare NAC and RAC, and while their composition is crucial, their fresh state properties are not as significant.

A.3.2 RAC - Concrete with Recycled Concrete Aggregates

The following section details the composition of the Recycled Aggregate Concrete (RAC), in which the natural aggregates from the reference concrete are replaced with recycled concrete aggregates at a constant volume fraction:

$$[P_{RCA}] = [P_{NA}] * \frac{\rho_{RCA}}{\rho_{NA}} \tag{A.5}$$

where ρ_{RCA} is equal to 2205 $\mathrm{kg/m^3}$.

As previously stated, it is necessary to reconstruct the PSD from various RCA fractions to replicate the NA size distribution. The RCA quantity is then distributed among the following size fractions: 2/4, 4/5, 5/6.3 and 6.3/8.

Additionally, the required amount of water is adjusted to account for the initial water content and absorption of the RCA. Figure A.4 illustrates the final results.

One could note that the water-to-cement ratio is relatively high (0.63) in comparison to that of the NAC (0.54). This is due to the RCA's water absorption, which is higher than that of the NA due to the presence of adherent mortar paste. The excess water is intended to be absorbed by the aggregates rather than remaining in the paste. Alternatively, other techniques, such as soaking the aggregates before using them in the composition, could be employed. Research indicates that aggregate saturation can be achieved through a 10-day soaking period or a 1-hour period with approximately 50% saturation. To achieve a soft consistency, the aggregates should be soaked for 3 minutes before use [García-González et al., 2014]. The "double mixing method" was employed in this thesis [Guo et al., 2018]. This approach has been moderately adjusted by delaying the addition of cement for 5 minutes, enabling the water blended with sand and aggregates to saturate the RCA.
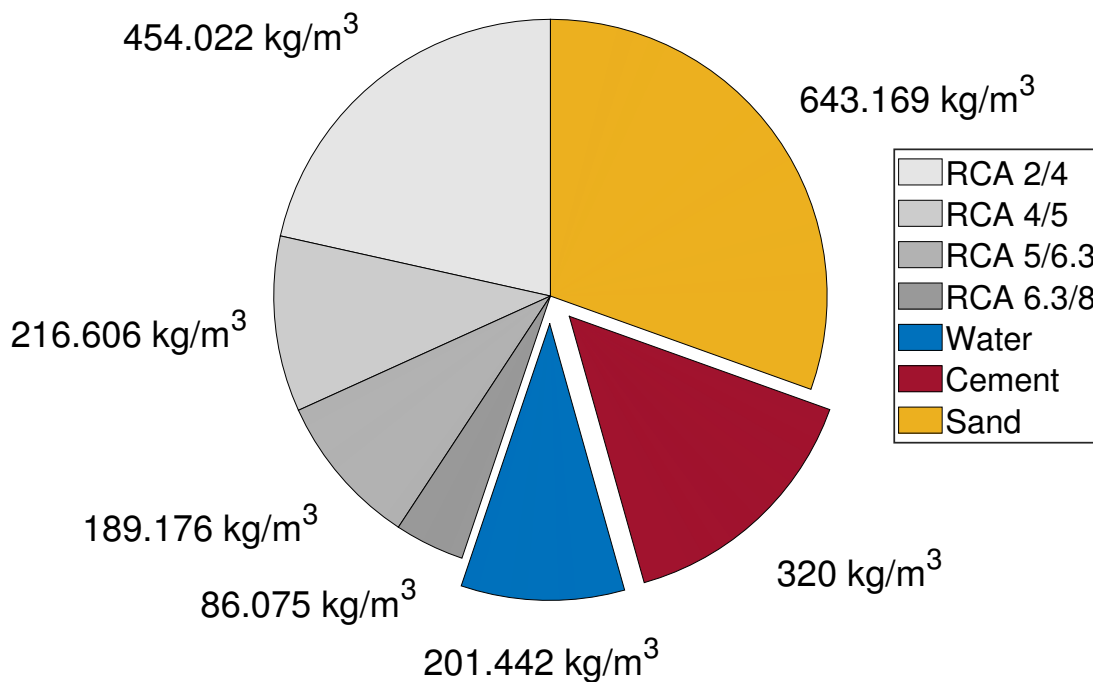
Figure A.4: Diagram illustrating the components of the RAC composition and their corresponding mass per cubic metre of concrete produced.

A.3.3   E-M - Concrete Equivalent Mortar

The Concrete Equivalent Mortar (C.E.M.) method is the basis for producing a mortar with the same rheological properties as the reference concrete [Schwartzentruber & Catherine, 2000, Erdem et al., 2009]. The composition of the E-M can be determined from the NAC's composition:

- same type and dosage of cement;

- same water-to-cement ratio;

- use of the sand which was used in the concrete;

- addition of a quantity of sand that replicates the same granular specific surface as the removed gravel.

Firstly, the volume of each component (namely water, cement, and sand) from the reference concrete mixture is calculated. These quantities are then combined to give a final volume that is less than the volume with the aggregates, denoted by $V_{\text{NAC,equiv.}}$. Finally, the necessary mass of each component is found by multiplying the ratio of the original volume (with aggregates) to the new volume (equal to one cubic metre) with the mass used in the reference mixture, such as with the water:

$$m_{\text{water,E-M}} = m_{\text{water,NAC}} \times \frac{1}{V_{\text{NAC,equiv.}}} \tag{A.6}$$

Once the quantities of each constituent are determined, the amount of sand required to replicate the same granular surface as the removed gravel can be calculated by:

$$S_{tot} = \sum_i n_{\text{aggregates},i} \, S_i = \sum_i \frac{M_i}{\rho \, V_{\text{grain},i}} \, S_i = \sum_i \frac{M_i}{\rho} \frac{4 \, \pi \, r_i^2}{\frac{4}{3} \, \pi \, r_i^3} = 6 \frac{M_{tot}}{\rho} \sum_i \frac{p_i}{d_i} \tag{A.7}$$

where an index i is used for each size fraction in the granulometric curve.

Composition of the E-M (W/C = 0.54)
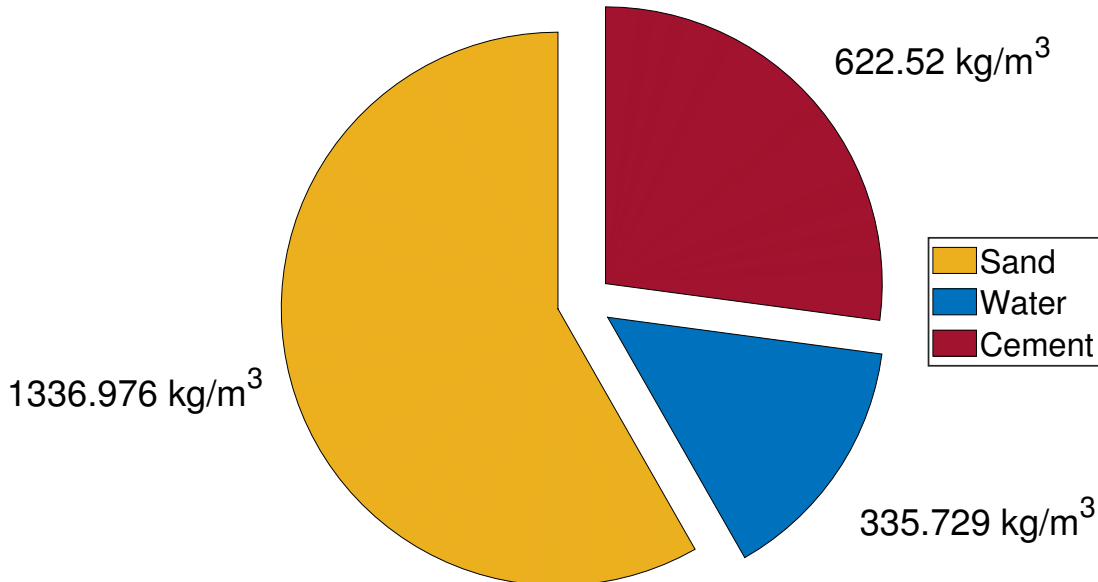
Figure A.5: Diagram showing components of the E-M mixture and their corresponding mass per cubic metre of mortar produced.

One issue with this approach is that the reference concrete composition and the equivalent mortar mix have different volume fractions of aggregates/sand. Specifically, the reference concrete mix has a solid volume fraction (aggregates and sand) of 70.78%, while the mortar mix has a solid volume fraction (sand) of 48.61%. This decrease in solid volume fraction increases the likelihood of paste and sand segregation in the mortar mix, ultimately reducing its tortuosity. This creates a fluid layer (primarily consisting of water) which will rise above the mortar mixture during the casting process, resulting in a reduced effective water-to-cement ratio.

A.3.4   E-CP - Cement Paste

The composition of the Equivalent Cement Paste (E-CP), derived from the reference concrete (NAC), adheres to the same theory as the Concrete Equivalent Mortar method. The technique replaces the sand and aggregates with cement particles at equal specific surface. The specific surface of the sand and aggregates particles used was calculated, and then divided by the Blaine specific surface of the CEM I 42.5 N, which is equal to 2750 cm^2/g.

Composition of the E-CP (W/C = 0.52)

647.167 kg/m^3

Water
Cement

1240.328 kg/m^3
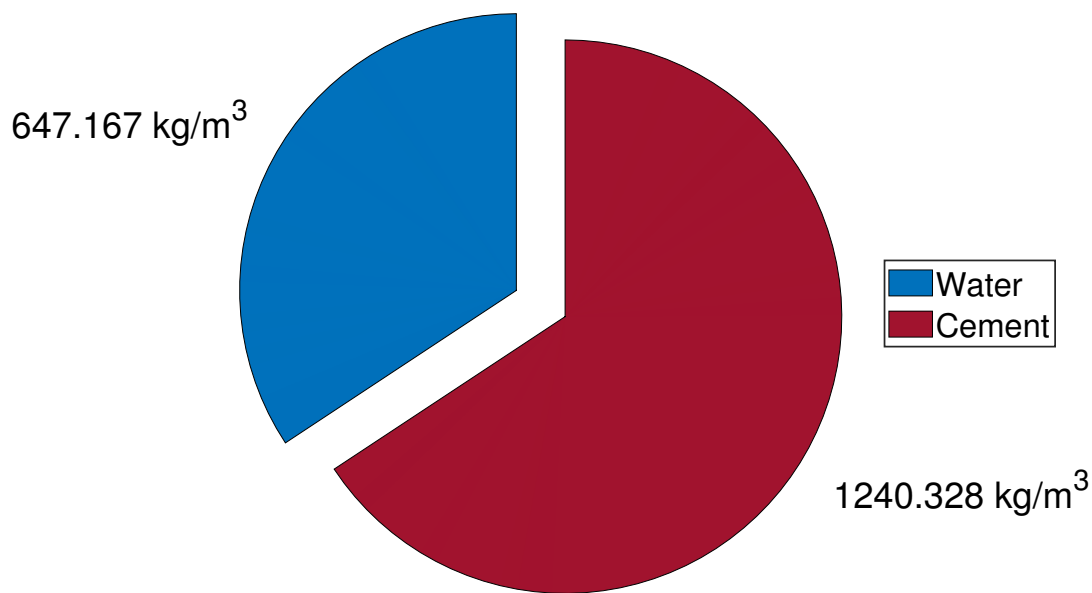
Figure A.6: Diagram illustrating the components of the E-CP composition, along with their corresponding mass per cubic metre of produced cement paste.

Segregation is a potential issue in this composition as well. To mitigate this risk, a particular experimental technique is employed to cast the samples: the paste is poured into a hermetically sealed bucket and subsequently placed on top of two cylinders. One of the cylinders is rotated via a motor, while the other follows the movement of the bucket. This approach ensures consistent mixing of the paste during its setting, reducing the occurrence of segregation.

B EXPERIMENTAL RESULTS

Contents

B.1   Introduction

This appendix gathers Figures and Tables that result from the experimentation performed in this thesis, but are not of significant importance.

B.2   Static Sorption and Desorption
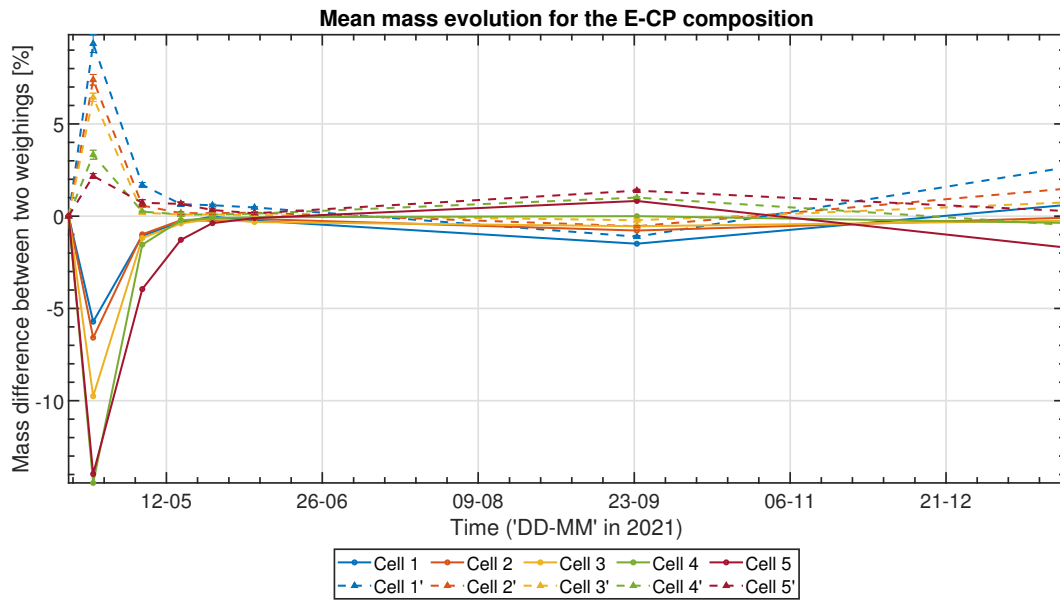
Figure B.1: Mass loss (desorption) and gain (sorption) for the E-CP composition.
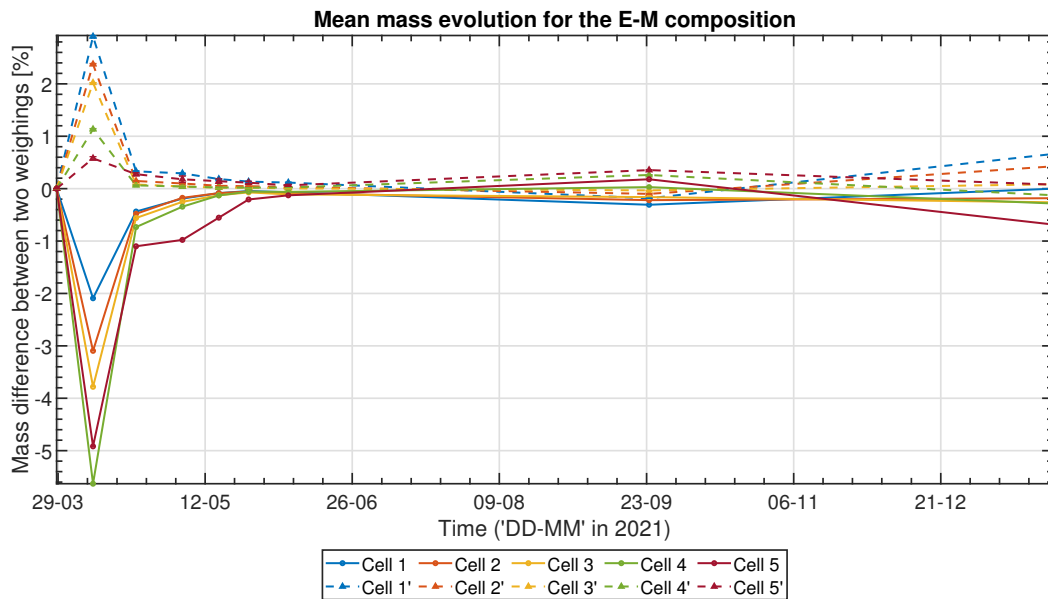
Figure B.2: Mass loss (desorption) and gain (sorption) for the E-M composition.
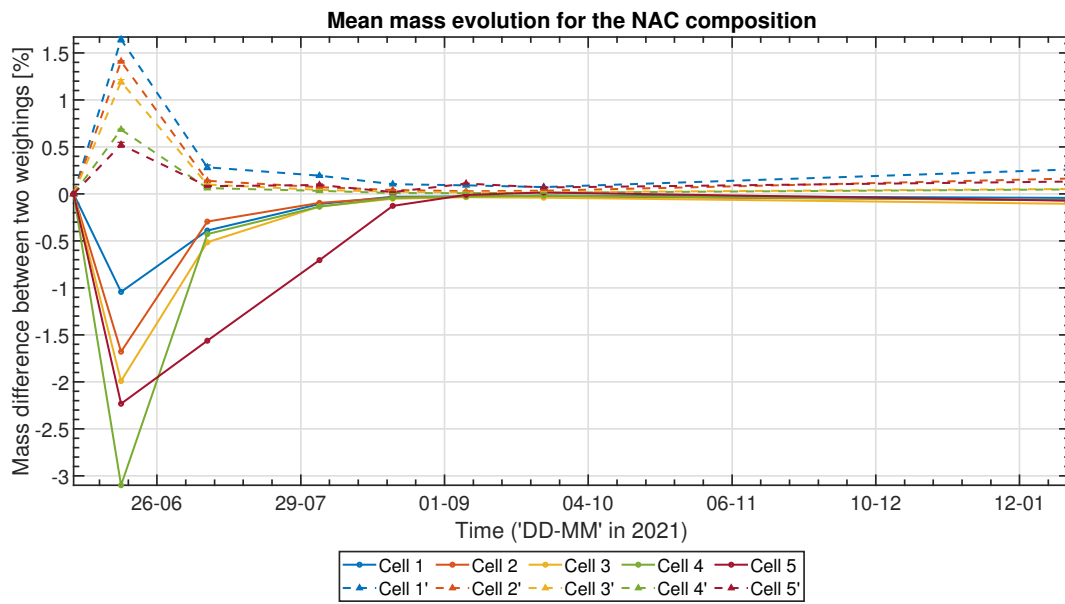
Figure B.3: Mass loss (desorption) and gain (sorption) for the NAC composition.
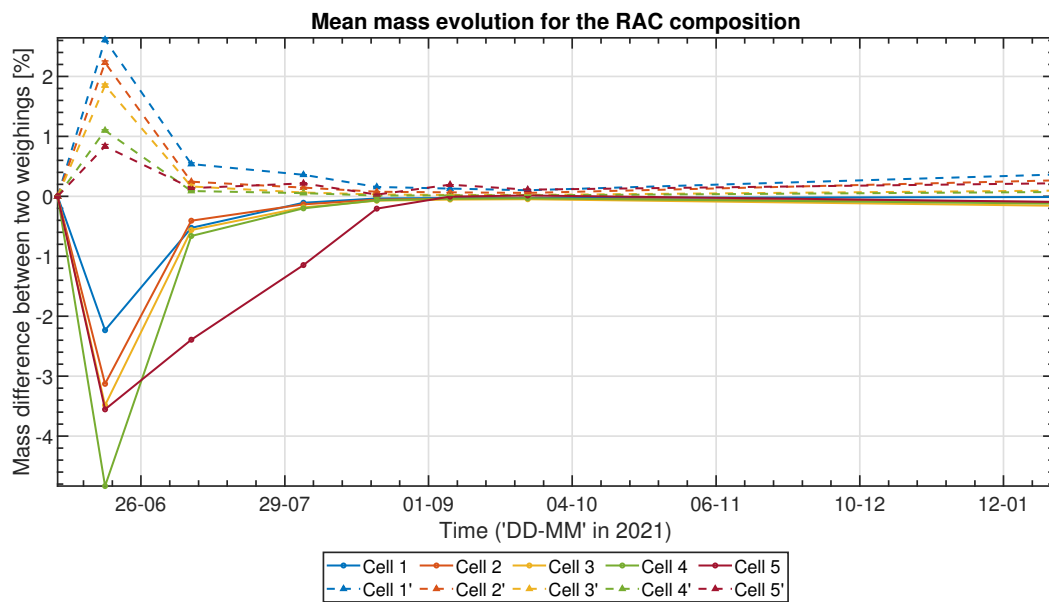
Figure B.4: Mass loss (desorption) and gain (sorption) for the RAC composition.
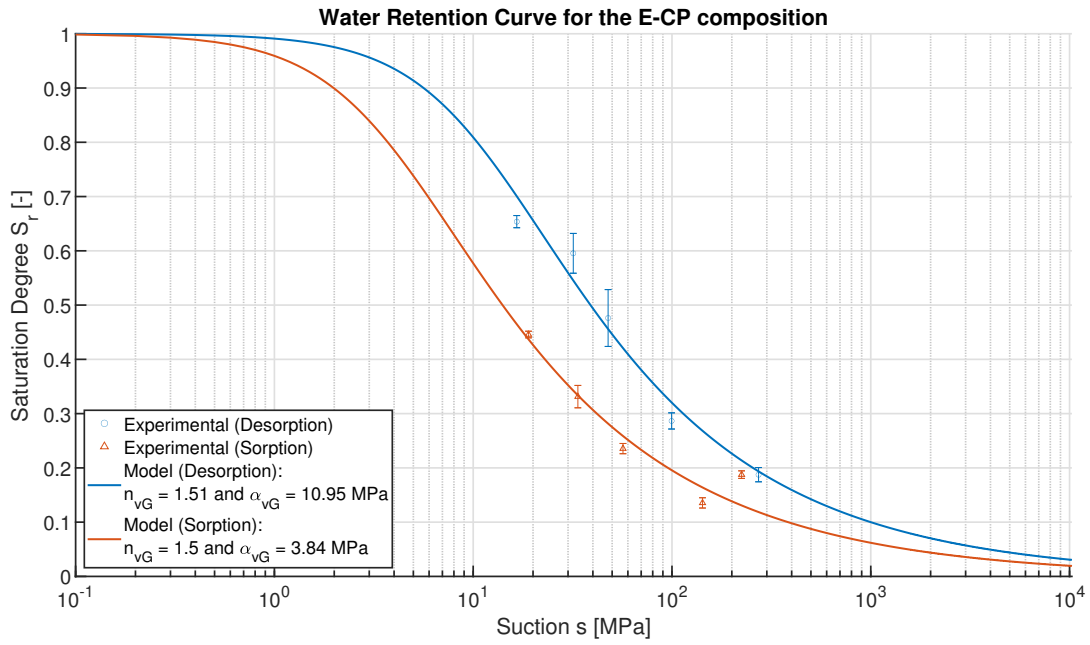
Figure B.5: Water Retention Curve for the E-CP composition, based on the results from the static sorption and desorption experiment, and using the Van Genuchten's model.
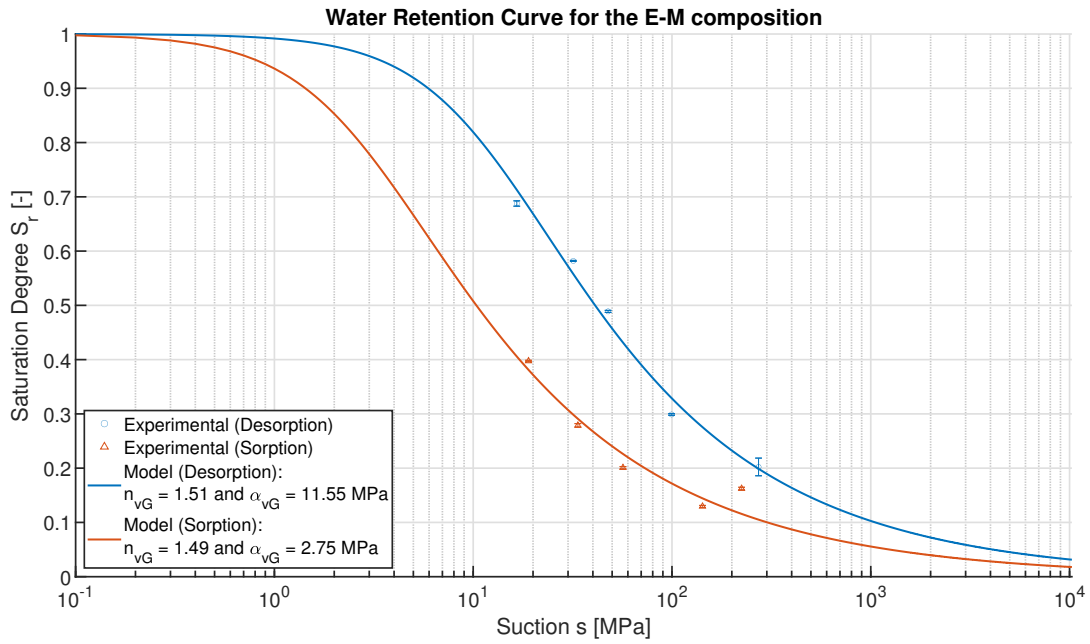
Figure B.6: Water Retention Curve for the E-M composition, based on the results from the static sorption and desorption experiment, and using the Van Genuchten's model.

B.3 Hysteresis
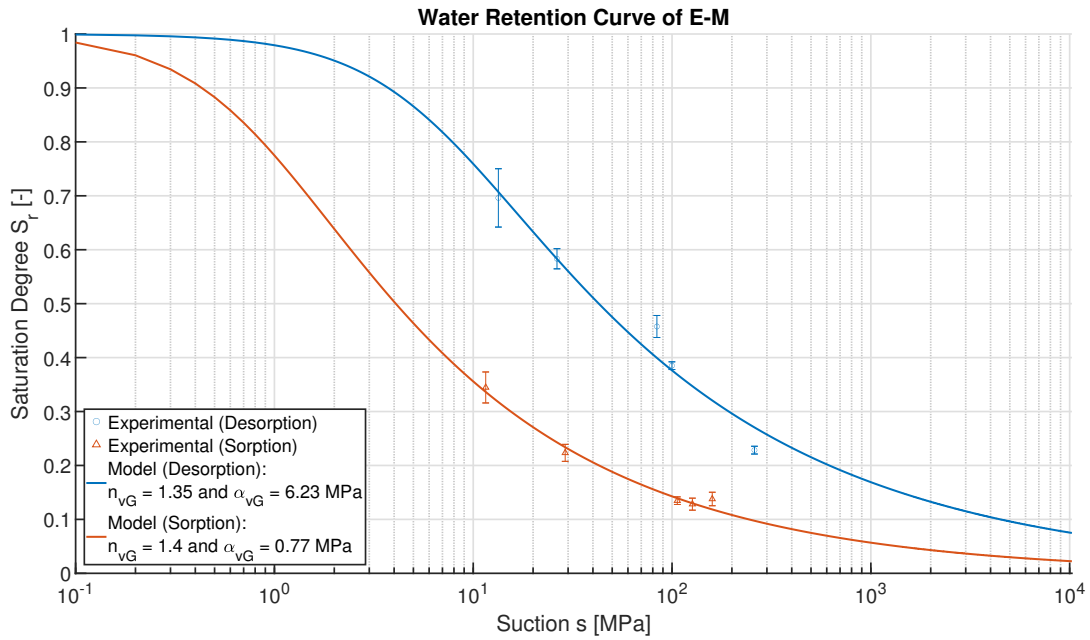
Figure B.7: Water Retention Curve for the E-M composition, based on the results from the static sorption and desorption experiment, and using the Van Genuchten's model.
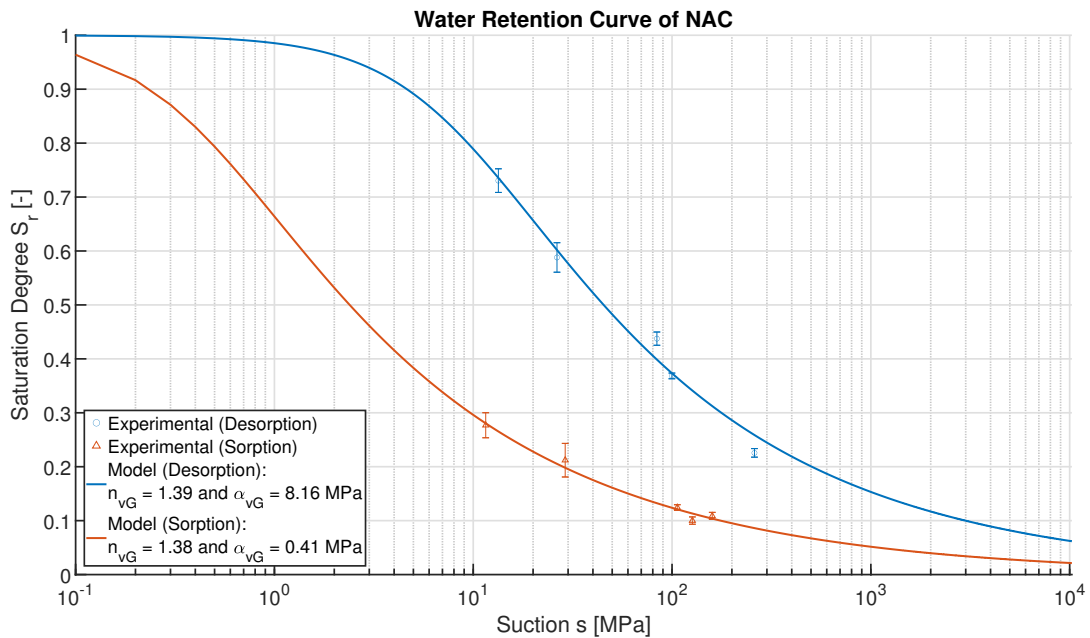
Figure B.8: Water Retention Curve for the NAC composition, based on the results from the static sorption and desorption experiment, and using the Van Genuchten's model.
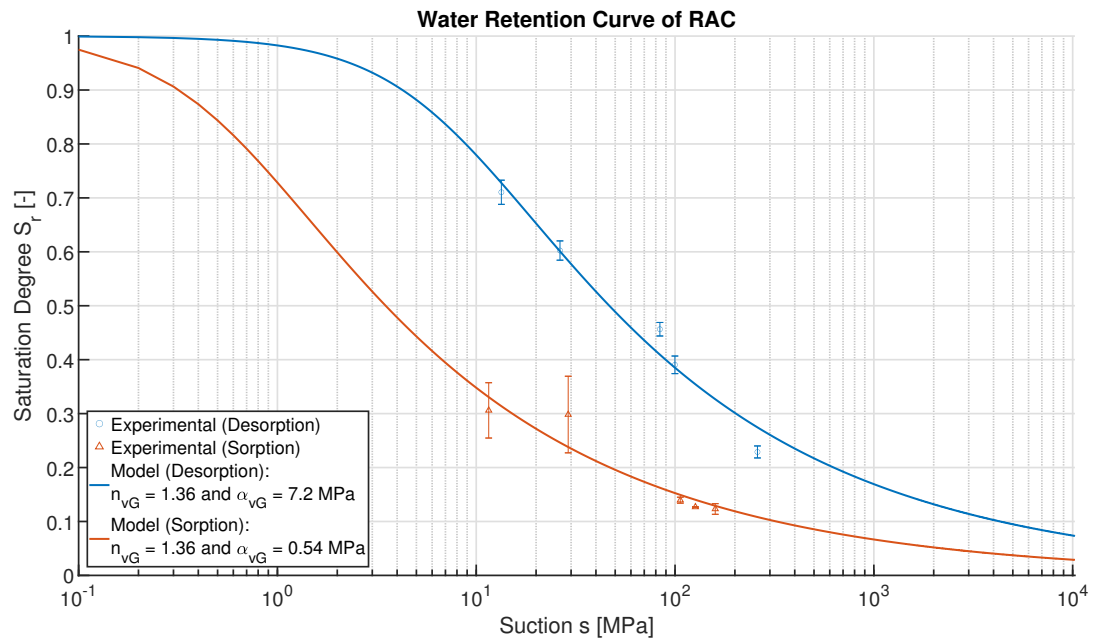
Figure B.9: Water Retention Curve for the RAC composition, based on the results from the static sorption and desorption experiment, and using the Van Genuchten's model.

C GENERATION OF A REPRESENTATIVE VOLUME ELEMENT (RVE)

Contents

C.1 Introduction

This appendix depicts the algorithm used to generate a Representative Volume Element (RVE). The main part of this algorithm is written in MATLAB R2019b, where a concrete sample (in the form of a slice) is created. However, it is part of a Python routine that calls, through an API (Application Programming Interface), both the MATLAB routines and the mesher GMSH [Geuzaine & Remacle, 2009], and create a .bat file to run the simulations automatically.

C.2 Algorithm generating the sample

This section lays down the main MATLAB routine created to generate a concrete RVE. It calls the many sub-routines required to fully generate a concrete sample, based on an input of Particle Size Distribution (PSD).

As for every MATLAB routine, the first commands are used to initialise the workspace and the many parameters the user must define. As it was mentioned in the introduction, this main routine is called by a Python script, and parameters are passed from Python to MATLAB through the `Input.mat` workspace file. It contains the following parameters:

- `Save`: true or false boolean parameter to save the Figures generated and the Workspace;

- `RCA`: true or false boolean parameter for the type of aggregates used in the concrete composition. True is for RCA, and False is for NA;

- `Circle`: the algorithm can be used to create aggregates that are based on either a circular shape (True) or an ellipsoidal shape (False);

- `C`: the length of a the sample, that is defined as a square;

- `Name`: name of the file to be used to save the parameters and to generate the several files;

- `TargetedAspectRatio`: if the aggregate is generated from an ellipsoidal shape (i.e. `Circle = 0`), a targeted aspect ratio can be defined in the form of a vector containing both a maximum and minimum aspect ratio;

- `RandomSeed`: the routines used introduce randomness through the function `rand`. This function is based on a seed that can be chosen to be `'default'` or `'shuffle'`, the latter depending on the time at which the algorithm is started.

```
1  % Loading the parameters fixed by the user.
2  load Input.mat
3  % Choice of the seed for the randomiser.
4  rng(RandomSeed)
```

The first part of this routine is to input the Particle Size Distribution (PSD) of the composition's aggregates, as well as some other parameters to determine the surface fraction of

aggregates required. Indeed, the volume fraction is computed by dividing the mass of aggregates used per cubic meter of concrete by their density. Then, multiplying this volume fraction by the area of the sample (here, a square whose side is C [mm] large) yields the surface of aggregates required to reach said volume fraction, under the hypothesis that the aggregates are spherical.

```
5  PSD = [D_min D_max Passers-By] ; % Input of the PSD by size fraction, ...
       with D in [mm] and Passers-By in [%]
6
7  % Determination of the size fraction of each passer-by' size.
8  Volume_Fraction = Mass_Aggregate/(Density_Aggregate) ; % Volume fraction
9  Surface_Fraction = Volume_Fraction*C^2 ; % Surface fraction
10 PSD(:,4) = round(PSD(:,3)/100*Surface_Fraction) ; % Surface required by ...
       each passer-by' size
11 PSD(:,5) = zeros(size(PSD,1),1) ; % Blank column to add the cumulative ...
       aggregates' surface
```

Then, the algorithm performs a loop on the size fraction defined in the PSD, starting from the biggest diameter to the smallest one in order to increase filling of the sample. After completing one size fraction (which is verified in the `CheckPSD.m` file), the `Size` index decreases by one. Therefore, once the PSD is completed, `Size = 0` and the loop is terminated.

```
12 % Initialisation of several parameters used in the loop
13 Num = 0 ; % Number of aggregates placed inside the sample, to be incremented.
14 Size = size(PSD,1); % Number of PSD size fractions
15
16 while Size ≥1 % While we have not run out of aggregates to place ...
       according to the PSD
```

The first step of the loop is to create an aggregate (from either a circular or an ellipsoidal shape) whose diameter is in between the bounds of the size fraction used, thanks to the `AggregateCreator.m` function.

Then, this aggregate is degenerated into an octagon whose vertices are sligthly modified with respect to the initial diameter, increasing the randomness of the aggregates. This deformation is the main cause of disparity between the real PSD (given in input) and the one obtained numerically. Moreover, the deformation depends on the size fraction studied, the bigger the diameter and the bigger the deformation may be.

After being deformed, the aggregate is randomly rotated through a rotation matrix.

Finally, the new radius of the aggregate is calculated, taking into account the real position of the vertices after deformation, and the aggregate is shifted to replace its center in the $(0;0)$ position.

```
17     run AggregateCreator % Create a random aggregate
```

Then, once the aggregate is created, the routine calls the `CheckPSD.m` function. First of all, this function verifies if the new radius of the aggregate, sourced by the deformation of the vertices, is still inside the bound of the size fraction being used. If not, it returns `AddAggregate = false` and a new aggregate is generated.

Otherwise, the function verifies if the surface area provided by the newly created aggregate, added to the surface area of the aggregates already placed, is inside the limit of the surface fraction required for said size fraction. If not, it means that the size fraction is complete and

therefore, the function returns `Size = Size - 1` and `AddAggregate = false`. If it is below the required surface area, it returns `AddAggregate = true`.

```
18      run CheckPSD % Check if PSD is complete or not
```

If `AddAggregate = true`, the algorithm calls the `CheckIntersection_Trace.m` function, whose role is to place the aggregate at a random position inside the sample and then verify that there is no overlapping with any other aggregate. To achieve that, it simply verifies if the traces of the two aggregates being checked do not intersect either along the horizontal axis or along the vertical one. If it is so for all aggregates already placed, it returns `AddAggregate = true` and add the surface of the aggregate in the total surface of the size fraction.

```
19      if AddAggregate % If the aggregate generated can be used
20
21          run CheckIntersection_Trace % Check for intersection and creates ...
                a random center position
22
23      end
```

Then, the algorithm checks if the sample uses RCA or NA. If it is made of RCA, it develops a layer of adherent mortar paste around the NA by defining a new, smaller aggregate (NA) inside the already existing one (RCA).

The size of the aggregate surrounded by adhered mortar is obtained by multiplying a fixed proportion of mortar (varying from 35% to 50% depending on the aggregate's diameter) by a random factor (between 95% and 105%) to add randomness. Then, the percentage of NA is multiplied by the area of the RCA, yielding the area of the natural aggregate inside the adhered mortar.
To obtain the radius of this aggregate, an equation is solved through a `for` loop, where the difference between the two sides of the equation must not exceed 1%:

$$\text{AreaNA} = \text{polyarea}(x * \text{Percentage}, y * \text{Percentage}) \tag{C.1}$$

where `Percentage` is a factor smaller than one, that multiplies the coordinates of the RCA to create the smaller NA inside of it, respecting the proportions of surface area dictated between the adhered mortar and the NA.

```
24  if AddAggregate && RCA
25
26          % The NA is generated with a certain percentage of adherent ...
                mortar paste around. The routine therefore calculates the ...
                required percentage of NA inside the RCA (based on a given ...
                cement paste content of [50 45 40 35] for the several size ...
                fraction studied, further randomised +-5%).
27          r = 0.95 + (1.05-0.95)*rand ;
28          Percentage_InnerNA = r*(1-[50 45 40 35]./100) ;
29
30          % The areas of both the NA (inside the RCA) and the total RCA ...
                (adherent mortar + NA) are then calculated.
31          AreaRCA(Num) = Surface(Num) ;
32          Area_InnerNA(Num) = Percentage_InnerNA(Size)*AreaRCA(Num) ;
33
```

```
34          % The following loop creates a smaller NA inside the RCA by ...
               multiplying all of its coordinates by a certain 'Percentage'. ...
               Then, it verifies if the area of the new NA is equal to the ...
               area required, with a precision of +-1%
35          for Percentage = 1:-0.001:0.001
36
37              Precision = ...
                   Area_InnerNA(Num)/polyarea(x*Percentage,y*Percentage) ;
38
39              if Precision >= 0.99 && Precision  <= 1.01
40                  MultRadius_InnerNA(Num) = Percentage ;
41                  break
42              end
43
44          end
45
46          % Computation of the radius of the NA inside the RCA
47          R = MultRadius_InnerNA(Num)*Radius(Num) ;
48
49      end
```

Finally, the algorithm just verifies if no aggregate is outside the border as the condition to place them is achieved with respect to their center and not the position of their extremities. However, the condition to place the aggregate already takes that into account and it is just a supplementary security.

```
50  % Check if no aggregate is outside the border
51  if max(Y_coord+Center(:,2)) > C | max(X_coord+Center(:,1)) > C
52
53      disp('Error: Aggregate outside the border')
54
55  end
```

C.2.1 Sub-routine: `AggregateCreator.m`

The following sub-routine, named `AggregateCreator.m`, is used to generate a random aggregate from the PSD in input. It can either create a circular aggregate or an ellipsoidal one, depending on the value of the boolean variable `'Circle'`.

It starts by incrementing the number of aggregates as the new one is created. Then, it determines a random radius from the Particle Size Distribution. As a reminder, the main script (and therefore this one too) start from the biggest size to the smallest to ensure efficient positioning of the aggregates generated (better use of the sample' space).

As the value in the PSD matrix is the diameter of the aggregate, those are divided by 2 to obtain the radius. It uses the `rand` function in order to add a random character to the size of the aggregate.

```
1  % Incrementation of the number of aggregates as this one is created.
2  Num = Num + 1 ;
3  % Determination of a random radius in the given PSD.
4  R = PSD(Size,1)/2 + (PSD(Size,2)-PSD(Size,1))/2*rand ; % mm
```

The aggregate generated is based on a perfect ellipsoid or circle (degenerated on 8 co-ordinates). A deformation is therefore introduced in order to move the vertices of those aggregates to the inside or the outside. This maximum deformation is equal to the smallest size of each fraction divided by 10.

```
5  Deform = PSD(Size,1)/10 ; % mm
```

If the user decides to create circular aggregates ('Circle' set to True), then $a = b = R$. Otherwise, the value of a and b are different to generate an ellipsoid. The value of the parameter b is based on the targeted aspect ratio given in input.

```
6  if Circle
7      a = R ;
8      b = R ;
9  else
10     a = R ;
11     b = R/(TargetedAspectRatio(1)+diff(TargetedAspectRatio)*rand) ;
12 end
```

Then, the aggregate is generated, and the vertices are deformed at the same time.

```
13 % Generation of the circular or ellipsoidal aggregate. The coordinates ...
      are numbered as follows:
14 %
15 %                          3
16 %            4                        2
17 % 5                                            1
18 %            6                        8
19 %                          7
20 %
21 x = a * cos( (0:7) * (2*pi/8) ) + Deform*rand(1,8) ;
22 y = b * sin( (0:7) * (2*pi/8) ) + Deform*rand(1,8) ;
```

Once the x and y coordinates are known, the aspect ratio is calculated: L is the biggest distance along the x dimension (between the coordinates 1 and 5) and E is the smallest, along the y dimension (between the coordinates 3 and 7).

```
23 % Calculation of the two perpendicular sizes of the aggregate, named L ...
      and E (L>E) in order to compute the aspect ratio of the aggregate.
24 E(Num)  = sqrt((x(3)-x(7))^2+(y(3)-y(7))^2) ;
25 L(Num)  = sqrt((x(1)-x(5))^2+(y(1)-y(5))^2) ;
26 AspectRatio(Num) = L(Num)/E(Num) ;
```

The aggregate is then rotated randomly, through a rotation matrix.

```
27 % Creation of a random angle of rotation (between 1 and 360 degrees) in ...
      order to rotate the aggregate.
28 Angle = 360*rand(1) ;
29 Rotation = [cosd(Angle) -sind(Angle); sind(Angle) cosd(Angle)];
30 Rotated_Coord = transpose([transpose(x) , transpose(y)]*Rotation) ;
31 x = Rotated_Coord(1,:) ;
32 y = Rotated_Coord(2,:) ;
```

As the radius given at the beginning of this routine has been changed due to the deformation applied to the vertices of the octagon, the new radius is to be calculated. At first, the center of the aggregate is the $(0; 0)$ point, but then the deformation also moves this center, requiring a complete calculation of the maximum distance between two points of the octagon, then divided by two to obtain the radius and not the diameter.

```
33  for k = 1:8
34     Distance(k,:) = sqrt((x-x(k)).^2 + (y-y(k)).^2);
35  end
36  R = max(Distance,[],'all')/2 ;
```

Finally, the aggregate is shifted to replace its center in the $(0; 0)$ point, which facilitates the positioning of the aggregate in the other sub-routine.

```
37  Current_Center = [(max(x)+min(x))/2 (max(y)+min(y))/2] ;
38  x = x - Current_Center(1) ;
39  y = y - Current_Center(2) ;
```

C.2.2   Sub-routine: `CheckPSD.m`

This sub-routine, named `CheckPSD.m`, verifies if the newly created aggregate is required to complete the Particle Size Distribution and/or if it is, due to the deformation applied previously, no longer in the correct size fraction.

If the radius of the new aggregate is outside the bound of the actual size fraction being completed, the aggregate cannot be placed. As the main routine starts from the bigger size to the smallest one, this is important to improve its efficiency.
If the aggregate doesn't belong to the current size fraction, the boolean variable `AddAggregate` is set to false and the counter `Num` is decreased by one. Then this script is ended by the `return` command.

```
1  if R > PSD(Size,2)/2 || R < PSD(Size,1)/2
2       AddAggregate = false ;
3       Num = Num-1 ;
4       return
5  end
```

If the radius is in the correct size fraction, its surface is computed to see if it doesn't exceed the required surface fraction. It first calculates the size of the newly generated aggregate.

Then, it verifies if the total surface fraction of the current size fraction, accounting for the new aggregate, exceeds the required one. If not, it can be added and `AddAggregate` is set to true. Otherwise, it may mean that the PSD is filled. It thus calculates the area of the smallest aggregate possible in the size fraction, and verifies if it may be added or if, even with the smallest aggregate, the size fraction is filled. If it isn't, then it goes on with generating a new aggregate (`AddAggregate = false` and `return`). Otherwise, it means that the size fraction is "filled" and returns `Size = Size-1` to continue with the following size fraction to be completed.

```matlab
6  AreaAggregate = polyarea(x,y) ; %mm2
7
8  if PSD(Size,5)+AreaAggregate ≤ PSD(Size,4)
9
10     AddAggregate = true ;
11     return
12
13 else
14
15     % Call to a local function to compute the smallest area possible in the
16     % current size fraction
17     MinAreaAggregate = ...
           SmallestAggregate(Size,PSD,TargetedAspectRatio,Circle) ;
18
19     if PSD(Size,5)+MinAreaAggregate < PSD(Size,4)
20
21         AddAggregate = false ;
22         Num = Num-1 ;
23         return
24
25     else
26
27         Size = Size-1 ;
28         AddAggregate = false ;
29         Num = Num-1 ;
30         return
31
32     end
33
34 end
```

The local function `SmallestAggregate.m` is used to determine the smallest aggregate that can be possibly generated using the `AggregateCreator.m` sub-routine. It does so by eliminating any randomness and deformation, and fixing the radius to the smallest possible in the size fraction studied. Note that the aggregate generated is perfectly circular or ellipsoidal.

Using this function means that the sample generated will always have a smaller surface fraction of aggregates than the one required, but it would be impossible to have exactly the same due to the random nature and the small number of aggregates required in a small sample.

```matlab
1  function MinAreaAggregate = ...
       SmallestAggregate(Size,PSD,TargetedAspectRatio,Circle)
2
3      if Circle
4          a = PSD(Size,1) ;
5          b = PSD(Size,1) ;
6      else
7          a = PSD(Size,1) ;
8          b = PSD(Size,1)/TargetedAspectRatio(1) ;
9      end
10     x_Min = a * cos( (0:7) * (2*pi/8)) ;
11     y_Min = b * sin(  (0:7) * (2*pi/8)) ;
12     MinAreaAggregate = polyarea(x_Min,y_Min) ;
13
14 end
```

C.2.3 Sub-routine: `CheckIntersection_Trace.m`

The last sub-routine to be explained is the one responsible to verify the overlapping of aggregates, called `CheckIntersection_Trace.m`. The role of this function is indeed to position the aggregate randomly inside the sample and then verify if it doesn't overlap with any other aggregate already in place.

The method used to verify if there is any intersection is the trace method. It consists of developing the horizontal and vertical traces of the two aggregates being investigated and then verifying if either the vertical ones or the horizontal ones intersect. If so, then the aggregate cannot be placed.

The first step is to position the aggregate randomly inside the sample, at a distance from the borders equal to at least the radius of the aggregate. Of course, if the aggregate being investigated is the first one, there is no need to check any overlapping.

```
1  % At the start of the main routine, there is only one aggregate and there ...
       is therefore no need to check for any overlapping of aggregates.
2  if Num == 1
3
4      x0 = R + (C-2*R)*rand(1) ;
5      y0 = R + (C-2*R)*rand(1) ;
```

Once the center has been defined, the aggregate can be permanently placed (if it is the first one) and therefore, its area must be added to the counter for the current size fraction, reaching toward the required surface fraction.

```
6      PSD(Size,5) = PSD(Size,5) + polyarea(x,y) ;
7      Surface(Num) = polyarea(x,y) ;
```

Once there is at least one aggregate placed on the sample, then the routine verifies if there is any overlapping. The overlapping algorithm is, as mentioned, based on the traces of the aggregates. A new matrix that contains the horizontal trace of the two aggregates investigated is therefore created (and the same for the vertical trace). It consists of the minimal and maximal coordinates of both the new aggregate and the one already placed. These matrices are then sorted and if there is any mixing, that is the output is not equal to either [1234] or [3412], it means that there is overlapping. The parameter `AddAggregate` is then set to false and the counter `Num` is decreased by one. Otherwise, if the condition is verified for every aggregate already placed, the new one can also be placed and its surface accounted for.

```
8   else
9
10      x0 = R + (C-2*R)*rand(1) ;
11      y0 = R + (C-2*R)*rand(1) ;
12
13      % 1-----------2  3++++++++++++4 OK
14      % 3++++++++++++4  1-----------2 OK
15      % 1------3+-+-2------4         KO
16      % 1------3++++4------2         KO
17      %
```

```
18      for i=1:Num-1
19
20          x_Trace = x0+x ;
21          y_Trace = y0+y ;
22          X_Trace = Center(i,1)+X_coord(i,:) ;
23          Y_Trace = Center(i,2)+Y_coord(i,:) ;
24
25          [¬,Trace_X] = sort( [min(x_Trace) max(x_Trace) min(X_Trace) ...
                max(X_Trace)] ) ;
26          [¬,Trace_Y] = sort( [min(y_Trace) max(y_Trace) min(Y_Trace) ...
                max(Y_Trace)] ) ;
27
28          if sum(Trace_X ≠ [1 2 3 4]) == 0 || sum(Trace_X ≠ [3 4 1 2]) ==0 ...
                || sum(Trace_Y ≠ [1 2 3 4]) ==0 || sum(Trace_Y ≠ [3 4 1 2]) ==0
29
30              AddAggregate = true ;
31
32          else
33
34              AddAggregate = false ;
35              Num = Num-1 ;
36              return
37
38          end
39
40      end
41
42      if AddAggregate
43      PSD(Size,5) = PSD(Size,5)+polyarea(x,y) ;
44      Surface(Num) = polyarea(x,y) ;
45      end
46
47  end
```

C.3   Generation of a `.geo` file

Once the sample has been created, all the coordinates are saved and must be transcripted into a `.geo` file to be fed to the GMSH software for meshing purposes.

The first step is to generate all the `Points` to be used, starting by the four corners of the sample and then all the coordinates of the aggregates. The `MeshSize` is not very important as it may be changed later as input parameter of the GMSH's mesher.

```
1  Point(i) = {X,Y,Z,MeshSize}
```

Then, the `Points` must be linked by `Lines`, creating closed surfaces. The following example of code represents the outer border of the sample as well as the first aggregate.

```
2  Line(1)   = {1,2};
3  Line(2)   = {2,3};
4  Line(3)   = {3,4};
5  Line(4)   = {4,1};
6  Line(5)   = {5,6};
7  Line(6)   = {6,7};
```

```
 8  Line(7)  = {7,8};
 9  Line(8)  = {8,9};
10  Line(9)  = {9,10};
11  Line(10) = {10,11};
12  Line(11) = {11,12};
13  Line(12) = {12,5};
```

The `Lines` must then be connected into what are called `Line Loop`, e.g. with the outer border and the first aggregate once again.

```
14  Line Loop(1) = {1,2,3,4};
15  Line Loop(2) = {5,6,7,8,9,10,11,12};
```

After creating the `Line Loops`, they are agglomerated into `Plane Surfaces`, following the expression `Plane Surface = {Outer Line Loop, Inner Line Loops}`. The first `Plane Surface` described is the one composed of the new mortar paste, with the RCA being inclusions (inner `Line Loops`). Then, when using RCA, each aggregate must also be defined as a `Plane Surface` to create the NA inclusion inside the adherent mortar paste, as shown below.

```
16  Plane Surface(1) = {1,2,3,...,252,253};
17  Plane Surface(2) = {2,128};
18  Plane Surface(3) = {3,129};
19  Plane Surface(4) = {4,130};
```

Finally, tags are associated to the two `Physical Surfaces` that are the new mortar paste and the adherent mortar paste from the RCA. Following this modelling vision, the aggregates are considered as holes in the meshing because they are far more impermeable than the mortar paste(s).

```
20  Physical Surface(1) = {1};
21  Physical Surface(2) = {2,3,...,126,127};
```

C.4   Meshing with GMSH

The `.geo` file newly created by the MATLAB routine is then fed to GMSH in order to mesh the sample. For automation purposes, GMSH is called by a Python file through an Application Programming Interface (API).

The first step is to import and start the GMSH API. Then, the `Name.geo` file is merged with the API to mesh the sample described by it.

```python
1  import gmsh # GMSH API
2  gmsh.initialize() # Start the GMSH API
3
4  gmsh.merge('%s.geo' %Name) # Read the .geo file in GMSH
```

The list of parameters used for the meshing is described below:

- The first two parameters set the minimum and maximum mesh element size to 3.

```
5  # Set minimum mesh element size
6  gmsh.option.setNumber('Mesh.MeshSizeMin', 3)
7  # Set maximum mesh element size
8  gmsh.option.setNumber('Mesh.MeshSizeMax', 3)
```

- Then, the nodes are snapped on the actual geometry and not by linear interpolation.

```
9  # If Mesh.SecondOrderLinear is set, the new nodes are inserted by linear
10 # interpolation. Otherwise they are snapped on the actual geometry.
11 # Should second order nodes (as well as nodes generated with subdivision
12 # algorithms) simply be created by linear interpolation?
13 gmsh.option.setNumber('Mesh.SecondOrderLinear', 0)
```

- The 2D meshing algorithm used is the `Frontal-Delaunay for Quads` one. Indeed, the modelling is better performed on quads than triangle. Moreover, the Frontal-Delaunay is recommended when high element quality is seeked. In the case where it would fail to mesh correctly, the `MeshAdapt` algorithm is automatically triggered by GMSH [Geuzaine & Remacle, 2009]. Moreover, the specificity "for Quads" aims at generating right-angle triangles that are more suitable for recombination.

```
14 # 2D mesh algorithm
15 # (1: MeshAdapt, 2: Automatic, 3: Initial mesh only,
16 #  5: Delaunay, 6: Frontal-Delaunay, 7: BAMG,
17 #  8: Frontal-Delaunay for Quads, 9: Packing of Parallelograms)
18 gmsh.option.setNumber('Mesh.Algorithm', 8)
```

- The mesh recombination algorithm chosen is the `Simple` algorithm. There is no need to use more complex algorithm as the meshing algorithm is built explicitly for quads and makes the recombination easier.

```
19 # Mesh recombination algorithm
20 # (0: simple, 1: blossom, 2: simple full-quad, 3: blossom full-quad)
21 gmsh.option.setNumber('Mesh.RecombinationAlgorithm', 0)
```

- Then, an "all quadrangles" mesh subdivision algorithm is used to refine the mesh.

```
22 # Mesh subdivision algorithm
23 # (0: none, 1: all quadrangles, 2: all hexahedra, 3: barycentric)
24 gmsh.option.setNumber('Mesh.SubdivisionAlgorithm', 1)
```

- Finally, the recombination algorithm is applied to all the surfaces of the sample.

```
25 # Apply recombination algorithm to all surfaces, ignoring ...
        per-surface spec
26 gmsh.option.setNumber('Mesh.RecombineAll', 1)
```

Finally, the meshing is performed in 2D, accounting for all the parameters set before. It is then exported into a MATLAB `Name.m` file to be read by a function that will translate the GMSH mesh into a working LAGAMINE file.

```python
27  # Meshing of the file described in the .geo and then writing the .m file
28  # corresponding to the mesh, in 2D
29  gmsh.model.mesh.generate(2)
30  gmsh.write('%s.m' %Name)
```

The two final steps are to show the results of the meshing (which is optional) and then close the GMSH API.

```python
31  gmsh.fltk.run() # Open GMSH to show the results
32  gmsh.finalize() # Close the GMSH API
```
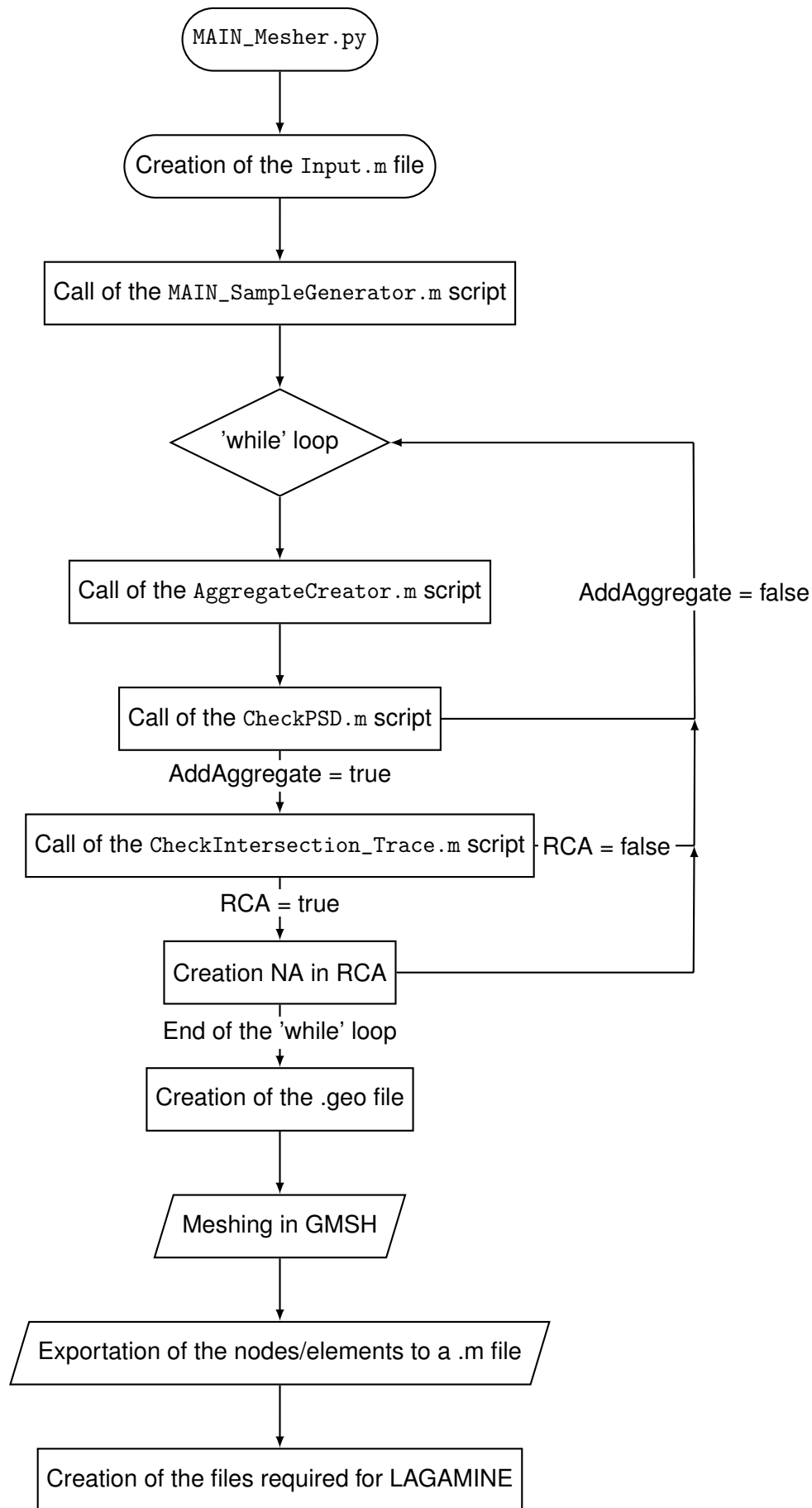
Figure C.1: Algorithm generating the RVE.

PART

6

BIBLIOGRAPHY

[Ababneh et al., 2003] Ababneh, A., Benboudjema, F., & Xi, Y. (2003). Chloride Penetration in Nonsaturated Concrete. *Journal of Materials in Civil Engineering*, 15(2), 183–191. `https://doi.org/10.1061/(asce)0899-1561(2003)15:2(183)`

[Abbasi et al., 2012] Abbasi, F., Javaux, M., Vanclooster, M., & Feyen, J. (2012). Estimating hysteresis in the soil water retention curve from monolith experiments. *Geoderma*, 189–190, 480–490. `https://doi.org/10.1016/j.geoderma.2012.06.013`

[Abedin Khan et al., 2024] Abedin Khan, Z., Balunaini, U., & Costa, S. (2024). Environmental feasibility and implications in using recycled construction and demolition waste aggregates in road construction based on leaching and life cycle assessment – a state-of-the-art review. *Cleaner Materials*, 12, 100239. `https://doi.org/10.1016/j.clema.2024.100239`

[Abyaneh et al., 2013] Abyaneh, S. D., Wong, H. S., & Buenfeld, N. R. (2013). Modelling the diffusivity of mortar and concrete using a three-dimensional mesostructure with several aggregate shapes. *Computational Materials Science*, 78, 63–73. `https://doi.org/10.1016/j.commatsci.2013.05.024`

[Akbarnezhad et al., 2013] Akbarnezhad, A., Ong., K. C. G., Tam, C. T., & Zhang, M. H. (2013). Effects of the Parent Concrete Properties and Crushing Procedure on the Properties of Coarse Recycled Concrete Aggregates. *Journal of Materials in Civil Engineering*, 25(12), 1795–1802. `https://doi.org/10.1061/(asce)mt.1943-5533.0000789`

[Alsheet & Razaqpur, 2018] Alsheet, F. & Razaqpur, A. G. (2018). Effect of Time-Dependent Chloride Profile and Temperature Variation on Chloride Diffusion in Concrete. *Sixth International Conference on Durability of Concrete Structures*.

[Andrade et al., 2015] Andrade, C., Climent, M. A., & de Vera, G. (2015). Procedure for calculating the chloride diffusion coefficient and surface concentration from a profile having a maximum beyond the concrete surface. *Materials and Structures*, 48, 863–869. `https://doi.org/10.1617/s11527-015-0543-4`

[Angst, 2011] Angst, U. (2011). *Chloride induced reinforcement corrosion in concrete*. Norwegian University of Science and Technology (NTNU).

[Angst et al., 2009] Angst, U., Elsener, B., Larsen, C. K., & Vennesland, Ø. (2009). Critical chloride content in reinforced concrete - A review. *Cement and Concrete Research*, 39, 1122–1138. `https://doi.org/10.1016/j.cemconres.2009.08.006`

[Apers & de Schutter, 2018] Apers, J. & de Schutter, G. (2018). *Technologie du béton - Chapitre 5 : V Durabilité*, volume 5. Groupement Belge du Béton (GBB).

[Arredondo-Rea et al., 2012] Arredondo-Rea, S., Corral-Higuera, R., Gómez-Soberón, J., Castorena-González, J., Orozco-Carmona, V., & Almaral-Sánchez, J. (2012). Carbonation Rate and Reinforcing Steel Corrosion of Concretes with Recycled Concrete Aggregates and Supplementary Cementing Materials. *International Journal of Electrochemical Science*, 7(2), 1602–1610. `https://doi.org/10.1016/s1452-3981(23)13438-9`

[Balafas & Burgoyne, 2010] Balafas, I. & Burgoyne, C. J. (2010). Environmental effects on cover cracking due to corrosion. *Cement and Concrete Research*, 40, 1429–1440. `https://doi.org/10.1016/j.cemconres.2010.05.003`

[Bao et al., 2020] Bao, J., Li, S., Zhang, P., Ding, X., Xue, S., Cui, Y., & Zhao, T. (2020). Influence of the incorporation of recycled coarse aggregate on water absorption and chloride penetration into concrete. *Construction and Building Materials*, 239, 117845. `https://doi.org/10.1016/j.conbuildmat.2019.117845`

[Baroghel-Bouny, 1994] Baroghel-Bouny, V. (1994). *Caractérisation microstructurale et hydrique des pâtes de ciment et des bétons ordinaires et à très hautes performances*. École Nationale des Ponts et Chaussées.

[Baroghel-Bouny et al., 2011] Baroghel-Bouny, V., Thiéry, M., & Wang, X. (2011). Modelling of isothermal coupled moisture–ion transport in cementitious materials. *Cement and Concrete Research*, 41, 828–841. `https://doi.org/10.1016/j.cemconres.2011.04.001`

[Barreto Santos et al., 2020] Barreto Santos, M., De Brito, J., & Santos Silva, A. (2020). A review on alkali-silica reaction evolution in recycled aggregate concrete. *Materials*, 13(11), 2625. `https://doi.org/10.3390/ma13112625`

[Bear & Verruijt, 1987] Bear, J. & Verruijt, A. (1987). *Modeling Groundwater Flow and Pollution*. D. Reidel Publishing Company. `https://doi.org/10.1007/978-94-009-3379-8`

[Beckett & Augarde, 2013] Beckett, C. T. & Augarde, C. E. (2013). Prediction of soil water retention properties using pore-size distribution and porosity. *Canadian Geotechnical Journal*, 50(4), 435–450. `https://doi.org/10.1139/cgj-2012-0320`

[Belin et al., 2014] Belin, P., Habert, G., Thiery, M., & Roussel, N. (2014). Cement paste content and water absorption of recycled concrete coarse aggregates. *Materials and Structures*, 47(9), 1451–1465.

[Bensoussan et al., 1978] Bensoussan, A., Lions, J.-L., & Papanicolaou, G. (1978). *Asymptotic analysis for periodic structures*, volume 5. North-Holland Publishing Company Amsterdam. `https://doi.org/10.1090/chel/374`

[Bentur & Odler, 1996] Bentur, A. & Odler, I. (1996). Development and nature of interfacial microstructure. *Interfacial Transition Zone in Concrete, RILEM REPORT*, volume 11, (Chapter 2, 21–50). E & FN Spon.

[Bertolini et al., 2004] Bertolini, L., Elsener, B., Pedeferri, P., & Polder, R. P. (2004). *Corrosion of Steel in Concrete*. WILEY-VCH Verlag GmbH and Co. KGaA, Weinheim. `https://doi.org/10.1002/9783527651696`

[Bertrand, 2020] Bertrand, F. (2020). *Hydro-mechanical modelling of multiphase flow in naturally fractured coalbeds applied to CBM recovery or CO_2 storage*. ULiège University.

[Biglarijoo et al., 2017] Biglarijoo, N., Nili, M., Hosseinian, S. M., Razmara, M., Ahmadi, S., & Razmara, P. (2017). Modelling and optimisation of concrete containing recycled concrete aggregate and waste glass. *Magazine of Concrete Research*, 69(6), 306–316. `https://doi.org/10.1680/jmacr.16.00279`

[Biver, 1993] Biver, P. (1993). *Phenomenal and Numerical study on the propagation of misicible pollutants in a medium with multiple porosity*. University of Liège.

[Bowen, 1980] Bowen, R. M. (1980). Incompressible porous media models by use of the theory of mixtures. *International Journal of Engineering Science*, 18, 1129–1148. `https://doi.org/10.1016/0020-7225(80)90114-7`

[Braga et al., 2017] Braga, A. M., Silvestre, J. D., & de Brito, J. (2017). Compared environmental and economic impact from cradle to gate of concrete with natural and recycled coarse aggregates. *Journal of Cleaner Production*, 162, 529–543. `https://doi.org/10.1016/j.jclepro.2017.06.057`

[Broomfield, 2007] Broomfield, J. P. (2007). *Corrosion of Steel in Concrete: Understanding, investigation and repair.* (2 ed.). Taylor and Francis. `https://doi.org/10.1201/9781003223016`

[Brunauer et al., 1940] Brunauer, S., Deming, L. S., Deming, W. E., & Teller, E. (1940). On a theory of the van de Waals Adsorption of Gases. *Journal of the American Chemical Society*, 62(7), 1723:1732. `https://doi.org/10.1021/ja01864a025`

[Brunauer et al., 1938] Brunauer, S., Emmet, P. H., & Teller, E. (1938). Adsorption of Gases in Multimolecular Layers. *Journal of the American Chemical Society*, 60, 309–319. `https://doi.org/10.1021/ja01269a023`

[Capparelli & Spolverino, 2020] Capparelli, G. & Spolverino, G. (2020). An Empirical Approach for Modeling Hysteresis Behavior of Pyroclastic Soils. *Hydrology*, 7(1), 14. `https://doi.org/10.3390/hydrology7010014`

[CEMBUREAU, 2021] CEMBUREAU (2021). European Cement Association: Activity Report 2020. Technical report, Brussels, Belgium.

[CEN, 2008] CEN (2008). EN-12620+A1 - Aggregates for concrete, with 2008 amendment. Technical report, CEN, Brussels, Belgium.

[CEN, 2013] CEN (2013). EN-206 - Concrete: Specification, performance, production and conformity. Incorporating corrigendum May 2014. Technical report, CEN, Brussels, Belgium.

[Chang et al., 2017] Chang, H., Mu, S., Xie, D., & Wang, P. (2017). Influence of pore structure and moisture distribution on chloride "maximum phenomenon" in surface layer of specimens exposed to cyclic drying-wetting condition. *Construction and Building Materials*, 131, 16–30. `https://doi.org/10.1016/j.conbuildmat.2016.11.071`

[Chatterji, 1999] Chatterji, S. (1999). Evidence of variable diffusivity of ions in saturated cementitious materials. *Cement and Concrete Research*, 29, 595–598. `https://doi.org/10.1016/s0008-8846(98)00193-8`

[Chen & Mahadevan, 2008] Chen, D. & Mahadevan, S. (2008). Chloride-induced reinforcement corrosion and concrete cracking simulation. *Cement and Concrete Composites*, 30, 227–238. `https://doi.org/10.1016/j.cemconcomp.2006.10.007`

[Chen et al., 2019] Chen, X., Zhang, X., & Wu, Z. (2019). Analytical Solution for One-Dimensional Transport of Particles considering Dispersion in Deposition Kinetics. *Geofluids*, 2019, 1–7. `https://doi.org/10.1155/2019/1941426`

[Choi et al., 2017] Choi, Y. C., Park, B., Pang, G.-S., Lee, K.-M., & Choi, S. (2017). Modelling of chloride diffusivity in concrete considering effect of aggregates. *Construction and Building Materials*, 136, 81–87. `https://doi.org/10.1016/j.conbuildmat.2017.01.041`

[Collepardi et al., 1972] Collepardi, M., Marcialis, A., & Turriziani, R. (1972). Penetration of Chloride Ions into Cement Pastes and Concretes. *Journal of the American Ceramic Society*, 55(10), 534–535. `https://doi.org/10.1111/j.1151-2916.1972.tb13424.x`

[Collin, 2003] Collin, F. (2003). *Couplages thermo-hydro-mécaniques dans les sols et les roches tendres partiellement saturés*. ULiège University.

[Collin & de Ville de Goyet, 2019] Collin, F. & de Ville de Goyet, V. (2019). *Non linear finite elements*. ULiège University.

[Collin et al., 2002] Collin, F., Li, X., Radu, J., & Charlier, R. (2002). Thermo-hydro-mechanical coupling in clay barriers. *Engineering Geology*, 64, 179–193. `https://doi.org/10.1201/9781003078487-64`

[Colman et al., 2023] Colman, C., Bulteel, D., Elkarim, B. M., Rémond, S., & Courard, L. (2023). Expansion of concrete by secondary ettringite formation due to fine recycled aggregates contaminated with gypsum. *Advances in Cement Research*, 35(11), 480–488. `https://doi.org/10.1680/jadcr.22.00043`

[Concha, 2014] Concha, F. A. (2014). *Solid-Liquid Separation in the Mining Industry*, volume Fluid Mechanics and Its Applications (Book 105). Springer International Publishing Switzerland. `https://doi.org/10.1007/978-3-319-02484-4`

[Courard, 2017] Courard, L. (2017). *Matériaux de construction*. ULiège University.

[Courard, 2018] Courard, L. (2018). *Technologie des bétons et matériaux nouveaux*. ULiège University.

[Courard, 2019] Courard, L. (2019). *Maintenance, repair and renforcement of constructions*. ULiège University.

[Courard & Bissonnette, 2016] Courard, L. & Bissonnette, B. (2016). Réparation des ouvrages en béton armé - partie 1 : pathologies et diagnostic. *Techniques de l'ingénieur*. `https://doi.org/10.51257/a-v1-c6300`

[Courard & Michel, 2014] Courard, L. & Michel, F. (2014). Aspects phénoménologiques relatifs aux processus de dégradation chimique des barrières ouvragées à base de liant hydraulique - évaluation de la phase d'initiation de la corrosion des armatures des structures en béton armé. Analyse du rapport ONDRAF/NIRAS - NIROND-TR 2011-58 F 31 - August 2012, ULiège University.

[Courard et al., 2011] Courard, L., Michel, F., & Martin, M. (2011). The evaluation of the surface free energy of liquids and solids in concrete technology. *Construction and Building Materials*, 25, 260–266. `https://doi.org/10.1016/j.conbuildmat.2010.06.030`

[da Costa et al., 2013] da Costa, A., Fenaux, M., Fernández, J., Sánchez, E., & Moragues, A. (2013). Modelling of chloride penetration into non-saturated concrete: Case study application for real marine offshore structures. *Construction and Building Materials*, 43, 217–224. `https://doi.org/10.1016/j.conbuildmat.2013.02.009`

[Dassargues, 2017] Dassargues, A. (2017). *Hydrogéologie*. ULiège University.

[de Juan & Gutiérrez, 2009] de Juan, M. S. & Gutiérrez, P. A. (2009). Study on the influence of attached mortar content on the properties of recycled concrete aggregate. *Construction and Building Materials*, 23, 872–877. `https://doi.org/10.1016/j.conbuildmat.2008.04.012`

[Debieb et al., 2010] Debieb, F., Courard, L., Kenai, S., & Degeimbre, R. (2010). Mechanical and durability properties of concrete using contaminated recycled aggregates. *Cement & Concrete Composites*, 32, 421–426. `https://doi.org/10.1016/j.cemconcomp.2010.03.004`

[Delage, 1987] Delage, P. (1987). Aspects du comportement des sols non saturés. *Revue française de géotechnique*, 40, 33–43. `https://doi.org/10.1051/geotech/1987040033`

[Delage et al., 1998] Delage, P., Howat, M., & Cui, Y. (1998). The relationship between suction and swelling properties in a heavily compacted unsaturated clay. *Engineering Geology*, 50, 31–48. `https://doi.org/10.1016/s0013-7952(97)00083-5`

[Delagrave et al., 1997] Delagrave, A., Bigas, J., Ollivier, J., Marchand, J., & Pigeon, M. (1997). Influence of the Interfacial Zone on the Chloride Diffusivity of Mortars. *Advanced Cement Based Materials*, 5(3–4), 86–92. `https://doi.org/10.1016/s1065-7355(96)00008-9`

[Deodonne, 2015] Deodonne, K. (2015). *Études des caractéristiques physico-chimiques de bétons de granulats recyclés et de leur impact environnemental*. Université de Strasbourg.

[Desaar, 2015] Desaar, F. (2015). Effet des additions de type 2 sur les écoulements multiphasiques dans les pâtes de ciment. ULiège University.

[Desrues et al., 2019] Desrues, J., Argilaga, A., Caillerie, D., Combe, G., Nguyen, T. K., Richefeu, V., & Dal Pont, S. (2019). From discrete to continuum modelling of boundary value problems in geomechanics: An integrated fem-dem approach. *International Journal for Numerical and Analytical Methods in Geomechanics*, 43(5), 919–955. `https://doi.org/DOI:10.1002/nag.2914`

[Dhir et al., 1989] Dhir, R. K., Hewlett, P. C., & Chan, Y. N. (1989). Near surface characteristics of concrete: intrinsic permeability. *Magazine of Concrete Research*, 41(147), 87–97. `https://doi.org/10.1680/macr.1989.41.147.87`

[Di Pillo & Todisco, 2020] Di Pillo, R. & Todisco, M. T. (2020). Transport and adsorption of pollutants in saturated porous media: integration into unlimited domain. *Pollution Research*, 39(3), 818–823.

[Dieudonné, 2016] Dieudonné, A.-C. (2016). *Hydromechanical behaviour of compacted bentonite: from micro-scale analysis to macro-scale modelling*. ULiège University.

[Diotti et al., 2020] Diotti, A., Perèz Galvin, A., Piccinali, A., Plizzari, G., & Sorlini, S. (2020). Chemical and leaching behavior of construction and demolition wastes and recycled aggregates. *Sustainability*, 12(24), 10326. `https://doi.org/10.3390/su122410326`

[Dreux & Festa, 1998] Dreux, G. & Festa, J. (1998). *Nouveau guide du béton et de ses constituants* (8 ed.).

[Dupré & Dupré, 1869] Dupré, A. & Dupré, P. (1869). *Théorie mécanique de la chaleur*. Gauthier-Villars.

[Erdem et al., 2009] Erdem, T. K., Khayat, K. H., & Yahia, A. (2009). Correlating Rheology of Self-Consolidating Concrete to Corresponding Concrete-Equivalent Mortar. *ACI Materials Journal*, 106(2), 154–160.

[Etxeberria et al., 2007] Etxeberria, M., Vázquez, E., Marí, A., & Barra, M. (2007). Influence of amount of recycled coarse aggregates and production process on properties of recycled aggregate concrete. *Cement and Concrete Research*, 37, 735–742. `https://doi.org/10.1016/j.cemconres.2007.02.002`

[EU, 2008] EU (2008). Directive 2008/98/EC of the European Parliament and of the Council of 19 November 2008 on waste and repealing certain Directives. *Official Journal of the European Union*.

[European Environment Agency, 2020] European Environment Agency (2020). Construction and demolition waste : challenges and opportunities in a circular economy. Technical report, European Environment Agency.

[EUROSTAT, 2023] EUROSTAT (2023). ENV_WAS: European statistics on waste. Technical report.

[Fanara, 2020] Fanara, A. (2020). Modelling of drying phenomena in concrete with recycled aggregates. University of Liège.

[Fanara et al., 2022] Fanara, A., Courard, L., Collin, F., & Hubert, J. (2022). Transfer properties in recycled aggregates concrete: Experimental and numerical approaches. *Construction and Building Materials*, 326, 126778. `https://doi.org/10.1016/j.conbuildmat.2022.126778`

[Fathifazl et al., 2011] Fathifazl, G., Ghani Razaqpur, A., Burkan Isgor, O., Abbas, A., Fournier, B., & Foo, S. (2011). Creep and drying shrinkage characteristics of concrete produced with coarse recycled concrete aggregate. *Cement and Concrete Composites*, 33(10), 1026–1037. `https://doi.org/10.1016/j.cemconcomp.2011.08.004`

[Florea & Brouwers, 2013] Florea, M. V. A. & Brouwers, H. J. H. (2013). Properties of various size fractions of crushed concrete related to process conditions and re-use. *Cement and Concrete Research*, 52, 11–21. `https://doi.org/10.1016/j.cemconres.2013.05.005`

[Fraj & Idir, 2017] Fraj, A. B. & Idir, R. (2017). Concrete based on recycled aggregates – recycling and environmental analysis: A case study of paris' region. *Construction and Building Materials*, 157, 952–964. `https://doi.org/10.1016/j.conbuildmat.2017.09.059`

[Fredlund et al., 2011] Fredlund, D. G., Sheng, D., & Zhao, J. (2011). Estimation of soil suction from the soil-water characteristic curve. *Canadian Geotechnical Journal*, 48, 186–198. `https://doi.org/10.1139/t10-060`

[Fu et al., 2010] Fu, C., Jin, X., & Jin, N. (2010). Modeling of Chloride Ions Diffusion in Cracked Concrete. *Earth and Space 2010: Engineering, Science, Construction, and Operations in Challenging Environments*, 3579–3589. `https://doi.org/10.1061/41096(366)343`

[Garboczi & Bentz, 1998] Garboczi, E. J. & Bentz, D. P. (1998). Multiscale Analytical/Numerical Theory of the Diffusivity of Concrete. *Advanced Cement Based Materials*, 8, 77–88. `https://doi.org/10.1016/s1065-7355(98)00010-8`

[García-González et al., 2014] García-González, J., Rodríguez-Robles, D., Juan-Valdés, A., del Pozo, J. M. M., & Guerra-Romero, M. I. (2014). Pre-Saturation Technique of the Recycled Aggregates: Solution to the Water Absorption Drawback in the Recycled Concrete Manufacture. *Materials*, 7, 6224–6236. `https://doi.org/10.3390/ma7096224`

[Gebremariam et al., 2020] Gebremariam, A. T., Maio, F. D., Vahidi, A., & Rem, P. (2020). Innovative technologies for recycling End-of-Life concrete waste in the built environment. *Resources, Conservation & Recycling*, 163, 104911. `https://doi.org/10.1016/j.resconrec.2020.104911`

[Gerard, 2011] Gerard, P. (2011). *Impact des transfers de gaz sur le comportement poromécanique des matériaux argileux*. ULiège University.

[Gerard et al., 2010] Gerard, P., Léonard, A., Masekanya, J., Charlier, R., & Collin, F. (2010). Study of the soil–atmosphere moisture exchanges through convective drying tests in non-isothermal conditions. *International Journal for Numerical and Analytical Methods in Geomechanics*, 34(12), 1297–1320. `https://doi.org/10.1002/nag.866`

[Geuzaine & Remacle, 2009] Geuzaine, C. & Remacle, J.-F. (2009). Gmsh: A 3-d finite element mesh generator with built-in pre- and post-processing facilities. *International Journal for Numerical Methods in Engineering*, 79(11), 1309–1331. `https://doi.org/10.1002/nme.2579`

[Ghorbani et al., 2019] Ghorbani, S., Sharifi, S., Ghorbani, S., Tam, V. W. Y., de Brito, J., & Kurda, R. (2019). Effect of crushed concrete waste's maximum size as partial replacement of natural coarse aggregate on the mechanical and durability properties of concrete. *Resources, Conservation & Recycling*, 149, 664–673. `https://doi.org/10.1016/j.resconrec.2019.06.030`

[Giles & Smith, 1974] Giles, C. H. & Smith, D. (1974). A General Treatment and Classification of the Solute Adsorption Isotherm - 1. Theoretical. *Journal of Colloid and Interface Science*, 47(3), 755–765. `https://doi.org/10.1016/0021-9797(74)90252-5`

[Gjørv, 2011] Gjørv, O. E. (2011). Durability of Concrete Structures. *Arabian Journal for Science and Engineering*, 36, 151–172. `https://doi.org/10.1007/s13369-010-0033-5`

[Glasser et al., 2008] Glasser, F. P., Marchand, J., & Samson, E. (2008). Durability of concrete — Degradation phenomena involving detrimental chemical reactions. *Cement and Concrete Research*, 38(2), 226–246. `https://doi.org/10.1016/j.cemconres.2007.09.015`

[Gonzalez & Etxeberria, 2014] Gonzalez, A. & Etxeberria, M. (2014). Experimental analysis of properties of high performance recycled aggregate concrete. *Construction and Building Materials*, 52, 227–235. `https://doi.org/10.1016/j.conbuildmat.2013.11.054`

[Grieb et al., 1962] Grieb, W. E., Werner, G., & Woolf, D. O. (1962). Resistance of Concrete Surfaces to Scaling by De-Icing Agents. *Highway Research Board Bulletin*, 323, 43–62.

[Grigoletto & Courard, 2022] Grigoletto, S. & Courard, L. (2022). Étude de la carbonatation des granulats de béton recyclé altéré par la réaction alcali-silice. *Nouveaux Matériaux et Durabilité 2022.*

[Guo et al., 2018] Guo, H., Shi, C., Guan, X., Zhu, J., Ding, Y., Ling, T.-C., Zhang, H., & Wang, Y. (2018). Durability of Recycled Aggregate Concrete - A Review. *Cement and Concrete Composites*, 89, 251–259. `https://doi.org/10.1016/j.cemconcomp.2018.03.008`

[Guzmán et al., 2011] Guzmán, S., Gálvez, J. C., & Sancho, J. M. (2011). Cover cracking of reinforced concrete due to rebar corrosion induced by chloride penetration. *Cement and Concrete Research*, 41, 893–902. `https://doi.org/10.1016/j.cemconres.2011.04.008`

[Gärtner, 2022] Gärtner, K. (2022). La plus grande écluse maritime du monde mise en service aux Pays-Bas. *Néomag.*

[Hall, 1989] Hall, C. (1989). Water sorptivity of mortars and concretes: a review. *Magazine of Concrete Research*, 41(147), 51–61. `https://doi.org/10.1680/macr.1989.41.147.51`

[Han, 2007] Han, S.-H. (2007). Influence of diffusion coefficient on chloride ion penetration of concrete structure. *Construction and Building Materials*, 21, 370–378. `https://doi.org/10.1016/j.conbuildmat.2005.08.011`

[Holla et al., 2021] Holla, V., Vu, G., Timothy, J. J., Diewald, F., Gehlen, C., & Meschke, G. (2021). Computational Generation of Virtual Concrete Mesostructures. *Materials*, 14(14), 3782. `https://doi.org/10.3390/ma14143782`

[Hu et al., 2018] Hu, Z., Mao, L., Xia, J., Liu, J., Gao, J., Yang, J., & Liu, Q. (2018). Five-phase modelling for effective diffusion coefficient of chlorides in recycled concrete. *Magazine of Concrete Research*, 70(11), 583–594. `https://doi.org/10.1680/jmacr.17.00194`

[Hubert, 2018] Hubert, J. (2018). *Experimental and numerical study of cracking during the drying of porous materials : application to the fields of chemical engineering and geomechanics.* ULiège University.

[Hubert et al., 2023] Hubert, J., Zhao, Z., Michel, F., & Courard, L. (2023). Effect of crushing method on the properties of produced recycled concrete aggregates. *Buildings*, 13(9), 2217. `https://doi.org/10.3390/buildings13092217`

[Hussain et al., 2000] Hussain, H., Levacher, D., Quenec'h, J.-L., Bennabi, A., & Bouvet, F. (2000). Valorisation des aggrégats issus de bétons de démolition dans la fabrication de nouveaux bétons. *Environnement, Ingénierie et Développement*, N19-3ème trimestre 2000, 17–22. `https://doi.org/10.4267/dechets-sciences-techniques.439`

[Idso et al., 1974] Idso, S. B., Reginato, R. J., Jackson, R. D., Kimball, B. A., & Nakayama, F. S. (1974). The Three Stages of Drying of a Field Soil. *Soil Science Society of America Journal*, 38(5), 831–837. `https://doi.org/10.2136/sssaj1974.03615995003800050037x`

[Inglezakis et al., 2018] Inglezakis, V. J., Poulopoulos, S. G., & Kazemian, H. (2018). Insights into the S-shaped sorption isotherms and their dimensionless forms. *Microporous and Mesoporous Materials*, 272, 166–176. `https://doi.org/10.1016/j.micromeso.2018.06.026`

[Isgor, 2001] Isgor, O. B. (2001). *A Durability Model for Chloride and Carbonation Induced Steel Corrosion in Reinforced Concrete Members*. Carleton University and University of Ottawa.

[Isgor & Razaqpur, 2006] Isgor, O. B. & Razaqpur, A. G. (2006). Modelling steel corrosion in concrete structures. *Materials and Structures*, 39, 291–302. `https://doi.org/10.1007/s11527-005-9022-7`

[Jin et al., 2022] Jin, L., Yu, H., Fan, T., Dong, T., Jiao, P., & Duan, J. (2022). Experimental and computational modeling of chloride transport behavior in fully recycled coarse aggregate concrete. *Construction and Building Materials*, 360, 129592. `https://doi.org/10.1016/j.conbuildmat.2022.129592`

[Jones et al., 2020] Jones, C., Ramanathan, S., Suraneni, P., & Hale, W. M. (2020). Calcium oxychloride: A critical review of the literature surrounding the formation, deterioration, testing procedures, and recommended mitigation techniques. *Cement and Concrete Composites*, 113, 103663. `https://doi.org/10.1016/j.cemconcomp.2020.103663`

[José M.V Gómez-Soberón, 2002] José M.V Gómez-Soberón (2002). Porosity of recycled concrete with substitution of recycled concrete aggregate - An experimental study. *Cement and Concrete Research*, 32, 1301–1311.

[Katz, 2003] Katz, A. (2003). Properties of concrete made with recycled aggregate from partially hydrated old concrete. *Cement and Concrete Research*, 33(5), 703–711. `https://doi.org/doi:10.1016/S0008-8846(02)01033-5`

[Khan et al., 2017] Khan, M. U., Ahmad, S., & Al-Gahtani, H. J. (2017). Chloride-Induced Corrosion of Steel in Concrete: An Overview on Chloride Diffusion and Prediction of Corrosion Initiation Time. *International Journal of Corrosion*, 2017, 1–9. `https://doi.org/10.1155/2017/5819202`

[Kohgo, 2008] Kohgo, Y. (2008). A Hysteresis Model of Soil Water Retention Curves Based on Bounding Surface Concept. *Soils and Foundations*, 48(5), 633–640. `https://doi.org/10.3208/sandf.48.633`

[Kool & Parker, 1987] Kool, J. B. & Parker, J. C. (1987). Development and Evaluation of Closed-Form Expressions for Hysteretic Soil Hydraulic Properties. *Water Resources Research*, 23(1), 105–114. `https://doi.org/10.1029/wr023i001p00105`

[Kouznetsova et al., 2001] Kouznetsova, V., Brekelmans, W. A. M., & Baaijens, F. P. T. (2001). An approach to micro-macro modeling of heterogeneous materials. *Computational Mechanics*, 27, 37–48. `https://doi.org/10.1007/s004660000212`

[Kouznetsova et al., 2002] Kouznetsova, V., Geers, M. G. D., & Brekelmans, W. A. M. (2002). Multi-scale constitutive modelling of heterogeneous materials with a gradient-enhanced computational homogenization scheme. *International Journal for Numerical Methods in Engineering*, 54, 1235–1260. `https://doi.org/10.1002/nme.541`

[Kowalski, 2003] Kowalski, S. J. (2003). *Thermomechanics of Drying Processes*. Springer-Verlag Berlin Heidelberg GmbH. `https://doi.org/10.1007/978-3-540-36405-4`

[Kumar & Bhattacharjee, 2003] Kumar, R. & Bhattacharjee, B. (2003). Porosity, pore size distribution and in situ strength of concrete. *Cement and Concrete Research*, 33, 155–164. `https://doi.org/10.1016/s0008-8846(02)00942-0`

[Lehmann et al., 2008] Lehmann, P., Assouline, S., & Or, D. (2008). Characteristic lengths affecting evaporative drying of porous media. *Physical Review*, 77(5), 056309. `https://doi.org/10.1103/physreve.77.056309`

[Léonard, 2002] Léonard, A. (2002). *Étude du séchage convectif de boues de stations d'épuration*. ULiège University.

[Levy & Helene, 2004] Levy, S. M. & Helene, P. (2004). Durability of recycled aggregates concrete: a safe way to sustainable development. *Cement and Concrete Research*, 34(11), 1975–1980. `https://doi.org/10.1016/j.cemconres.2004.02.009`

[Li & Song, 2022] Li, C.-z. & Song, X.-b. (2022). Mesoscale modeling of chloride transport in unsaturated concrete based on voronoi tessellation. *Cement and Concrete Research*, 161, 106932. `https://doi.org/10.1016/j.cemconres.2022.106932`

[Li et al., 2015] Li, L., Easterbrook, D., Xia, J., & Jin, W.-L. (2015). Numerical simulation of chloride penetration in concrete in rapid chloride migration tests. *Cement and Concrete Composites*, 63, 113–121. `https://doi.org/10.1016/j.cemconcomp.2015.09.004`

[Likos et al., 2014] Likos, W. J., Lu, N., & Godt, J. W. (2014). Hysteresis and Uncertainty in Soil Water-Retention Curve Parameters. *Journal of Geotechnical and Geoenvironmental Engineering*, 140(4). `https://doi.org/10.1061/(asce)gt.1943-5606.0001071`

[Limbachiya et al., 2000] Limbachiya, M. C., Leelawat, T., & Dhir, R. K. (2000). Use of recycled concrete aggregate in high-strength concrete. *Materials and Structures*, 33(9), 574–580. `https://doi.org/10.1007/bf02480538`

[Limousin et al., 2007] Limousin, G., Gaudet, J.-P., Charlet, L., Szenknect, S., Barthès, V., & Krimissa, M. (2007). Sorption isotherms: A review on physical bases, modeling and measurement. *Applied Geochemistry*, 22, 249–275. `https://doi.org/10.1016/j.apgeochem.2006.09.010`

[Liu et al., 2020] Liu, J., Jiang, Z., Zhao, Y., Zhou, H., Wang, X., Zhou, H., Xing, F., Li, S., Zhu, J., & Liu, W. (2020). Chloride Distribution and Steel Corrosion in a Concrete Bridge after Long-Term Exposure to Natural Marine Environment. *Materials*, 13(17), 3900. `https://doi.org/10.3390/ma13173900`

[Liu et al., 2015] Liu, Q., Easterbrook, D., Yand, J., & Li, L. (2015). A three-phase, multi-component ionic transport model for simulation of chloride penetration in concrete. *Engineering Structures*, 86, 122–133. `https://doi.org/10.1016/j.engstruct.2014.12.043`

[Liu & Weyers, 1998] Liu, T. & Weyers, R. W. (1998). Modeling the dynamic corrosion process in chloride contaminated concrete structures. *Cement and Concrete Research*, 28(3), 365–379. `https://doi.org/10.1016/s0008-8846(98)00259-2`

[Lovato et al., 2012] Lovato, P. S., Possan, E., Molin, D. C. C. D., Masuero, A. B., & Ribeiro, J. L. D. (2012). Modeling of mechanical properties and durability of recycled aggregate concretes. *Construction and Building Materials*, 26(1), 437–447. `https://doi.org/10.1016/j.conbuildmat.2011.06.043`

[Lu et al., 2002] Lu, X., Li, C., & Zhang, H. (2002). Relationship between the free and total chloride diffusivity in concrete. *Cement and Concrete Research*, 32, 323–326. `https://doi.org/10.1016/s0008-8846(01)00664-0`

[Mangat & Molloy, 1994] Mangat, P. S. & Molloy, B. T. (1994). Prediction of long term chloride concentration in concrete. *Materials and Structures*, 27, 338–346. `https://doi.org/10.1007/bf02473426`

[Marinelli et al., 2016] Marinelli, F., van den Eijnden, A., Sieffert, Y., Chambon, R., & Collin, F. (2016). Modeling of granular solids with computational homogenization: Comparison with Biot's theory. *Finite Elements in Analysis and Design*, 119, 45–62. `https://doi.org/10.1016/j.finel.2016.05.003`

[Martin-Morales et al., 2011] Martin-Morales, M., Zamorano, M., Ruiz-Moyano, A., & Valverde-Espinosa, I. (2011). Characterization of recycled aggregates construction and demolition waste for concrete production following the spanish structural concrete code ehe-08. *Construction and Building Materials*, 25(2), 742–748. `https://doi.org/10.1016/j.conbuildmat.2010.07.012`

[Martin-Perez et al., 2001] Martin-Perez, B., Pantazopoulou, S., & Thomas, M. (2001). Numerical solution of mass transport equations in concrete structures. *Computers and Structures*, 79(13), 1251–1264. `https://doi.org/10.1016/s0045-7949(01)00018-9`

[Massart et al., 2006] Massart, T. J., Peerlings, R. H. J., & Geers, M. G. D. (2006). An enhanced multi-scale approach for masonry wall computations with localization of damage. *International Journal for Numerical Methods in Engineering*, 69(5), 1022–1059. `https://doi.org/10.1002/nme.1799`

[Mehta & Monteiro, 1988] Mehta, P. K. & Monteiro, P. J. M. (1988). Effect of aggregate, cement, and mineral admixtures on the microstructure of the transition zone. *Materials Research Society Symp. Proc.*, 114, 65–75.

[Meyer, 2008] Meyer, C. (2008). Recycled Materials in Concrete. *Developments in the Formulation and Reinforcement of Concrete*, 208–230. `https://doi.org/10.1533/9781845694685.208`

[Morga & Marano, 2015] Morga, M. & Marano, G. C. (2015). Chloride Penetration in Circular Concrete Columns. *International Journal of Concrete Structures and Materials*, 9(2), 173–183. `https://doi.org/10.1007/s40069-014-0095-y`

[Nagataki et al., 2004] Nagataki, S., Gokce, A., Saeki, T., & Hisada, M. (2004). Assessment of recycling process induced damage sensitivity of recycled concrete aggregates. *Cement and Concrete Research*, 34, 965–971. `https://doi.org/10.1016/j.cemconres.2003.11.008`

[Nagesh & Bhattacharjee, 1998] Nagesh, M. & Bhattacharjee, B. (1998). Modeling of Chloride Diffusion in Concrete and Determination of Diffusion Coefficients. *ACI Materials Journal*, 95(2), 113–120.

[Neville, 1995] Neville, A. (1995). Chloride attack of reinforced concrete: an overview. *Materials and Structures*, 28(2), 63–70. `https://doi.org/10.1007/bf02473172`

[Nilenius, 2014] Nilenius, F. (2014). *Moisture and Chloride Transport in Concrete - Mesoscale Modelling and Computational Homogenization*. Chalmers University of Technology.

[Nilenius et al., 2013] Nilenius, F., Larsson, F., Lundgren, K., & Runesson, K. (2013). *A 3D/2D Comparison between Heterogeneous Mesoscale Models of Concrete*, 249–259. Springer Netherlands. `https://doi.org/10.1007/978-94-007-6878-9_18`

[Nilenius et al., 2014] Nilenius, F., Larsson, F., Lundgren, K., & Runesson, K. (2014). FE^2 Method for Coupled Transient Diffusion Phenomena in Concrete. *Journal of Engineering Mechanics*, 141(2), 04014110. `https://doi.org/10.1061/(ASCE)EM.1943-7889.0000684`

[Nilsson et al., 1996] Nilsson, L.-O., Poulsen, E., Sandberg, P., Sørensen, H. E., & Klinghoffer, O. (1996). Chloride penetration into concrete, State-of-the-Art, Transport processes, corrosion initiation, test methods and prediction models. Technical Report 53, HETEK, Danish Road Directorate.

[Nitka et al., 2011] Nitka, M., Combe, G., Dascalu, C., & Desrues, J. (2011). Two-scale modeling of granular materials: a DEM-FEM approach. *Granular Matter*, 13(3), 277–281. `https://doi.org/10.1007/s10035-011-0255-6`

[Nokken et al., 2006] Nokken, M., Boddy, A., Hooton, R. D., & Thomas, M. D. A. (2006). Time dependent diffusion in concrete—three laboratory studies. *Cement and Concrete Research*, 36(1), 200–207. `https://doi.org/10.1016/j.cemconres.2004.03.030`

[Nuth & Laloui, 2008] Nuth, M. & Laloui, L. (2008). Advances in modelling hysteretic water retention curve in deformable soils. *Computers and Geotechnics*, 35(6), 835–844. `https://doi.org/10.1016/j.compgeo.2008.08.001`

[Ollivier & Massat, 1996] Ollivier, J.-P. & Massat, M. (1996). The effect of the transition zone on transfer properties of concrete. *Interfacial Transition Zone in Concrete, RILEM REPORT*, volume 11, (Chapter 7, 130–145). E & FN Spon.

[Ollivier & Torrenti, 2008] Ollivier, J.-P. & Torrenti, J.-M. (2008). *La structure poreuse des bétons et les propriétés de transfert*, (Chapter 3, 51–134). Presses de l'école nationale des ponts et chaussées.

[Ollivier et al., 1995] Ollivier, K. P., Maso, J. P., & Bourdette, B. (1995). Interfacial Transition Zone in Concrete. *Advanced Cement Based Materials*, 2, 30–38. `https://doi.org/10.1016/1065-7355(95)90037-3`

[Pacheco et al., 2023] Pacheco, J. N., de Brito, J., & Tornaghi, M. L. (2023). *Use of recycled aggregates in concrete: opportunities of upscaling in Europe*. JRC131294. Publications Office of the European Union. `https://doi.org/10.2760/144802`

[Page et al., 1981] Page, C., Short, N., & El Tarras, A. (1981). Diffusion of chloride ions in hardened cement pastes. *Cement and Concrete Research*, 11(3), 395–406. `https://doi.org/10.1016/0008-8846(81)90111-3`

[Pan et al., 2015] Pan, Z., Chen, A., & Ruan, X. (2015). Spatial variability of chloride and its influence on thickness of concrete cover: A two-dimensional mesoscopic numerical research. *Engineering Structures*, 95, 154–169. `https://doi.org/10.1016/j.engstruct.2015.03.061`

[Pap et al., 2018a] Pap, M., Mahler, A., & Nehme, S. G. (2018a). Analysis and Finite Element Modelling of Water Flow in Concrete. *Periodica Polytechnica Civil Engineering*. `https://doi.org/10.3311/PPci.13005`

[Pap et al., 2018b] Pap, M., Mahler, A., & Nehme, S. G. (2018b). Measurement of water retention curve for different concrete mixtures.

[Patel et al., 2017] Patel, R. A., Janez, P., & Diederik, J. (2017). Multi-scale modeling strategies to improve durability models for service life predictions of concrete structures. *XIV DBMC - 14th International Conference on Durability of Building Materials and Components*, 309–310.

[Pedro et al., 2014a] Pedro, D., de Brito, J., & Evangelista, L. (2014a). Influence of the use of recycled concrete aggregates from different sources on structural concrete. *Construction and Building Materials*, 71, 141–151. `https://doi.org/10.1016/j.conbuildmat.2014.08.030`

[Pedro et al., 2014b] Pedro, D., de Brito, J., & Evangelista, L. (2014b). Performance of concrete made with aggregates recycled from precasting industry waste: influence of the crushing process. *Materials and Structures*, 48(12), 3965–3978. `https://doi.org/10.1617/s11527-014-0456-7`

[Petcherdchoo, 2018] Petcherdchoo, A. (2018). Closed-form solutions for modeling chloride transport in unsaturated concrete under wet-dry cycles of chloride attack. *Construction and Building Materials*, 176, 638–651. `https://doi.org/10.1016/j.conbuildmat.2018.05.083`

[Pham et al., 2005] Pham, H. Q., Fredlund, D. G., & Barbour, S. L. (2005). A study of hysteresis models for soil-water characteristic curves. *Canadian Geotechnical Journal*, 42(6), 1548–1568. `https://doi.org/10.1139/t05-071`

[Ployaert, 2008] Ployaert, C. (2008). La corrosion des armatures des bétons armés et précontraints. Bulletin - technologie, FEBELCEM.

[Poulsen, 1995] Poulsen, E. (1995). Chloride Profiles: Analysis and Interpretation of Observations. Technical report.

[Pourebrahimi et al., 2023] Pourebrahimi, M., Shahhosseini, V., & Ramezanianpour, A. A. (2023). Innovative image analysis-based methods for the estimation of conventional concrete mixture proportions from hardened concrete. *Journal of Building Engineering*, 73, 106678. `https://doi.org/10.1016/j.jobe.2023.106678`

[Powers, 1958] Powers, T. C. (1958). Structure and Physical Properties of Hardened Portland Cement Paste. *Journal of the American Ceramic Society*, 41(1), 1–6. `https://doi.org/10.1111/j.1151-2916.1958.tb13494.x`

[Qi et al., 2018] Qi, B., Gao, J., Chen, F., & Shen, D. (2018). Chloride penetration into recycled aggregate concrete subjected to wetting–drying cycles and flexural loading. *Construction and Building Materials*, 174, 130–137. `https://doi.org/10.1016/j.conbuildmat.2018.04.122`

[Rangel et al., 2020] Rangel, C. S., Amario, M., Pepe, M., Martinelli, E., & Toledo Filho, R. D. (2020). Influence of Wetting and Drying Cycles on Physical and Mechanical Behavior of Recycled Aggregate Concrete. *Materials*, 13(24), 5675. `https://doi.org/10.3390/ma13245675`

[Rao et al., 2007] Rao, A., Jha, K. N., & Misra, S. (2007). Use of aggregates from recycled construction and demolition waste in concrete. *Resources, Conservation and Recycling*, 50, 71–87. `https://doi.org/10.1016/j.resconrec.2006.05.010`

[Raupach & Büttner, 2014] Raupach, M. & Büttner, T. (2014). *Concrete Repair to EN 1504: Diagnosis, Design, Principles and Practice*. CRC Press, Taylor and Francis Group. `https://doi.org/10.1201/b16852`

[Rouquerol et al., 1994] Rouquerol, J., Avnir, D., Fairbridge, C. W., Everett, D. H., Haynes, J. H., Pernicone, N., Ramsay, J. D. F., Sing, K. S. W., & Unger, K. K. (1994). Recommendations for the characterization of porous solids. *Pure and Applied Chemistry*, 66(8), 1739–1758. `https://doi.org/10.1515/iupac.66.0925`

[Russo & Lollini, 2022] Russo, N. & Lollini, F. (2022). Effect of carbonated recycled coarse aggregates on the mechanical and durability properties of concrete. *Journal of Building Engineering*, 51, 104290. `https://doi.org/10.1016/j.jobe.2022.104290`

[Sabău et al., 2021] Sabău, M., Bompa, D. V., & Silva, L. F. (2021). Comparative carbon emission assessments of recycled and natural aggregate concrete: Environmental influence of cement content. *Geoscience Frontiers*, 12(6), 101235. `https://doi.org/10.1016/j.gsf.2021.101235`

[Saetta et al., 1993] Saetta, A. V., Scotta, R. V., & Vitaliani, R. V. (1993). Analysis of Chloride Diffusion into Partially Saturated Concrete. *ACI Materials Journal*, 90(5), 441–454.

[Salomao, 2019] Salomao, D. P. (2019). Effets des méthodes de fragmentation sur la qualité des granulats de béton recyclé. ULiège University.

[Samson & Marchand, 1999] Samson, E. & Marchand, J. (1999). Numerical Solution of the Extended Nernst-Planck Model. *Journal of Colloid and Interface Science*, 215(1), 1–8. `https://doi.org/10.1006/jcis.1999.6145`

[Samson & Marchand, 2007] Samson, E. & Marchand, J. (2007). Modeling the transport of ions in unsaturated cement-based materials. *Computers and Structures*, 85(23–24), 1740–1756. `https://doi.org/10.1016/j.compstruc.2007.04.008`

[Samson et al., 2000] Samson, E., Marchand, J., & Beaudoin, J. (2000). Modeling the influence of chemical reactions on the mechanisms of ionic transport in porous materials - an overview. *Cement and Concrete Research*, 30(12), 1895–1902. `https://doi.org/10.1016/s0008-8846(00)00458-0`

[Schwartzentruber & Catherine, 2000] Schwartzentruber, A. & Catherine, C. (2000). La méthode du mortier de béton équivalent (MBE) - Un nouvel outil d'aide à la formulation des bétons adjuvantés. *Materials and Structures*, 33(8), 475–482. `https://doi.org/10.1007/bf02480524`

[Shi et al., 2012] Shi, X., Xie, N., Fortune, K., & Gong, J. (2012). Durability of steel reinforced concrete in chloride environments: An overview. *Construction and Building Materials*, 30, 125–138. `https://doi.org/10.1016/j.conbuildmat.2011.12.038`

[Simunek et al., 1999] Simunek, J., Kodesova, R., Gribb, M. M., & van Genuchten, M. T. (1999). Estimating hysteresis in the soil water retention function from cone permeameter experiments. *Water Resources Research*, 35(5), 1329–1345. `https://doi.org/10.1029/1998wr900110`

[Smit et al., 1998] Smit, R. J. M., Brekelmans, W. A. M., & Meijer, H. E. H. (1998). Prediction of the mechanical behavior of nonlinear heterogeneous systems by multi-level finite element modeling. *Computer Methods in Applied Mechanics and Engineering*, 155, 181–192. `https://doi.org/10.1016/s0045-7825(97)00139-4`

[Snyder, 1965] Snyder, M. J. (1965). Protective coatings to prevent deterioration of concrete by deicing chemicals. *National Cooperative Highway Research Program*, 16.

[Spiesz et al., 2012] Spiesz, P., Ballari, M. M., & Brouwers, H. J. H. (2012). RCM: A new model accounting for the non-linear chloride binding isotherm and the non-equilibrium conditions between the free- and bound-chloride concentrations. *Construction and Building Materials*, 27, 293–304. `https://doi.org/10.1016/j.conbuildmat.2011.07.045`

[Sun et al., 2020] Sun, C., Chen, Q., Xiao, J., & Liu, W. (2020). Utilization of waste concrete recycling materials in self-compacting concrete. *Resources, Conservation & Recycling*, 161, 104930. `https://doi.org/10.1016/j.resconrec.2020.104930`

[Sun et al., 2022] Sun, D., Cao, Z., Huang, C., Wu, K., De Schutter, G., & Zhang, L. (2022). Degradation of concrete in marine environment under coupled chloride and sulfate attack: A numerical and experimental study. *Case Studies in Construction Materials*, 17, e01218. `https://doi.org/10.1016/j.cscm.2022.e01218`

[Sun et al., 2011] Sun, G., Zhang, Y., Sun, W., Liu, Z., & Wang, C. (2011). Multi-scale prediction of the effective chloride diffusion coefficient of concrete. *Construction and Building Materials*, 25, 3820–3831. `https://doi.org/10.1016/j.conbuildmat.2011.03.041`

[Tang, 1996] Tang, L. (1996). Electrically accelerated methods for determining chloride diffusivity in concrete - current development. *Magazine of Concrete Research*, 48(176), 173–179. `https://doi.org/10.1680/macr.1996.48.176.173`

[Tang & Nilsson, 1993] Tang, L. & Nilsson, L.-O. (1993). Chloride binding capacity and binding isotherms of OPC pastes and mortars. *Cement and Concrete Research*, 23, 247–253. `https://doi.org/10.1016/0008-8846(93)90089-r`

[Thomas et al., 2013] Thomas, C., Setien, J., Polanco, J., Alaejos, P., & Sanchez de Juan, M. (2013). Durability of recycled aggregate concrete. *Construction and Building Materials*, 40, 1054–1065. `https://doi.org/10.1016/j.conbuildmat.2012.11.106`

[Tian et al., 2019] Tian, Y., Chen, C., Jin, N., Jin, X., Tian, Z., Yan, D., & Yu, W. (2019). An investigation on the three-dimensional transport of chloride ions in concrete based on X-ray computed tomography technology. *Construction and Building Materials*, 221, 443–455. `https://doi.org/10.1016/j.conbuildmat.2019.05.144`

[UEPG, 2020] UEPG (2020). European Aggregates Association: Annual Review 2019-2020. Technical report, European Aggregates Association (Union Européenne des Producteurs de Granulats).

[UEPG, 2021] UEPG (2021). European Aggregates Association: Annual Review 2020-2021. Technical report, Brussels, Belgium.

[Ukrainczyk & Koenders, 2016] Ukrainczyk, N. & Koenders, E. A. B. (2016). Numerical Model for Chloride Ingress in Cement Based Materials: Method of Lines Implementation for Solving Coupled Multi-species Diffusion with Binding. *Computations and Materials in Civil Engineering*, 1(3), 109–119.

[Van den Eijden, 2015] Van den Eijden, B. (2015). *Multi-scale modelling of the hydro-mechanical behaviour of argillaceuous rocks*. Université Grenoble Alpes.

[Van Genuchten, 1980] Van Genuchten, M. T. (1980). A Closed-form Equation for Predicting the Hydraulic Conductivity of Unsaturated Soils. *Soil Science Society of America Journal*, 44, 892:898. `https://doi.org/10.2136/sssaj1980.03615995004400050002x`

[Verruijt & Van Baars, 2007] Verruijt, A. & Van Baars, S. (2007). *Soil mechanics*. VSSD Delft.

[Whiting, 1981] Whiting, D. (1981). Rapid Measurement of the Chloride Permeability of Concrete. *Public Roads*, 45(3), 101–112.

[Winslow et al., 1994] Winslow, D. N., Cohen, M. D., Bentz, D. P., Snyder, K. A., & Garboczi, E. J. (1994). Percolation and pore structure in mortars and concrete. *Cement and Concrete Research*, 24(1), 25–37. `https://doi.org/10.1016/0008-8846(94)90079-5`

[Wu et al., 2017] Wu, L., Li, W., & Yu, X. (2017). Time-dependent chloride penetration in concrete in marine environments. *Construction and Building Materials*, 152, 406–413. `https://doi.org/10.1016/j.conbuildmat.2017.07.016`

[Wu et al., 2020] Wu, L., Wang, Y., Wang, Y., Ju, X., & Li, Q. (2020). Modelling of two-dimensional chloride diffusion concentrations considering the heterogeneity of concrete materials. *Construction and Building Materials*, 243, 118213. `https://doi.org/10.1016/j.conbuildmat.2020.118213`

[Xi et al., 1994] Xi, Y., Bazant, Z. P., Molina, L., & Jennings, H. M. (1994). Moisture Diffusion in Cementitious Materials. *Advanced Cement Based Materials*, 1, 258–266.

[Xi & Bažant, 1999] Xi, Y. & Bažant, Z. P. (1999). Modeling Chloride Penetration in Saturated Concrete. *Journal of Materials in Civil Engineering*, 11(1), 58–65. `https://doi.org/10.1061/(asce)0899-1561(1999)11:1(58)`

[Xiao et al., 2012] Xiao, J., Ying, J., & Shen, L. (2012). FEM simulation of chloride diffusion in modeled recycled aggregate concrete. *Construction and Building Materials*, 29, 12–23. `https://doi.org/10.1016/j.conbuildmat.2011.08.073`

[Xiong et al., 2020] Xiong, Q., Wang, X., & Jivkov, A. P. (2020). A 3D multi-phase meso-scale model for modelling coupling of damage and transport properties in concrete. *Cement and Concrete Composites*, 109, 103545. `https://doi.org/10.1016/j.cemconcomp.2020.103545`

[Xuan et al., 2017] Xuan, D., Zhan, B., & Poon, C. S. (2017). Durability of recycled aggregate concrete prepared with carbonated recycled concrete aggregates. *Cement and Concrete Composites*, 84, 214–221. `https://doi.org/10.1016/j.cemconcomp.2017.09.015`

[Ye et al., 2012] Ye, H., Jin, N., Jin, X., & Fu, C. (2012). Model of chloride penetration into cracked concrete subject to drying-wetting cycles. *Construction and Building Materials*, 36, 259–269. `https://doi.org/10.1016/j.conbuildmat.2012.05.027`

[Ying et al., 2013a] Ying, J., Shen, L., Xiao, J., & Bradford, M. A. (2013a). Five-phase composite sphere model for chloride diffusivity prediction of recycled aggregate concrete. *Magazine of Concrete Research*, 65(3), 573–588. `https://doi.org/10.1680/macr.12.00180`

[Ying et al., 2013b] Ying, J., Xiao, J., & Tam, V. W. Y. (2013b). On the variability of chloride diffusion in modelled recycled aggregate concrete. *Construction and Building Materials*, 41, 732–741. `https://doi.org/10.1016/j.conbuildmat.2012.12.031`

[Yiotis et al., 2006] Yiotis, A. G., Tsimpanogiannis, I. N., Stubos, A. K., & Yortsos, Y. C. (2006). Pore-network study of the characteristic periods in the drying of porous materials. *Journal of Colloid and Interface Science*, 297(2), 738–748. `https://doi.org/10.1016/j.jcis.2005.11.043`

[Yuan et al., 2009] Yuan, Q., Shi, C., De Schutter, G., Audenaert, K., & Deng, D. (2009). Chloride binding of cement-based materials subjected to external chloride environment – A review. *Construction and Building Materials*, 23, 1–13. `https://doi.org/10.1016/j.conbuildmat.2008.02.004`

[Zhang et al., 2022] Zhang, M., Zhou, B., Ruan, X., & Li, Y. (2022). A 3D random porous media model for cement mortar based on X-ray computed tomography. *Construction and Building Materials*, 341, 127750. `https://doi.org/10.1016/j.conbuildmat.2022.127750`

[Zhao et al., 2020] Zhao, Z., Courard, L., Groslambert, S., Jehin, T., Léonard, A., & Xiao, J. (2020). Use of recycled concrete aggregates from precast block for the production of new building blocks: An industrial scale study. *Resources, Conservation and Recycling*, 157, 104786. `https://doi.org/10.1016/j.resconrec.2020.104786`

[Zhao et al., 2018] Zhao, Z., Courard, L., Michel, F., Delvoie, S., Bouarroudj, M. E., & Colman, C. (2018). *Properties of concrete with recycled construction and demolition wastes: a research experience in Belgium*. Industry-Academia Forum on Advances in Structural Engineering, Tongji University, Shangai (7-9 September 2018).

[Zhao et al., 2017] Zhao, Z., Courard, L., Michel, F., Remond, S., & Damidot, D. (2017). Influence of granular fraction and origin of recycled concrete aggregates on their properties. *European Journal of Environmental and Civil Engineering*, 22(12), 1457–1467. `https://doi.org/10.1080/19648189.2017.1304281`

[Zhao et al., 2022] Zhao, Z., Xiao, J., Damidot, D., Rémond, S., Bulteel, D., & Courard, L. (2022). Quantification of the Hardened Cement Paste Content in Fine Recycled Concrete Aggregates by Means of Salicylic Acid Dissolution. *Materials*, 15(9), 3384. `https://doi.org/10.3390/ma15093384`

[Zhou et al., 2012] Zhou, A.-N., Sheng, D., Sloan, S. W., & Gens, A. (2012). Interpretation of unsaturated soil behaviour in the stress – Saturation space, I: Volume change and water retention behaviour. *Computers and Geotechnics*, 43, 178–187. `https://doi.org/10.1016/j.compgeo.2012.04.010`

[Zhou et al., 2019] Zhou, S., Sheng, W., Wang, Z., Yao, W., Huang, H., Wei, Y., & Li, R. (2019). Quick image analysis of concrete pore structure based on deep learning. *Construction and Building Materials*, 208, 144–157. `https://doi.org/10.1016/j.conbuildmat.2019.03.006`

[Zhu et al., 2019] Zhu, J., Zhang, R., Zhang, Y., & He, F. (2019). The fractal characteristics of pore size distribution in cement-based materials and its effect on gas permeability. *Scientific Reports*, 9(1). `https://doi.org/10.1038/s41598-019-53828-5`

[Zingg, 2013] Zingg, L. (2013). *Influence de la porosité et du degré d'humidité interne sur le comportement triaxial du béton*. Université de Grenoble.

[Zuquan et al., 2018] Zuquan, J., Xia, Z., Tiejun, Z., & Jianqing, L. (2018). Chloride ions transportation behavior and binding capacity of concrete exposed to different marine corrosion zones. *Construction and Building Materials*, 177, 170–183. `https://doi.org/10.1016/j.conbuildmat.2018.05.120`

[Özdemir et al., 2007] Özdemir, I., Brekelmans, W. A. M., & Geers, M. G. D. (2007). Computational homogenization for heat conduction in heterogeneous solids. *International Journal for Numerical Methods in Engineering*, 73(2), 185–204. `https://doi.org/10.1002/nme.2068`